Seismic tomography of plume-like upwellings in the French Polynesia region using Backus-Gilbert inversion

Franck Latallerie

École et observatoire des **sciences de la Terre** de l'Université de Strasbourg et du CNRS

Institut **Terre & Environnement** de **Strasbourg** | ITES | UMR 7063 de l'Université de Strasbourg & CNRS & ENGEES

Université de Strasbourg

École doctorale n°413 : Sciences de la Terre et Environnement
Institut Terre et Environnement de Strasbourg

THÈSE

présentée par
Franck Latallerie

soutenue le 5 décembre 2022

pour obtenir le grade de : **Docteur de l'Université de Strasbourg**
Discipline/ Spécialité : **Sciences de la Terre et de l'univers - Géophysique**

Seismic tomography of plume-like upwellings in the French Polynesia region using Backus-Gilbert inversion

Thèse dirigée par:
Alessia Maggi, Professeur, Université de Strasbourg
Christophe Zaroli, Maître de conférences, Université de Strasbourg
Sophie Lambotte, Physicien-adjoint, Université de Strasbourg

Rapporteurs:
Frederik J Simons, Professeur, Université de Princeton
Karin Sigloch, Directeur de recherches, Université de Nice

Autres membres du jury:
Ana Ferreira, Professeur, Université College de Londres
Laurent Stehly, Physicien-adjoint, Université de Grenoble Alpes

Président du jury:
Jérôme Vergne, Physicien, Université de Strasbourg

Abstract

Seismic tomography models play a key role in visualizing and discussing the internal structure and dynamics of the Earth. However interpreting these models is complicated by seismic data uncertainties that propagate into model uncertainties and by imperfect data coverage that produces uneven resolution; these complications can create biases and artifacts in the tomographic images. Large-scale data fitting inversions can struggle to compute and/or constrain the model resolution and uncertainties, making even harder to interpret their tomographic models. A fundamentally different type of inversion recently adapted to seismic tomography, the Backus–Gilbert SOLA inversion, provides direct control on the model resolution and uncertainties and produces them together with the model solution. In this Ph.D. thesis we aim to apply the SOLA inversion to surface wave tomography to improve the interpretations about the upper mantle structure, with a particular interest on the Pacific region.

Firstly we apply the SOLA inversion with ray theory using a two-step approach. We regionalize path-averaged profiles of S-wave velocity as a function of depth to produce a set of two-dimensional S-wave velocity maps at discrete depths. We design an interpretation workflow that helps us to interpret the tomographic model accounting for the model uncertainties and resolution provided by SOLA. Using this workflow we use statistical arguments to argue for the robustness of an anomalous pattern of slow and fast velocity bands elongated in the southeast-northwest direction below the Pacific lithosphere at $\sim$ 275 km depth. However applying SOLA in the second step of a two-step surface wave inversion suffers from certain limitations: (1) data uncertainty estimates are poor and (2) the SOLA inversion is only two-dimensional (it does not constrain the vertical resolution).

Secondly, we apply the SOLA inversion with finite frequency theory. In this framework Rayleigh-wave phase delay data can be inverted into a 3D S-wave velocity model in one linear step. We design a measurement process and estimate data uncertainties by taking into account both measurement and source errors. We apply our tomographic scheme to a synthetic case to show that the SOLA inversion is indeed applicable to finite frequency surface wave tomography. The model resolution allows us to pinpoint potential artifacts. Although further work

is required, finite frequency SOLA surface wave tomography could soon be applied on real data.

Long-term developments of the technique would allow us to improve the estimation of data uncertainties and crustal corrections or to consider other types of observables and parameters. The finite frequency SOLA surface wave tomography could also be extended into a joint inversion with body waves in the future.

Résumé

Les modèles tomographiques ont un rôle clé dans l'observation et la compréhension de la structure et de la dynamique interne de la Terre. Cependant, leur interprétation est compliquée par la propagation des incertitudes sur les données en incertitudes sur le modèle et la couverture imparfaite des données qui induit une résolution complexe ; ces complications créent des biais et artéfacts dans les images tomographiques. Pour les gros problèmes, les inversions basées sur la minimisation de l'écart entre données prédites et observées ont de grandes difficultées à contraindre et à produire la résolution et les incertitudes, rendant l'interprétation des modèles difficile. L'inversion SOLA récemment adaptée à la tomographie sismique, basée sur la théorie Backus–Gilbert, offre un contrôle direct sur les incertitudes et la résolution et, par construction, produit ces informations avec le modèle tomographique. L'objectif de cette thèse est d'appliquer l'inversion SOLA à la tomographie en ondes de surface, dans le but d'améliorer les interprétations sur la structure du manteau supérieur, avec un regard particulier sur la région du Pacifique.

Dans un premier temps, nous appliquons l'inversion SOLA dans le cadre de la théorie des rais, en utilisant une approche en deux étapes. Nous régionalisons des profils de vitesses moyennes des ondes S le long de trajets source-récepteur pour produire des cartes de vitesses des ondes S à différentes profondeurs. Nous proposons aussi une démarche d'interprétation qui intrègre les incertitudes et la résolution produites par SOLA pour analyser le modèle. Cette démarche d'interprétation nous offre des arguments statistiques robustes pour discuter l'existence d'hétérogénéités de vitesses allongées dans la direction sud-est nord-ouest sous la lithosphère du Pacifique à $\sim$275 km de profondeur. Cependant, cette première approche souffre de certaines limitations : (1) les incertitudes sur les données ne sont pas très robustes et (2) l'inversion SOLA est uniquement latérale (aucune contrainte sur la résolution verticale).

Dans un second temps, nous appliquons l'inversion SOLA dans le cadre d'une théorie fréquence-finie. Avec cette approche, les délais de phase des ondes de Rayleigh peuvent être inversés en un modèle tri-dimensionel de la vitesse des ondes S en une unique étape linéaire. Nous développons un processus de mesure et estimons les incertitudes sur les données qui incluent les erreurs sur la mesure

et sur la source sismique. Nous effectuons une tomographie synthétique pour montrer que l'inversion SOLA est en effet applicable à la tomographie fréquence-finie en ondes de surface. La résolution du modèle nous permet de pointer des artéfacts potentiels. Bien que cette approche nécessite encore quelques travaux, l'inversion SOLA en tomographie fréquence-finie des ondes de surface devrait pouvoir être appliquée bientôt avec des données réelles.

Des développements à plus long terme de cette technique pourraient inclure une meilleure estimation des incertitudes sur les données, une meilleure prise en compte de la croûte ou encore la considération d'autres types d'observables et de paramètres physiques. La tomographique fréquence-finie en ondes de surface en utilisant l'inversion SOLA pourra aussi être jointe à une inversion avec des ondes de volume.

Acknowledgements/Remerciements

Mes trois années en tant que doctorant à l'IPGS, puis à l'ITES, se terminent déjà. Je pense avoir eu beaucoup de chance d'évoluer dans ce laboratoire, et en particulier dans l'équipe sismo. J'ai pu travailler dans un environnement favorable grâce à tous les chercheurs et personnels administratifs qui font vivre ce laboratoire. J'ai eu la chance de travailler avec trois encadrants, Alessia Maggi, Sophie Lambotte et Christophe Zaroli, que j'ai d'abord croisé dans leur salle de classe lorsque j'étais étudiant à l'EOST ; puis avec qui j'ai travaillé en stage de master ; et qui m'ont fait confiance pour poursuivre nos recherches en thèse. Je les remercie tous les trois pour avoir su trouver le bon équilibre entre me laisser la liberté suffisante pour que ce travail de recherche me représente et pour avoir toujours été présents pour m'aider lorsque j'étais dans une impasse et m'aiguiller pour prendre de bonnes directions. Nos discussions informelles et nos 'meeting hebdo' du lundi matin vont beaucoup me manquer.

My three years as a PhD student at IPGS, then at ITES, are already ending. I believe I was very lucky to develop in this lab, and in particular in the seismo team. The environment was favorable thanks to all research and administration staff who give life to this lab. I was very lucky to work with three advisors, Alessia Maggi, Sophie Lambotte and Christophe Zaroli, that I met first in their classes as I was a student at EOST; then with who I worked during my master internship; and who trusted in me to continue our investigations in this PhD thesis. They gave me enough freedom for this research to represent myself and I could always find them when I needed help because I was stuck or to help me find the right directions. I will miss a lot our informal discussions and our 'meeting hebdo' every Monday mornings.

Alessia Maggi

Merci Alessia d'avoir dirigé ma thèse. Je voudrais rappeler que c'est dans votre cours de sismologie en 3ème année d'école d'ingénieurs que j'ai entendu parler de Backus-Gilbert pour la première fois et que le sujet m'a tout de suite plu. Je vous remercie pour vos conseils, sur la manière de mener la recherche, sur l'écriture scientifique, et pour l'ouverture d'esprit que vous m'avez donnée sur la tomographie en général, lorsque je n'avais que Backus–Gilbert dans mon champ

de vision.

Sophie Lambotte

Merci Sophie d'avoir co-encadré ma thèse. Tous tes conseils ont toujours été d'une grande valeur et je te remercie d'avoir souvent pris le temps de m'aider lorsque j'étais bloqué, sans hésiter parfois à mettre les mains dans mes codes.

Christophe Zaroli

Merci Christophe d'avoir co-encadré ma thèse. Toute la recherche que je présente dans ce manuscrit n'aurait pas été possible sans tes idées sur la tomograhie Backus-Gilbert. Merci pour les discussions stimulantes que nous avons pu avoir sur SOLA! Je te dois beaucoup de ma compréhension sur les méthodes inverses. Et je suis très heureux de savoir que je vais continuer à travailler en étroite collaboration sur SOLA avec toi encore quelques temps.

Frederik Simons

Merci Pr. Simons d'avoir accepté d'être dans mon comité de suivi de thèse, puis dans mon jury en tant que rapporteur. Vos conseils étaient très éclairants. Merci pour les discussions que nous avons eues quand vous êtes venu à Strasbourg pour ma soutenance. C'était un honneur pour moi. Je serai très heureux de jeter un oeil aux données de Mermaids bientôt.

Karin Sigloch

Thank you Pr. Sigloch for accepting to review my manuscript. I really appreciated the discussion on uncertainties and how SOLA may be compared with other inverse methods like Bayesians. This really stimulated me to be more open to other approaches.

Jérôme Vergne

Merci Jérôme d'avoir accepté d'être président de mon jury de thèse. C'était un plaisir pour moi que tu sois dans mon jury. J'appréciais beaucoup quand on se croisait à la terrasse du premier, dans cette période où je rédigeais ce manuscrit, et qu'on échangeait quelques mots.

Ana Ferreirai & Laurent Stehly

Merci Pr. Ferreira et Dr. Stehly d'avoir accepté d'être dans mon jury de thèse en tant qu'examinateurs, pour votre intérêt concernant mon travail de thèse et la discussion intéressante lors de la soutenance.

Dimitri Zigone

Merci Dimitri pour ta participation dans mon comité de suivi. Tes commentaires après les réunions de suivi m'ont été très utiles pour bien orienter mon travail de recherche.

Finallement j'aimerais remercier tous ceux qui ont été proche de moi durant la thèse. En particulier mes deux colocs, et amis, Simone et Hugo. Le temps de la coloc était formidable et le sous-sol me manque ;-). J'aimerais aussi remercier mes collègues et amis au labo, Luc, Rémi, Emmanuel, Mérédith, Clément, Lucille, Saman, Weiwei, Dariush et tous les autres avec qui j'ai partagé de très bons moments pendant les pauses midi, les pauses café et en dehors du labo. Vous allez beaucoup me manquer mais je suis sûr qu'on se retrouvera souvent à l'avenir. Aussi je remercie ma soeur qui m'a toujours soutenu pendant mes études. Enfin je remercie Elise, ma petite amie, qui m'a toujours soutenu et a suivi mon évolution et celle de ma thèse ces trois dernières années.

Finally I'd like to thank everyone who were close to me during the PhD. In particular my two roomates, and friends, Simone and Hugo. That was wonderful time and I miss the 'sous-sol' so much ;-). I wish to thank all my colleagues and friends in the lab, Luc, Rémi, Emmanuel, Mérédith, Clément, Lucille, Saman, Weiwei, Dariush and all the others with who I shared good time during luch breaks, coffee breaks and outside the lab. I will miss you so much but I am sure we will meet each other very often in the future. Also, I thank my sister for always supporting me during my studies. Last I thank Elise, my girlfriend, who has always supported me and followed my evolution and that of my thesis these last three years.

À ma grand-mère Marthe...

An important part of this work was achieved using the C, Fortran and Python programming languages and GNU/Linux. This manuscript was written using LaTeX.

Contents

Résumé étendu en français

Introduction

Une Terre dynamique

De nombreuses observations faites à la surface du globe montrent que la Terre est un système dynamique. En particulier, la région du Pacifique contient des modelés géologiques intéressants. Des rides océaniques sont visibles sur la carte de bathymétrie (figure 1), par exemple la ride Est-Pacifique ou la ride Pacifique-Antarctique. La profondeur du plancher océanique augmente avec la distance à la ride et la majeure partie du pourtour nord de l'océan Pacifique est consitué de fosses océaniques. Les régions d'arrière-arc qui constituent le côté continental de ces fosses océaniques sont le siège d'un volcanisme intense. Au milieu des plaques tectoniques se trouvent aussi des zones volcaniques localisées, les points chauds, par exemple Hawaï ou la Polynésie Française. Des modèles géodynamiques sont proposés pour expliquer ces observations de surface, mais des observations de l'intérieur de la Terre sont nécessaires pour les discuter. Observer la structure tri-dimensionelle interne de la Terre est le rôle de la tomographie sismique.

L'augmentation de la profondeur du plancher océanique s'explique par le refroidissement de la lithosphère lorsque celle-ci s'éloigne de la ride. Plusieurs études tomographiques ont imagé le manteau supérieur du Pacifique pour discuter différents modèles de refroidissement de la lithosphère. Par exemple une image de Ritzwoller, Shapiro & Zhong (2004) représentée sur la figure 1 montre la vitesse moyenne des ondes S en fonction de la distance à la ride dans leur modèle. En observant la transition entre les vitesses faibles et fortes, Ritzwoller, Shapiro & Zhong (2004) discutent de la profondeur de la lithosphère et comparent leur résultats à des prédictions géodynamiques. Les fosses océaniques marquent les zones de subduction, où une plaque lithosphérique plonge dans le manteau. Le contraste entre les propriétés physiques de la lithosphère et du manteau sous-jacent rend ces plaques plongeantes très visibles dans les modèles tomographiques. Par exemple une image de Zhao, Maruyama & Omori (2007) représentée sur la figure 1 illustre le plongement de la plaque Philippine dans

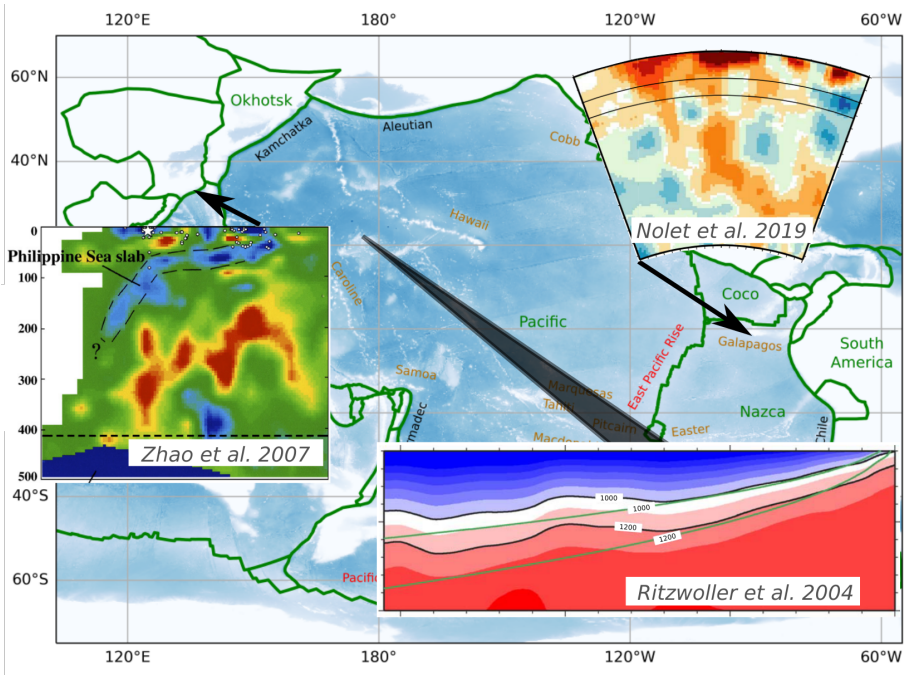

FIGURE 1: Carte de la bathymétrie dans la région du Pacifique. Sont superposées des figures extraites de Ritzwoller, Shapiro & Zhong (2004) (vitesse moyenne des ondes S en fonction de la distance à la ride), Zhao, Maruyama & Omori (2007) (plaque Philippine plongeant dans le manteau) et Nolet et al. (2019) (un panache mantellique sous les îles Galapagos).

le manteau. Il a été proposé que le volcanisme de points chauds serait alimenté par des panaches mantelliques, remontées de matériaux chauds et peu denses à travers le manteau, qui seraient déclenchés par des instabilités au niveau de la discontinuité manteau-noyau. Plusieurs études tomographiques ont cherché à imager ces panaches mantelliques avec plus ou moins de succès. Par exemple une image de Nolet et al. (2019) représentée sur la figure 1 semble montrer un panache mantellique sous les îles Galapagos.

Ces exemples illustrent les grandes avancées permises par la tomographie sismique pour la compréhension de la dynamque interne du globe ces 50 dernières années. Cependant, l'interprétation de ces images dans le détail peut s'avérer particulièrement difficile. La figure 2 oppose deux modèles tomographiques de la vitesse des ondes S à 75 km de profondeur. Bien que ces images s'accordent pour les larges anomalies de forte amplitude, de fortes différences existent pour des anomalies plus petites et de plus faible amplitude. Par exemple, sous Hawaï le modèle de gauche montre une anomalie de vitesses faibles, le modèle de droite une anomalie de vitesses fortes.

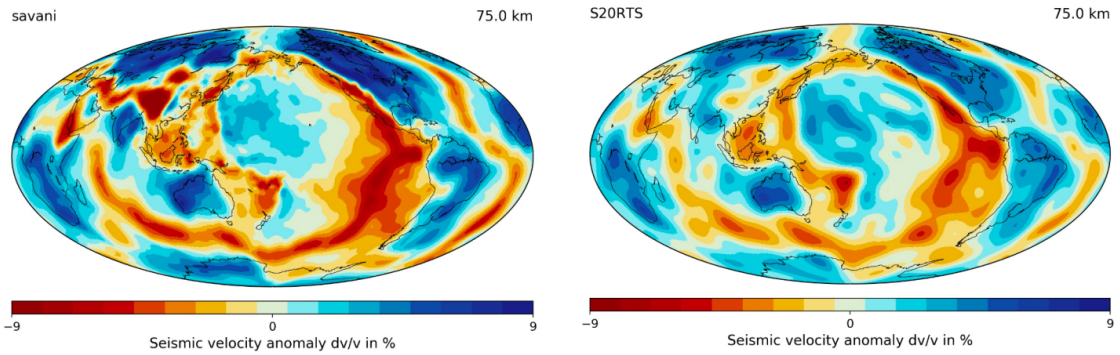

FIGURE 2: Deux modèles de la vitesse des ondes S à 75 km de profondeur. Gauche : modèle Savani de Auer et al. (2014); droite : modèle S20RTS de Ritsema, Heijst & Woodhouse (1999). Les figures ont été produites avec l'outil en ligne Submachine (Hosseini et al., 2018).

Imager la structure interne de la Terre

La tomographie sismique utilise l'information collectée par les ondes sismiques lors de leur propagation à l'intérieur de la Terre. Les ondes sismiques sont générées par les séismes qui ont lieu dans des régions géologiquement actives, comme les zones de subduction ou les rides océaniques. Les ondes sismiques sont enregistrées par les stations sismologiques qui sont réparties majoritairement sur les continents ou les îles volcaniques. La figure 3 montre que la répartition spatiale des séismes et des stations simologiques est très hétérogène, donc la couverture des données est très imparfaite. De plus, des incertitudes sont liées aux données sismologiques. Ainsi, les images tomographiques ont une résolution complexe et leur propres incertitudes. La résolution peut être vue comme un filtre, au travers duquel nous observons l'intérieur de la Terre, et qui déformerait la réalité. Par exemple une hétérogénéité circulaire peut apparaître plus ou moins forte, grossie, étalée, ou déplacée par rapport à sa position réelle. Ces deux aspects, incertitude sur le modèle tomographique et résolution, compliquent l'interprétation des images et peuvent même nous induire en erreur. Afin d'améliorer la robustesse des interprétations en tomographie, il est nécessaire de considérer la résolution et les incertitudes attachées au modèle tomographique.

L'approche classique pour construire un modèle tomographique, dite de *minimisation de l'écart aux données* (minimisation de la distance entre les données prédites par le modèle et les données observées) permet difficilement d'obtenir la résolution et les incertitudes du modèle, notamment pour les gros problèmes (beaucoup de données et de paramètres à estimer). Ces méthodes nécessitent aussi l'ajout d'un *a priori* sur la solution à trouver et n'offrent pas de contrôle sur la résolution et les incertitudes, celles-ci ne pouvant être estimées qu'une fois le

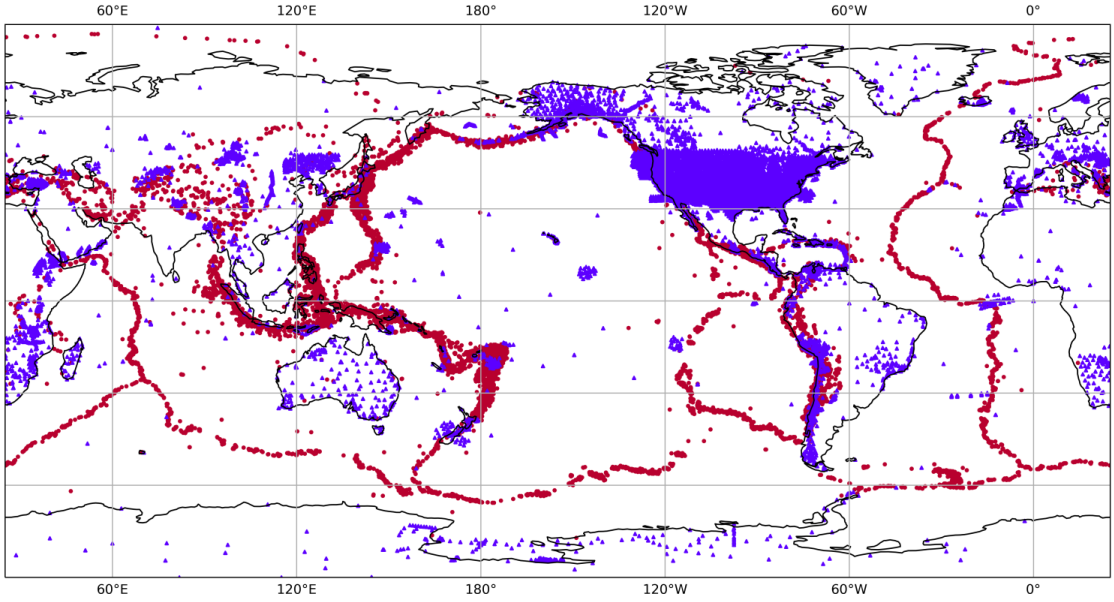

FIGURE 3: Carte illustrant un grand nombre de stations (triangles bleus) et évènements sismiques (cercles rouges) entre le 1er janvier 2010 et le 31 décembre 2017. La répartition spatiale des stations et évènements est très hétérogène.

modèle obtenu. L'objet de cette thèse est de permettre un meilleur contrôle sur les incertitudes et la résolution en tomographie en ondes de surface et d'intégrer ces informations pour mieux interpréter les modèles du manteau supérieur.

A la fin des années 60, les chercheurs Backus et Gilbert ont proposé une approche d'inversion originale permettant de résoudre certains problèmes inhérents aux approches classiques (Backus & Gilbert, 1967; Backus & Gilbert, 1968; Backus & Gilbert, 1970). La méthode Backus-Gilbert ne nécessite pas d'information *a priori*, elle offre un certain contrôle sur la résolution et les incertitudes du modèle et, par construction, produit ces informations. Dans cette thèse, nous cherchons donc à appliquer l'inversion Backus–Gilbert dans le cadre de la tomographie en ondes de surface. Nous appliquons d'abord l'inversion Backus–Gilbert dans le cadre simple de la théorie des rais pour construire des modèles 2D à profondeurs discrètes, puis dans le cadre plus élaboré d'une théorie fréquence-finie, pour construire un modèle 3D.

Théorie inverse

Considérons que nous avons établi la théorie directe, c'est-à-dire une relation $\boldsymbol{g}$, qui pour un modèle de Terre $\boldsymbol{m}$ prédit des données $\boldsymbol{d}$. Nous pouvons écrire cette relation $\boldsymbol{d} = \boldsymbol{g}(\boldsymbol{m})$. Idéalement en inversant l'opérateur $\boldsymbol{g}$ et à partir d'un jeu de

données nous pourrions retrouver le modèle de Terre. Cependant, la couverture de données étant imparfaite, l'opérateur $\boldsymbol{g}$ n'est pas inversible. Trouver un modèle de Terre à partir d'un jeu de données est une tâche difficile ; c'est l'objet du problème inverse.

Inversion de type minimisation de l'écart aux données

L'approche classique d'inversion pour obtenir un modèle de Terre est basée sur la minimisation de l'écart aux données. Puisque la théorie directe $\boldsymbol{d} = \boldsymbol{g}(\boldsymbol{m})$ permet de prédire des données pour un modèle de Terre, un modèle est recherché tel que les données prédites sont suffisamment proches des données vraiment observées. Ainsi, le modèle de Terre obtenu produit des données similaires à ce qui est observé. Cependant, la solution peut ne pas être unique : différents modèles de Terre pourraient produire un écart aux données similaire. Afin de résoudre ce problème de non-unicité de la solution, il est nécessaire d'ajouter des informations *a priori* pour mieux contraindre le problème ; c'est la *régularisation*. Par exemple, un modèle avec de grandes variations pourrait sembler physiquement inacceptable ; une contrainte sur la norme du modèle peut donc être ajoutée. Un compromis apparaît entre deux objectifs antagonistes : l'inversion doit produire un modèle qui d'une part explique les données, mais qui d'autre part ne s'éloigne pas trop de l'information *a priori*. Etant donné un *a priori*, les inversions dites minimisation de l'écart aux données (régularisées) produisent une solution qui satisfait à la fois les données et l'*a priori*. Un schéma illustrant les inversions de type minimisation de l'écart aux données est représenté sur la partie gauche de la figure 4.

Cette approche nécessite une information *a priori* ; mais dans certains cas il peut être difficile de justifier un *a priori*. C'est notamment le cas en tomographie globale où la connaissance de la structure du manteau reste encore imparfaite. A noter aussi que la solution obtenue dépend de l'information *a priori*. Ainsi, une information *a priori* érronée conduira à une solution érronée. Nous observons aussi qu'avec cette approche il n'est pas fait mention ni des incertitudes du modèle ni de sa résolution. En effet, dans les inversions de type minimisation de l'écart aux données, le modèle est obtenu sans considération de sa résolution et de ses incertitudes. Des méthodes ont été développées pour estimer ces informations mais, pour les gros problèmes tomographiques, elles ont un coût calcul important et ne conduisent souvent qu'à des estimations imparfaites. Plus important encore, si la résolution et les incertitudes du modèle sont obtenues, elle ne le sont qu'*a posteriori*, c'est-à-dire qu'aucun contrôle n'est possible sur ces quantités. Une approche

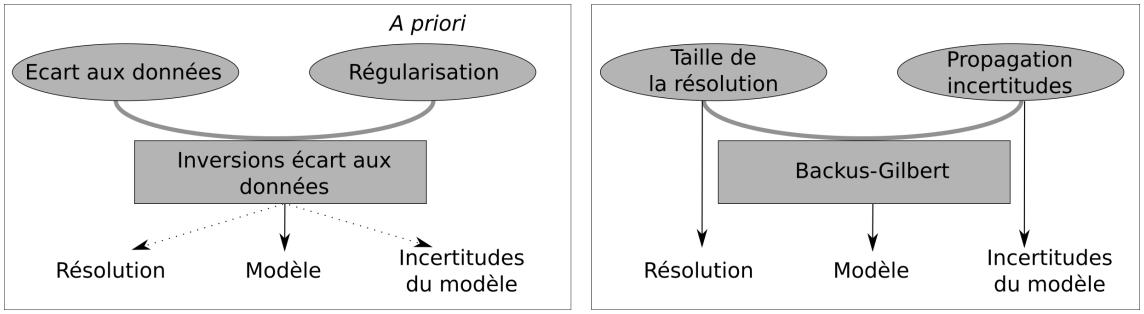

FIGURE 4: Schéma comparatif des inversions classiques dites *minimisation de l'écart aux données* à gauche et des inversions SOLA-Backus–Gilbert à droite.

fondamentalement différente, proposée par Backus et Gilbert dans les années 60, peut apporter des solutions à ces problèmes.

Inversion Backus–Gilbert

L'inversion Backus–Gilbert prend le point de vue de la résolution et des incertitudes du modèle pour résoudre le problème inverse. Elle offre ainsi un certain contrôle sur ces quantités et, par construction, les produit sans surcoût. Aussi, cette approche résout le problème inverse sans considération des données et ne nécessite aucun *a priori*.

L'inversion Backus–Gilbert ne s'applique que pour des problèmes linéaires, c'est-à-dire que la relation directe entre le modèle de Terre et les données est linéaire. Nous pouvons écrire cette relation $\boldsymbol{d} = \boldsymbol{G}\boldsymbol{m}$ où $\boldsymbol{G}$ peut être vue comme une matrice. Comme précédemment, $\boldsymbol{G}$ n'est pas inversible. Nous cherchons donc ce que l'on appelle une *inverse généralisée*, $\boldsymbol{G}^{\dagger}$, qui lie une solution $\widetilde{\boldsymbol{m}}$ aux données $\boldsymbol{d}$, soit $\widetilde{\boldsymbol{m}} = \boldsymbol{G}^{\dagger}\boldsymbol{d}$. En combinant les relations directe et inverse nous obtenons une relation entre le modèle de Terre estimé et la vraie Terre : $\widetilde{\boldsymbol{m}} = \boldsymbol{G}^{\dagger}\boldsymbol{G}\boldsymbol{m}$. Un point du modèle estimé est une combinaison linéaire des éléments du vrai modèle. Autrement dit, un point du modèle estimé est une moyenne spatiale du vrai modèle. Ce moyennage spatial est donné par le produit $\boldsymbol{G}^{\dagger}\boldsymbol{G}$. La figure 5 illustre ce concept : si l'on cherche à estimer un paramètre physique au point bleu, alors la résolution fait que la valeur estimée est une moyenne locale du paramètre physique dans une région étendue de l'espace, par exemple la région rouge ; cette fonction est appelée une *fonction de résolution*. Ainsi, chaque point du modèle estimé a sa propre fonction de résolution. L'inversion Backus-Gilbert s'applique à chaque point du modèle indépendamment : Pour un point donné, l'objectif de l'inversion Backus–Gilbert est de calculer l'inverse généralisée $\boldsymbol{G}^{\dagger}$ telle que la fonction de résolution soit la plus compacte possible. Ainsi, le

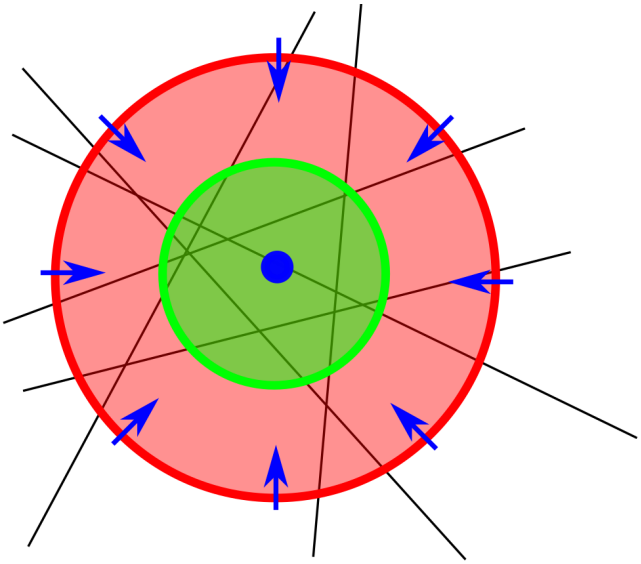

FIGURE 5: Illustration de la résolution pour la tomographie Backus–Gilbert. Le problème est d'estimer un paramètre physique au point bleu à partir des données obtenues pour les trajets illustrés par les lignes noires. La résolution signifie que la valeur estimée au point bleu sera une moyenne spatiale de la vraie Terre, par exemple la région en rouge : la *fonction de résolution*. L'inversion Backus–Gilbert cherche à minimiser la taille de cette région. L'inversion SOLA cherche à minimiser l'écart entre la fonction de résolution et une *fonction de résolution cible*, par exemple la région en vert.

point est une moyenne locale précise spatialement.

Cependant, il faut noter que les incertitudes du modèle augmentent lorsque la résolution s'améliore. En effet, lorsque l'on fixe l'inverse généralisée $G^\dagger$ on fixe aussi la propagation des incertitudes sur la donnée en incertitudes sur le modèle par la relation $C_{\tilde{m}} = (G^\dagger)^T C_d G^\dagger$. Intuitivement, plus la résolution est bonne en un point du modèle plus la quantité de données utilisée pour contraindre la valeur à estimer en ce point est faible (longueur de rai qui tombe dans la fonction de résolution) et donc les incertitudes attachées à la valeur estimée en ce point sont plus élevées. L'inversion Backus–Gilbert cherche donc une inverse généralisée telle que la résolution soit la meilleure possible, tout en garantissant une propagation faible des incertitudes. Le schéma de droite sur la figure 4 illustre le compromis dans le cadre de l'inversion Backus–Gilbert.

La formulation originale de l'inversion Backus–Gilbert n'a pas trouvé de nombreuses applications en tomographie sismique car elle s'avère avoir un coût calcul très important. Dans les années 90, les chercheurs Pijepers et Thompson ont proposé une formulation alternative plus efficace en terme de coûts calcul, tout en conservant les avantages de l'inversion Backus–Gilbert originale (Pijpers & Thompson, 1992; Pijpers & Thompson, 1993). Ils ont nommé cette reformulation

l'inversion SOLA pour *Subtractive Optimally Localized Averages* (que l'on pourrait traduire par *moyennes locales optimales par différences*).

L'inversion SOLA cherche toujours à calculer une inverse généralisée $\boldsymbol{G}^{\dagger}$ en considérant un compromis entre résolution et incertitudes. Cependant, contrairement à l'inversion originale qui cherche à minimiser l'étalement spatial d'une fonction de résolution, l'inversion SOLA cherche à minimiser l'écart entre la fonction de résolution et une *fonction de résolution cible* prédéfinie. Le schéma de droite sur la figure 4 illustre le compromis dans le cadre de l'inversion SOLA en remplaçant le label *taille de la résolution* par *écart à la résolution cible*. L'inversion SOLA a été introduite et adaptée à la tomographie sismique par Zaroli (2016) et appliquée à la tomographie en ondes de volume. L'objet de cette thèse est d'appliquer l'inversion SOLA à la tomographie en ondes de surface.

Tomographie SOLA en théorie des rais

Classiquement, la tomographie en ondes de surface commence par une mesure de dispersion qui détermine un délai de phase (ou de groupe) en fonction de la fréquence pour chaque paire source-récepteur. Ensuite, l'inversion fait appel à un processus en deux étapes. Une approche possible est de considérer d'abord chaque paire source-récepteur indépendammment. Pour une paire donnée, une inversion (non-linéaire) avec la profondeur permet d'obtenir un modèle radial de vitesses moyennées le long du trajet en fonction de la profondeur. La seconde étape considère alors les profondeurs indépendamment : une inversion linéaire latérale permet de construire un modèle 2D à une profondeur donnée à partir des vitesses moyennes le long des trajets à cette profondeur. Cette seconde étape, dite *régionalisation*, est linéaire donc l'inversion SOLA est applicable. Appliquer l'inversion SOLA pour l'étape de régionalisation dans le cadre de la théorie des rais est l'objet de cette première approche.

Données et méthode

Le problème direct considéré dans cette première approche est illustré sur la figure 6. Nous utilisons les profils de vitesses moyennes des ondes S le long des rais obtenus par Maggi et al. (2006b). Une estimation de leur incertitude, obtenue en comparant les trajets proches, est aussi disponible. Pour une profondeur, nous avons donc un jeu de données et leur incertitude que nous pouvons relier linéairement, avec la théorie des rais, à un modèle 2D de la vitesse des ondes S à la profondeur considérée.

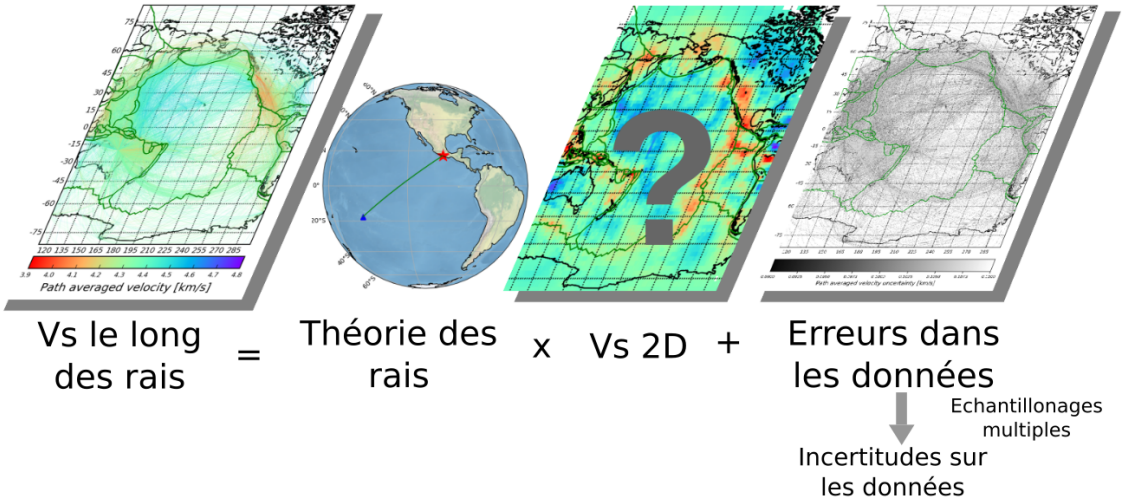

FIGURE 6: Illustration du problème direct pour la régionalisation (deuxième étape de l'inversion en deux étapes) dans le cadre de la théorie des rais. A gauche sont représentés les trajets source-récepteur, colorés en fonction des vitesses moyennes des ondes S le long des rais issues de la première étape à 75 km de profondeur. La théorie des rais permet de relier ces données à la vitesse des ondes S à 75 km de profondeur. A droite est représentée l'incertitude pour chaque rai obtenue en comparant les trajets proches.

En chaque point du modèle, la résolution cible est définie comme une région circulaire dont le rayon est calculé à partir de la couverture de données. Aux endroits où la couverture est bonne, nous cherchons une bonne résolution et *vice versa*. De cette manière nous homogénéisons spatialement la distribution des incertitudes du modèle. Sur la figure 4.1(b) est représentée la densité de données à 75 km de profondeur (la somme des longueurs de rais qui tombe dans une cellule normalisée par la somme des longueurs de rais totale). A partir de la densité de données, nous calculons le rayon de la fonction de résolution cible en chaque point. Les rayons des fonctions de résolution cibles à 75 km de profondeur sont donnés sur la figure 4.1(c). Quelques exemples de fonctions de résolution cibles sont donnés sur la figure 4.2(a).

Résultats

Nous inversons les profils de vitesses à différentes profondeurs avec l'inversion SOLA pour trois compromis résolution-incertitudes différents. Les figures 4.2(b), (c) et (d) montrent quelques fonctions de résolution obtenues à 75 km de profondeur, pour les trois compromis choisis, des résultats les moins bien résolus aux mieux résolus respectivement.

La figure 4.3 montre l'ensemble des résultats tomographiques obtenus pour les trois compromis résolution-incertitudes à 75 km de profondeur. Les colonnes gauche, centrale et droite correspondent respectivement aux résultats les moins, moyennement et mieux résolus. La première ligne montre les cartes de résolution qui sont un résumé de l'information sur la résolution. En chaque point du modèle, ces cartes donnent le rayon d'un cercle qui contient 68% de la fonction de résolution. On observe en effet que la résolution est meilleure pour la carte la plus à droite. Bien sûr, à une amélioration de la résolution doit correspondre une augmentation des incertitudes du modèle. Les incertitudes du modèle sont données sur les cartes de la deuxième ligne. En effet les résultats les mieux résolus sont aussi les plus incertains. Enfin les cartes de la dernière ligne montrent les modèles tomographiques obtenus. On observe qu'un modèle mieux résolu montre plus de détails ; mais ces détails sont aussi plus incertains.

Cette première approche montre que l'inversion SOLA est applicable à la tomographie en ondes de surface dans le cadre de la théorie des rais. L'inversion SOLA produit des modèles tomographiques au moins aussi satisfaisants qu'avec d'autres méthodes d'inversion, tout en offrant un contrôle direct sur la résolution et les incertitudes du modèle.

Interprétations

Avec le modèle tomographique et l'information sur sa résolution et ses incertitudes, l'objectif est maintenant de faire des interprétations robustes. Dans la suite de l'analyse, nous nous concentrons sur les résultats du compromis résolution-incertitudes correspondant aux résultats de la colonne centrale de la figure 4.3. Pour cette analyse nous avons développé une démarche d'interprétation qui intègre l'information sur la résolution et les incertitudes ; notamment pour discuter des anomalies de vitesses par rapport à un modèle de référence. La figure 7 illustre cette démarche d'interprétation.

Il faut commencer par définir un modèle de référence que nous allons tester avec nos observations tomographiques. Cette référence peut être une prédiction géodynamique. Dans cette étude nous utilisons un modèle de refroidissement de la lithosphère, qui modélise le manteau comme un demi-espace infini qui refroidit par diffusion.

Contrairement aux valeurs du modèle de référence qui sont des prédictions

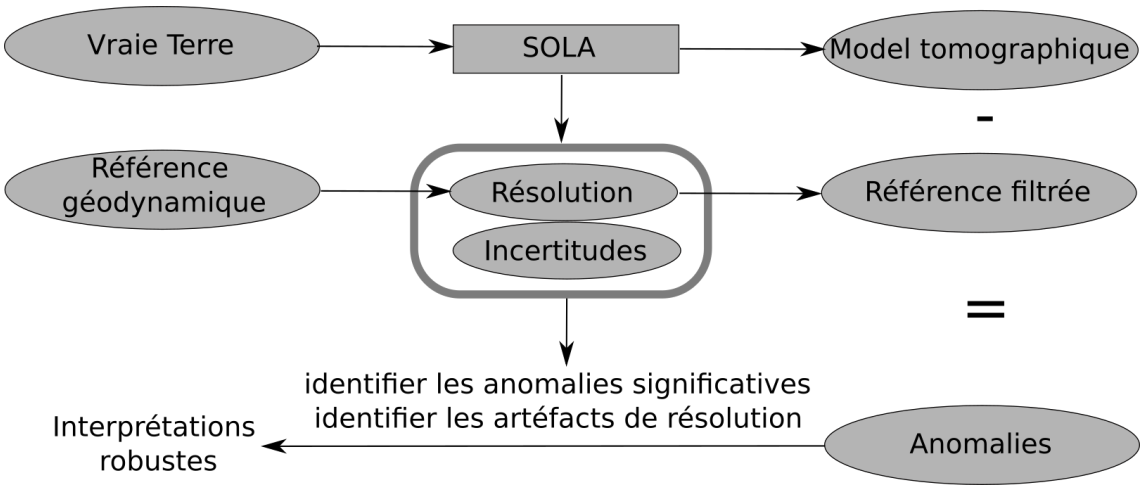

FIGURE 7: Schéma illustrant la démarche d'interprétation du modèle qui intrègre la résolution et les incertitudes du modèle.

en des points absolus de l'espace, les valeurs estimées dans le modèle tomographique sont des moyennes locales ; le modèle tomographique est une version déformée de la réalité, 'filtrée' par la résolution. Ainsi, les modèles tomographiques ne devraient pas être comparés directement aux modèles de référence. Dans cette étude, puisque l'inversion SOLA nous a fourni l'information complète sur la résolution du modèle tomographique, nous pouvons 'filtrer' le modèle de référence par la résolution pour obtenir deux quantités comparables : des observations de la Terre et des valeurs de référence qui sont toutes deux des moyennes locales. Les figures 4.6(a) et (b) représentent le modèle tomographique et le modèle de référence filtré par la résolution à 75 km de profondeur.

Nous pouvons alors calculer les anomalies de vitesses dans le manteau comme la différence entre le modèle tomographique et la référence filtrée par la résolution. Les anomalies de vitesses sont données sur la figure 4.6(c). Comme nous connaissons les incertitudes sur le modèle, nous pouvons diviser chaque valeur d'anomalie par l'incertitude correspondante pour exprimer les anomalies de vitesses en termes de barres d'erreur $\sigma_{\widetilde{m}}$. Ainsi, par exemple, une valeur supérieure à 1 peut être interprétée comme une vitesse anormalement grande qui sort des barres d'erreur (au sens Gaussien). Les anomalies exprimées sous cette forme sont données sur la figure 4.6(d). Pour focaliser l'interprétation sur les anomalies significatives, les figures 4.6(e) et (f) représentent ces anomalies de vitesses avec les valeurs dans l'intervalle $[-1, 1]$ et $[-2, 2]$ masquées respectivement.

A 75 km de profondeur, on observe que les masques pour $1\sigma_{\widetilde{m}}$ et $2\sigma_{\widetilde{m}}$ (figures 4.6(e) et (f)) cachent environ 68% et 95% des pixels respectivement. Aussi, les pixels restant ne semblent pas agrégés localement en structures cohérentes. Ces

observations sont attendues dans le cas où le modèle tomographique ne dévie pas significativement du modèle de référence. Nous pouvons donc conclure que le jeu de données utilisé dans cette étude ne permet pas de rejeter ce modèle de refroidissement de la lithosphère à 75 km de profondeur.

La figure 4.8 montre les résultats obtenus à 275 km de profondeur. A cette profondeur, les masques laissent apparaître une structure en bandes allongées dans la direction sud-est–nord-ouest, comme indiquée sur la figure par les lignes noires. Ces bandes apparaissent avec le masque à $1\sigma_m$ mais aussi avec le masque à $2\sigma_m$. Elles sont donc robustes au sens des incertitudes. Cependant, de telles structures allongées peuvent être un artéfact produit par une résolution anisotrope. Dans notre étude, puisque nous avons l'information complète sur la résolution, nous pouvons vérifier cette hypothèse. La figure 4.10 représente une sélection de fonctions de résolution dans le Pacifique. On observe que la résolution semble bien focalisée et circulaire. Ces bandes allongées ne sont donc sûrement pas un artéfact dû à une distribution azimutale hétérogène des données : elles sont robustes au sens de la résolution. De telles bandes ont aussi été observées par Montagner (2002) et French, Lekic & Romanowicz (2013a). Il est intéressant de noter que ces bandes sont allongées dans la direction du mouvement absolu de la plaque Pacifique. Il est possible que nous imagions ici un mode de convection qui apparaît naturellement perpendiculairement au mouvement d'une plaque rigide (lithosphère) sur un milieu ductile (asthénosphère) : les *cellules de convection sous-lithosphèriques à petite échelle* (e.g. Ballmer et al., 2009).

Conclusion

Dans cette première approche basée sur la théorie des rais, nous avons construit un modèle tomographique du manteau supérieur dans le Pacifique à partir de données d'ondes de surface en utilisant un processus en deux étapes. La première étape, effectuée par Maggi et al. (2006b) en utilisant une inverison non-linéarie, a produit des profils de vitesses moyennées le long des rais. La seconde étape est linéaire et nous avons pu utiliser l'inversion SOLA pour construire un jeu de modèles de vitesses 2D à différentes profondeurs. L'inversion SOLA s'est avérée être un outil très puissant dans cette régionalisation de données d'ondes de surface pour contrôler la résolution et les incertitudes du modèle tomographique, et considérer ces informations pour intepréter avec robustesse le modèle. Cependant, cette approche souffre de certaines limites, dont notamment : (1) l'estimation des incertitudes sur les données peut être améliorée et

(2) l'inversion SOLA n'a pu produire que des modèles 2D à profondeurs discrètes (la résolution verticale n'est pas considérée). Dans la section suivante, nous appliquons l'inversion SOLA dans le cadre d'une théorie plus élaborée, dite fréquence-finie, pour construire un modèle 3D de la vitesse des ondes S dans le manteau supérieur avec l'inversion SOLA.

Tomographie SOLA en théorie fréquence-finie

Dans le dernier volet de cette thèse, nous utilisons une théorie fréquence-finie pour relier des mesures de délais de phase à la distribution tri-dimensionelle de la vitesse des ondes S dans le manteau supérieur. Afin de linéariser le problème, pour pouvoir appliquer l'inversion SOLA, nous travaillons dans le cadre de l'approximation de Born.

Données et méthode

La théorie directe utilisée dans cette deuxième approche est basée sur le phénomène de diffusion. Les hétérogénéités du manteau ont pour effet de diffuser une partie de l'énergie du champ d'ondes primaire émis par une source sismique, produisant des champs d'ondes diffusés, qui sont tous observés au niveau des stations sismologiques. Ainsi, la donnée mesurée à une station contient de l'information sur les propriétés physiques tri-dimensionelles du manteau. Le problème direct est illustré sur la figure 8. Un délai de phase pour une paire source-récepteur, à une fréquence donnée, est relié à la distribution 3D de la vitesse des ondes S dans la Terre par un *noyau de sensibilité* 3D. Les incertitudes sur les données sont estimées par une technique de type *Monte Carlo*.

Nous utilisons les programmes informatiques de Zhou, Dahlen & Nolet (2004) pour calculer les noyaux de sensibilité. Nous avons développé un programme informatique pour calculer un délai de phase entre un sismogramme synthétique pour une Terre de référence radiale et un sismogramme observé. La figure 9 illustre le processus de mesure. Nous utilisons le programme *MINEOS* (e.g. Masters, Misha & Susan, 2014) pour calculer le sismogramme synthétique par sommation de modes propres. Nous utilisons ensuite une technique de fenêtrage multiple pour isoler, en temps, la partie du signal concernée. Cette technique a l'avantage de faire appel à plusieurs fenêtres temporelles et nous pouvons donc obtenir une estimation de l'incertitude en observant la dispersion des mesures. Nous filtrons ensuite les signaux dans des bandes de fréquences étroites et nous calculons leur

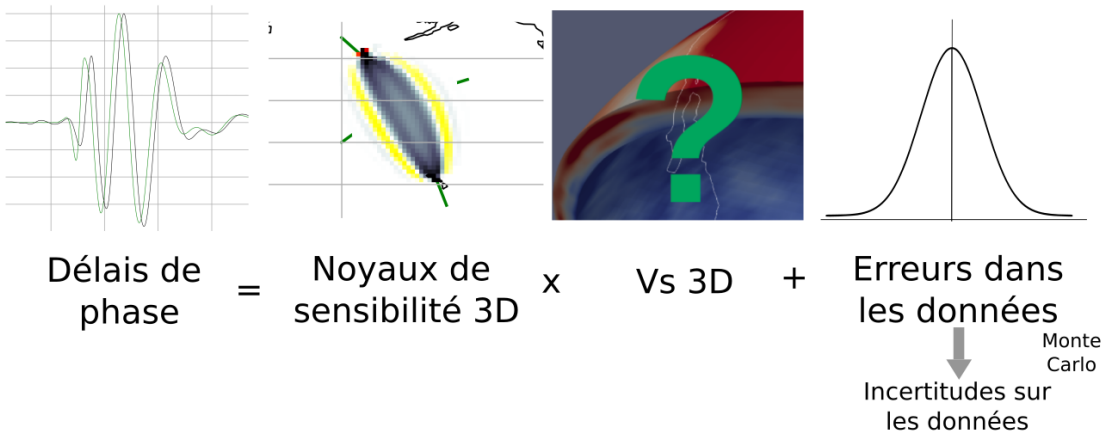

FIGURE 8: Illustration du problème direct dans le cadre de la théorie fréquence-finie. Un noyau de sensibilité 3D relie un délai de phase à la distribution 3D de la vitesse des ondes S. Une estimation des incertitudes sur les données est obtenue par une technique de type *Monte Carlo*.

spectre en phase. Par soustraction, nous obtenons le délai de phase en fonction de la fréquence pour chaque fenêtre temporelle.

Nous estimons aussi les incertitudes dues à la connaissance imparfaite de la source sismique. Une erreur est associée à chaque paramètre de la source (origine spatiale et temporelle et composantes du tenseur des moments sismiques). Nous simulons donc des sources en perturbant ces paramètres et nous effectuons les mesures. En observant la dispersion des mesures nous pouvons déduire une incertitude en fonction de la fréquence que nous ajoutons à l'incertitude obtenue par la technique de fenêtrage multiple.

Nous commençons par un cas synthétique dans lequel le rôle de la vraie Terre est joué par un modèle de Terre 3D connu. Les formes d'ondes pour ce modèle de Terre sont calculées avec le programme *specfem*, basé sur une méthode aux éléments spectraux. Cette tomographie synthétique doit nous permettre d'évaluer la robustesse et le potentiel du processus tomographique développé dans cette section. Notons que cette étude est restreinte à la composante verticale du mode fondamental des ondes de Rayleigh.

Résultats

Les résultats de cette tomographie synthétique sont représentés sur la figure 5.21. La colonne de gauche montre le modèle d'entrée à 37 km et 112 km de profondeur et la colonne de droite le modèle obtenu aux profondeurs correspondantes. Bien

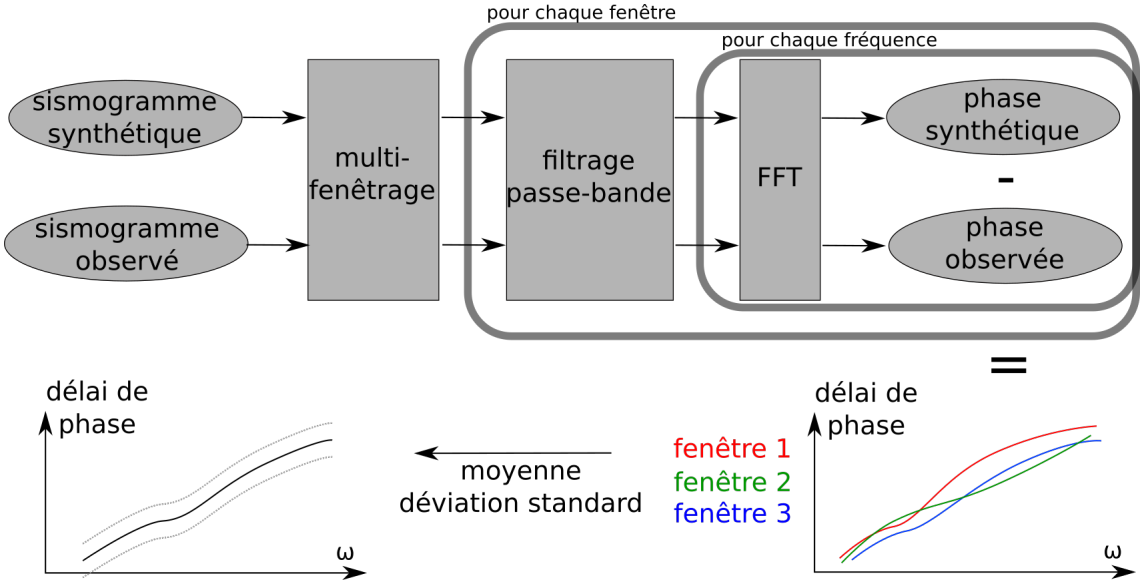

FIGURE 9: Illustration du processus de mesure de délais de phase en utilisant la technique de fenêtrage multiple et la transformation de Fourier rapide (FFT pour *Fast Fourier Transform*).

que le jeu de données soit extrêmement petit, nous retrouvons les structures majeures : l'anomalie de vitesses faibles correspondant à la ride Est Pacifique, les anomalies de vitesses faibles qui encerclent les plaques Nazca et Philippine et l'augmentation des vitesses avec la distance à la ride. L'anomalie de vitesses faibles au niveau de Samoa est bien identifiée à 37 km de profondeur et l'anomalie de vitesses élevées correspondant au craton Australien est aussi bien marquée à 112 km de profondeur.

Les incertitudes sur le modèle sont extrêmement faibles. Ceci est sûrement dû à une forte sous-estimation des incertitudes sur les données. Il faudra améliorer l'estimation des incertitudes sur les données à l'avenir pour pouvoir prendre en compte les incertitudes sur le modèle dans l'analyse.

Nous pouvons observer la résolution pour évaluer son potentiel dans l'analyse du modèle. L'encadré à gauche de la figure 10 montre la résolution au niveau de l'anomalie de vitesses faibles dans la région de Samoa (cercle vert), pour un point à 37 km et un point à 112 km de profondeur. A 37 km de profondeur, la fonction de résolution centrée sur Samoa est bien focalisée. En observant une telle fonction de résolution, nous pourrions dire que l'anomalie de vitesses faibles au niveau de Samoa est bien résolue ; or cette anomalie est en effet bien présente dans le modèle d'entrée. A 112 km de profondeur, la résolution latérale est un peu moins bonne car la sensibilité est moins forte. Dans cette approche la résolution est 3D ; ainsi nous pouvons analyser la résolution verticale. Sur les coupes verticales de la figure 10 pour la région de Samoa, nous observons que la fonction de résolution

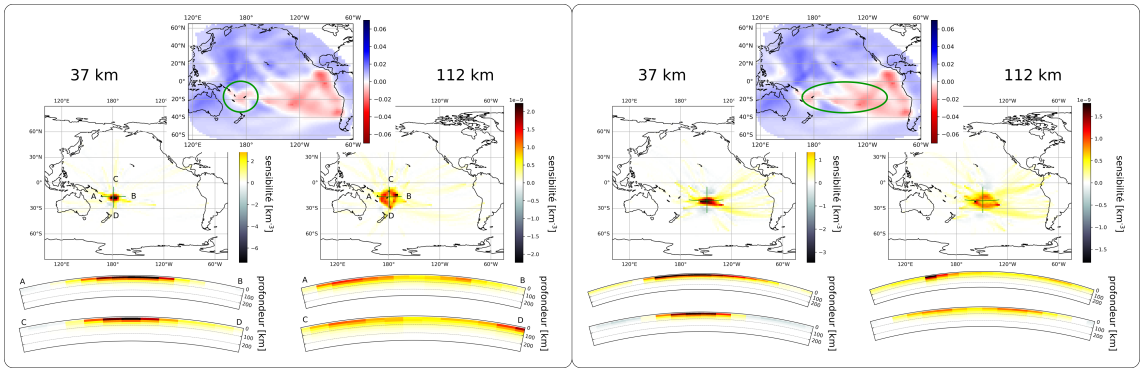

FIGURE 10: Illustration de la résolution tri-dimensionelle dans la région de Samoa (gauche) et à l'est de Samoa (droite) pour un point à 37 km et un point à 112 km de profondeur.

pour un pixel à 112 km de profondeur semble avoir des valeurs significatives à des profondeurs plus superficielles ; une partie non négligeable de l'information pour estimer la vitesse à 112 km de profondeur provient de profondeurs plus superficielles. On observe ici un artéfact vertical ; il y a 'fuite d'information avec la profondeur'. Si nous voulions discuter en détail la profondeur d'une structure, par exemple la profondeur de la lithosphère, cet artéfact vertical pourrait induire en erreur nos conclusions. Dans un cas réel, l'information sur la résolution 3D produite par l'inversion SOLA dans le cadre de la théorie fréquence-finie nous permettrait d'être au fait de ce problème. Pour éviter cet artéfact vertical, il faudra augmenter la densité de données en profondeur, en considérant notamment les modes supérieurs.

A l'est de Samoa, nous observons une anomalie de vitesses faibles qui ne se trouve pas dans le modèle d'entrée (ellipse verte, encadré à droite de la figure 10). La fonction de résolution dans cette région montre que le moyennage spatial pour estimer la vitesse à l'est de Samoa a pris en compte l'information de Samoa à l'ouest, et de la ride Est-Pacifique à l'est ; or ces régions ont des vitesses faibles ce qui peut expliquer la vitesse apparente faible à l'est de Samoa. Il y a un artéfact latéral ; la résolution a pour effet d'étaler latéralement l'information dans cette région. Dans un cas réel, la résolution nous permettrait d'être au fait de cet artéfact latéral.

Conclusion

Dans cette section nous avons appliqué l'inversion SOLA dans le cadre d'une théorie fréquence-finie avec l'approximation de Born. Cette théorie nous permet de relier directement, en une unique relation linéaire, des délais de phase à la

distribution 3D de la vitesse des ondes S. Ainsi, l'inversion SOLA est applicable en trois dimensions.

Nous avons développé un algorithme de mesure de délais de phase entre une forme d'onde observée et une forme d'onde synthétique obtenue par sommation de modes propres pour un modèle de Terre radial. Cet algorithme utilise la technique de fenêtrage multiple pour produire des délais de phase robustes avec une estimation de l'incertitude de mesure. Nous avons aussi estimé l'incertitude due la connaissance imparfaite de la source sismique.

Afin de valider le processus tomographique, et cerner avec précision l'apport de l'inversion SOLA dans le cadre de la théorie fréquence-finie, nous avons fait une tomographie synthétique où la vraie Terre est remplacée par un modèle 3D que nous cherchons à retrouver. Cette tomographie synthétique a montré que l'inversion SOLA est applicable pour la tomographie en ondes de surface en 3D, dans le cadre de la théorie fréquence-finie. L'inversion SOLA offre un contrôle sur la propagation des incertitudes et la forme de la résolution 3D. La comparaison du modèle d'entrée au modèle obtenu permet de valider le processus tomographique. Nous constatons cependant que les incertitudes sur le modèle sont extrêmement faibles. Il faudra améliorer à l'avenir l'estimation des incertitudes sur les données. Nous montrons que la résolution permet d'analyser finement le modèle, notamment en mettant au jour des artéfacts, comme des artéfacts verticaux (fuite verticale d'information en profondeur), ou latéraux (étalements latéraux d'anomalies de vitesses).

Maintenant que le processus tomographique est validé par la tomographie synthétique, de nombreuses voies d'amélioration et d'application sont possibles, notamment:

- Augmenter le jeu de données pour qu'il soit plus réaliste ;
- Appliquer le processus tomographique à des données réelles ;
- Améliorer l'estimation des incertitudes sur les données ;
- Considérer les modes supérieurs ;
- Considérer d'autres observables (e.g. amplitude, polarisation) ;
- Considérer d'autres paramètres (e.g. Vp, attenuation, anisotropie).

Lorsque le processus tomographique développé dans cette section sera appliqué avec des vraies données, la démarche d'interprétation proposée dans la section précédente (figure 7) nous permettra d'analyser avec robustesse les structures tri-dimensionnelles imagées dans le manteau supérieur.

Conclusion générale et perspectives

Les modèles tomographiques jouent le rôle d'observations afin de mieux comprendre la dynamique interne de la Terre. Cependant, les données sismiques sont bruitées et la couverture spatiale des données est imparfaite. Ainsi, les modèles tomographiques ont une résolution complexe qui peut induire des biais et des artéfacts et les incertitudes sur les données se propagent en incertitudes sur le modèle. Les méthodes classiques basées sur une minimisation de l'écart aux données ont de grandes difficultées pour contrôler et produire la résolution et les incertitudes des modèles tomographiques.

L'inversion SOLA récemment introduite en tomographie sismique par Zaroli (2016) prend le point de vue de la résolution et des incertitudes du modèle pour résoudre le problème inverse. Bien que l'inversion SOLA ne soit applicable que pour des problèmes linéaires, elle offre un certain contrôle sur la résolution et les incertitudes et produit ces informations sans surcoût calcul. L'objectif de ce travail de thèse était d'appliquer l'inversion SOLA à la tomographie en ondes de surface pour intépréter avec robustesse la structure du manteau supérieur dans la région du Pacifique.

En première approche nous avons appliqué l'inversion SOLA dans le cadre de la théorie des rais. Une première inversion non-linéaire, effectuée par Maggi et al. (2006b), a produit des profils de vitesses moyennes des ondes S le long de trajets source-récepteur. Nous utilisons l'inversion SOLA pour régionaliser ces profils en des cartes de vitesses à différentes profondeurs. L'inversion SOLA offre un certain contrôle sur la résolution et les incertitudes et les modèles sont très satisfaisants. Nous proposons aussi un schéma d'interprétation qui intègre les incertitudes et la résolution pour analyser avec robustesse le modèle tomographique par rapport à un modèle de référence. Ainsi, nous pouvons conclure que le jeu de données utilisé dans cette étude ne permet pas de rejeter un modèle simple de refroidissement de la lithosphère à 75 km de profondeur, mais qu'il existe dans l'asthénosphère des anomalies de vitesses allongées dans la direction de mouvement absolu de la plaque Pacifique. Cette première approche est une étape vers des interprétations plus robustes pour la tomographie du manteau supérieur avec les ondes de surface. Cependant, cette approche présente deux grandes limites : (1) l'estimation des incertitudes sur les données doit être améliorée et (2) l'inversion SOLA n'a pu être appliquée que latéralement, ne produisant que des cartes 2D à profondeurs discrètes (pas de résolution verticale).

En deuxième approche nous avons appliqué l'inversion SOLA dans le cadre

d'une théorie fréquence-finie pour relier des mesures de délais de phase à la distribution 3D de la vitesse des ondes S. Nous avons développé un algorithme pour mesurer les délais de phase et estimer leur incertitude. Nous avons fait une tomographie synthétique qui nous a permi d'évaluer la robustesse et le potentiel de cette seconde approche. Nous avons montré comment l'inversion SOLA, combinée à la théorie fréquence-finie, permet de contrôler et produire la résolution et les incertitudes avec le modèle tomographique, le tout en trois dimensions. Enfin nous avons montré que l'information sur la résolution 3D est un atout essentiel pour identifier des artéfacts dans le modèle, comme des artéfacts verticaux (fuite d'information avec la profondeur), ou latéraux (étalements latéraux d'anomalies de vitesses). Lorsque cette approche sera appliquée à des données réelles, la démarche d'interprétation qui intrègre résolution et incertitudes pourra être appliquée pour discuter les structures tri-dimensionelles imagées dans le manteau supérieur. Cette seconde approche ouvre la voie à de nombreuses améliorations possibles. Par exemple il sera possible d'imager d'autres paramètres physiques que la vitesse des ondes S ; et des comparaisons entre les modèles plus robustes seront possibles grâce au contrôle et à l'information sur la résolution et les incertitudes.

Comme la tomographie en théorie fréquence-finie rend la tomographie en ondes de surface tri-dimensionelle, il sera possible de mettre en place une inversion jointe avec des ondes de volume. Dans ce cas l'inversion SOLA nous permettra d'évaluer le gain de résolution, notamment aux profondeur où ondes de surface et ondes de volumes sont complémentaires, par exemple dans la zone de transition entre le manteau supérieur et le manteau inférieur (discontinuités à 410 km et 670 km de profondeur).

Le travail achevé dans cette thèse permet de contrôler et de quantifier la résolution et les incertitudes des modèles tomographiques du manteau supérieur construits à partir de données d'ondes de surface. A terme, ce travail permettra d'avoir une connaissance plus fiable de la structure tri-dimensionnelle du manteau supérieur et ainsi de mieux comprendre la dynamique interne de la Terre.

Chapter 1

Introduction

Maheu disait:
-C'est le premier accrochage. Nous sommes à trois cent vingt mètres... Regardez la vitesse.
Levant sa lampe, il éclaira un madrier des guides, qui filait ainsi qu'un rail sous un train lancé à toute vapeur ; et, au-delà, on ne voyait toujours rien. Trois autres accrochages passèrent, dans un envolement de clartés. La pluie assourdissante battait les ténèbres.
- Comme c'est profond ! murmura Etienne.

Zola, *Germinal*, 1885.

1.1 Toward a three-dimensional picture of the Earth

The seismicity and volcanism observable at the surface show that the Earth is a dynamic system that is cooling. Therefore it must have a three-dimensional structure. Over three centuries ago, Kircher, in his *Mundus Subterraneus* (1664) proposed that the Earth was an old sun that cooled down, but that still contained remaining magma reservoirs connected to the surface that fed the volcanism (figure 1.1). Of course the modern picture of the Earth interior has greatly changed with the improvement of physical theories and the accumulation of data. However, there is still no model that makes complete consensus. In 1915 Alfred Wegener proposed that continents were once grouped into one that he named 'Pangea' (Wegener, 1922). The idea that continents could drift over thousands of kilometers was first received with strong criticism. At that time, a correct mechanism to explain how continents could drift over such distances was lacking. Soon, it became the *plate tectonic* hypothesis that is widely assumed in the Earth science community today.

In the modern version of plate tectonics, the shallowest layer of the Earth, the lithosphere (ranging from 0 km to ∼150 km below the oceans) is mechanically rigid and split into several plates (DeMets et al., 1990; Bird, 2003). These plates move with respect to each other over a softer layer: the asthenosphere (McKenzie & Parker, 1967). Temperature can be used as a proxy for the mechanical behaviour and the limit between the strong lithosphere and the underlying ductile asthenosphere (for example Parker & Oldenburg (1973) set it to the 1200° isotherm). The Pacific hemisphere contains 12 major plates: Phillipine, Okhotsk, Bering, North America, Coco, Nazca, South America, Antarctic, Australia and Pacific (see figure 1.2).

The boundary between two plates can be a *ridge*, often in the middle of an ocean and thus called *mid-oceanic ridge*. Along a mid-oceanic ridge the warm asthenosphere is very shallow and melting occurs because of adiabatic decompression giving rise to an intense volcanism that forms the oceanic crust, made of the so-called *mid-oceanic ridge basalts* (MORB). Examples in the Pacific hemisphere are the East-Pacific-Rise, or the Pacific-Antarctic ridge. Melting produces a strong linear low velocity anomaly along ridges in tomograhic models (e.g. Toomey et al., 1998; Baba et al., 2006) up to ∼80 km.

The lithospheric plates move horizontally in opposite directions from the ridge. This can be observed by dating the oceanic seafloor using rock samples or magnetic anomalies or using GPS data (e.g. Gripp & Gordon, 1990; Müller et al., 1997;

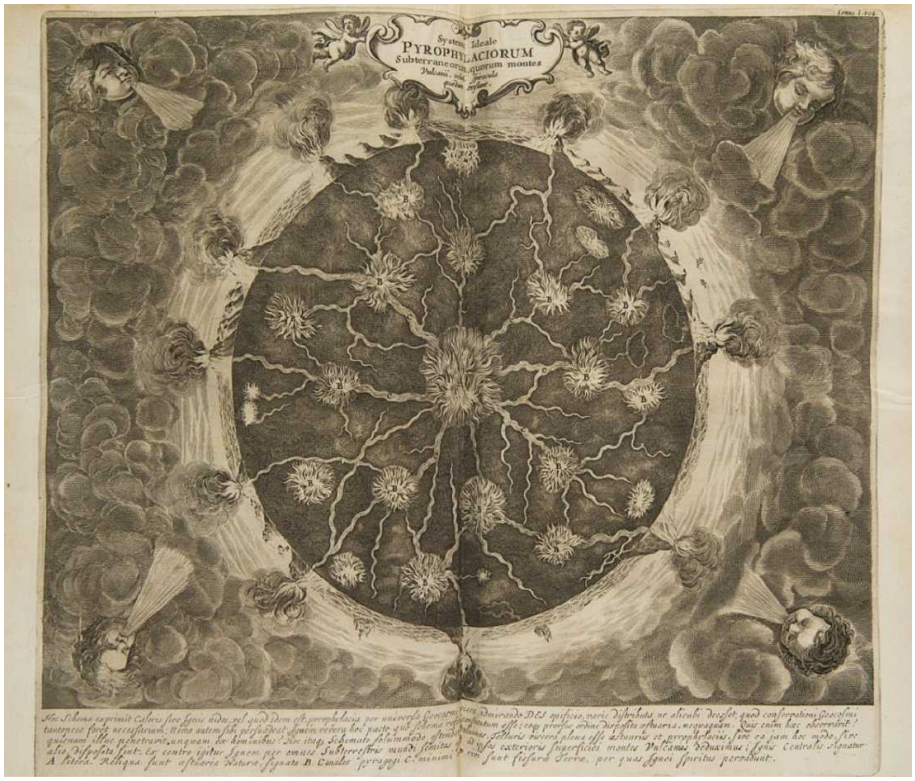

FIGURE 1.1: The interior of the Earth, from Kircher's *Mundus Subterraneus* (1664).

Wessel & Kroenke, 2000; Müller et al., 2008). At the ridges the lithosphere thickness is close to zero (Parker & Oldenburg, 1973). With increasing distance from the ridge, since heat is removed from the mantle by the surface, the thickness of the lithosphere increases. This is the well known *lithosphere cooling* process. Several geodynamical models have been proposed for the lithosphere cooling (e.g. Parsons & Sclater, 1977; Parsons & McKenzie, 1978; Hoggard et al., 2017). The relation with ocean bathymetry has been investigated and seismic tomography observations have been compared to various model predictions (e.g. Ritzwoller, Shapiro & Zhong, 2004; Priestley & Mckenzie, 2006; Maggi et al., 2006b; Steinberger & Becker, 2018; Isse et al., 2019). The cooling mode may be more complicated than has been presumed, for example hydrothermal cooling may play a role (e.g. Kooi, 2016; Schmeling, Marquart & Nawa, 2017), some reheating processes may occur and the spreading rate of ridges may not be symmetrical (e.g. Müller et al., 2008).

Since lithosphere drifts appart at the mid-oceanic ridges it must be destroyed somewhere for matter conservation. Almost all around the Pacific ocean is found a convergent plate boundary: the *subduction zones*, where one lithospheric plate 'sinks' below the other. There the bathymetry is usually marked by a deep trench in between the two plates. Examples are the Mariana trench, the Aleutian trench,

the Chile trench or the Tonga-Kermadec trench. These regions are marked by a strong seismicity, where hypocenters are distributed on a plane (the Wadati-Benioff plane) that roughly corresponds to the sinking slab. Since the subducting plate is a cool slab within the warm mantle, the temperature difference produces a strong contrast of seismic velocities in the tomographic models wich makes it one of the most striking features (e.g. Zhao, Maruyama & Omori, 2007). However it is not clear whether the subducting slab reaches the lower mantle or whether the Clapeyron slope at the 660 km discontinuity is such that it is confined to the upper mantle (see e.g. Foulger, 2011, section 5.1). The picture too may be more complicated. For example Chang, Ferreira & Faccenda (2016) propose that the sinking slab from the Tonga-Kermadec trench interacts both with the 660 km discontinuity and deep rooted mantle convection processes. A similar hypothesis is proposed for the Farallon slab under North America by Tian et al. (2011).

During its stay below the ocean, the lithosphere has been hydrated. In the subduction, the increasing pressure causes changes in the mineral phases that dehydrate the slab. The water is transfered from the slab into the overlying asthenosphere with the effect of lowering its solidus. Thus partial melting occurs giving rise to volcanism above the subducting slab forming the so-called *back-arc* regions (e.g. Ghosh et al., 2020). The melting has the effect of producing strong low velocity anomalies in tomographic models (e.g. Maggi et al., 2006b; Zhao, Maruyama & Omori, 2007).

Plate tectonics is now a widely accepted theory. It explains many observable features (ocean seafloor magnetic anomalies, oceanic bathymetry, GPS data, back-arc volcanism, trenches, seismicity distribution) and tomographic observations (low velocity below ridges, high velocity slab signature, low velocity above slabs, thickening of a high velocity layer with distance from the ridge). However some observations are not directly explained. The most striking example is the existence of intraplate volcanism (figure 1.3), *hotspots*, usually associated with a linear volcanic chain and a large igneous province. Examples in the Pacific are Hawaii, the French Polynesia, the Masquesas, the Galapagos or Pitcairn (Neall & Trewick, 2008).

W. Jason Morgan (1972) proposed that instabilities within the D" layer (right above the core-mantle boundary) produces low density warm materials that rise within the mantle toward the surface. These *mantle plumes* take the form of a mushroom. When the head reaches the surface an intense volcanism creates a large igneous province (for example the Deccan trapps or the Ontong-Java plateau). These events have even been linked with mass extinctions by Sobolev

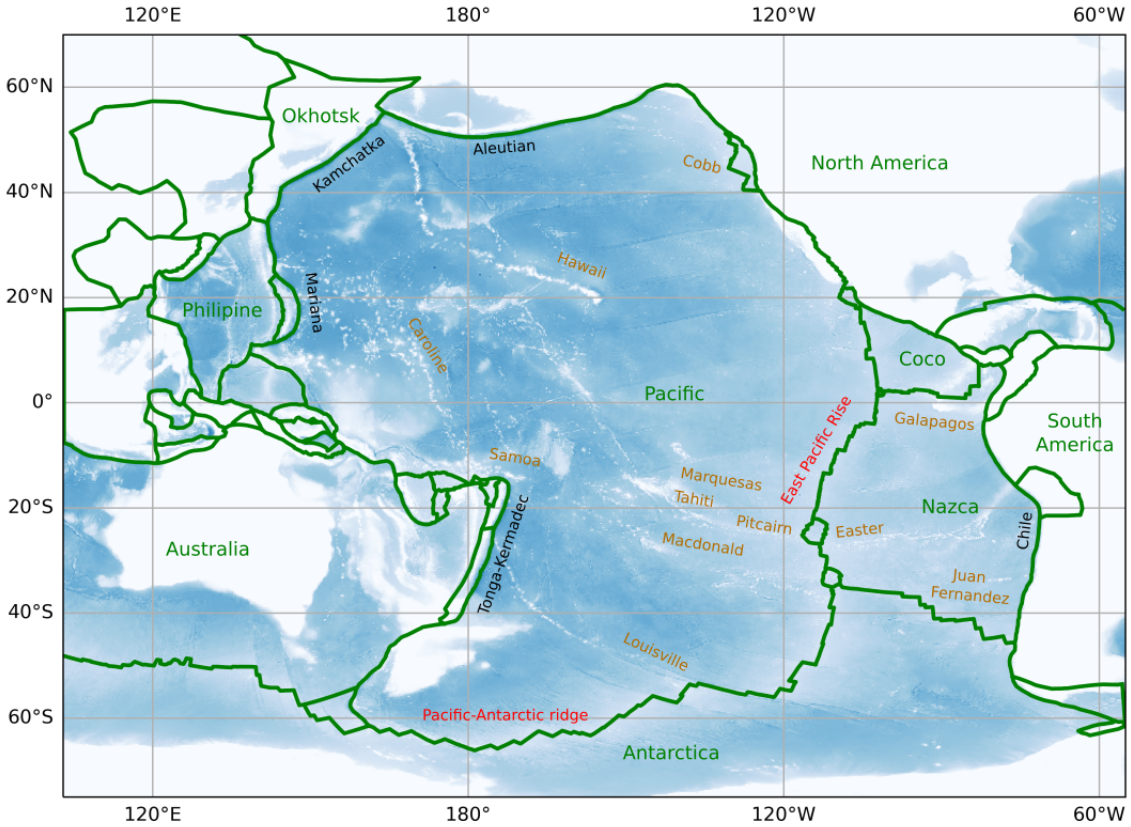

FIGURE 1.2: Map of the bathymetry in the Pacific and the main geological features. The bathymetry is from the GEBCO Compilation Group (2022), the plates (green names) from Bird (2003), the presumed hotspots (brown names) from the list of Courtillot et al. (2003). The main mid-oceanic ridges are named in red and the main trenches in black.

FIGURE 1.3: The 'Chaîne des Puys' in the Massif central (Auvergne, France) that has been supposed to originate from a mantle plume (Granet, Wilson & Achauer, 1995). Picture from the author.

et al. (2011). Later the plume tail continues to feed the volcanism but since lithospheric plates are moving over a fixed mantle, a linear volcanic chain is created. Many tomographic studies attempted to image the predicted plumes (e.g. Granet, Wilson & Achauer, 1995; Bijwaard & Spakman, 1999; Ritsema, Heijst & Woodhouse, 1999; Montelli et al., 2004; Nolet et al., 2019; Tsekhmistrenko et al., 2021). However seismic tomography images come with their uncertainties, they have a poor resolution, they may be biased and contain artifacts. Interpreting plume strucures in the tomographic images is a difficult and tricky task (Foulger et al., 2013; Zaroli, Koelemeijer & Lambotte, 2017; Maguire et al., 2018). When a plume is not found, one may argue that the resolution is not good enough; when a plume is found, others may argue that it is an artifact. For example, Bijwaard & Spakman (1999) considered that they were able to resolve a deep rooted plume below Iceland but Foulger et al. (2001) wrote two years later that "upwelling beneath Iceland is confined to the upper mantle". Marignier, Ferreira & Kitching (2020) analyse several tomographic models to derive a list of possible mantle plumes with a probability attached to each. It is also difficult to define what a mantle plume really is. Since the proposition of W. Jason Morgan (1972) the plume hypothesis has derived into many different definitions to fit the tomographic observations. For example Arndt (2000) proposed that plumes may have a cold tail or more recently (Tsekhmistrenko et al., 2021) proposed that many plumes may be related into a plume-tree originating from the large low velocity provinces close to the core-mantle boundary.

Haxby & Weissel (1986) observed a pattern of elongated anomalous bands

in the direction perpendicular to the East-Pacific-Rise in satellite altimetric data. This pattern has been interpreted as *small scale sublithospheric convection cells* that should naturally arise in the upper mantle because of the lithospheric motion and has been proposed as a mechanism to explain the intraplate volcanism (Ballmer et al., 2009). Recent seismic tomography studies seem to image such a pattern of elongated anomalies (Montagner, 2002; French, Lekic & Romanowicz, 2013b).

The origin of intraplate volcanism and the motor of plate tectonics are still debated (e.g. Foulger, 2011; Chen et al., 2020, www.mantleplume.org). Since many interesting processes seem to occur in the Pacific upper mantle, I aim in my thesis to take part to the discussion using surface wave tomography in the Pacific region.

1.2 Tomographic images: behind the scenes

The amount of data available for seismic tomography has considerably increased with the development of international networks of seismometers. The data coverage has improved with temporary deployments such as the PLUME experiment that deployed oceanic bottom seismometers around volcanic archipelagos (Barruol, 2002) thus improving the quality of tomographic images in oceanic regions (Isse et al., 2019). More recently floating seismometers were deployed (Simons, 2021; Simon, Simons & Irving, 2021; Pipatprathanporn & Simons, 2021). For example such seismometers are used by Nolet et al. (2019) to image a plume-like structure beneath the Galapagos. Where seismicity is too low, ambient noise tomography has been applied to reconstruct signal between two stations (e.g. Shapiro et al., 2005; Ouattara, Zigone & Maggi, 2019; Movaghari & Doloei, 2020). New advances in tomographic methods allow to consider various types of data (body-waves travel times, surface waves phase or group dispersion, polarization, amplitude, full waveform) to estimate various kinds of physical parameters within the Earth (P- or S-wave velocity, attenuation, anisotropy) and their relation with different physical parameters such as temperature, degree of melting or composition (though through complicated relations, see e.g. Priestley & McKenzie, 2013; Foulger, 2011, section 5.1.2, page 147). Theoretical advances in seismic tomography allow to model the seismic wavefield in three-dimensional media with spectral element methods (Komatitsch & Vilotte, 1998; Komatitsch & Tromp, 2002a; Komatitsch & Tromp, 2002b). These methods allow for solving non-linear problems using iterative inversion scheme (Tarantola & Valette, 1982) or adjoint methods to take full advantage of the three-dimensional simulations (Liu & Gu, 2012) thus leading to high resolution tomographic models (e.g. Lekić

& Romanowicz, 2011; French, Lekic & Romanowicz, 2013b; French & Romanowicz, 2014; Monteiller et al., 2015).

Seismic tomography has to deal with various kinds of data errors that propagate into the tomographic result. Some tomographic studies rely on the knowledge of the seismic source (spatial and origin-time, moment tensor, spectrum). Catalogs that provide this information are available, like the GCMT catalog (Ekström, Nettles & Dziewoński, 2012). But the source recovery remains imperfect. Duputel et al. (2012) write: "Here, like in any observational problem, the error estimation should be part of the solution". Errors may also come from the crust when it is not inverted for. For example Panning, Lekić & Romanowicz (2010) shows that deep structures may be biased by incorrect crustal corrections. If not accounted for, Liu & Zhou (2013) and Marone & Romanowicz (2007) show that finite-frequency and non-linear effects may lead to significant errors. Other sources of error in tomography come for example from the parameterization (for example splitting the space into blocks of finite size), from the inaccuracy of the theory describing the seismic wavefield or from the measurement itself (see for example a comparison of data sets obtained with various methods in Moulik et al., 2021).

The spatial coverage of the data used in seismic tomography is usually strongly heterogeneous. As a consequence tomographic images have a very complicated *resolution*. The resolution can be thought as a filter (sometimes called the *tomographic filter*) through which the object to image would pass. Each estimated value in the model is actually a *spatial average* of the true object to map. The averaging may *bias* the solution (averaging weights summing to more or less than one), it smooths the solution, and it may introduce artifacts (such as smearing effects if the averaging is spatially anisotropic). A comparative example is the *point spread functions* used in astronomy. Because of the observational setup, the image of a distant star does not appear as a simple point, but it has more a star-like shape as can be seen on figure 1.4. The resolution of the Hubble space telescope (top) makes stars look like fuzzy balls surrounded by four spikes whereas the resolution of the James Webb space telescope (below) makes them look more distinct but with eight long spikes. The problem is even worse in seismic tomography where the object to map is continuous and where we aim to interpret also the shape of anomalous patterns. Very soon the misleading effects of the resolution were recognized. For example, while doing the tomography of the subduction zone in the north-west of the Pacific, Spakman et al. (1989) also inverted synthetic P wave travel time data from a simple thermal model of the lithosphere and concluded: "we have demonstrated that large scale resolution artifacts in the

FIGURE 1.4: Observations of the 'Cosmic Cliffs' at the edge of the Carina nebula. Top: observation in visible light by the Hubble space telescope (NASA, STScI). Bottom: observation in the infrared range of the electromagnetic spectrum made with the James Webb space telescope (NASA, ESA, CSA, and STScI).

synthetic inversion results resemble anomaly patterns in the real data results". Resolution investigation in the form of *checkerboard tests*, i.e. application of the tomographic process to retrieve an input model that looks like a checkerboard, is now routinely applied in most seismic tomography studies to investigate the effect of the resolution (e.g. Zhou et al., 2006; French & Romanowicz, 2014; Auer et al., 2014; Liu & Zhou, 2016a; Ouattara, Zigone & Maggi, 2019; Tsekhmistrenko et al., 2021; Magrini et al., 2022; Greenfield et al., 2022). However Lévêque, Rivera & Wittlinger (1993) have shown that checkerboard tests can be misleading, but Rawlinson & Spakman (2016) recognize that "the widespread use of synthetic reconstruction tests in seismic tomography is likely to continue for some time yet" and propose some best practices. For example French, Lekic & Romanowicz (2013b) design very specific synthetic models to investigate whether the resolution would produce the anomalies they observe perpendicular to the ridge.

On figure 1.5 are represented two tomographic models that estimate the S-wave velocity at 75 km depth. At large scale, for strong amplitude anomalies, the agreement between the models is good (linear low velocity corresponding to mid-oceanic ridges, increasing velocity with distance from the ridge, back-arc regions marked by strong low velocity anomalies, cratons). However, at shorter scale, for lower amplitude anomalies, many discrepancies arise. For example, there

is a slow anomaly connecting the East-Pacific rise to Tonga-Kermadec in *savani* (left) but not in *S20RTS* (right). While Hawaii is above a slow velocity anomaly in *savani*, it is above a high velocity anomaly in *S20RTS*, but there are two slow anomalies in the north and south of Hawaii that do not appear in *savani*. Such discrepancies can be attributed to the uncertainties and resolution of both models. This shows that reliable interpretations of tomographic models require good estimates of their resolution and uncertainties. This information would be useful also to compare the tomographic results with other geophysical data. For example, it may be worth to filter geodynamical models with the tomographic filter before comparison with tomographic results (e.g. Simmons et al., 2019; Freissler et al., 2020).

Usually tomographic models are built using a *data fitting inversion* method. One set up a forward problem that produces data for a given Earth model; then one looks for a model that predicts data close enough to the observations. With such an approach the estimation of the resolution and uncertainties of the model is very difficult. Various methods have been proposed to estimate the resolution. For example Shapiro et al. (2005) estimate the resolution with the method of Barmin, Ritzwoller & Levshin (2001): while fitting the data a spatial smoothing is applied and is used as a proxy for the resolution. However this estimate of the resolution depends on the data, an *a priori* on the model solution and is tractable only on small scale problems. An (2012) proposes a statistical estimation of the resolution (some kind of *Monte Carlo approach*) but it relies on the approximation that resolving kernels are Gaussians. Nolet, Montelli & Virieux (1999) propose an approach based on the *singular value decomposition* but applicable only to small scale problems. Another example to estimate the resolution is based on the concept of point spread functions (e.g. Ritsema, McNamara & Bull, 2007b; Ritsema, Heijst & Woodhouse, 2004; Bonadio et al., 2021; Simmons et al., 2019). A synthetic model with a punctual anomaly produces synthetic data that are inverted with the tomographic process. The result is used as a proxy for the resolution at the location of the punctual anomaly. The full resolution is obtained by applying this process to each cell in the model. This task is computationally expensive since it requires as many inversions as the number of cells in the model. Moreover this estimate of the resolution depends on the data and on an *a priori* on the model. A common problem with all these approaches is that the resolution is obtained only *a posteriori*. No control on the resolution is possible.

Over 50 years ago Backus and Gilbert (Backus & Gilbert, 1967; Backus & Gilbert, 1968; Backus & Gilbert, 1970) proposed an original inversion scheme that takes the point of view of the model resolution and uncertainties to solve

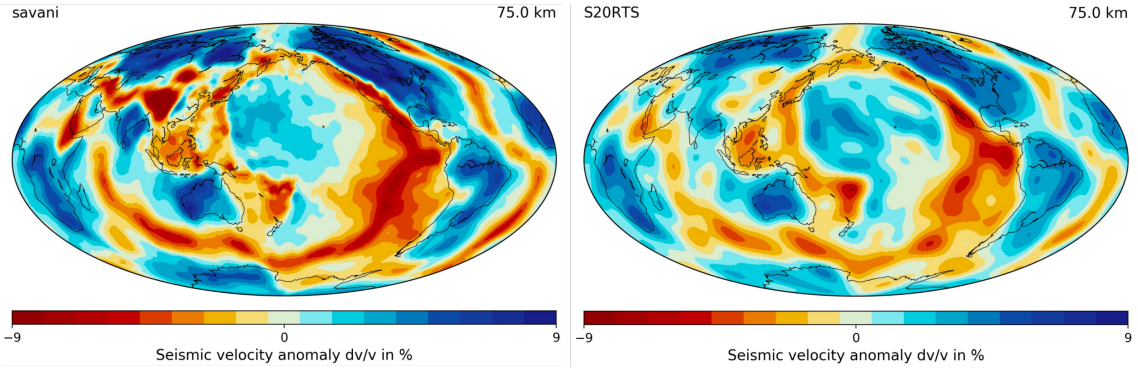

FIGURE 1.5: Two models that aim to estimate the S wave velocity at 75 km depth. Left: model *Savani* from Auer et al. (2014); right: model *S20RTS* from Ritsema, Heijst & Woodhouse (1999). The figures have been produced using the *Submachine* web-based tool (Hosseini et al., 2018).

the inverse problem. They recognized that, for one location of the tomographic model, the better the resolution the higher the uncertainties. They proposed to solve the inverse problem by optimizing the balance between resolution and uncertainties. The method turned out to be computationally expensive but it was later reformulated by Pijpers & Thompson (1992) and Pijpers & Thompson (1993) to be applied in the field of helioseismology. Their reformulation was named the *Subtractive Optimally Localized Averages* (SOLA) inversion. The SOLA inversion has been recently adapted to seismic tomography and applied with body-waves by Zaroli (2016), Zaroli, Koelemeijer & Lambotte (2017) and Zaroli (2019). The method is still computationally expensive because it is necessary to solve an inverse problem for each location in the tomographic model. However this task is embarassingly parallel (i.e. the inverse problems to solve are completely independent to each other) so that it is no longer a problem with computational facilities available today. With the SOLA inversion a target resolution is designed giving a direct control on the resolution. This way it is also possible to remove the bias (in the sens of *averaging bias*) and design the target resolution such that artifacts like smearing effects are reduced. Moreover, contrary to data fitting inversions, the SOLA inversion requires no *a priori* information on the model solution. By construction, the model statistics are produced together with the model solution and available for robust interpretations. Though the SOLA inversion is limited to linear problems it is very appealing to overcome some of the issues tomography has to deal with. The Pacific region is interesting but it is also highly unevenly sampled and I aim in my thesis to apply the SOLA inversion in the context of surface waves to overcome the issues induced by the uneven data coverage.

1.3 From ray to finite frequency surface wave tomography

Usually surface wave tomography starts with dispersion measurements where the phase velocity (velocity of a surface with constant phase) or group velocity (velocity of a wave packet) is determined as a function of frequency for each source-station path. Then two schemes, involving two steps, can lead to a three-dimensional model.

One possibility (e.g. Debayle & Lévêque, 1997; Lévêque, Debayle & Maupin, 1998; Debayle, 1999; Debayle & Kennett, 2000; Simons et al., 2002; Lebedev & Nolet, 2003; Priestley, 2003; Debayle & Sambridge, 2004; Maggi et al., 2006b; Maggi et al., 2006a; Priestley & Mckenzie, 2006), illustrated with the top row of figure 1.6, is to start with a forward theory that is non-linear to relate the dispersion measurement for a source-receiver path to a physical parameter (e.g. S-wave velocity) averaged along the ray as a function of depth. Recovering the model can be done using one of the many variations of data fitting inversions (e.g. Menke, 1989; Tarantola, 2005). In the second step the path-averaged models play the role of the data. A forward theory that is linear can be used to map the parameter of interest at a specific depth. This is called a *regionalization*. Finally a quasi three-dimensional model is obtained. 'Quasi' stands for that the model is more like a set of two-dimensional maps at discrete depths rather than a real three-dimensional model; two independent inversions, a non-linear depth inversion then a linear lateral regionalization have been used. No information about the vertical correlations remains in such a model.

The second possibility (e.g. Ekström, Tromp & Larson, 1997; Montagner, 2002; Yoshizawa & Kennett, 2004; Ekström, 2011; Ouattara, Zigone & Maggi, 2019; Seredkina, 2019; Isse et al., 2019; Magrini et al., 2022; Greenfield et al., 2022), illustrated with the second row of figure 1.6, is to switch the two steps. It starts with the linear regionalization of many dispersion measurements at fixed frequencies to obtain phase or group velocity maps. In the second step, at a given latitude-longitude location, the frequency dependent maps are non-linearly inverted for the depth. Again the model thus obtained is 'quasi' three-dimensional. The first step is only lateral and the second step is only with depth: each frequency dependent 'column' (at a given latitude-longitude location) is inverted with depth, indepently from the others. This can be seen on vertical cross-sections within such models where there is a great variability from column to column. No information about the horizontal correlations remains in such a model.

Since the regionalization step is linear, it is tractable with the SOLA inversion.

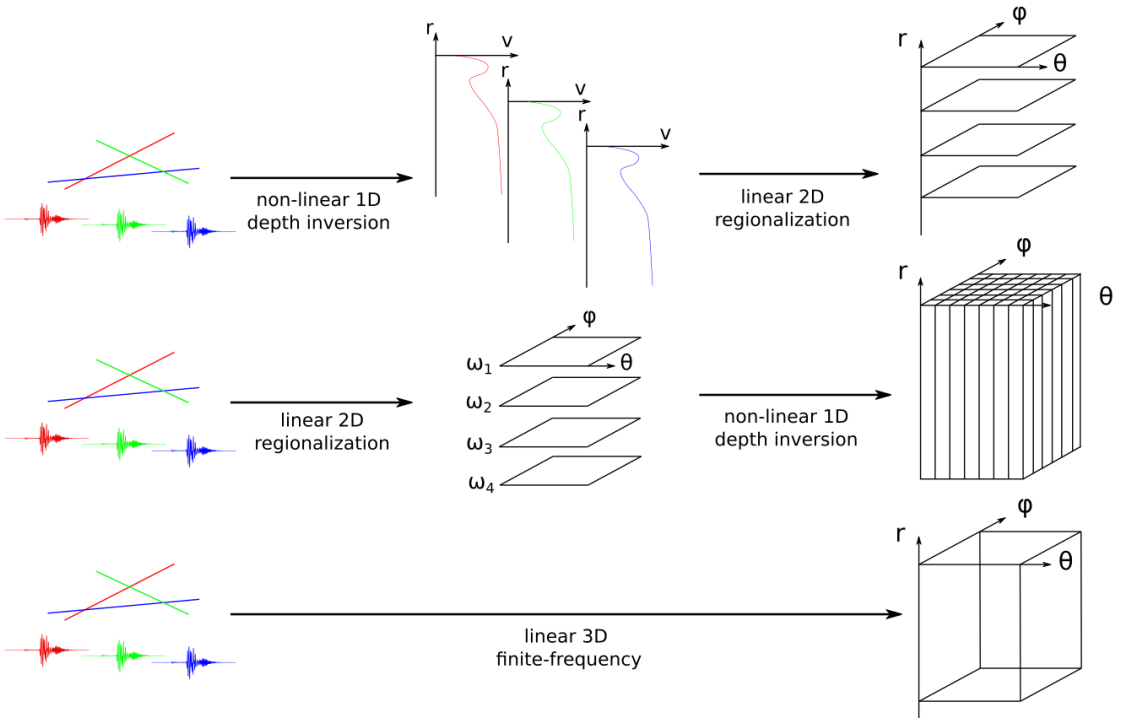

FIGURE 1.6: Illustration of several approaches in surface wave tomography. Top and middle rows illustrate the two-step approaches. The last row illustrates the one-step approach.

I will attempt in this thesis to apply the SOLA inversion to produce S-wave velocity maps at discrete depths using the first two-step approach.

There are two main issues with the two-step formalism. First all dimensions are not constrained all together: the model is only 'quasi' three-dimensional. Second, in both cases, the regionalization relies on ray theory. At a given depth, or at a given frequency, the production of the two-dimensional map assumes all the information sampled by the ray is confined within the zero width ray path. Yet physical observations and simple physical arguments show that this cannot be true.

Huygens' principle states that, given an initial wavefield, each point in space behaves as a secondary source. If the medium is heterogeneous, these secondary sources disperse the initial wavefield, producing *scattered wavefields*, and an observer sees the interference of all. The strength of scattering depends on the wavelength and on the size of the heterogeneities. If heterogeneities are small with respect to the wavelength scattering is weak (and we retrieve the predictions of ray theory). But if the size of the heterogeneities approaches that of the wavelength, scattering becomes stronger and ray theory fails to describe what would be observed. A nice example comes from astronomy again. On figure 1.4 are two 'pictures' of the same region of space, the so-called 'Cosmic Cliffs' at

the edge of the Carina nebula. The top panel was taken by the Hubble space telescope observing in the visible range of the electromagnetic spectrum. What looks like cliffs are actually gases emanating from the star-forming region. The particles composing theses gases are of the size of the wavelength of the visible light. Therefore strong scattering interferences occur in the visible range and the Hubble space telescope sees the 'Cosmic Cliffs' as cloudy regions. The bottom panel was taken by the James Webb Space telescope that has the particularity to observe in the infrared range of the electromagnetic spectrum. Since infrared is larger wavelength, the observed waves are less sensitive to scattering in the gas region. Thus the 'Cosmic cliffs' look more transparent. The same phenomenon occurs with mechanical waves within the Earth.

A way to extend ray theory to account for scattering is illustrated on figure 1.7. Part of the energy emanating from the source (solid red star) propagates along the shortest path with length L toward the receiver (blue triangle). Part of the radiated energy follows another path (in green) toward some scatterer (empty red star). Following Huygens' principle the scatterer behaves as a secondary source and if the scatterer represents a local heterogeneity in the medium, part of the energy of the initial wavefield is scattered toward the receiver. If the difference between the distance propagated by the initial wave and the scattered wave is less than one half of a wavelength, then both wavefields interfere constructively and modify what the observer would see in an otherwise homogeneous medium. This half-a-wavelength limit defines the Fresnel zone. Therefore, the measured data are sensitive to that region with a non-zero surface, whose size depends on the frequency. The only way for this region to have zero surface (a true ray) would be for the wavelength to be zero, or the frequency to be infinite. Of course, the influence of the scattered wave depends on where exactly it has passed within the Fresnel zone (for example the blue path would change the observation in another manner). Obtaining the detailed lateral sensitivity of the observations has been the subject of recent work, and this goes with the name *finite-frequency*, as opposed to the infinite-frequency ray theory. Theoretical advances have been made in the 80's and 90's (Snieder & Nolet, 1987; Snieder, 1986; Marquering, Nolet & Dahlen, 1998; Dahlen, 2000). In 1998, Dahlen and Tromp ended their treatise on the free oscillations of the Earth by stating that the development of finite-frequency was the "current frontier in global seismic tomography" (Dahlen & Tromp, 1998). Montelli et al. (2004) argue that they are able to reveal plumes in the mantle using finite-frequency in body-wave tomography. Yoshizawa & Kennett (2004) incorporate finite-frequency effects in their surface wave tomography but they actually consider the width of the Fresnel zone

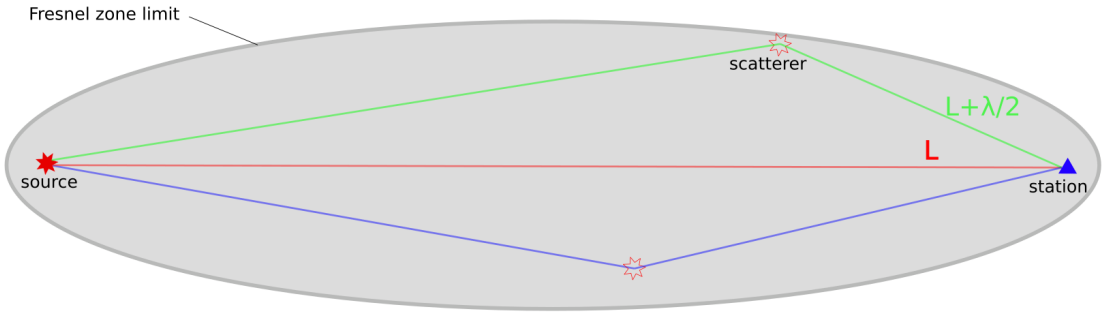

FIGURE 1.7: Illustration of the scattering principle and the Fresnel zone.

without detail inside, i.e. some kind of *fat rays*. Major advances to compute the detailed finite-frequency sensitivity have been made by the works of Yoshizawa & Kennett (2005) and Zhou, Dahlen & Nolet (2004). Recent advances allow to consider anisotropy (Zhou, 2009a), anelasticity (Zhou, 2009b) or near-field effects (Liu & Zhou, 2016b). Finite frequency has been subsequently applied in surface wave tomography in various studies (Zhou et al., 2005; Zhou et al., 2006; Ruan & Zhou, 2010; Tian et al., 2011; Liu & Zhou, 2016a).

One advantage of the finite-frequency approach is that it allows to relate linearly frequency and path dependent data directly to the three-dimensional model in one step. Also, where the two-step approach uses various frequencies to contrain the depth, finite-frequency uses the frequencies to constrain also lateral variations, so that we may expect a better lateral resolution. Since the finite-frequency approach is linear, it is tractable with the SOLA inversion.

I will attempt, as part of this thesis, to apply the SOLA inversion to produce a S-wave velocity three-dimensional model using the finite frequency approach on surface waves.

The challenge of my thesis is twofold: to apply the SOLA inversion in the context of surface waves (first using the simple framework of ray theory, then with the more powerful framework of finite-frequency) and to interpret robustly the three-dimensional structure of the Earth using all the advantages provided by the SOLA inversion. An illustration of the content of this manuscript is given on figure 1.8. The chapters 2 and 3 are dedicated to describe the tools necessary to address the challenges. In chapter 2 I describe the forward theory that relates the data to the three-dimensional Earth. The first part is about ray theory and the second part is the extension to finite-frequency theory. Chapter 3 is about the inverse theory. It starts with the classical data fitting point of view and continues with the SOLA inversion method. The chapters 4 and 5 are dedicated to the application of the SOLA inversion. Chapter 4 is the application of the SOLA

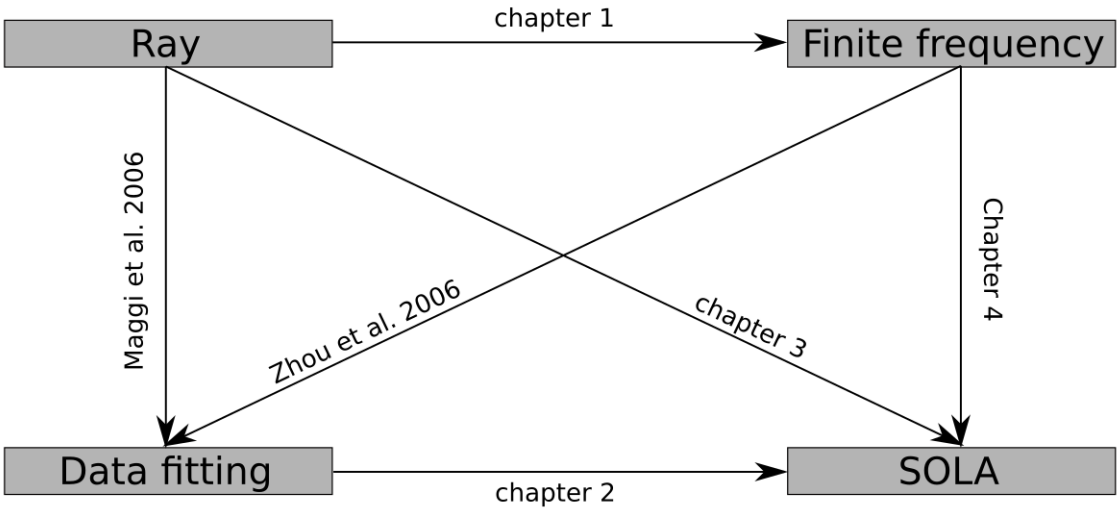

FIGURE 1.8: Plan for the manuscript. Top to down arrows represent the combination of one forward theory (top row) with one inversion method (bottom row). Maggi et al. (2006b) used ray theory with a data fitting inversion and Zhou et al. (2006) used finite-frequency theory with a data fitting inversion. In chapter 4 I apply the SOLA inversion with ray theory. In chapter 5 I apply the SOLA inversion with finite-frequency theory.

inversion in the simple ray theory framework with real data, from which first conclusions about the Earth structure can be drawn though limited by the issues relative to ray theory. Chapter 5 is the application of the SOLA inversion with the more elaborate finite-frequency theory. Since chapter 5 relies on relatively new concepts, it is applied on synthetic data.

Chapter 2

Forward theory

The waves in the layer which are analogous to Rayleigh-waves are subject to slight dispersion, both on account of gravity, as was seen in the solution of the second problem, and on account of the change of mechanical properties at the under surface of the layer, and, on both accounts, the wave-velocity of a simple harmonic wave-train increases as the wave-length increases.

Love, *Some Problems of Geodynamics*, 1911.

2.1 Introduction

To infer the physical properties of the deep Earth (a model $\boldsymbol{m}$) only surface observations (some data that we may write $\boldsymbol{d}$) are available. The forward problem is to find a relation, or a *forward theory* $\boldsymbol{g}$ that relates the data to the model: $\boldsymbol{d} = \boldsymbol{g}(\boldsymbol{m})$. Obtaining the model solution from the data under a given forward theory is not an easy task and it is the subject of the next chapter. The aim of this chapter is to set up the forward theory.

The oscillations of the Earth, when it is subject to disturbances (like the effect of external bodies or an earthquake) depend on its internal properties. Early in the 19th century Poisson derived theoretical equations relating the oscillations of a spherical system to its internal properties. For example, Lord Kelvin compared the observed period of a particular oscillation (the fundamental ${}_0S_2$ mode) with predictions and showed that the Earth had a rigidity close to steel. His observations added to the debate regarding whether the interior of the Earth is molten or not (see for example the introductory chapter of Dahlen & Tromp, 1998). This early work was further developed over the two last centuries leading to the modern *normal modes* theory. From normal modes theory it is possible to predict synthetic waveforms that an earthquake would produce for a given radial model of the Earth; and from that a forward theory can be established. Normal modes theory is the framework of this thesis. This choice is motivated by the simplicity, the robustness and the computational efficiency of the normal modes approach, especially with long period data which characterizes surface waves.

The first part of this chapter presents normal modes theory and the construction of a synthetic seismogram for a radial model, i.e. the response of a laterally homogeneous system to an earthquake. The second part of this chapter is dedicated to present the finite frequency theory based on the Born approximation. It predicts in one linear relation the response of a laterally heterogeneous system.

2.2 Laterally homogeneous system

Most of this section is a synthesis of results extracted from Dahlen & Tromp (1998) and Nolet (2008), with the aim to converge toward the results of Zhou, Dahlen & Nolet (2004). In this section the Earth is assumed to be a spherically non-rotating elastic and transversally isotropic system, or a so-called *SNREI* model. Under this assumption the elasto-dynamic equation can be written in the frequency domain:

$$\rho(r)\omega^2\boldsymbol{u} + \nabla(\lambda(r)\nabla.\boldsymbol{u}) + \nabla.[\mu(r)(\nabla\boldsymbol{u} + \nabla\boldsymbol{u}^T)] = 0, \tag{2.1}$$

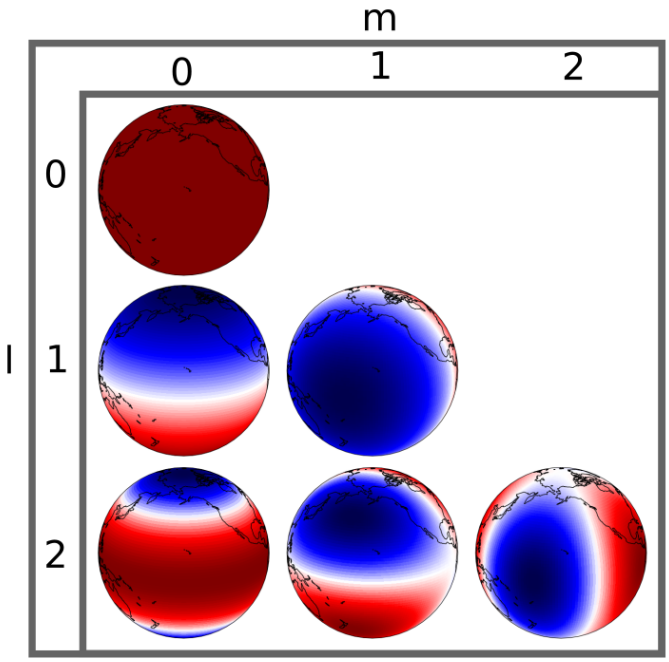

FIGURE 2.1: Real part of the first spherical hamonics with harmonic degree l and angular order m up to 2.

where $\rho(r)$ is the density, $\lambda(r)$ and $\mu(r)$ are the Lamé parameters that vary only with depth and $\boldsymbol{u}$ is the wavefield. For simplicity, we introduce the operator $\mathcal{L}$ defined as:

$$\mathcal{L}\boldsymbol{u} \equiv \rho(r)\omega^2\boldsymbol{u} + \nabla(\lambda(r)\nabla.\boldsymbol{u}) + \nabla.[\mu(r)(\nabla\boldsymbol{u} + \nabla\boldsymbol{u}^T)]. \tag{2.2}$$

2.2.1 Normal modes

Since the Earth is a finite body, its vibrations can be decomposed into a sum of particular vibrations with a specific shape, amplitude and frequency: the *normal modes* (or *free oscillations*). Any propagating wavefield can be seen as a sum of standing waves. Given the spherical geometry of the Earth, the shape of normal modes are given by the spherical harmonics which are identified by two integers l and m (some of them are illustrated on figure 2.1). For a model of the Earth, the amplitude and frequency for each of these modes of vibration are obtained by solving a set of differential equations. It turns out that there is an infinite number of solutions identified by a third integer n. Finally, from these solutions and a given seismic source and receiver, one can compute the observed seismic wavefield as summation of normal modes. Within the approximation $l/4 \gg n$, a description in terms of *surface waves* derives from that normal mode summation.

Spherical harmonics

Any scalar function $f(\theta,\phi)$ that takes value on the unit sphere can be decomposed into spherical harmonics $Y_{lm}(\theta,\phi)$ that are orthogonal to each other; in other words, spherical harmonics are scalar functions of the unit sphere that form a basis. The integer l is the *harmonic degree* and ranges from 0 to ∞ and the second integer m is the *azimuthal order* and ranges from $-l$ to l. We write,

$$f(\theta,\phi) = \sum_{lm} f_{lm} Y_{lm}(\theta,\phi). \tag{2.3}$$

A formal derivation of these spherical harmonics can be found in Dahlen & Tromp (1998, appendix B, pp. 838-868). The spherical harmonics are given by:

$$Y_{lm}(\theta,\phi) = X_{lm}(\theta) e^{im\phi}, \tag{2.4}$$

where,

$$X_{lm}(\theta) = (-1)^m \left(\frac{2l+1}{4\pi}\right)^{1/2} \left[\frac{(l-m)!}{(l+m)!}\right]^{1/2} P_{lm}(\cos\theta), \tag{2.5}$$

with P_{lm} the associated Legendre function defined as,

$$P_{lm}(\mu) = \frac{1}{2^l l!}(1-\mu^2)^{m/2} \left(\frac{d}{d\mu}\right)^{l+m} (\mu^2-1)^l. \tag{2.6}$$

The definition of the spherical harmonics shows a harmonic dependence on the longitude in the exponential term that depends on the number m. Therefore, the real part of the spherical harmonic is zero $2m$ times along a parallel (m meridians). On the other hand the associated Legendre function turns out to have $|l-m|$ nodes along a meridian. Figure 2.1 shows the real part of some spherical harmonics.

If we now have a function of the three-dimensional sphere that also depends on radius, then the projection (equation 2.3) still holds for any spherical shell and we can write:

$$f(r,\theta,\phi) = \sum_{lm} f_{lm}(r) Y_{lm}(\theta,\phi). \tag{2.7}$$

Equation 2.7 defines the spherical harmonics decomposition of any scalar field that takes value within the three-dimensional sphere.

Vector spherical harmonics

The displacement wavefield in the Earth is a vector quantity. For this reason we need to extend the spherical harmonics decomposition to a vector field of the

three-dimensional sphere. A formal derivation can be found in Dahlen & Tromp (1998, appendix B12, pp. 868-876). The idea is to first decompose the vector onto a basis of vectors of the three-dimensional space; then to decompose the coefficient functions into spherical harmonics. We start by writting,

$$\boldsymbol{u}(r,\theta,\phi) = u_r(r,\theta,\phi)\hat{\boldsymbol{r}} + u_\theta(r,\theta,\phi)\hat{\boldsymbol{\theta}} + u_\phi(r,\theta,\phi)\hat{\boldsymbol{\phi}}. \tag{2.8}$$

The first term involves only a displacement in the radial direction: it is the *radial field*. The two last terms involve a displacement only on the spherical shell: they form the *tangential field*. The tangential field can be rewritten in terms of a surface gradient $\boldsymbol{\nabla_1}$ and a surface curl $\hat{\boldsymbol{r}} \times \boldsymbol{\nabla_1}$ following the Helmholtz representation:

$$\boldsymbol{u}(r,\theta,\phi) = U(r,\theta,\phi)\hat{\boldsymbol{r}} + \boldsymbol{\nabla_1} V(r,\theta,\phi) - \hat{\boldsymbol{r}} \times \boldsymbol{\nabla_1} W(r,\theta,\phi). \tag{2.9}$$

Another distinction arises with this expression: the two first terms are rotation free and form the so-called *spheroidal field* while the last term is only rotational (divergeance free) and is called *toroidal field*. We will see in section 2.2.1 that both fields are completely independent. We will see in section 2.2.2 that the spheroidal field can describe Rayleigh surface waves or the equivalent P-SV body waves while the toroidal field can describes Love surface waves or SH body waves. Now we can decompose the scalar functions U, V and W into spherical harmonics using equation 2.7 and insert them in equation 2.9:

$$\boldsymbol{u}(r,\theta,\phi) = \sum_{lm} U_{lm}(r)Y_{lm}(\theta,\phi)\hat{\boldsymbol{r}} + \sum_{lm} \boldsymbol{\nabla_1} V_{lm}(r)Y_{lm}(\theta,\phi) - \sum_{lm} \hat{\boldsymbol{r}} \times \boldsymbol{\nabla_1} W_{lm}(r)Y_{lm}(\theta,\phi). \tag{2.10}$$

We can rewrite this equation as:

$$\boldsymbol{u}(r,\theta,\phi) = \sum_{lm} [U_{lm}(r)\boldsymbol{P_{lm}}(\theta,\phi) + V_{lm}(r)\boldsymbol{B_{lm}}(\theta,\phi) + W_{lm}(r)\boldsymbol{C_{lm}}(\theta,\phi)], \tag{2.11}$$

where the vector spherical harmonics are thus defined as $\boldsymbol{P_{lm}}(\theta,\phi) = \hat{\boldsymbol{r}}Y_{lm}(\theta,\phi)$, $\boldsymbol{B_{lm}}(\theta,\phi) = \boldsymbol{\nabla_1} Y_{lm}(\theta,\phi)$ and $\boldsymbol{C_{lm}} = -\hat{\boldsymbol{r}} \times \boldsymbol{\nabla_1} Y_{lm}(\theta,\phi)$.

Eigenvalue-eigenfunction problem

The seismic (or displacement) wavefield $\boldsymbol{u}(r,\theta,\phi)$ is a vector quantity of a three dimensional space that takes values everywhere in the three-dimensional sphere. Therefore it can be decomposed into vector spherical harmonics following equation 2.11. A perturbation in the gravitational potential $\Phi(r,\theta,\phi)$ accompanies the seismic wavefield. Since it is a scalar function it can be decomposed into scalar

spherical harmonics following equation 2.7:

$$\Phi(r,\theta,\phi) = \sum_{lm} P_{lm}(r) Y_{lm}(\theta,\phi), \tag{2.12}$$

where $P_{lm}(r)$ are the coefficients of the spherical harmonics decomposition of the gravitational potential (not to be confused with the vector spherical harmonics $\boldsymbol{P}_{lm}$).

We use the operator $\mathcal{L}$ for the elasto-dynamic equations and the operator $\mathcal{L}_{\mathcal{B}}(r_b)$ for the boundary conditions (at the boundary radius r_b). We start by considering no forcing term, therefore we have:

$$\mathcal{L}(\boldsymbol{u}(r,\theta,\phi), \Phi(r,\theta,\phi)) = \boldsymbol{0}, \tag{2.13}$$

$$\mathcal{L}_{\mathcal{B}}(r_b)(\boldsymbol{u}(r,\theta,\phi), \Phi(r,\theta,\phi)) = \boldsymbol{0}. \tag{2.14}$$

Note that this is an *eigenvalue-eigenfunction problem*. Physically *eigen* means that there is no forcing term so that the solution is proper to the system itself. It also justifies the terminology used for the solutions: the *free oscillations*. We look for an eigensolution to the wavefield $\boldsymbol{u}$ and gravitational potential Φ for these equations. Substituting the harmonic expansions for the wavefield (equation 2.11) and gravitational potential (equation 2.12) into the elastodynamic equations (2.13) leads to four second-order differential equations (one for each vector spherical harmonics $\boldsymbol{P}_{lm}$, $\boldsymbol{B}_{lm}$ and $\boldsymbol{C}_{lm}$ and one for the scalar spherical harmonics associated with the gravitational potential):

$$\begin{aligned}
&r^{-2}\frac{d}{dr}[r^2(\lambda+2\mu)\dot{U} + \lambda r(2U - kV)] \\
&+r^{-1}[(\lambda+2\mu)\dot{U} + \lambda r^{-1}(2U - kV)] \\
&-3(\lambda + \frac{2}{3}\mu) r^{-1}(\dot{U} + 2r^{-1}U - kr^{-1}V) \\
&-k\mu r^{-1}(\dot{V} - r^{-1}V + kr^{-1}U) + \omega^2\rho U \\
&-\rho[\dot{P} + (4\pi G\rho - 4gr^{-1})U + kgr^{-1}V] = 0,
\end{aligned} \tag{2.15}$$

$$\begin{aligned}
&r^{-2}\frac{d}{dr}[\mu r^2(\dot{V} - r^{-1}V + kr^{-1}U)] \\
&+\mu r^{-1}(\dot{V} - r^{-1}V + kr^{-1}U) \\
&+k\lambda r^{-1}\dot{U} + k(\lambda + \frac{4}{3}\mu) r^{-2}(2U - kV) \\
&+[\omega^2\rho - (k^2-2)\mu r^{-2}]V - k\rho r^{-1}(P + gU) = 0,
\end{aligned} \tag{2.16}$$

$$r^{-2}\frac{d}{dr}[\mu r^2(\dot{W}-r^{-1}W)]+\mu r^{-1}(\dot{W}-r^{-1}W) \\ +[\omega^2\rho-(k^2-2)\mu r^{-2}]W=0, \tag{2.17}$$

$$\ddot{P}+2r^{-1}\dot{P}-k^2r^{-2}P=-4\pi G\dot{\rho}U-4\pi G\rho[\dot{U}+r^{-1}(2U-kV)], \tag{2.18}$$

where G is the gravitational constant and $k=\sqrt{l(l+1)}$. It is shown in section 2.2.2 that $\sqrt{l(l+1)}$ can also be interpreted as the surface wave wavenumber, justifying the notation used here. Inserting the spherical harmonics decomposition for the gravitional potential and the seismic wavefield into the boundary conditions (equations 2.14) leads to four first order differential equations:

$$(\lambda+2\mu)\dot{U}+\lambda r^{-1}(2U-kV)=0, \tag{2.19}$$

$$\mu(\dot{V}-r^{-1}V+kr^{-1}U)=0, \tag{2.20}$$

$$\mu(\dot{W}-r^{-1}W)=0, \tag{2.21}$$

$$[\dot{P}+4\pi G\rho U]^{+}_{-}=0, \tag{2.22}$$

where $[\,]^{+}_{-}$ stands for the discontinuous variation of the quantity within the brackets at the boundary. Note that the expression of 2.19, 2.20 and 2.21 may change a little whether the boundary separates fluids or solid regions; but this is enough for the purpose of the discussion (see section 8.1, pp. 268-271 of Dahlen & Tromp, 1998, for more details).

For each (l,m) couple the differential equations lead to an infinite number of solutions. The eigenvalues ω_{lm} and associated eigenfunctions (U_{lm}, $\dot{U}_{lm}$, V_{lm},...) take discrete values. Each of them can be identified by another integer n: the *overtone number*. Each solution, i.e. each eigenfunction of displacement, can be written ${}_nU_{lm}$, ${}_n\dot{U}_{lm}$ etc. and the associated eigenfrequency ${}_n\omega_{lm}$. The modes with $n=0$ are called *fundamental modes* and those with higher n are called *overtones* (*first overtone*, *second overtone*,...).

A first observation is that the equations do not depend on m. This is due to the spherical symmetry assumed here. Therefore, for a given overtone number n and harmonic degree l, the $2l+1$ eigenfrequencies and eigenfunctions (for $-l\leq m\leq l$) are equal. The problem is said to be *degenerate*. The group of free oscillations with equal eigenfunctions is called a multiplet while each of its components is called a singlet. The true Earth departs from spherical symmetry (due to lateral heterogeneities or rotation for example) so that observations tend to separate the singlets: this is what we call *mode splitting*. This observation allows to constrain some physical parameters within the Earth, but not directly relevant to my thesis. We shall drop the index m wherever it is not necessary in the following (but the

summation still holds on it).

Another observation is that some equations involve the terms U, V, P and their derivatives only, while the others involve W and $\dot{W}$ only. It is related to what we mentioned in the analysis of equation 2.9: there is a rotational-free motion that involves only the eigenfunctions U, V, P and their derivatives with eigenfrequency ${}_n\omega_l^S$ (the *spheroidal field*); and a divergence-free motion that involves only the eigenfunctions W and $\dot{W}$ with eigenfrequency ${}_n\omega_l^T$ (the *toroidal field*). The former is the normal mode equivalent of the P-SV body waves or Rayleigh surface waves, while the latter is the equivalent of the SH-body waves or Love surface waves. In chapters 4 and 5, we only consider the vertical component of the seismogram. Therefore only modes U, V, P and their derivatives will be relevant. There are softwares that solve the equations for a given Earth model, i.e. calculate the eigenfunctions and associated eigenfrequencies for a given radial distribution of the elastic parameters λ, μ and ρ. We will use the software *minos_bran* from the package *MINEOS* of Masters, Misha & Susan (2014) for this purpose.

A closer look at normal modes

Here I analyse the normal mode solutions, i.e. the eigenfunctions and eigenfrequencies for various integers n and l. For simplicity I restrict the analysis to the spheroidal modes by looking at the eigenfrequencies ${}_n\omega_l^S$. I restrict even more the analysis to the radial field by looking at the eigenfunctions ${}_nU_l(r)$ only.

I used the model drawn on figures D.1 and D.2 of appendix D.2 to compute the normal mode solutions. Figure 2.2 shows the eigenvalues ${}_n\omega_l^S$ as a function of the harmonic degree l. The lowest blue line corresponds to the *fundamental mode* ($n = 0$), the lowest orange line to the *first overtone* ($n = 1$) etc. The branches also take the name of *dispersion curves* and the whole diagram is therefore called a *dispersion diagram*. This terminology will be justified in section 2.2.2.

One may see the propagating seismic wavefield as a sum of normal modes; but this is equivalent to seeing the normal modes as interfering propagating waves. On the dispersion diagram it is possible to see patterns other than the one depicted by the continuous lines. These patterns are caused by interefering propagating body waves (e.g. PKIKP within the whole Earth, Jsv within the inner core, ScSsv within the mantle). The most important for the present study is that, for $l/4 \gg n$, the corresponding eigendisplacement is mostly confined near the surface. This is clear on figure 2.3 which shows the eigendisplacement for the fundamental normal mode and the two first overtones (i.e. $n = 0, 1, 2$) for harmonic degrees l ranging from 50 to 100. These normal modes can be seen as multiply-reflected interfering body waves within the upper-mantle (e.g. SSSSS, SSSSSS)

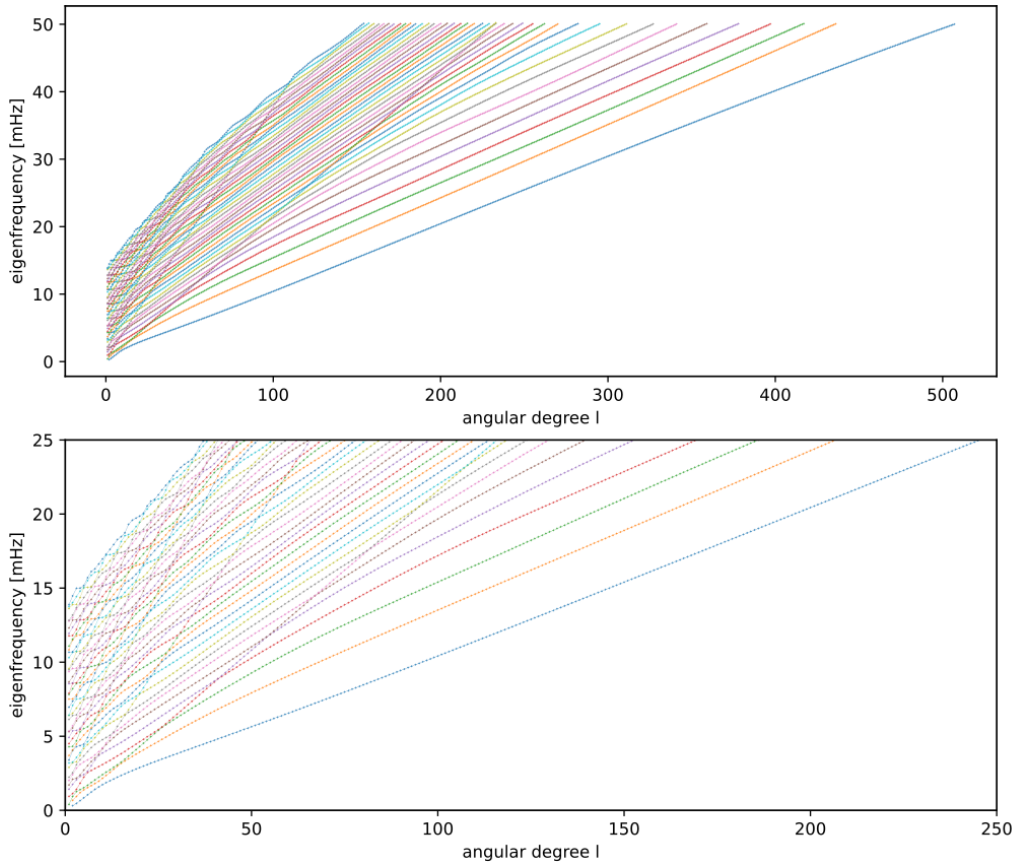

FIGURE 2.2: Dispersion diagram (top) with a close-up (bottom). Crosses are the eigenvalues ${}_n\omega_l^S$ as a function of the angular degrees l for various overtone numbers n. Crosses linked by a continuous line with the same color have the same overtone numbers n. Such an alignment is called a *mode branch*. The branches are ordered from bottom to top in increasing angular order n, starting from $n = 0$ (lowest blue line) to $n = 40$ (highest blue line). For $l/4 \gg n$, the *normal mode branches* tend to the *surface wave mode branches*. The Earth model used is given in appendix D.2

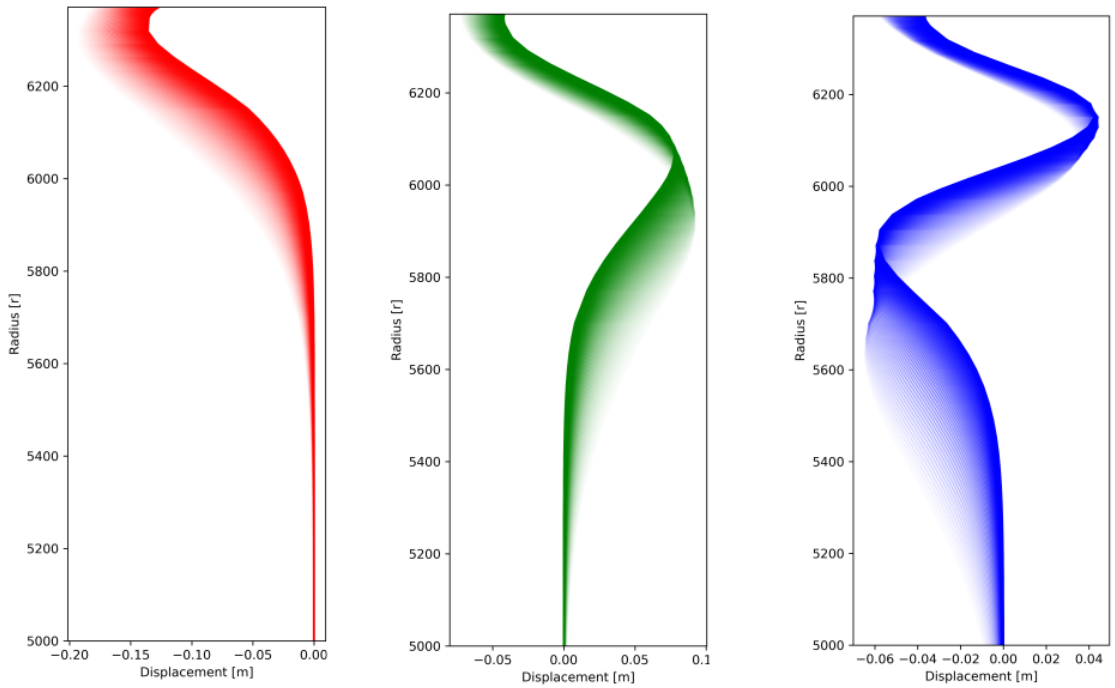

FIGURE 2.3: Displacement eigenfunctions ${}_0U_l(r)$ (left, red), ${}_1U_l(r)$ (middle, green) and ${}_2U_l(r)$ (right, blue) for various harmonic degree l ranging from 50 to 100. The stronger the color, the higher the harmonic degree. Note that the y-axis is truncated below 5000 km radius. The Earth model used is given in appendix D.2.

which constitute the surface waves. I present in the following (section 2.2.2) the derivation of the surface wave seismic wavefield from the normal modes. Analysing the eigendisplacement is interesting because it tells us how the surface wave, at some frequencies, has made the system vibrate. In other words, it tells us how the surface wave is sensitive to the medium as a function of depth and frequency. On figure 2.3 we observe that the displacement eigenfunctions have as many nodes (zeroes along the radius) as the overtone number n. Also, for a given l, the higher the overtone number the deeper the displacement. On the contrary, for one overtone number n, the higher the harmonic degree l (and therefore the eigenfrequency) the shallower the eigendisplacement. Therefore, if one wants to illuminate the mantle at great depths, one needs to consider lower frequencies or, most importantly, higher modes. However, as we will see later, observing higher modes is challenging because the most energetic modes are usually the fundamental modes (at least for shallow earthquakes that excite surface waves most efficiently) and that other modes tend to interfer with each other.

2.2.2 Surface waves

So far we have derived the free oscillations for an Earth model. But what is the actual response to a seismic source and how can we reconciliate the fact that normal modes are standing waves while surface waves are propagating waves? The elasto-dynamic equation and boundary conditions (equations 2.13 and 2.14) still hold; but now they are subject to initial conditions (a source term). Before $t = 0$ the displacement wavefield is zero everywhere. At $t = 0$ and $\boldsymbol{x} = \boldsymbol{x'}$ we impose a unit displacement along each direction of the coordinate system: mathematically it is a Heaviside function. For such a source, the response of a spherically symmetric and anelastic Earth can be written as a sum of normal modes $\boldsymbol{u_k}$ (Dahlen & Tromp, 1998, section 4.1, pages 118-120):

$$\boldsymbol{G}(\boldsymbol{x}, \boldsymbol{x'}, t) = \sum_k (i\nu_k)^{-1} \boldsymbol{u_k}(\boldsymbol{x}) \boldsymbol{u_k}(\boldsymbol{x'}) e^{i\nu_k t}, \tag{2.23}$$

where the subscript k stands for all the triplets $\{n, l, m\}$ and $\nu_k = \omega_k + i\gamma_k$ is the complex eigenfrequency that accounts for anelasticity (in the following I omit the anelastic term in the formulas for simplicity). The wavefield is a sum of waves of the form $\boldsymbol{u}(\boldsymbol{x}, t) = \boldsymbol{A}(\boldsymbol{x}) e^{i\omega t}$ whose amplitudes do not depend on time (except for anelasticity). Therefore it is a sum of 'standing waves'. They are waves with fixed peaks and troughs within the three-dimensional sphere that oscillate at the frequency ω.

Since we want to derive an expression in terms of propagating waves, we need to define a coordinate system that is natural for the ray path. An illustration of this coordinate system is given on figure 2.4. At any location on Earth, the basis unit vector $\hat{\boldsymbol{r}}$ is in the vertical direction and points outside the Earth. The vector $\hat{\boldsymbol{k}}$ is tangent to the spherical shell and points in the direction of the wave propagation. Then the last vector $\hat{\boldsymbol{r}} \times \hat{\boldsymbol{k}}$ is tangent to the spherical shell and orthogonal to the ray-path.

By mean of the Watson transformation (or the Poisson's sum formula), it is possible to transform the summation over l into integration over continuous wavenumber k. Then the Legendre function can be decomposed into the Legendre functions of the first and second kind that are travelling waves. Formal derivations can be found for example in Dahlen & Tromp (1998, pp. 405-414), Snieder & Nolet (1987, their appendix), Nolet (2008, appendix C pp. 197-202) or Gilbert (1976). The frequency domain Green tensor takes the form:

$$\boldsymbol{G}(\boldsymbol{x}, \boldsymbol{x'}, \omega) = \sum_n \frac{\boldsymbol{p_n}(\boldsymbol{x}) \boldsymbol{p_n'^*}(\boldsymbol{x'}) e^{i[-k_n \Delta + s\pi/2 - \pi/4]}}{cCI\sqrt{8\pi k_n |\sin \Delta|}}, \tag{2.24}$$

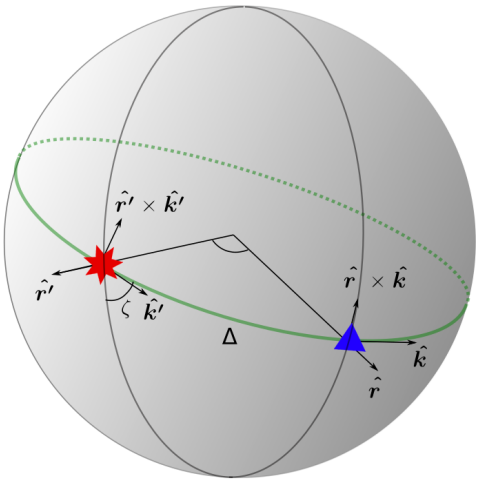

FIGURE 2.4: Ray-specific coordinate system. The vector $\hat{\boldsymbol{r}}$ points vertically ouside the Earth and the vector $\hat{\boldsymbol{k}}$ is tangent to the Earth surface and points in direction of wave propagation. The vector $\hat{\boldsymbol{r}} \times \hat{\boldsymbol{k}}$ is perpendicular to the two others, it is tangent to the Earth surface and orthogonal to the ray. The red star and blue triangle illustrate the seismic source and the receiver respectively. The primed (not primed) vectors denote the coordinate system at the source (receiver). Δ is the source-receiver distance and ζ is the takeoff angle.

where * denotes the complex conjugate, n is the overtone number, and,

$$\boldsymbol{p}_n(\boldsymbol{x}) = \hat{\boldsymbol{r}}_n U(\boldsymbol{x}) - i\hat{\boldsymbol{k}}_n V(\boldsymbol{x}) + i(\hat{\boldsymbol{r}} \times \hat{\boldsymbol{k}})_n W(\boldsymbol{x}), \tag{2.25}$$

and,

$$\boldsymbol{p}'^*_n(\boldsymbol{x}') = \hat{\boldsymbol{r}}'_n U(\boldsymbol{x}') + i\hat{\boldsymbol{k}}'_n V(\boldsymbol{x}') - i(\hat{\boldsymbol{r}}' \times \hat{\boldsymbol{k}}')_n W(\boldsymbol{x}'). \tag{2.26}$$

Note that this expression is valid in the *far-field* only. The vectors $\boldsymbol{p}$ and $\boldsymbol{p}'$ are called the *polarization vectors* by Snieder (1986). The polarization vector $\boldsymbol{p}'$ is evaluated at the source location, and it involves, in particular, the evaluation of the eigenfunctions of displacement at the source depth. Therefore, the depth of the source determines which modes will influence the wave. For instance, a shallow source will mostly excite the modes whose eigenfunctions have high amplitudes close to the surface. The polarization vector $\boldsymbol{p}$ is evaluated at the receiver location, which is (almost) always situated at the Earth's surface. However care must be taken if the Earth model contains an oceanic layer. In my study I am interested in the Pacific region so that I consider an ocean on top of the Earth model (see figure D.2 in appendix D.2). However the stations are on islands or at the border of the continents; they are not floating in the water (though it would be possible, e.g. Pipatprathanporn & Simons, 2021; Simons, 2021). For this reason, I will set them at the bottom of the ocean, considering that 3 km in station depth

will not bias significatively the result, at least less that evaluating the eigenfunctions in the water layer. The juxtaposition of the two polarization vectors may seem strange at first but the Green tensor is a second order tensor that represents the response to a point source in any direction recorded by a sensor in any other direction. Given the source and sensor orientations we obtain a scalar wavefield by projection. The amplitude also contains the term $cCI\sqrt{8\pi k|\sin\Delta|}$ at the denominator. The cCI is simply a normalizing constant for the eigenfunctions that we set to 1 Nm in the following. The rest of the expression accounts for the two-dimensional geometrical spreading.

The exponential in equation 2.24 is a propagating factor. First it contains the $s\pi/2$ term that is a correction for caustics. The integer s (that appears with the Poisson's sum formula) is the *Maslov index*. It has a very simple geometrical interpretation as illustrated in figure 2.5. The propagating wave leaving the source starts with a Maslov index of zero and it increases by one each time the path passes by the source or its antipode. For instance it is zero for the wave leaving in the minor arc path direction (i.e. the shortest path from the source to the receiver) and it increases by two each time it arrives at the station after passing through the source and its antipode. It is one for the major arc path, then three the next time this wave arrives at the station again. This gives rise to a notation for surface waves where the letter R and G are used for the Rayleigh and Love waves respectively and the Maslov index is juxtaposed as in R0, G0, R1, G1, R2 etc. The term $-\pi/4$ is a phase shift correction at the source. The most important term is $-k\Delta$: k is the *wavenumber* that counts the number of phase cycles per meter propagated and Δ is the source to receiver distance. The term $k\Delta$ is the cumulated phase along the total distance between the source and the receiver. For a given reference Earth model and seismic source we can therefore compute a predicted phase. Differences between the true Earth and the reference one produce differences between the observed and the predicted phases. Therefore this phase difference contains some information about the true Earth.

Note that equation 2.24 shows that surface waves are *dispersive*. In the time domain the propagating term becomes $(k\Delta - \omega t)$. Therefore a surface of constant phase would travel a distance Δ during a time $t = \Delta k/\omega$ or $t = \Delta p(\omega)$ where $p(\omega) = k/\omega$ is the *phase slowness* of the wave. The distance propagated as a function of time is illustrated on figure 2.6. If the slowness is constant with frequency, i.e. if $p(\omega) = k/\omega =$ constant, then waves with various frequencies follow the same time-distance curve (or *hodochrone*). On the contrary, if the slowness (or equivalently the phase velocity $c(\omega) = 1/p(\omega) = \omega/k$) is not constant with frequency, a fixed observer would observe waves with different frequencies arriving

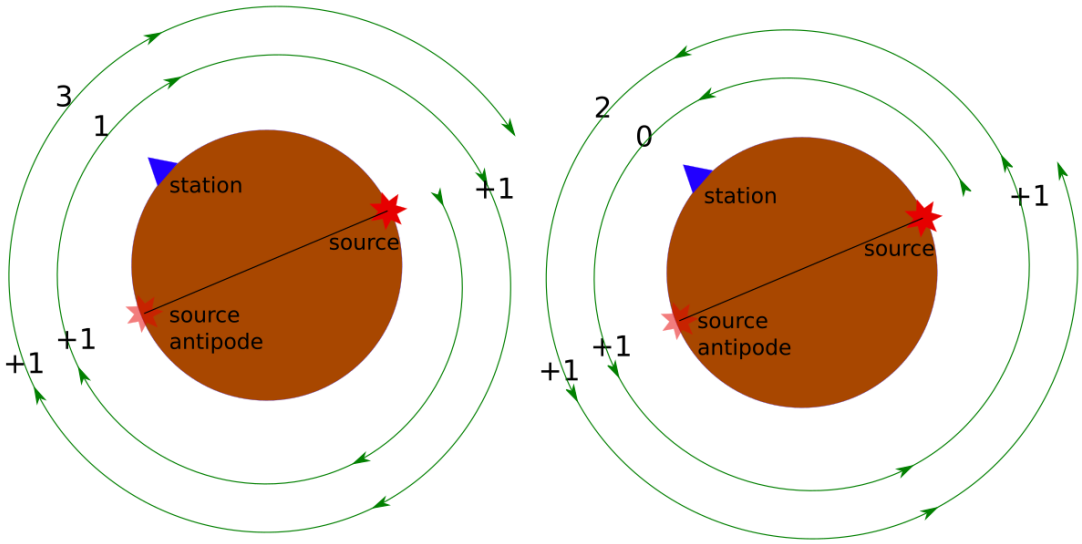

FIGURE 2.5: Interpretation of the Maslov index s in terms of spherical turns the wave has travelled. Each time the wave passes the source or its antipode s is incremented by one. Left: the wave starting with the major arc arrives at the station with a Maslov index $s = 1$ since it passed by the source antipode. The next time it arrives at the station it passed the source and its antipode so that the Maslov index is $s = 3$ and so on. For such a wave the Maslov index is always an odd number. Right: a wave starting with the minor arc arrives at the station with a Maslov index $s = 0$, the next time it arrives at the station it passed the source and its antipode so that the Maslov index is $s = 2$ and so on. For such a wave, the Maslov index is always an even number. This leads to a naming convention for surface waves, in which we identify the Rayleigh (respectively Love) wave arrivals by writting next to each other the letter R (respectively G) and the maslov index, as in R0, R1 etc. (G0, G1 etc.).

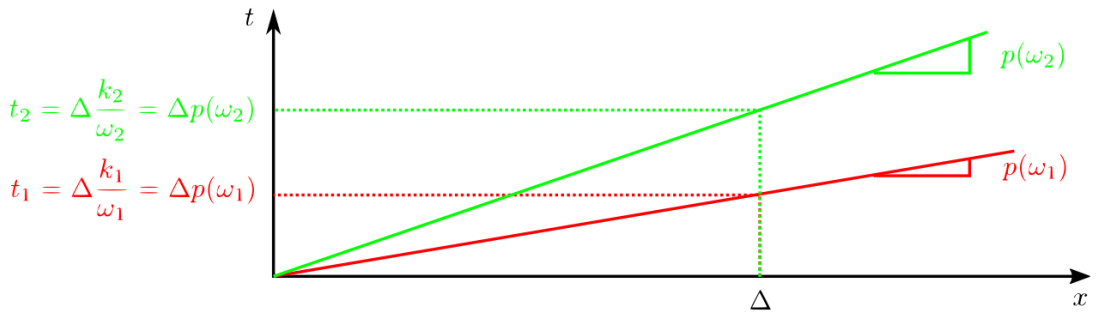

FIGURE 2.6: Illustration of dispersion. The travel time of a constant phase surface along a distance Δ for a wave with frequency ω_1 is given by $t_1 = \Delta p(\omega_1)$ with $p(\omega_1) = k_1/\omega_1$ the phase slowness. The time-distance curve (or hodochrone) for this wave is represented by the red line. If the phase slowness is not a constant of frequency (i.e. $k/\omega \neq$ constant), then another wave with frequency ω_2 has a different slowness and the time-distance curve is different. It arrives at the observer at distance Δ at another time t_2. The medium is dispersive.

at different times. For example, a Dirac source would spread out along its way and look more like a Gaussian far from the source. The dispersivity property depends on the medium. The dispersion diagram of figure 2.2 shows the frequency as a function of the harmonic degree l. But if we replace l by $k = \sqrt{l(l+1)}$ we can say if the slowness $p(\omega) = k/\omega$ is constant or not, which justifies the name *dispersion diagram*. An informative version of the dispersion diagram is the one showing the phase velocity as a function of frequency (figure 2.7). Clearly, the Earth model used to compute the normal modes is dispersive. Since waves with different frequencies are associated with different sensitivities with depth (eigendisplacement), this property will help to constrain the Earth properties as a function of depth.

The derivative of the phase velocity $C(\omega) = dc(\omega)/d\omega$ is known as the *group velocity*. It is the velocity at which the energy of a certain mode travels. The group velocity dispersion diagram for the fundamental mode and the first three overtones is drawn on figure 2.8. This diagram is useful to predict the arrival time of a wave packet corresponding to some mode order. The fundamental mode is particular in that it has a relatively low group velocity distinct from the overtones at frequencies relevant in this thesis (i.e. from $\sim$5 mHz to $\sim$60 mHz). It is always late on the seismograms. Overtones are faster. At low frequency their velocities are different so that they arrive at distinct times. At high frequency however their velocities tend to be close so that an observer will see them interfering. Of course this also depends on the distance to the source; the greater the distance the most separate the various modes can be.

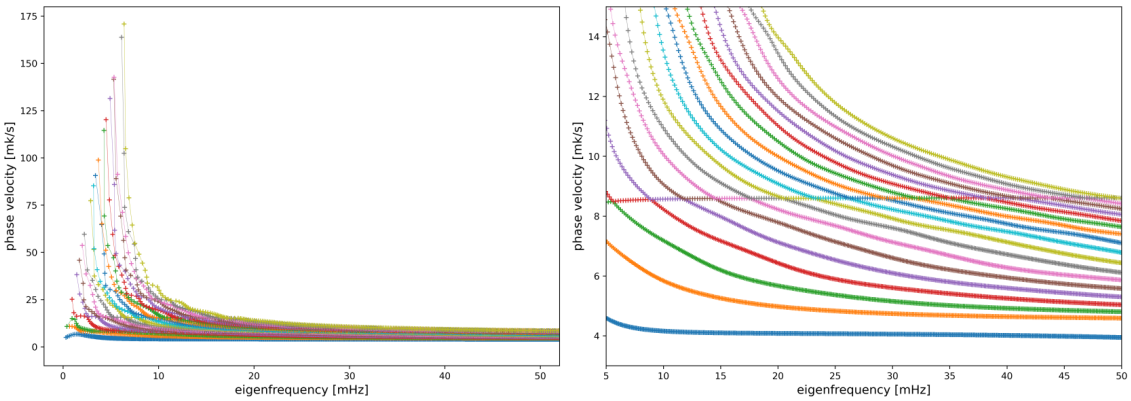

FIGURE 2.7: Dispersion diagram (top) and a close-up (bottom). Same data as in figure 2.2, but the phase velocity as a function of frequency is plotted: $c(\omega)$ or simply ω/k with $k = \sqrt{l(l+1)}$ as function of ω.

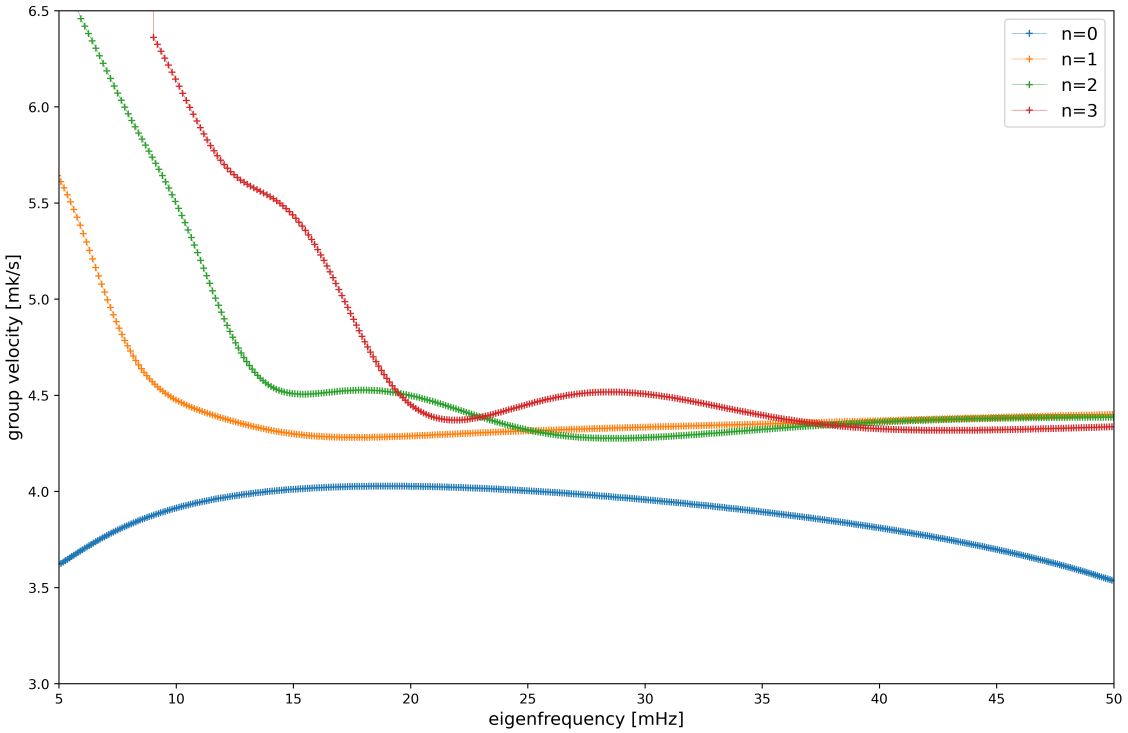

FIGURE 2.8: Dispersion diagram representing the group velocity as a function of eigenfrequency for the fundamental modes and the first three overtones. It actually represents the derivatives of the first four mode orders of figure 2.7.

In practice we will use the routine *green* from the package *MINEOS* of Masters, Misha & Susan (2014) to compute the Green tensor given the coordinates of a point source and a receiver. The *green* routine uses the eigensolutions that have been computed with the *minos_bran* routine, for the considered Earth model.

Using equation A.9 (see appendix A) we can write the frequency domain response to a moment tensor at the receiver location, projected onto the sensor orientation $\hat{\boldsymbol{v}}$ as:

$$s(\omega) = (i\omega)^{-1}[\boldsymbol{M} : \nabla_{x'}\boldsymbol{G}(\boldsymbol{x}, \boldsymbol{x'}, \omega)^T].\hat{\boldsymbol{v}}. \tag{2.27}$$

The difference in the term $i\omega$ with respect to equation A.9 comes from a slightly different definition of the Green tensor (defined as the response to a Dirac in appendix A, not a Heaviside) and normalization of the eigenfunctions. Inserting 2.24 leads to,

$$s(\omega) = \sum_n (i\omega)^{-1}(\boldsymbol{M} : \boldsymbol{E_n}(\boldsymbol{x'})^*) \times (\frac{e^{-i(k_n\Delta - s\pi/2 + \pi/4)}}{\sqrt{8\pi k_n |\sin\Delta|}}) \times \boldsymbol{p_n}(\boldsymbol{x}).\hat{\boldsymbol{v}}, \tag{2.28}$$

with the strain tensor defined as $\boldsymbol{E} = \frac{1}{2}[\boldsymbol{\nabla p} + \boldsymbol{\nabla p}^T]$. The first term is the radiation at the source; following Zhou, Dahlen & Nolet (2004) we write it S. The fraction term is related to the propagation. As described above the exponential term accounts for the phase variation along the path and the square root accounts for the geometrical attenuation. The last term is related to the receiver. It accounts for the displacement eigenfunctions at the receiver depth and for the projection of the arrival wave onto the seismological sensor orientation. We will write this term R in the following. Finally equation 2.28 can be rewritten in a simpler form,

$$s(\omega) = \sum_n S_n(\omega, \zeta) \times (\frac{e^{-i(k_n\Delta - s\pi/2 + \pi/4)}}{\sqrt{8\pi k |\sin\Delta|}}) \times R_n, \tag{2.29}$$

where the explicit expression for the source term is:

$$\begin{aligned}
S(\omega,\zeta) = &-i\omega^{-1}[M_{rr}\dot{U} + (M_{\theta\theta} + M_{\phi\phi})r^{-1}(U - \frac{1}{2}kV)] \\
&+\omega^{-1}(-1)^n(\dot{V} - r^{-1}V + kr^{-1}U)(M_{r\phi}\sin\zeta + M_{r\theta}\cos\zeta) \\
&+i\omega^{-1}krV[M_{\theta\phi}\sin 2\zeta + \frac{1}{2}(M_{\theta\theta} - M_{\phi\phi}\cos 2\zeta] \\
&+\omega^{-1}(-1)^n(\dot{W} - r^{-1}W)(M_{r\theta}\sin\zeta - M_{r\phi}\cos\zeta) \\
&+i\omega^{-1}kr^{-1}W[\frac{1}{2}(M_{\theta\theta} - M_{\phi\phi})\sin 2\zeta - M_{\theta\phi}\cos 2\zeta],
\end{aligned} \tag{2.30}$$

and for the receiver term is:

$$R = [\hat{\boldsymbol{r}}' U(\boldsymbol{x}') - i\hat{\boldsymbol{k}}' V(\boldsymbol{x}') + i(\hat{\boldsymbol{r}}' \times \hat{\boldsymbol{k}}' W(\boldsymbol{x}')].\hat{\boldsymbol{v}}. \tag{2.31}$$

The variable ζ is the takeoff angle – measured counter-clockwise from the south. Since the source is oriented in space, it is natural that the azimuth of the receiver matters. It is worth mentioning that the source radiation depends both on depth and frequency (e.g. Rösler & Lee, 2020).

This formulation is powerful for its interpretability. In practice the full response is obtained by convolving the Green tensor with the full moment tensor, then projected onto the sensor orientation. We will use the routine *syndat* from the package *MINEOS* of Masters, Misha & Susan (2014) for that purpose.

I represent synthetic Rayleigh-wave waveforms for the vertical component calculated independently for the fundamental mode and the first three overtones for sources at two depths and within two frequency bands in figure 2.9. We observe both the minor-arc arrival R0 and later the major-arc arrival R1. The R1 arrival has lower amplitude. Since it is observed later it had more time to attenuate. The fundamental mode has a greater amplitude than the overtones but for a deeper source the relative amplitude of the overtones is increased. This is related to the eigenfunctions of displacement: the most excited modes are those whose eigenfunctions of displacement have high amplitude at the source depth. To observe overtones, it is necessary to consider deep sources. The wavepackets for all modes are better separated in the R1 arrival than R0. Since modes propagate with their specific group velocity (see figure 2.8), the greater the source-receiver distance the more separated they are. We also observe that modes are better separated at low frequency. As we observed on figure 2.8, the velocities of various modes are very different at low frequency but they become close as frequency increases, explaining the overlap of modes at high frequency. If one wants to observe modes independently, one needs to use source-receiver pairs with long enough distances. One also needs to consider low enough frequencies. Observing the fundamental mode is the easiest since it is usually the most energetic and it is well separated from the overtones. However, higher overtones are necessary to illuminate deeper parts of the mantle.

2.2.3 Path-specific forward problem

In a laterally homogeneous system the elastic parameters vary only with depth. Therefore, a discrepancy between the observed and synthetic seismograms is related to a perturbation between the reference model and the true Earth averaged

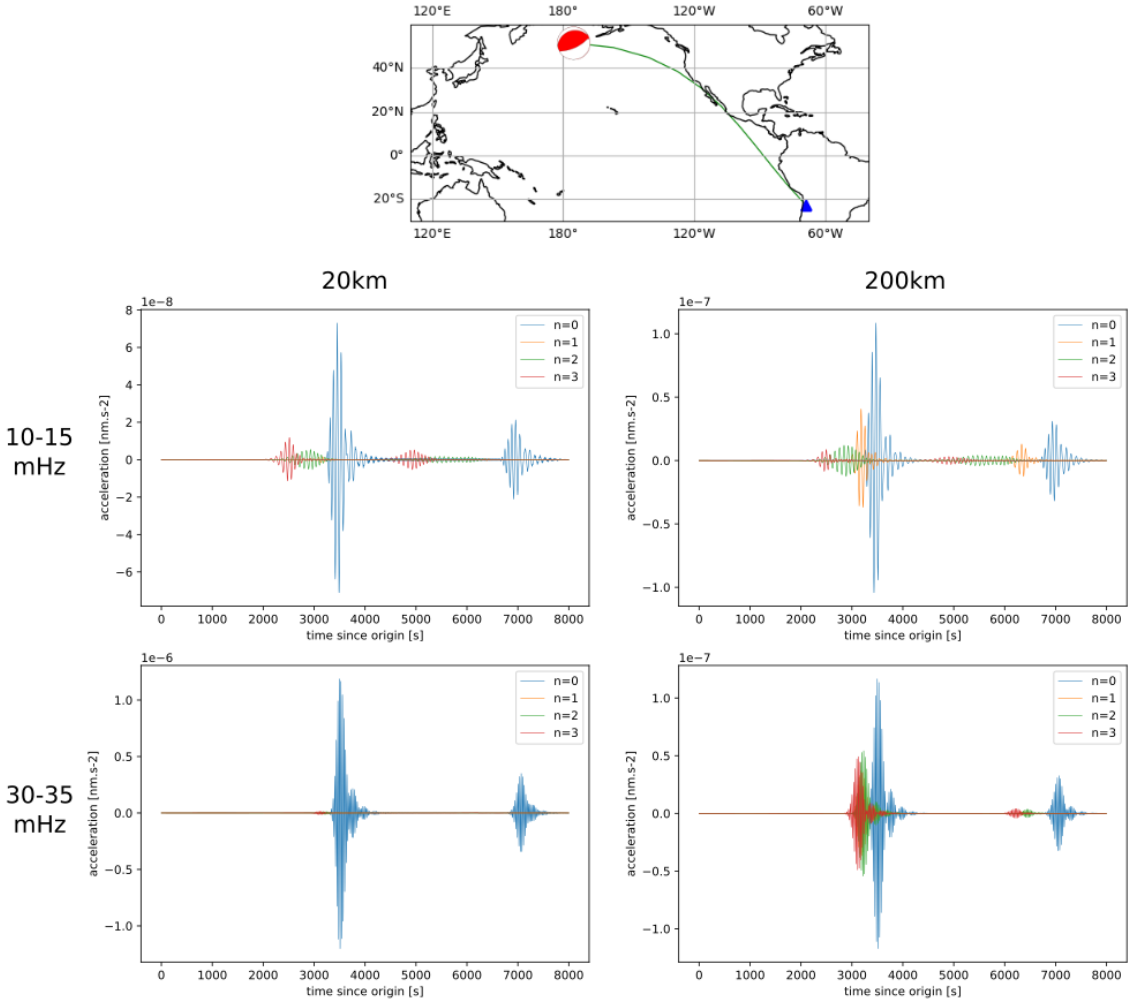

FIGURE 2.9: Relative amplitude of the fundamental and the three first overtones for two sources at 20 km (left column) and 200 km (right column) in two distinct frequency bands : 10-15 mHz (top line) and 30-35 mHz (bottom line). The map locates the seismic source as a red beachball (GCMT name C201308301625B) and the station as a blue triangle (LVC) used to produce the synthetic waveforms. Parameters for the sources and stations used to illustrate this chapter are given in appendix D. Each simulated mode has one color as indicated by the legend.

along the ray-path. Elaborate methods have been proposed to recover the perturbations. For example Nolet, Trier & Huisman (1986) invert the full waveform using a non-linear inversion scheme. However, a simpler forward problem were the data are – almost – lineary related to the Earth model is usually prefered (for reasons of computational cost). For example Dziewonski, Mills & Bloch (1972), followed by Lerner-Lam & Jordan (1983) propose a scheme based on cross-correlation with pure-mode synthetics. Cara & Lévêque (1987) propose to measure what they call *secondary observables* from the cross-correlation method of Dziewonski, Mills & Bloch (1972) to relate almost linearly these data to the path-averaged S-wave velocity perturbations. Later automated by Debayle (1999), this technique is applied by Maggi et al. (2006b) to compute path-averaged S-wave velocities for paths crossing the Pacific ocean.

Producing path-averaged models for a set of source-receiver paths is the first step of a two-step scheme toward a three-dimensional model as discussed in the introductory chapter. The second step is a linear regionalization to produce a set of two-dimensional maps at discrete depths. For example Maggi et al. (2006b) use the regionalization process based on a data fitting approach proposed by Montagner (1986) to produce such maps. Since the regionalization step is linear, it is tractable with the SOLA (Subtractive Optimally Localized Averages) inversion. In chapter 4 we take advantage of the SOLA inversion to regionalize the path-averaged models produced by Maggi et al. (2006b).

With the two-step approach, all spatial dimensions are not constrained together at the same time. This will be clear in chapter 4 where the SOLA inversion can only produce the lateral resolution information. Also the regionalization relies on ray theory that does not account for finite frequency effects (such as detailed off-ray sensitivity). In the next part I present the finite frequency theory based on the Born approximation. It is an extension of the ray theory to account also for lateral heterogeneity so that a forward theory can relate data to the three-dimensional Earth in a single step.

2.3 Laterally heterogeneous system

In a laterally homogeneous medium, the density and Lamé parameters are laterally constant in a layer: $\rho(r)$, $\lambda(r)$, $\mu(r)$. In such a case, the energy released at the source that travels along a great circle stays in that plane. In a laterally heterogeneous medium the elastic parameters are locally perturbed by some amount: $\rho(r) \rightarrow \rho(r) + \delta\rho(r,\theta,\phi)$, $\lambda(r) \rightarrow \lambda(r) + \delta\lambda(r,\theta,\phi)$, $\mu(r) \rightarrow \mu(r) + \delta\mu(r,\theta,\phi)$.

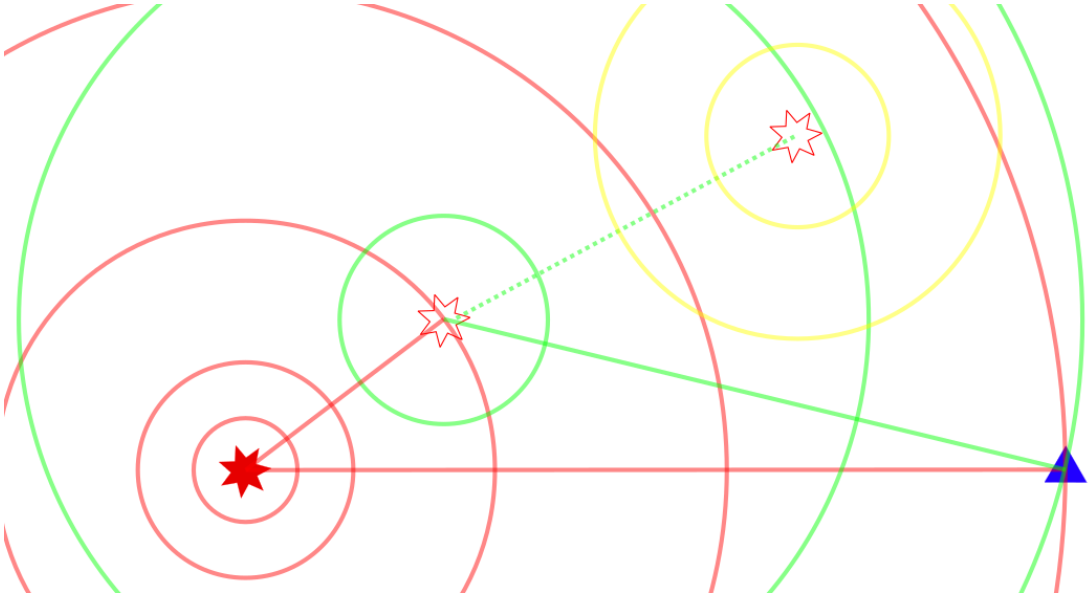

FIGURE 2.10: Illustration of the scattering principle. From a seismic source (red star) radiates an initial wavefield (red circles). Some ray (red line) in the initial wavefield hits a scatterer (an heterogeneity, red empty star). The scatterer acts like a secondary source from which radiates a scattered wavefield (green circles). Some ray (green line) in the scattered wavefield arrives at the station (blue triangle) and adds to the initial wavefield. Some other rays of the scattered wavefield may hit another scatterer giving rise to a secondary scattered wavefield (yellow circles). In the Born approximation, such a secondary scattered wavefield is ignored.

The wavefield becomes more complicated. The Born approximation gives a way to extend the ray theory to describe such a wavefield.

2.3.1 Principle

Figure 2.10 illustrates the principle of scattering. A seismic source produces an initial wavefield. This wavefield may encounter a punctual heterogeneity. This heterogeneity, *a scatterer*, acts like a secondary source that is excited by the incoming wavefield; it radiates a portion of the energy of the initial wavefield in all directions: a scattered wavefield adds to the initial one. If the medium is considered continously heterogeneous, we may integrate the scattered waves produced continuously by the whole medium $\iiint_{\oplus}$.

One may note that the scattered wavefield may encounter another heterogeneity and give rise to a secondary scattered wavefield. On figure 2.10 the secondary scattered wavefield is represented by the yellow circles. However, this secondary wavefield only contains a portion of the energy of the scattered wavefield that is already a portion of the energy of the initial one. Therefore we assume that

only the initial wavefield produces significant scattered waves. This is the *Born approximation* or the so-called *single-scattering* approximation.

2.3.2 Born approximation

Let us give a formal derivation of the single scattering following Nolet (2008). Again, for simplicity we use the linear operator $\mathcal{L}$ for the elasto-dynamic equation.

Far from a point source in an homogeneous medium the response observed by a receiver in $\mathbf{x}$ to a point source in $\mathbf{x}'$ is the Green tensor:

$$\mathcal{L}\boldsymbol{G}(\boldsymbol{x},\boldsymbol{x}') = 0. \tag{2.32}$$

In a laterally heterogeneous medium, the operator $\mathcal{L}$ is perturbed: $\mathcal{L} \rightarrow \mathcal{L} + \delta\mathcal{L}(\boldsymbol{x})$. As a consequence the wavefield is also perturbed: $\boldsymbol{G}(\boldsymbol{x},\boldsymbol{x}') \rightarrow \boldsymbol{G}(\boldsymbol{x},\boldsymbol{x}') + \delta\boldsymbol{G}(\boldsymbol{x},\boldsymbol{x}')$. Therefore, in an heterogeneous medium we have,

$$(\mathcal{L} + \delta\mathcal{L})(\boldsymbol{G}(\boldsymbol{x},\boldsymbol{x}') + \delta\boldsymbol{G}(\boldsymbol{x},\boldsymbol{x}')) = 0. \tag{2.33}$$

Developing we obtain,

$$\mathcal{L}\boldsymbol{G}(\boldsymbol{x},\boldsymbol{x}') + \delta\mathcal{L}\boldsymbol{G}(\boldsymbol{x},\boldsymbol{x}') + \mathcal{L}\delta\boldsymbol{G}(\boldsymbol{x},\boldsymbol{x}') + \delta\mathcal{L}\delta\boldsymbol{G}(\boldsymbol{x},\boldsymbol{x}') = 0. \tag{2.34}$$

Far from the source we still have $\mathcal{L}\boldsymbol{G}(\boldsymbol{x},\boldsymbol{x}') = 0$. Moreover we may neglect the second order term in δ: $\delta\mathcal{L}\delta\boldsymbol{G}(\boldsymbol{x},\boldsymbol{x}') = 0$. This approximation is the mathematical equivalent of neglecting that the scattered wavefield gives rise to multiply-scattered wavefields. So finally,

$$\mathcal{L}\delta\boldsymbol{G}(\boldsymbol{x},\boldsymbol{x}') = -\delta\mathcal{L}\boldsymbol{G}(\boldsymbol{x},\boldsymbol{x}'). \tag{2.35}$$

The left-hand side is the non-perturbed elasto-dynamic operator, it is known since it contains the elastic parameters of the reference homogeneous Earth model. Therefore we should be able to find a solution for the perturbed wavefield $\delta\boldsymbol{G}(\boldsymbol{x},\boldsymbol{x}')$. The right-hand side can be seen as a forcing term. We see in this equation the interpretation of single scattering given above. On the right-hand side an initial wavefield strikes an heterogeneity. The heterogeneity is excited and acts as a secondary source. This secondary source produces a wavefield that propagates in the reference model (no multiple scattering), so the response to this scattered wavefield is given as a solution of the non-perturbed elasto-dynamic equation. Now the medium is continuously heterogeneous so the source term has value

everywhere. Using equation A.6 from appendix A that gives the response of the system to an extended source as a function of the source function and the response to a point source, we obtain:

$$\delta \boldsymbol{G}(\boldsymbol{x},\boldsymbol{x}') = \iiint_{\oplus} \boldsymbol{G}(\boldsymbol{x},\boldsymbol{x}'')(-\delta\mathcal{L}\boldsymbol{G}(\boldsymbol{x}'',\boldsymbol{x}))d^3\boldsymbol{x}'', \tag{2.36}$$

Here we should understand that the initial point source at $\boldsymbol{x}'$ produces an initial wavefield that strikes a point scatterer at $\boldsymbol{x}''$ that produces a scattered wavefield that is observed at $\boldsymbol{x}$. The integration is over all the point scatters, i.e. the whole medium. Developing the forcing term we obtain:

$$\begin{aligned}\delta \boldsymbol{G}(\boldsymbol{x},\boldsymbol{x}') &= \iiint_{\oplus} \omega^2\delta\rho(\boldsymbol{x}'')\boldsymbol{G}(\boldsymbol{x},\boldsymbol{x}'')\boldsymbol{G}(\boldsymbol{x}'',\boldsymbol{x}')d^3\boldsymbol{x}'' \\ &+ \iiint_{\oplus} \boldsymbol{G}(\boldsymbol{x},\boldsymbol{x}'')\nabla_{\boldsymbol{x}''}(\delta\lambda(\boldsymbol{x}'')\cdot\boldsymbol{G}(\boldsymbol{x}''\boldsymbol{x}')d^3\boldsymbol{x}'' \\ + \iiint_{\oplus} \boldsymbol{G}(\boldsymbol{x},\boldsymbol{x}'')\nabla_{\boldsymbol{x}''}\cdot[\delta\mu(\boldsymbol{x}'')(\nabla_{\boldsymbol{x}''}\boldsymbol{G}(\boldsymbol{x}'',\boldsymbol{x}'+\nabla_{\boldsymbol{x}''}\boldsymbol{G}(\boldsymbol{x}'',\boldsymbol{x}')^T)]d^3\boldsymbol{x}''.\end{aligned} \tag{2.37}$$

After some algebraic transformations we obtain,

$$\begin{aligned}\delta \boldsymbol{G}(\boldsymbol{x},\boldsymbol{x}') &= \iiint_{\oplus} \omega^2\delta\rho\boldsymbol{G}(\boldsymbol{x},\boldsymbol{x}'')\boldsymbol{G}(\boldsymbol{x}'',\boldsymbol{x}')d^3\boldsymbol{x}'' \\ &- \iiint_{\oplus} \delta\lambda(\nabla_{\boldsymbol{x}''}\cdot\boldsymbol{G}(\boldsymbol{x},\boldsymbol{x}''))(\nabla_{\boldsymbol{x}''}\cdot\boldsymbol{G}(\boldsymbol{x}'',\boldsymbol{x}')d^3\boldsymbol{x}'' \\ - \iiint_{\oplus} \delta\mu(\nabla_{\boldsymbol{x}''}\boldsymbol{G}(\boldsymbol{x},\boldsymbol{x}'') : (\nabla_{\boldsymbol{x}''}\boldsymbol{G}(\boldsymbol{x}'',\boldsymbol{x}')+\nabla_{\boldsymbol{x}''}\boldsymbol{G}(\boldsymbol{x}'',\boldsymbol{x}')^T)d^3\boldsymbol{x}''.\end{aligned} \tag{2.38}$$

Here we can make an important observation: the perturbation in the elastic wavefield is linear in the elastic parameters. Therefore, it is tractable with SOLA to estimate perturbations in the elastic parameters from observation of the perturbed wavefield within the framework of the Born approximation. Actually the linearity already appeared first in the linear non-perturbed forced wave equation (equation 2.35). The linearity is produced by neglecting the term of order 2 in δ; the linearity of the Born approximation arises from neglecting multiple-scattered waves.

2.3.3 Perturbed surface waves

In the following I use a lighter notation that fits with the notation of Zhou, Dahlen & Nolet (2004). The location of the point scatterer is now designated as $\boldsymbol{x}$. Primed symbols denote any quantity associated to the propagation from the source to the scatterer and double primed symbol any quantity associated to the propagation

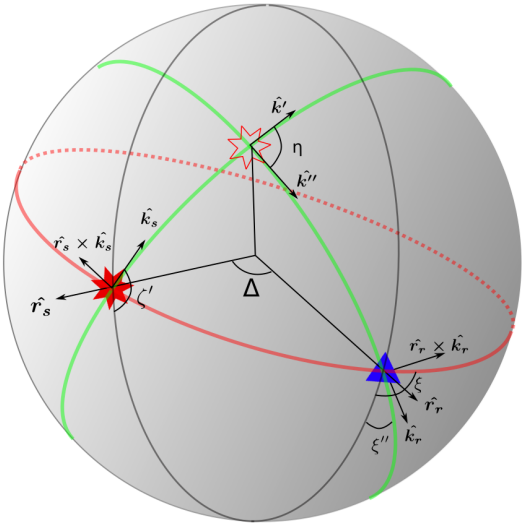

FIGURE 2.11: Ray-specific coordinate system (as in figure 2.4 but in the case of single-scattering). ζ' is the leaving angle of the wave along the source-scatterer path and ξ'' is the arrival angle of the wave along the scatterer-receiver path. η is the scattering angle, i.e. the angle between the great-circle paths that meet the source, the receiver, and the scatterer. ξ is the arrival angle of the unperturbed wave.

from the scatterer to the receiver. The coordinate system is still path-specific as in figure 2.4 but now it involves two rays, one from the seismic source to the scatterer and one from the scatterer to the receiver. It is illustrated in figure 2.11. Moreover, we use the subscripts s and r to specify the source and the receiver respectively.

With this notation equation 2.38 becomes,

$$\begin{aligned} \delta \boldsymbol{G}_{\boldsymbol{rs}} = & \iiint_{\oplus} \omega^2 \delta\rho \boldsymbol{G}'' \boldsymbol{G}' d^3\boldsymbol{x} \\ & - \iiint_{\oplus} \delta\lambda (\nabla_{\boldsymbol{x}} \cdot \boldsymbol{G}'')^T (\nabla_{\boldsymbol{x}} \cdot \boldsymbol{G}') d^3\boldsymbol{x} \\ & - \iiint_{\oplus} \delta\mu (\nabla_{\boldsymbol{x}} \boldsymbol{G}'')^T : (\nabla_{\boldsymbol{x}} \boldsymbol{G}' + (\nabla_{\boldsymbol{x}} \boldsymbol{G}')^T) d^3\boldsymbol{x}, \end{aligned} \tag{2.39}$$

where $\delta \boldsymbol{G}_{\boldsymbol{rs}}$ is the perturbed Green tensor for the source at $\boldsymbol{x_s}$ observed at the receiver location $\boldsymbol{x_r}$, $\boldsymbol{G'}$ is the Green tensor observed at the scatterer location $\boldsymbol{x}$ for the source at $\boldsymbol{x_s}$, and $\boldsymbol{G''}$ is the Green tensor observed at the receiver $\boldsymbol{x_r}$ for the 'source' (the secondary source) at the scatterer location $\boldsymbol{x}$. We already have the non-perturbed Green tensor in a laterally homogeneous system (equation 2.24). Inserting the Green tensor and its gradient with respect to the scatterer location

in equation 2.39 gives:

$$\delta G_{rs} = \sum_{n'} \sum_{n''} \iiint_{\oplus} \frac{\boldsymbol{p}^{s*}_{n'} \boldsymbol{p}^{r}_{n''} e^{-i[k'\Delta' + k''\Delta'' - (s'+s'')\pi/2}}{\sqrt{8\pi k' |\sin \Delta'|} \sqrt{8\pi k'' |\sin \Delta''|}} \cdot {}_{n'}\Omega_{n''} d^3\boldsymbol{x}, \tag{2.40}$$

where ${}_{n'}\boldsymbol{\Omega}_{n''}$ is the *interaction matrix*, defined as:

$${}_{n'}\boldsymbol{\Omega}_{n''}(\boldsymbol{x}) = \omega^2 \delta\rho(\boldsymbol{p'} \cdot \boldsymbol{p''}^*) - \delta\lambda(\mathrm{tr}\boldsymbol{E})(\mathrm{tr}\boldsymbol{E''}^*) - 2\delta\mu(\boldsymbol{E'} : \boldsymbol{E''}^*), \tag{2.41}$$

and $\boldsymbol{E} = 1/2[\boldsymbol{\nabla p} + (\boldsymbol{\nabla p})^T]$ is the strain tensor.

I do not detail the lengthy derivation here. It was first derived by Snieder (1986) in cartesian coordinates and then extended to spherical coordinates by Snieder & Nolet (1987). Here we use the formulation of Zhou, Dahlen & Nolet (2004). Most terms in this formulation have already been discussed in section 2.2.2.

The first sum on n' is associated with the Green tensor from the source to the scatterer. The second sum on n'' corresponds to the Green tensor from the scatterer to the receiver. There is a double sum because all modes n' leaving the source excite all modes n'' at the scatterer. Considering many modes in the summation is the so-called *mode-coupling*. The approximation that there is no mode-coupling allows to consider one mode at a time, i.e. the mode that leaves the source excites only itself at the scatterer: $n' = n'' = n$. Zhou, Dahlen & Nolet (2004) showed that given the present computational power that allows only coarse parameterizations, it is a good approximation. I use this approximation in the application of the finite frequency theory in chapter 5. Future developments may extend the present study to include mode-coupling.

The denominator is the geometrical spreading factor for a path that passes by the scatterer; it is the product of the geometrical attenuation along the source to scatterer path by that along the scatterer to receiver path. The last term in the exponential involves the Maslov index s which corrects the phase for caustics (see figure 2.5). The exponential is the propagating term. It is the accumulated phase with wavenumber k' along the source-to-scatterer path-length Δ' plus that with wavenumber k'' along the scatterer-to-receiver path-length Δ''. The polarization vectors $\boldsymbol{p}^{s}_{n'}$ and $\boldsymbol{p}^{r}_{n''}$ are the source polarization vector of $\boldsymbol{G'}$, and the receiver polarization vector of $\boldsymbol{G''}$. They are evaluated at the depth of the source and receiver respectively.

All terms related to the propagation along the source-to-scatterer path and the scatterer-to-receiver path have been analysed. They all depend only on the laterally homogeneous medium. All terms related to what happens at the scatterer

location are in ${}_{n'}\boldsymbol{\Omega}_{n''}(\boldsymbol{x})$. It contains the relation between the perturbed Green tensor and the elastic parameters at the scatterer location and is still linear in the elastic parameters. The polarization terms $\boldsymbol{p'}$ and $\boldsymbol{p''}$ can be seen as the 'receiver' or 'source' (which are both the scatterer) of the Green tensor in the first or second part of the path respectively. They are located at the same location (same depth) but they may be different because they may concern different modes n; if we ignore mode-coupling, then they are the same (in magnitude).

As we did in section 2.2.2, we can use equation A.9 from appendix A to derive the response to a moment tensor from the perturbed Green tensor and project it onto the receiver orientation $\hat{\boldsymbol{v}}$:

$$\delta s(\omega) = (i\omega)^{-1}\boldsymbol{M} : \nabla_s[\delta \boldsymbol{G_{rs}}^T(\omega)].\hat{\boldsymbol{v}}. \tag{2.42}$$

Finally the perturbed response to a full moment tensor in a laterally heterogeneous medium is written:

$$\begin{aligned}\delta s(\omega) = \sum_{n'}\sum_{n''}\iiint_{\oplus} \mathcal{S}'(\zeta') \times \left(\frac{e^{-i(k'\Delta' - s'\pi/2+\pi/4)}}{\sqrt{8\pi k'|\sin\Delta'|}}\right) \times_{s'} \Omega_{s''} \\ \times \left(\frac{e^{-i(k''\Delta'' - s''\pi/2+\pi/4}}{\sqrt{8\pi k''|\sin\Delta''|}}\right) \times \mathcal{R}'' d^3\boldsymbol{x},\end{aligned} \tag{2.43}$$

where $\mathcal{S}'$ is the source term. It is the same as in a laterally homogeneous case. It is given in equation 2.30. However the takeoff angle is that of the source-to-scatterer ray-path ζ' (see figure 2.11), not that of the source-to-receiver great-circle ζ. $\mathcal{R}$ is the receiver term. Here the receiver term is not the same as in the laterally homogeneous case. It accounts for the projection of the arrival wave onto the seismic sensor but the wave arrives with an angle ξ'' that depends on the location of the source, receiver, and scatterer (see figure 2.11). It is written:

$$\begin{aligned}\mathcal{R} = \{U_r''\hat{\boldsymbol{r}} - i[V_r''\cos(\xi'' - \xi) + W_r''\sin(\xi'' - \xi)]\hat{\boldsymbol{k}} \\ + i[W_r''\cos(\xi'' - \xi) - V_r''\sin(\xi'' - \xi)]\hat{\boldsymbol{r}} \times \hat{\boldsymbol{k}}\}.\hat{\boldsymbol{v}},\end{aligned} \tag{2.44}$$

where $\hat{\boldsymbol{v}}$ is the orientation of the sensor.

The single scattering principle is clear in equation 2.43. A seismic source (first term) generates an initial wavefield that propagates (first exponential) and attenuates geometrically (first square-root) toward the scatterer. There the scatterer acts as a secondary source. It is excited by the incoming wavefield and its behaviour is given by the interaction matrix that depends on the elastic parameters at its location. A secondary wavefield is thus produced and propagates (second

fraction) toward the receiver where the observation along some sensor is obtained with the receiver term. Snieder (1986) writes that this formulation is the 'life history of the scattered wave'.

The interaction matrix is linear in the elastic parameter perturbations (equation 2.41). To make it explicit we may write the interaction matrix:

$$ {}_{n'}\Omega_{n''} =_{n'} \Omega^{\boldsymbol{m}}_{n''}\delta\boldsymbol{m}. \tag{2.45}$$

2.3.4 Three-dimensional forward problem

We derived the seismic response in a laterally heterogeneous system. The response is a function of small three-dimensional perturbations in the elastic parameters with respect to some laterally homogeneous reference model. It should therefore be possible to relate an observable that measures the difference between a synthetic waveform in a laterally homogeneous system and the real one with the three-dimensional perturbations in the elastic parameters. Since the response that has been derived within the Born approximation is linear in the elastic parameters, this relation can be linear. Such relation has been derived by Zhou, Dahlen & Nolet (2004) for various kinds of measurements. In my thesis I use phase-delay observables. Therefore I recall only this relation here.

Let $s = Ae^{-i\phi}$ be the waveform observed at the receiver from the initial wavefield in the laterally homogeneous reference system. Let $\delta s = \delta A e^{-i\delta\phi}$ be the observed waveform from the scattered wavefield from a particular scattering location. In the Born approximation, both wavefields sum together so that the observed waveform is $o = s + \delta s$.

On the one hand we have,

$$\ln\left(\frac{o}{s}\right) = \ln\left(\frac{(A+\delta A)e^{-i(\phi+\delta\phi)}}{Ae^{-i\delta\phi}}\right) = \ln\left(\frac{A+\delta A}{A}\right) - i\delta\phi. \tag{2.46}$$

On the other hand we have (first using the Born approximation, then by assuming that $\delta s/s$ is small),

$$\ln\left(\frac{o}{s}\right) = \ln\left(\frac{s+\delta s}{s}\right) \approx \frac{\delta s}{s}. \tag{2.47}$$

Therefore, taking the imaginary part, the following expression is valid in the approximation of small perturbations,

$$-\Im\left\{\frac{\delta s(\omega)}{s(\omega)}\right\} = \delta\phi(\omega). \tag{2.48}$$

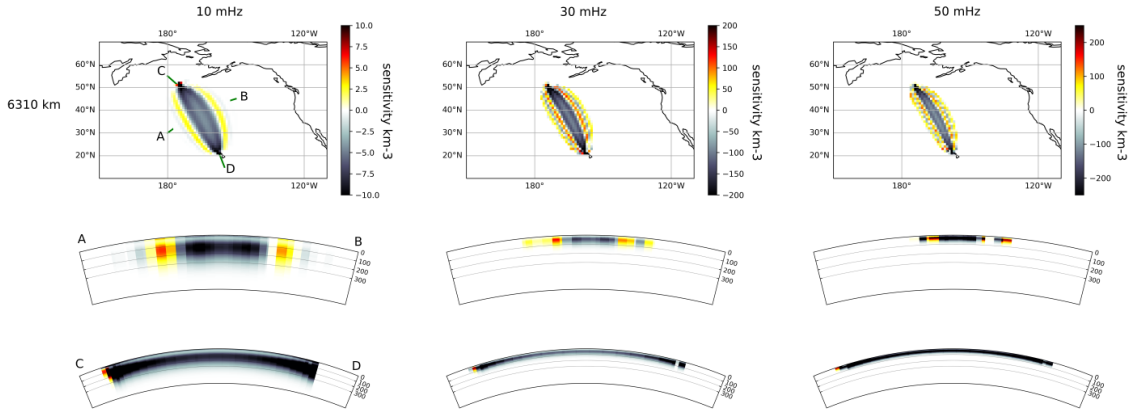

FIGURE 2.12: Finite-frequency three-dimensional phase delay sensitivity kernels to S-wave velocity for the fundamental mode (top) and third overtone (bottom) at 10 mHz (left), 30 mHz (middle) and 50 mHz (right). The depth of maps are indicated in the upper-left corner. The vertical cross-sections are all the same as indicated on the first map. The colorscale is the sensitivity in km^{-3}. The top map illustrates the seismic source as red beachball (with GCMT name C201403152351A) and station as blue triangle (PTCN) used to compute the kernels.

Finally, inserting the response in a laterally homogeneous medium and the response in a laterally heterogeneous medium derived above (equations 2.29 and 2.43) we obtain,

$$\delta\phi(\omega) = \iiint_{\oplus} K^m_\phi(\boldsymbol{x},\omega)\delta m(\boldsymbol{x}) d^3\boldsymbol{x}, \tag{2.49}$$

where $K^m_\phi(\boldsymbol{x},\omega)$, the phase delay sensitivity kernel, is

$$K^m_\phi(\boldsymbol{x},\omega) = -\Im\left(\sum_{n'}\sum_{n''} \frac{S'_{n'}\Omega^m_{n''}R''e^{-i[k'\Delta+k''\Delta''-k\Delta-(n'+n''-n)\pi/2+\pi/4]}}{SR\sqrt{8\pi(k'k''/k)(\sin|\Delta'||\sin\Delta''|/|\sin\Delta|)}}\right). \tag{2.50}$$

The phase delay (some observable data) is linearly explained by the three-dimensional perturbation in the elastic parameters. It will be possible, using the SOLA inversion, to invert phase-delays directly for a three-dimensional model. In practice I use the routines from Zhou, Dahlen & Nolet (2004) and Zhou (2009a) to produce the sensitvity kernels. Figure 2.12 shows some finite frequency three-dimensional kernels that express the sensitivity of phase delay measurements to S-wave velocity at various frequencies for the fundamental mode and the third overtone. The lateral region of high sensitivity is elliptic ; its external shape resembles the Fresnel zone, but with greater complexity inside. As expected the region narrows as frequency increases. On the vertical cross-sections we observe that the sensitivity shallows as frequency increases. This could have been predicted with the eigenfunctions of displacement and the path-specific forward

problem (see figure 2.3 and section 2.2.3). Also, the higher the overtone the deeper the sensitivity. Though it is a challenging task, observing overtones is necessary to illuminate deeper parts of the mantle. Note that the sensitivity is also particularly high close to the source and the station. We will observe this effect in the sensitivity of the global dataset in the tomographic study in chapter 5. However, care must be taken in these regions close to the source and receiver since the kernels are based on the far-field Green tensor. Recent developments have accounted for the near-field Green tensor close to the source (Liu & Zhou, 2016b) and we too should account for them in the future.

2.4 Conclusion

In the first part of this chapter, I presented an expression for the seismic wavefield produced by a seismic source in a laterally homogeneous medium. From that expression a synthetic seismogram can be computed and the discrepancy with the real one can be measured. A relation between the data and the path-averaged physical parameter between the source and the receiver can be established. This is the first step of the two-step approach in surface wave tomography. The second step is a linear regionalization that produces two-dimensional maps at discrete depths. Since this second step is linear, we can regionalize the path-averaged profiles of Maggi et al. (2006b) using the SOLA inversion in chapter 4.

Unfortunately the two-step approach has limits. It does not constrain all the spatial dimensions at the same time and the regionalization is based on ray theory that does not account for finite frequency effects. In the second part of this chapter, I presented a finite frequency theory based on the Born approximation. It extends ray theory to relate data to the three-dimensional Earth in a single linear equation. Since this relation is linear, we can apply this finite frequency approach together with a SOLA inversion in chapter 5.

However, once the forward problem $\boldsymbol{d} = \boldsymbol{G}\boldsymbol{m}$ is set, retrieving the model is not an easy task. Before we apply the SOLA inversion in one case or the other, I need to describe how to solve the *inverse problem* and obtain the model $\boldsymbol{m}$. This is the subject of the next chapter.

Chapter 3

Inverse theory

We argue that without a more systematic and realistic error and resolution analysis, interpretations might be misleading.

Trampert, *Global seismic tomography: the inverse problem and beyond*, 1998.

3.1 Introduction

In the previous section I built the forward problem: for a physical system (a model of the Earth), I described the law of physics (surface wave propagation, response to a seismic source) that leads to some observations (phase delay). The forward problem can be written in the abstract form $\boldsymbol{d} = \boldsymbol{g}(\boldsymbol{m})$ (ignoring noise for the moment) where $\boldsymbol{g}$ is an operator that describes the physical theory through which the system $\boldsymbol{m}$ produces the predicted data $\boldsymbol{d}$. The tomographer observes the data at the surface and is interested in the physical system that produced them. Ideally the operator $\boldsymbol{g}$ would be invertible such that given the data one obtains the model from $\boldsymbol{g}^{-1}$ (assuming $\boldsymbol{g}^{-1}\boldsymbol{g}(\boldsymbol{m}) = \boldsymbol{m}$). Actually retrieving the model from the data is not an easy task. If we solve the forward problem by deduction, we solve the *inverse problem* by induction.

The model may be a continuous function of space so that constraining the model would require an infinite number of data while in reality the dataset is finite (e.g. a finite set of source-receiver pairs). Moreover, some components of the model (some location in the tomographic image) may be weakly constrained. The seismic network is much denser in the northern hemisphere and on the continents and earthquakes occur mostly in geologically active regions like ridges or subduction zones that are unevenly distributed. As a consequence, the seismological data has a highly uneven distribution leading to overdetermination in some regions and undertermination in some others. This may induce strong spatial biases in the tomographic images, making their interpretation particularly tricky. This is particularly true in the Pacific hemisphere which is the region of interest in this thesis.

Seismological data are noisy. The noise is the part of the data produced by physical processes not taken into account in the forward theory or by the imperfect measurement process. The forward theory also is erroneous in that it is based on some assumptions (e.g. that the seismic source is perfectly known) or that it neglects many physical processes that may affect the data (note that errors in the theory and in the data are overlapping in some sense). Because of data noise and imperfect coverage, the existence and uniqueness of a model solution is not guaranteed and the construction and interpretation of one model solution is difficult (e.g. Parker, 1977; Scales & Snieder, 1997; Ritsema, 2005; Foulger, 2011; Foulger et al., 2013).

Many approaches have been proposed to solve the inverse problem (e.g. Wiggins, 1972; Parker, 1977; Tarantola & Valette, 1982; Nolet, 1985; Scales & Snieder,

1997; Trampert, 1998; Nolet, 2008). The classical philosophy is to look for a solution that predicts data close enough to the observed ones by minimizing the so-called *data misfit*. But there is not only one solution and fitting the data too closely may lead to physically unrealistic models. Usually a criterion is added for the model to be smooth and one optimizes the tradeoff between data misfit and 'model coherency'. Adding such a criterion is called *regularizing* the model solution. Unfortunately these methods need to add an *ad-hoc* constraint on the model itself that may be difficult to justify in some context (like in seismic tomography where the deep Earth structure remains poorly known).

Since our knowledge of the quantities involved in the forward problem is imperfect, there is the question of the precision (or variability, or uncertainties, or 'error bars') of the solution obtained by one method or another. Also one may wonder what are the correlations between the elements of the model. In seismic tomography where the model is spatial, this is equivalent to ask how different locations in the model vary together. This is closely related to the concept of resolution (like the photographic resolution or the point spread functions in astronomy). An estimate somewhere is a *local average* of the true Earth. The model uncertainty and model resolution appear to be very important concepts in inverse problems. Unfortunately classical data fitting methods have great difficuties in controlling them and obtaining them (especially for large scale problems like a tomographic model with many cells). Since the data fitting inversions do not control the resolution, they can even produce models that represent biased local averages (Zaroli, Koelemeijer & Lambotte, 2017).

The Backus–Gilbert theory (Backus & Gilbert, 1967; Backus & Gilbert, 1968; Backus & Gilbert, 1970) focuses on the resolution and the uncertainties of the model to find a solution to the inverse problem. Therefore, one has some control on these quantities and obtains them by construction. Moreover there is no need for *ad-hoc a priori* information on the model solution itself: "the non-uniqueness of the solution is broken by averaging rather than regularizing" (Zaroli, 2016). Last, the resolution can be designed such that the estimate is made of unbiased local averages. Given all its advantages, the Backus–Gilbert approach is very appealing. The *SOLA* variant of the Backus–Gilbert theory (Pijpers & Thompson, 1992; Pijpers & Thompson, 1993) was introduced and adapted in seismic tomography by Zaroli (2016) and Zaroli (2019). He applied this original approach with body waves. The central objective of my thesis is the application of the SOLA-Backus–Gilbert inversion in the context of surface waves. I hope, with the control on the resolution and model uncertainties, to extract the information from the data as well as possilble and, with the knowledge of the resolution and model

uncertainties, to make robust interpretations of the model solution.

In the first part of this section I define precisely the quantities involved in the inverse problem using the very general probabilistic description of Tarantola (2005). In the second part I present briefly the data fitting approaches and the very general Bayesian point of view. In the last section, I present the SOLA-Backus–Gilbert approach that may overcome some limits of the data fitting inversions. In general I assume that the imperfect knowledge of some quantities may be described using Gaussian probabilities. I also assume that the theory relating the model and the data is perfectly linear. A discussion on the linearity is given at the end of the chapter.

3.2 Understanding the inverse problem

In this section I define the various terms of the inverse problem. The best way to handle mathematically poorly known and noisy quantities is to use probabilities: a noisy quantity follows some probabilistic distribution with a particular shape and quantitative features.

3.2.1 Model

The model $\boldsymbol{m}$ is a mathematical abstraction that represents some properties of the system under study. For example, in chapter 4, in the first step, the model is the S-wave velocity averaged along the source-receiver path; in the second step it is the S-wave velocity in a two dimensional spherical shell at some depth. In chapter 5, the model is the three-dimensional distribution of the S-wave velocity within the Earth. The set of all possible values the model may take is called the *model space* $\mathcal{M}$. Conceptually the model space may be infinite-dimensional (i.e. one solution is defined by an infinite number of components). For example the S-wave velocity is a function of space that takes values everywhere within the Earth: the model $\boldsymbol{m}(\boldsymbol{x})$ is a function of some spatial variable (in chapter 5 it is the three-dimensional space, $\boldsymbol{x} \in \mathbb{R}^3$). In seismic tomography the model space is the set of all possible tomographic images and the value of some $\boldsymbol{x}$ corresponds to some spatial location.

For practical purposes, we define a *parameterization* of the model space. Let $\{h_l\}_{l=1,..,\infty}$ be a set of elements of the model space that form an orthonormal basis. Then any element of the model space $\boldsymbol{m}$ can be written:

$$\boldsymbol{m}(\boldsymbol{x}) = \sum_{l=1}^{\infty} m_l h_l(\boldsymbol{x}). \tag{3.1}$$

There are two classes of parameterizations: global and local. *Global parameterizations* have basis functions that may be non-zero everywhere in the model. An exemple of such a parameterization is the spherical harmonics decomposition that we already used to build the forward problem in chapter 2. In my thesis the use of a *local parameterization* is more natural (since we regard the model parameter estimates as *local averages* as we will see later). Local parameterizations have 'local' basis functions in that they are non-zero only in a limited region of the model. This corresponds to splitting the model space into blocks. Note that in the case of *irregular* parameterization, that is when basis functions are non-zero in regions of variable size (as is the case in chapters 4 and 5), the value of the function itself must take into account the size of the region to guanrantee the orthonormality of the basis, that is:

$$\int_{\boldsymbol{x}\in\mathcal{M}} h_i(\boldsymbol{x})h_j(\boldsymbol{x})d\boldsymbol{x} = \delta_{ij}. \tag{3.2}$$

A definition that satisfies equation 3.2 is,

$$h_l(\boldsymbol{x}) = \begin{cases} \mathcal{V}_l^{-1/2} & \text{if } \boldsymbol{x} \text{ in cell } \ell, \\ 0 & \text{if } \boldsymbol{x} \text{ elsewhere.} \end{cases} \tag{3.3}$$

where $\mathcal{V}_l$ is the surface of the cell ℓ (as in chapter 4) or the volume of the voxel ℓ (as in chapter 5), depending on the context.

To be perfect the expansion (equation 3.1) should consider an infinite number of basis functions. Obviously it must be truncated to some upper limit M. In a local parameterization this corresponds to using M blocks of finite volume. In doing so, the model is a M-dimensional vector of scalars: $\boldsymbol{m} = (m_l)_{l=1..,M} \in \mathbb{R}^M$ and the model space is thus M-dimensional. The model space is the set of all possible 'pixelated' tomographic images and an element of the model vector, a *model parameter*, corresponds the value assigned to one of these 'pixels'. The truncation is not without importance. Trampert (1998) points that the use of different parameterizations in various studies complicates the comparison of their results. Moreover the parameterization acts as a filter that smooths the solution. Another undesirable effect shown by Trampert & Snieder (1996) is that part of the truncated solution may leak into the model estimate. In chapter 5, the sensitivity kernels are degraded by their projection onto the model grid but the parameterization is good enough to retain their main properties. However, Zhou, Dahlen & Nolet (2004) show that the current parameterizations, limited by the current computational power, cannot handle differences in the projected sensitivity kernels including mode-coupling, which leads us to ignore this effect.

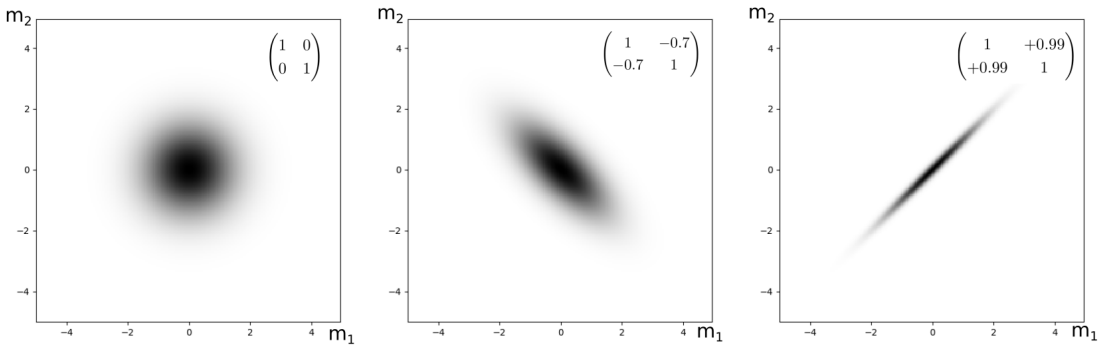

FIGURE 3.1: Illustration of the multi-dimensional Gaussian probability density function $\rho(\boldsymbol{m})$ in the case $\boldsymbol{m} \in \mathbb{R}^2$. The center (or top) of the 'bell' is at $\boldsymbol{m_0} = (0, 0)$ for all graphs and the covariance matrix is given in the upper-right part of the graph.

Of course the model may represent more than one physical quantity, for example the S and P wave velocity. Then the basis functions and the model parameters would simply be vectors of dimension the number of physical parameters. For simplicity we will consider only the case where the model represents only one physical parameter. The extension of the theory to multiple physical parameters is straightforward (though in practice it adds complications regarding the correlations between the parameters).

Following Tarantola (2005), we use the language of probabilities to describe the inverse problem in very general terms. For the model, one may already have some *prior information*. A good way to represent this prior information is to define a *probability density function* (or *probability distribution*) for the model: $\rho_m(\boldsymbol{m})$. We commonly make the assumption that the *a priori* model distribution is Gaussian. In such a case the probability density function for prior model information is written as a multi-dimensional Gaussian function:

$$\rho_m(\boldsymbol{m}) = \frac{1}{(2\pi)^M |\boldsymbol{C_m}|} e^{-\frac{1}{2}(\boldsymbol{m}-\boldsymbol{m_0})^T \boldsymbol{C_m}^{-1}(\boldsymbol{m}-\boldsymbol{m_0})}, \tag{3.4}$$

where $\boldsymbol{m_0}$ is the prior model, the center of the Gaussian bell-curve (the highest probability value), and $\boldsymbol{C_m}$ is the prior model covariance matrix describing the spread of the curve in all directions within the model space. The symbols $\boldsymbol{C_m}^T$, $\boldsymbol{C_m}^{-1}$ and $|\boldsymbol{C_m}|$ denote the transposition, inverse and determinant of the matrix $\boldsymbol{C_m}$. I illustrate such a probability on figure 3.1.

3.2.2 Data

The data are some observables that are produced by the system and the measurement process. For example the three-dimensional distribution of the elastic parameters within the Earth produces seismograms and we may measure phase delays from them. To recover the model from the data we need many data. Say we have N data, they can be grouped into a data vector $\boldsymbol{d}$ that belongs to some N-dimensional *data space* $\mathcal{D}$. Unfortunately the measuring process is not perfect. For example, while measuring the phase delay at some frequency for the fundamental mode, the first overtone may be already in the measurement window and bias the measurement. Therefore, the data are better described by a probability density function rather than a single value. As for the model the probability may be assumed Gaussian so that the probability that the actual data is $\boldsymbol{d}$ given the measured value $\boldsymbol{d_0}$ can be written:

$$\rho_d(\boldsymbol{d}) = \frac{1}{(2\pi)^N |\boldsymbol{C_d}|} e^{-\frac{1}{2}(\boldsymbol{d}-\boldsymbol{d_0})^T \boldsymbol{C_d}^{-1}(\boldsymbol{d}-\boldsymbol{d_0})}, \tag{3.5}$$

where $\boldsymbol{C_d}$ is the *data covariance matrix*. The diagonal terms of $\boldsymbol{C_d}$ are measures of how far the actual data can be from the observed ones. It can be interpreted in terms of 'error bars'. The off-diagonal terms are the covariances between different data. In this study we assume that there is no covariance between different data, i.e. that the data are independent of each other. Therefore the data covariance matrix is diagonal. We may write $\boldsymbol{C_d} = \text{diag}(\sigma_{d_i}^2), i = 1, .., N$ (σ_{d_i} represent the 'data errors').

3.2.3 Theory

The theory (or the forward theory) is the physics-based relation between the physical system properties and the data that it produces and that can be observed. Mathematically the theory is an operator $\boldsymbol{g}$ that acts on a model to predict data: $\boldsymbol{d} = \boldsymbol{g}(\boldsymbol{m})$ (ignoring noise). For example, in seismic tomography, a very fundamental theory would relate the Earth to the observed waveforms it produces. Often, simpler relations are established. For example Cara & Lévêque (1987) build a relation between what they call 'secondary observables' and the S-wave velocity averaged along the path between the source and the receiver under consideration. In chapter 5 we use a relation between the phase delay with respect to a reference system and the three-dimensional distribution of the S-wave velocity.

In chapter 4, we use a relation between the averaged S-wave velocity along ray-paths and the S-wave velocity within a two-dimensional spherical shell at some depth.

The forward theory relies on some assumptions. For example the forward theory I presented in chapter 2 assumes that the seismic source is known, that there is no multiple-scattering, that the single-scattering occurs in some reference medium. Say that for a given model $\boldsymbol{m}$ the theory we use predicts the data $\boldsymbol{g}(\boldsymbol{m})$. Since the theory is not perfect, the data that should be predicted given some model is better described using a probability distribution. Again within the Gaussian hypothesis we write the conditional probability of predicting some data given a model:

$$\theta(\boldsymbol{d},\boldsymbol{m}) = \frac{1}{(2\pi)^N |\boldsymbol{C_T}|} e^{-\frac{1}{2}(\boldsymbol{d}-\boldsymbol{g}(\boldsymbol{m}))^T C_T^{-1}(\boldsymbol{d}-\boldsymbol{g}(\boldsymbol{m}))}, \tag{3.6}$$

where $\boldsymbol{g}(\boldsymbol{m})$ is the predicted data from the theory and $\boldsymbol{C_T}$ is the covariance operator for the modeling errors.

3.2.4 Combining information

The probability density function for the data in the data space $\mathcal{D}$ and the prior model probability density function in the model space $\mathcal{M}$ can be combined to give the joint probability to obtain some model and some data together in the $\mathcal{D} \times \mathcal{M}$ space: $\rho(\boldsymbol{d},\boldsymbol{m}) = \rho_d(\boldsymbol{d})\rho_m(\boldsymbol{m})$. Of course this is true given that the distributions are independent. I illustrate this combination of information on figure 3.2 in the case of one-dimensional data and model spaces. If both the prior model and data probability distributions are Gaussian then the joint probability distribution is a two-dimensional Gaussian.

On the middle panel of figure 3.2, I reproduced the data and prior model joint probability in the background. On the foreground the conditional probability distribution for the data given the model (i.e. the imperfect theory) is in black. Both lie into the same $\mathcal{D} \times \mathcal{M}$ space. Tarantola & Valette (1982) and Tarantola (2005) postulate that the combination of information from both probability density functions is: $\sigma(\boldsymbol{d},\boldsymbol{m}) = \rho(\boldsymbol{d},\boldsymbol{m})\theta(\boldsymbol{d},\boldsymbol{m})$. The result is illustrated in the panel on the right. The combination of all input information leaves the two shady black stains for the joint probability to have some value for the model and data: we learnt something. Finally the *posterior* probability density function for the model

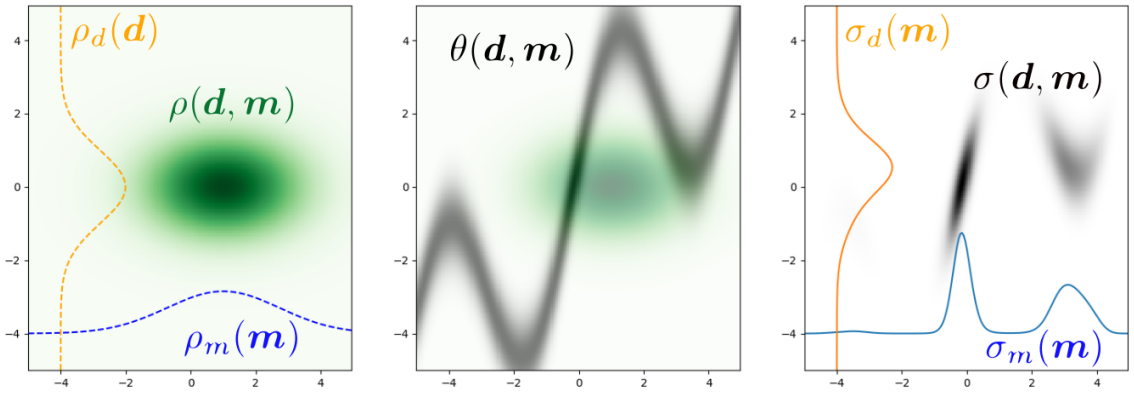

FIGURE 3.2: Illustration of the combination of prior information (after Tarantola, 2005). For all panels the horizontal axis is the model space $\mathcal{M}$, the vertical axis is the data space $\mathcal{D}$ and the plane spanned by these axes is the $\mathcal{D} \times \mathcal{M}$ space. On the left panel, the dashed orange and blue lines represent the data and prior model probability distributions. The joint probability distribution is the green two-dimensional Gaussian. On the middle panel the black shady line is the imperfect theory. On the right panel the black shady stains are the posterior joint probability for the model and data. From that derives the posterior probability distribution for the data (continuous orange line) and model (continuous blue line).

can be obtained as the marginal probability:

$$\sigma_m(\boldsymbol{m}) = \int_D \sigma(\boldsymbol{d},\boldsymbol{m})d\boldsymbol{d} = \int_D \rho(\boldsymbol{d},\boldsymbol{m})\theta(\boldsymbol{d},\boldsymbol{m})d\boldsymbol{d} = \int_D \rho_d(\boldsymbol{d})\rho_m(\boldsymbol{d})\theta(\boldsymbol{d},\boldsymbol{m})d\boldsymbol{d}. \tag{3.7}$$

The model posterior probability is the blue continuous line. The same applies for the data, it is the orange line. The combination of information from the data and theory has refined the probability distribution of the model. Depending on the form of the *a priori* probability density functions and theory, the *a posteriori* probability distribution for the model may be very complicated (e.g. it may be multimodal as on figure 3.2). As we will see in the next section, if we assume input distributions to be Gaussian and the theory to be perfectly linear, then the posterior model probability distribution is also Gaussian and analytic formulae exist (analytic mean and covariances).

Tarantola (2005) shows that, in the case of Gaussian probabilities, equation 3.7 can be further simplified into:

$$\sigma_m(\boldsymbol{m}) = \text{constant} \times \rho_m(\boldsymbol{m}) e^{-\frac{1}{2}(g(\boldsymbol{m})-\boldsymbol{d}_0)^T \boldsymbol{C_D}^{-1}(g(\boldsymbol{m})-\boldsymbol{d}_0)}, \tag{3.8}$$

where $\boldsymbol{C_D} = \boldsymbol{C_T} + \boldsymbol{C_d}$. This equation shows that, within the Gaussian hypothesis, we can consider that the theory is perfect (error-free), and that all the sources of

error come from the data.

Finally, inserting the *a priori* probability distribution for the model (equation 3.4) into equation 3.8 we obtain the *a posteriori* probability distribution for the model in the Gaussian hypothesis:

$$\sigma_m(\boldsymbol{m}) = \text{constant} \times e^{-\frac{1}{2}((g(m)-d_o)^T {C_D}^{-1}(g(m)-d_0)+(m-m_0)^T {C_m}^{-1}(m-m_0))}. \quad (3.9)$$

3.3 Data fitting inversions

We defined all the terms involved in the inverse problem under the hypothesis that all the input probability distributions are Gaussian. From now on I write the forward problem $\boldsymbol{d} = \boldsymbol{g}(\boldsymbol{m}) + \boldsymbol{n}$ where $\boldsymbol{d}$ is the observed data and $\boldsymbol{n}$ is a noise term. The noise term follows a Gaussian distribution with zero mean and covariance the data covariance matrix $\boldsymbol{C_d}$. As stated previously, we assume that the data are uncorrelated so that $\boldsymbol{C_d} = \text{diag}(\sigma_{d_i}^2), i = 1, .., N$.

In this section I further assume that the forward problem is linear. In that case, the predicted data $\boldsymbol{g}(\boldsymbol{m})$ can be rewritten $\boldsymbol{Gm}$ with $\boldsymbol{G}$ a linear operator; the forward problem reduces to a simple matrix-vector product. At the end of the chapter I discuss the question of linearity. Finding a solution to the inverse problem is not straightforward. As we have discussed in introduction the data are noisy, finite-dimensional and they may constrain the model parameters unevenly. These bad characteristics pose the question of the existence and uniqueness of a solution and justify the plethora of approaches to obtain one (e.g. Parker, 1977; Trampert, 1998; Scales & Snieder, 1997; Nolet, 1985; Tarantola & Valette, 1982; Wiggins, 1972; Nolet, 2008). In this section I present the most traditional inversion methods that belong to the class of data fitting inversions. I discuss classical optimization techniques and the Bayesian view point that naturally arises from the probabilistic description of the inverse problem. We recognize some limits with data fitting inversions: *ad-hoc* constraints and no direct control on the model resolution and uncertainties. In the next section I will present the *Backus–Gilbert* inversion, and its reformulation named *Subtractive Optimally Localized Averages* (SOLA) inversion, that may help to overcome these limits.

One may first ignore the *a priori* information on the model and consider only the exponential term appearing in equation 3.8. In the linear case, if we further assume no correlation between the data, this term is written (see Nolet, 2008, section 14.1):

$$\chi^2(\boldsymbol{m}) = \sum_{i=1}^{N} \frac{(\sum_{j=1}^{M} G_{ij} m_j - d_i)^2}{\sigma_{d_i}^2}, \quad (3.10)$$

where $\sigma_{d_i}^2$ are the diagonal terms of the data covariance matrix (σ_{d_i} represent the 'data errors'). $\sum_{j=1}^{M} G_{ij} m_j$ is the i-th data predicted by the theory and d_i is the actual data. χ^2 is a data misfit normalized by the data uncertainties. χ^2 can be seen as a sum of N squared independent standard normal random variables. It is distributed according to the well-known χ^2-distribution with N degrees of freedom. The data misfit is a quadratic equation, which justifies the term *least-squares* inversion. In a perfect case there would be a model $\boldsymbol{m}$ for which the predicted data $\boldsymbol{Gm}$ equals the observed data $\boldsymbol{d}$ so that χ^2 would be zero. However there is no such a solution. Instead one wants a model that fits the data at the level of their errors. For a large amount of data this is equivalent to find a model such that χ^2 is close to the number of data N (the mode of the χ^2-distribution with N degrees of freedom is $N-2$). It turns out that there is not only one solution that satisfies this criterion. Also, when minimizing χ^2, the model norm increases leading to a physically unrealistic model. The solution is not unique and there is a trade-off between the data misfit and the 'model coherency' (for example measured by the model norm). The minimization of the χ^2 follows a L-shaped tradeoff curve as illustrated on figure 3.3. To get a unique solution, we need to add some criterion on this 'model coherency' to the problem. This leads us to the field of regularized data fitting inversions.

Adding some criterion to obtain a unique solution to the inverse problem is called *regularization*. In very general terms we can express the quest for a regularized solution as the minimization of a cost function as (Trampert, 1998):

$$C_\lambda = \Delta_{\mathcal{D}}(\boldsymbol{d}, \boldsymbol{Gm}) + \lambda \Delta_{\mathcal{M}}(\boldsymbol{m}, \boldsymbol{m_0}), \tag{3.11}$$

where the first term represents the data misfit under a given norm over the data space and the second term is the *model coherency* under a given norm over the model space. The scalar λ is a *tradeoff parameter*. In rough words it allows to give more weight to the data misfit or to the model coherency. In other words it allows to choose a position on the L-shape curve of figure 3.3. Increasing λ gives more significance to the model coherency in the optimization so that the solution will have a low model norm (lower right side of the L-curve) and *vice versa*. A simple form of a cost function is known as the *Tikhonov regularization* (Tikhonov, 1963) where it writes: $C_\lambda = ||\boldsymbol{Gm} - \boldsymbol{d}||_2^2 + \lambda^2 ||\boldsymbol{m}||_2^2$. The Tikhonov regularization is equivalent to adding M equations to the system to damp model parameters toward zero when not well constrained by the data.

A more general approach is to use the data covariance matrix $\boldsymbol{C_d}$ as a measure

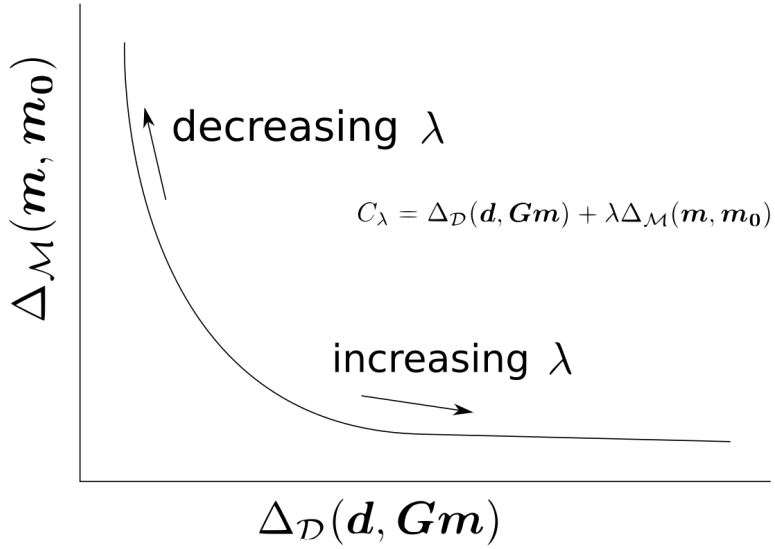

FIGURE 3.3: L-shaped tradeoff curve for the classical data fitting optimization problem (data misfit versus model coherency). The curve draws the model coherency as a function of the data misfit for varying tradeoff parameter λ. For increasing values of λ, the data misfit term gets less and less significant with respect to the model coherency term. Therefore the resolution of the optimization problem lead to a more coherent model with greater data misfit (lower-right side of the curve). On the contrary lower values of the tradeoff parameter lead to good data misfit but poor model coherency, leading to physically unrealistic models (upper-left side of the curve).

in the data space for the data misfit term and to define an *a priori* model covariance matrix $\boldsymbol{C_m}$ as a measure in the model space to quantify the 'model coherency' (or the deviation from the *a priori*). Then the cost function directly derives from equation 3.9:

$$C_\lambda = (\boldsymbol{d} - \boldsymbol{Gm})^T {\boldsymbol{C_d}}^{-1} (\boldsymbol{d} - \boldsymbol{Gm}) + (\boldsymbol{m} - \boldsymbol{m_0})^T {\boldsymbol{C_m}}^{-1} (\boldsymbol{m} - \boldsymbol{m_0}). \tag{3.12}$$

Note that in this formulation of the cost function the λ term is absorbed in the *a priori* model covariance matrix. Within the Gaussian hypothesis and given the linearity of the theory the minimization of the cost function leads to analytical solution for the model estimate:

$$\tilde{\boldsymbol{m}} = (\boldsymbol{G}^T \boldsymbol{C_d^{-1}} \boldsymbol{G} + \boldsymbol{C_m^{-1}})^{-1} (\boldsymbol{G}^T \boldsymbol{C_d^{-1}} \boldsymbol{d} + \boldsymbol{C_m^{-1}} \boldsymbol{m_0}). \tag{3.13}$$

This solution is the maximum of the Gaussian probability distribution for the *a posteriori* model (or model estimate). There is also analytical solution for the model estimate covariance matrix:

$$\boldsymbol{C_{\tilde{m}}} = (\boldsymbol{G}^T \boldsymbol{C_d^{-1}} \boldsymbol{G} + \boldsymbol{C_m^{-1}})^{-1}. \tag{3.14}$$

This is the Bayesian point of view where the aim is to replace the subjective choice of the ad-hoc parameter λ by an objectively defined prior model probability distribution ($\boldsymbol{m_0}$ and $\boldsymbol{C_m}$) and the aim is not to look for one solution but for the whole *a posteriori* probability distribution. However, defining objectively some prior information can be difficult (especially in tomography where the deep Earth remains poorly known). To simplify these results let us assume that the model is expressed as perturbations with respect to some reference so that $\boldsymbol{m_0} = \boldsymbol{0}$. Then the model estimate can be written:

$$\tilde{\boldsymbol{m}} = [(\boldsymbol{G}^T \boldsymbol{C_d^{-1}} \boldsymbol{G} + \boldsymbol{C_m^{-1}})^{-1} \boldsymbol{G}^T \boldsymbol{C_d^{-1}}] \boldsymbol{d}. \tag{3.15}$$

This equation is of the form

$$\tilde{\boldsymbol{m}} = \boldsymbol{G^\dagger} \boldsymbol{d}, \tag{3.16}$$

where $\boldsymbol{G^\dagger}$ is called the *generalized inverse* of $\boldsymbol{G}$ and, in the case of data fitting inversions,

$$\boldsymbol{G^\dagger} = (\boldsymbol{G}^T \boldsymbol{C_d^{-1}} \boldsymbol{G} + \boldsymbol{C_m^{-1}})^{-1} \boldsymbol{G}^T \boldsymbol{C_d^{-1}}. \tag{3.17}$$

We also have:

$$\boldsymbol{C_{\tilde{m}}} = \boldsymbol{G^\dagger} \boldsymbol{C_d} {\boldsymbol{G^\dagger}}^T. \tag{3.18}$$

If we use $\boldsymbol{d} = \boldsymbol{G}\boldsymbol{m} + \boldsymbol{n}$ in equation 3.16 we have:

$$\tilde{\boldsymbol{m}} = \boldsymbol{G}^{\dagger}\boldsymbol{d} = \boldsymbol{G}^{\dagger}\boldsymbol{G}\boldsymbol{m} + \boldsymbol{G}^{\dagger}\boldsymbol{n} = \boldsymbol{R}\boldsymbol{m} + \boldsymbol{G}^{\dagger}\boldsymbol{n}, \tag{3.19}$$

which defines the resolution operator $\boldsymbol{R}$. Ignoring the noise term, this equation shows that the solution $\tilde{\boldsymbol{m}}$ is linear combinations of the parameters of the 'true' model $\boldsymbol{m}$. For example, the k-th row of $\boldsymbol{R}$ contains the weights to average the true Earth to estimate the k-th parameter. In a hypothetical perfect case $\boldsymbol{G}$ would be invertible so that the generalized inverse would be the inverse of $\boldsymbol{G}$ and the resolution operator $\boldsymbol{R}$ would be the identity matrix $\boldsymbol{I}_M$. Therefore the solution would equal the true model. In reality $\boldsymbol{R}$ cannot be the identity but it should to be as close as possible to the identity such that the model estimates represent *local averages* of the true model. The resolution operator acts as a filter through which the true model is seen, some call it the *tomographic filter*. Note that if the sum of weights in a local average (namely a line of $\boldsymbol{R}$) do not sum to one, then the local average is said to be biased (see Zaroli, Koelemeijer & Lambotte, 2017). The resolution is related to the model estimate covariances (in the case of data fitting inversions) by:

$$\boldsymbol{R} = \boldsymbol{I} - \boldsymbol{C}_{\tilde{m}}{\boldsymbol{C}_m}^{-1}, \tag{3.20}$$

which shows that the resolution also controls the model covariances. There is also the term $\boldsymbol{G}^{\dagger}\boldsymbol{n}$ in equation 3.19 which is the propagation of the noise part of the data into the model solution.

A first difficulty in the classical data fitting inversions is either the choice of some subjective criterion (like the ad-hoc λ parameter in Tikhonov-like inversions) or the definition of an objective prior model probability distribution as in Bayesian-like inversions (Scales & Snieder, 1997). A second difficulty is that for large-scale problems (like in tomographic inversions with many data and parameters) the computation of the resolution and model estimate covariances is expensive. Yet these quantities are necessary to robustly interpret the solution. Although some authors have computed them (e.g. Ritsema, Heijst & Woodhouse, 2004), resolution and uncertainties are obtained at the end of the process. However it may be desirable to have some direct control on these quantities, to shape the resolution and consider the propagation of uncertainties and to guarantee that the resolution will not lead to biased local averages.

3.4 Backus–Gilbert inversions

The Backus–Gilbert inversion takes the point of view of the resolution and model uncertainties to solve the inverse problem; thus it gives some direct control on these quantities and, by construction, produces them together with the model solution. Moreover, it avoids the need for prior information nor subjective choices on the model itself. Tarantola (2006) writes: "The [Backus–Gilbert philosophy] carefully avoids using any *a priori* information on the model parameters that could 'bias' the inferences to be drawn from the data." It was proposed by Backus and Gilbert over fifty years ago (Backus & Gilbert, 1967; Backus & Gilbert, 1968; Backus & Gilbert, 1970). Unfortunatly the method turned out to be non-tractable for large scale problems. In the 90's Pijpers and Thompson proposed a computationally more efficient formulation that they named *Subtractive Optimally Localized Averages* (hereafter SOLA) inversion (Pijpers & Thompson, 1992; Pijpers & Thompson, 1993). Recently Zaroli (2016) introduced and adapted the SOLA method to seismic tomography. He applied it with body waves for discrete and continuous problems (Zaroli, 2016; Zaroli, Koelemeijer & Lambotte, 2017; Zaroli, 2019). The center of my thesis is the application of the SOLA approach in the context of surface waves. We could summarize the main question as: 'Can we apply the SOLA approach in the context of surface wave tomography, to control the resolution and model uncertainties, to extract as much as possible information from the data, and to make robust interpretations given the model resolution and uncertainties?' In this section I present the original Backus–Gilbert approach and the SOLA formulation.

3.4.1 Principle

Recall the forward theory,

$$\boldsymbol{d} = \boldsymbol{G}\boldsymbol{m} + \boldsymbol{n}, \tag{3.21}$$

where $\boldsymbol{n}$ is the noise term. We assume zero-mean uncorrelated Gaussian noise. Even though $\boldsymbol{G}$ is not invertible, we may look for a *generalized inverse* operator $\boldsymbol{G}^{\dagger}$, that relates the data to a model solution:

$$\tilde{\boldsymbol{m}} = \boldsymbol{G}^{\dagger}\boldsymbol{d}, \tag{3.22}$$

where $\tilde{\boldsymbol{m}}$ is a model estimate. Combining equation 3.21 and 3.22 we obtain a relation between the model estimate and the 'true' model:

$$\tilde{\boldsymbol{m}} = \boldsymbol{G}^{\dagger}\boldsymbol{G}\boldsymbol{m} + \boldsymbol{G}^{\dagger}\boldsymbol{n}. \tag{3.23}$$

As stated previously the matrix product $\boldsymbol{G}^{\dagger}\boldsymbol{G}$ is the resolution matrix $\boldsymbol{R}$ and it shows that an estimated model parameter is an average of the true model parameters. For exemple the k-th row of $\boldsymbol{R}$ contains the weights of the weighted average that leads to the k-th model parameter estimate. For optimal image interpretability, we want the rows of the resolution matrix to represent averages that are localized around the corresponding model parameter location. I illustrate this principle on figure 3.4. The red lines represent ray paths between sources (red stars) and stations (blue triangles). Say we want to estimate the model parameter at some locations (black dots). The local averages that lead to estimated model parameters are illustrated by the shades of yellow. In the Backus–Gilbert approach we simply want these local averages to have a spatial extent as small as possible. Note that if $\boldsymbol{G}$ was invertible so that $\boldsymbol{R}$ was the identity matrix, then these local averages would actually be Dirac functions localized at the model parameter locations. One may also take the problem reversely. Say the true model is zero everywhere except at the exact location of some parameter. Then, looking at the model through the resolution matrix (the 'tomographic filter') would show that point spread as the averaging region. This justifies the name *point spread function* found in the astronomy literature. This is actually the idea followed by some studies to estimate the resolution matrix after a data fitting inversion (e.g. Ritsema, Heijst & Woodhouse, 2004).

The second term is the data noise propagation into the model solution. It turns out that the smaller the spatial extent of the local averages, the higher the model uncertainties. This can be understood intuitively. If the local average is large, then the quantity of data taken into account (the red lines that fall into the yellow averaging region) will be greater, giving more chances to the Gaussian noises to cancel each other. Averaging kernels should have a larger extent in regions with poorer data coverage (as the one on the right on figure 3.4).

The Backus–Gilbert approach consists in minimizing both the size of the local averages and the model uncertainties. In the Backus–Gilbert approach we shape optimally the resolution given the model uncertainties. At the end of the inversion an optimal resolution is obtained and from that the model solution can be computed, together with the model uncertainties. To compare with classical data fitting approaches presented above (section 3.3), the Backus–Gilbert inversion breaks the non-uniqueness of the solution by averaging rather than damping. There is still a tradeoff, but now it is between the model resolution and uncertainties. This approach is interesting in that it gives some control on the final resolution and model uncertainties and it avoids the definition of *a priori* information on the model that may be difficult to justify.

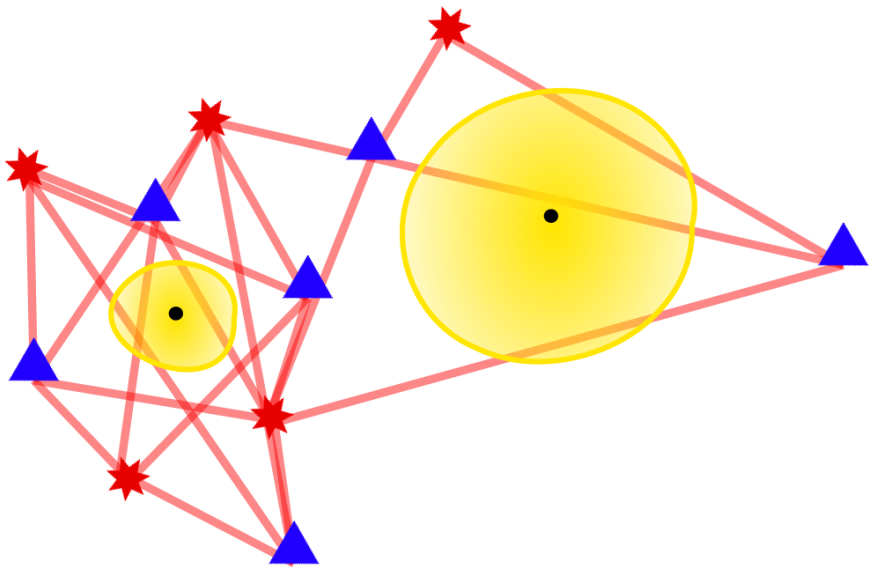

FIGURE 3.4: Illustration of local averaging. The blue triangles represent a seismological network, the red stars represent earthquakes and the red lines are seismic ray paths (each of them bearing a data). The yellow shaded region for each black dot represents a local average.

3.4.2 Original Backus-Gilbert inversion

Let us give a formal derivation of the Backus–Gilbert approach. The k-th parameter of the model estimate can be written as a linear combination of the true model parameters (ignoring noise):

$$\tilde{m}^k = \sum_{j=1}^{M} A_j^k \mathcal{V}_j m_j, \tag{3.24}$$

where the term $\mathcal{V}_j$ is introduced to account for the variable surface or volume of the cells or voxels in an irregular paramterization (like those encountered in chapters 4 and 5). We recognize the resolution matrix $R_j^k = \sum_i G^{\dagger k}_i G_{ij} = A_j^k \mathcal{V}_j$. For obvious reasons now $\boldsymbol{A^k} = (A_j^k)_{j=1,..,M}$ is called the *averaging kernel* of the k-th model parameter. The use of the superscript notation is to make explicit that the quantities are specific to cell k. We want to minimize the spatial extent of the averaging kernels. For that we need to define a measure of the size of the averaging kernel. There are different possibilities but this would be written in general:

$$S^k = \sum_{j=1}^{M} [A_j^{k2} J_j^{k2}], \tag{3.25}$$

where J is a function that is designed to make the averaging kernel as close as possible to a Dirac delta function at the k-th cell location. For example Parker (1977) proposes to use:

$$J_j^k = \text{constant} \times (r_k - r_j)^2, \tag{3.26}$$

where r_k and r_j are the locations of the k-th and j-th cells. The term $(r_k - r_j)^2$ increases as the distance between the cells j and k so that minimizing S^k is equivalent to minimizing A^k far from the k-th cell. We also add the constraint that we want the averaging kernel to be 'unimodular', to produce unbiased local averages:

$$\sum_{j=1}^{M} A_j^k \mathcal{V}_j = 1. \tag{3.27}$$

Since $A_j^k = \sum_i G^{\dagger k}_i G_{ij} / \mathcal{V}_j$, finding the k-th averaging kernel as a solution to the minimization of S^k is equivalent to find a solution for the k-th row of the generalized inverse matrix.

The model uncertainties depend on the data uncertainties through the generalized inverse:

$$\sigma_{\tilde{m}^k} = \sqrt{\sum_{i=1}^{N} (G^{\dagger k}_i \sigma_{d_i})^2}. \tag{3.28}$$

The second part of the optimization problem for the generalized inverse is to minimize the model uncertainties. Finally the optimization problem in the Backus–Gilbert point of view is written:

$$\boldsymbol{G}^{\dagger \boldsymbol{k}} = \arg \min_{\boldsymbol{G}^{\dagger \boldsymbol{k}} \in \mathbb{R}^N} S^k + {\eta^k}^2 \sigma^2_{\tilde{m}^k}, \quad \text{subject to } \sum_{j=1}^{M} A_j^k \mathcal{V}_j = 1, \tag{3.29}$$

where the scalar η^k is a tradeoff parameter that allows to give more weight to the final resolution or model uncertainties. This equation looks like the cost function in data fitting inversions (equation 3.11). Drawing the resolution size as a function of the model uncertainties would lead to an L-shaped curve like in figure 3.3. But there is a strong difference: while the cost function in data fitting inversions is a tradeoff between the data misfit and the 'model coherence', the cost function in Backus–Gilbert inversions is a tradeoff between the model resolution and the model uncertainties.

Note that the optimization problem only involves the k-th model parameter; it solves only for the k-th row of the generalized inverse, independently from the others. This is a particular feature of the Backus–Gilbert approach. Each model cell can be estimated independently from the others. Then one may solve only

for some region of interest (were the data density is high enough for example). Moreover it makes the problem embarassingly parallel, which means that the computation of M cells of the model could be done theoretically on M independent computer Central Processing Units (CPUs). This is an advantage that I use on High Performance Computer (HPC) facilities.

The Backus–Gilbert optimization problem (equation 3.29) leads to the set of equations (namely by taking the gradient with respect to $\boldsymbol{G}^{\dagger k}$ and equating to zero):

$$(\hat{\boldsymbol{G}}^k \hat{\boldsymbol{G}}^{k^T} + \eta^{k^2} \boldsymbol{I_N}) \boldsymbol{G}^{\dagger k} = \boldsymbol{O_N}, \quad \text{subject to } \sum_{j=1}^{M} A_j^k \mathcal{V}_j = 1, \tag{3.30}$$

where,

$$\hat{\boldsymbol{G}}^k = \left(\frac{J_j^k}{\sqrt{\mathcal{V}_j}} G_{ij} \right)_{i=1,..,N; j=1,..,M}, \tag{3.31}$$

$\boldsymbol{I_N}$ is the $N \times N$ identity matrix and $\boldsymbol{O_N}$ is the null vector of size N. The matrix $\hat{\boldsymbol{G}}^k$ depends on the location of the parameter k because of J_j^k. Therefore, for each parameter it has to be recomputed. This is a computationally expensive task in the case the model has many parameters. This is one reason why the Backus–Gilbert approach has not been applied in large scale tomographic problems and why a reformulation is necessary.

In the Backus–Gilbert approach we may say that the averaging kernels that we obtain are optimal in that they are not biased, they tend to be local with a circular shape (thus reducing smearing effect) and they are designed such that the model uncertainties are not too high. Therefore one may say that the Backus–Gilbert approach is an *Optimally Localized Averages* (OLA) inversion. Since the averaging kernels are obtained by minimizing the function S^k in which they are multiplied with another function J^k, one may say that the Backus–Gilbert approach is a *Multiplicative Optimally Localized Averages* (MOLA) inversion. This terminology has been proposed by Pijpers & Thompson (1993) but it does not seem to be used in practice. To overcome the computational drawback of the Backus–Gilbert 'MOLA' approach, Pijpers & Thompson (1992) and Pijpers & Thompson (1993) proposed a reformulation that they named *Subtractive Optimally Localized Averages* (SOLA) inversion. From the name one may guess the difference with the original Backus–Gilbert inversion. I present this method in the next section.

3.4.3 Subtractive Optimally Localized Averages (SOLA) inversion

The SOLA reformulation differs from the Backus–Gilbert original approach in the process to shape the averaging kernels. In the original approach (MOLA), an averaging kernel is obtained by minimizing its product with another function. In the SOLA approach, the averaging kernel is obtained by minimizing its squared difference with another function T, hence the term *subtractive* in the name SOLA. The minimization tends to make the averaging as close as possible to that function T. Therefore T is called a *target kernel*. The key idea of the SOLA inversion is that the actual resolution will tend to be as close as possible to a pre-defined target resolution. We can write the SOLA equivalent of equation 3.25:

$$S^k = \sum_{j=1}^{M} (T_j^k - A_j^k)^2 \mathcal{V}_j \quad \text{subject to} \quad \sum_{j=1}^{M} A_j^k \mathcal{V}_j = 1. \tag{3.32}$$

This replaces the first term in the optimization problem (equation 3.29). Of course one must also take care of the propagation of the data uncertainties into model uncertainties when looking for the actual resolution; the second term in the optimization problem is unchanged. Finally the SOLA optimization problem is still written:

$$\boldsymbol{G}^{\dagger k} = \arg \min_{\boldsymbol{G}^{\dagger k} \in \mathbb{R}^N} S^k + {\eta^k}^2 \sigma^2_{\tilde{m}^k}, \quad \text{subject to} \quad \sum_{j=1}^{M} A_j^k \mathcal{V}_j = 1, \tag{3.33}$$

Here the tradeoff parameter η^k gives more weight to the fit to the target resolution or to the model uncertainties. In fact, if the target resolution is defined to be very close to the Dirac function, the original Backus–Gilbert inversion would in principle be retrieved.

The SOLA optimization problem leads to the following set of equations:

$$(\hat{\boldsymbol{G}} \hat{\boldsymbol{G}}^T + {\eta^k}^2 \boldsymbol{I_N}) \boldsymbol{G}^{\dagger k} = \hat{\boldsymbol{G}} \boldsymbol{t^k}, \tag{3.34}$$

where,

$$\hat{\boldsymbol{G}} = \left(\frac{G_{ij}}{\sqrt{\mathcal{V}_j}} \right)_{i=1,..,N; j=1,..,M}, \tag{3.35}$$

and,

$$\boldsymbol{t^k} = \left(T_j^k \sqrt{\mathcal{V}_j} \right)_{j=1,..,M}. \tag{3.36}$$

In these equations the $\hat{\boldsymbol{G}}$ matrix does not depend on the parameter location anymore; we do not have to compute as many matrices as there are model parameters. That the problem is location specific is found in the vector $\boldsymbol{t}^k$ that depends on the target kernel which depends on k. Computing a vector for each location is cheaper than computing a full matrix for each location. The only term that may reduce the computational efficiency of the SOLA approach is the tradeoff parameter since it depends on k. But the local role played by η^k can be taken by the target resolution. For example, small target kernels can be designed where a good resolution is desired. Then only one tradeoff parameter η that does not depend on location, but that controls the global tradeoff for the whole model is needed; the local weighting is carried out by the location specific target kernels. The SOLA approach turns out to be very efficient, even for large scale tomographic problems, where the original Backus–Gilbert inversion couldn't be applied in practice. Note that designing the target resolution is advantageous not only for computational purposes, but also because it helps to have a stronger control on the final model resolution.

I propose an illustration of the whole SOLA workflow on figure 3.5. From the physical law relating the data and the model the sensitivity matrix $\boldsymbol{G}$ is built (see chapter 2). The uncertainties attached to the data $\boldsymbol{\sigma_d}$ are estimated. Given the dataset a target resolution $\boldsymbol{T}$ is defined and some tradeoff parameter η between the fit to the target resolution and the model uncertainties $\boldsymbol{\sigma_{\tilde{m}}}$ is chosen. These four quantities are the inputs for the SOLA inversion. The SOLA inversion optimizes the fit to the target resolution while keeping the model uncertainties at a reasonable level. It outputs the generalized inverse of the sensitivity matrix for this balance. Then the model uncertainties are computed from $\sigma_{\tilde{m}^k} = (\sum_i (G_i^{\dagger k} \sigma_{di})^2)^{1/2})$, the model resolution is computed from $A_j^k = \sum_i G_i^{\dagger k} G_{ij}$ and the model estimate is obtained from $\tilde{m}^k = \sum_i G_i^{\dagger k} d_i$. Note that there is one inversion for one cell, and it is completely independent from that for the other cells. Solving for all the model parameters requires M independent inversions but this task is embarassingly parallel. Also it allows to solve only for regions of interest, there is no need to invert for the full model. Note also that the role played by the data comes only after the inversion. The SOLA inversion is driven by the physical law and the geometry of the path coverage, not by the data. It is also possible to use the SOLA inversion without data uncertainty estimate. In this case we do not account for the data uncertainties to design the $\boldsymbol{G^\dagger}$ matrix and we obtain some 'propagation factors' instead of the propagated model uncertainties. Last, only a constraint on the resolution has been introduced, which is fundamentally different than adding an *a priori* on the model itself.

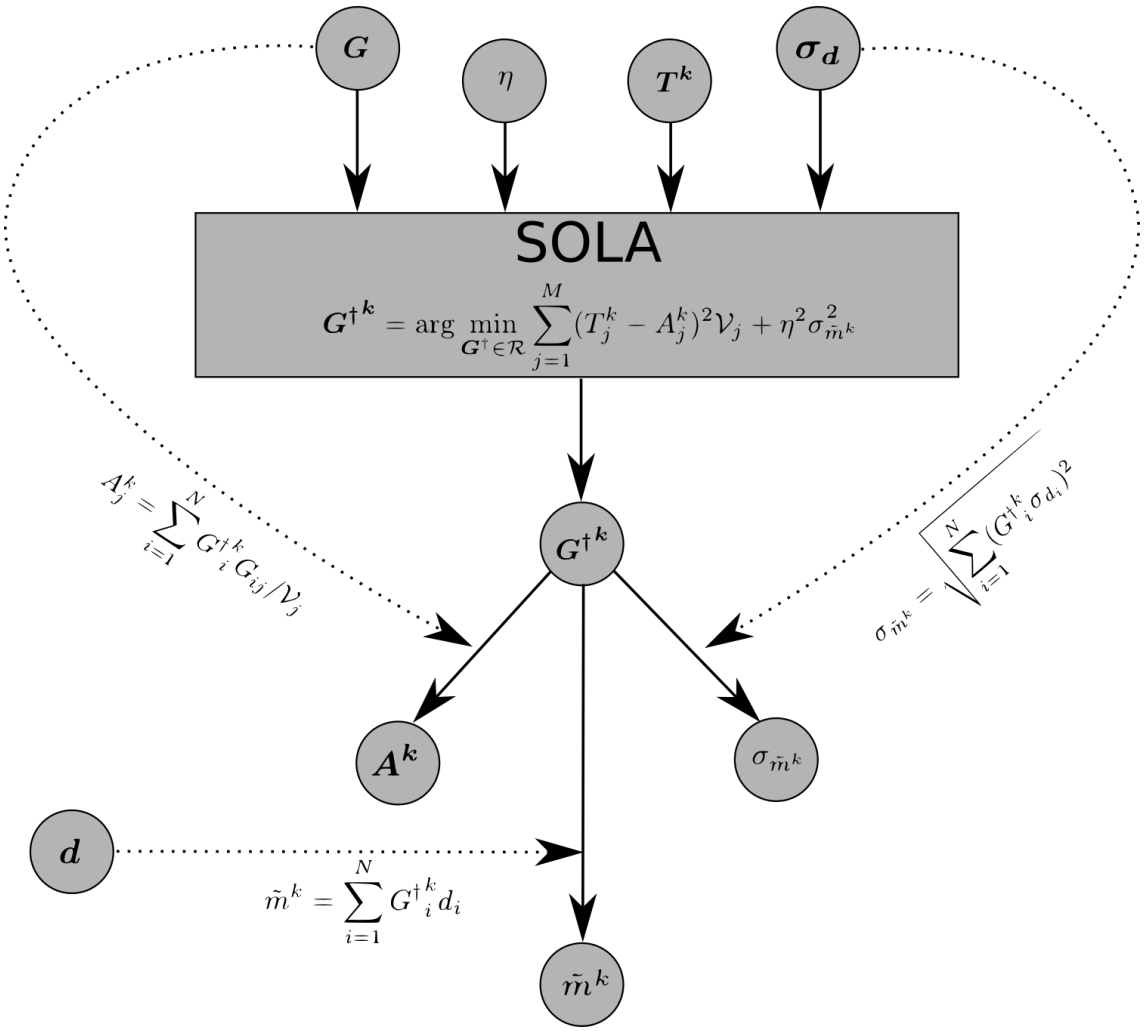

FIGURE 3.5: SOLA workflow. The sensitivity matrix $\boldsymbol{G}$ contains the data distribution and the physical law that relates the model to the data. The data uncertainties $\boldsymbol{\sigma_d}$ are estimated. Given the dataset, a target resolution $\boldsymbol{T}$ is defined and a tradeoff parameter η balancing the fit to the target resolution and the resulting model uncertainties is chosen. These four quantities are the inputs for the SOLA inversion. The SOLA inversion looks for a generalized inverse of the sensitivity matrix $\boldsymbol{G^\dagger}$ such that the resolution is close enough to the target resolution and that the model uncertainties $\sigma_{\tilde{m}}$ are reasonable. Finally one combines the generalized inverse with the data uncertainties to produce the model uncertainties, with the sensitivity matrix to produce the actual resolution (or the averaging kernels $\boldsymbol{A^{(k)}}$), and with the data $\boldsymbol{d}$ to produce the model estimate $\tilde{\boldsymbol{m}}$. Note that the data play a role only after the inversion and that no *a priori* on the model itself has been introduced.

3.5 About the linearity

All the analytical results that we derived in the previous sections are based on the assumption that the forward theory is linear. But what happens if the theory is non linear? We will see that in some cases it is possible to use the concepts of linear theory if the forward problem is 'weakly' non-linear. This discussion is based on Tarantola (2005, section 1.7).

The data and prior model probability distributions are assumed to be Gaussian. Then the joint probability of both forms a Gaussian in the $\mathcal{D} \times \mathcal{M}$ space as illustrated in green on figure 3.6. With the hypothesis that all distributions are Gaussian the theory errors can be assimilated to data errors, therefore the theory can be seen as a perfect line, as the solid black lines on figure 3.6.

If the forward theory is purely linear (figure 3.6 a), it can be seen as a straight line in the $\mathcal{D} \times \mathcal{M}$ space. The posterior probability for the model is Gaussian (dotted black curve on figure 3.6) and analytical formulae exist. In chapter 4, the relation between the path-average S-wave velocity and the S-wave velocity on a two-dimensional spherical layer at a given depth is assumed purely linear.

If the forward problem is weakly non-linear (figure 3.6 b), the tangent (red solid line) to the theory at the prior model location (blue dot) is still a good linear approximation of the theory. The posterior distribution for the model in the linearized case (red dotted line) is close to the real one (black dotted line). Mathematically the linearized theory is a Taylor expansion of the theory where the terms of order two and higher are neglected:

$$\boldsymbol{g}(\boldsymbol{m}) \approx \boldsymbol{g}(\boldsymbol{m_0}) + \boldsymbol{G}(\boldsymbol{m} - \boldsymbol{m_0}). \tag{3.37}$$

In this case $\boldsymbol{G}$ is a linear operator, namely a matrix, that contains the derivatives of the forward theory (or the predicted data) with respect to the model around the prior model location:

$$G_{ij} = \left(\frac{\partial g_i(\boldsymbol{m})}{\partial m_j} \right)_{\boldsymbol{m_0}} = \left(\frac{\partial d_i}{\partial m_j} \right)_{\boldsymbol{m_0}}. \tag{3.38}$$

Solving the inverse problem is not more difficult than in the linear case since only the linear operator $\boldsymbol{G}$ that contains the derivatives of the data with respect to the model parameters is considered. One calls the elements of $\boldsymbol{G}$ the *Fréchet derivatives* and $\boldsymbol{G}$ may be called the *Fréchet matrix*. The rows of $\boldsymbol{G}$ are called *Fréchet kernels*. The i-th row of $\boldsymbol{G}$ is the Fréchet kernel of the i-th data. It represents the sensitivity of the data to the model parameters; thus a row of $\boldsymbol{G}$ may also be called

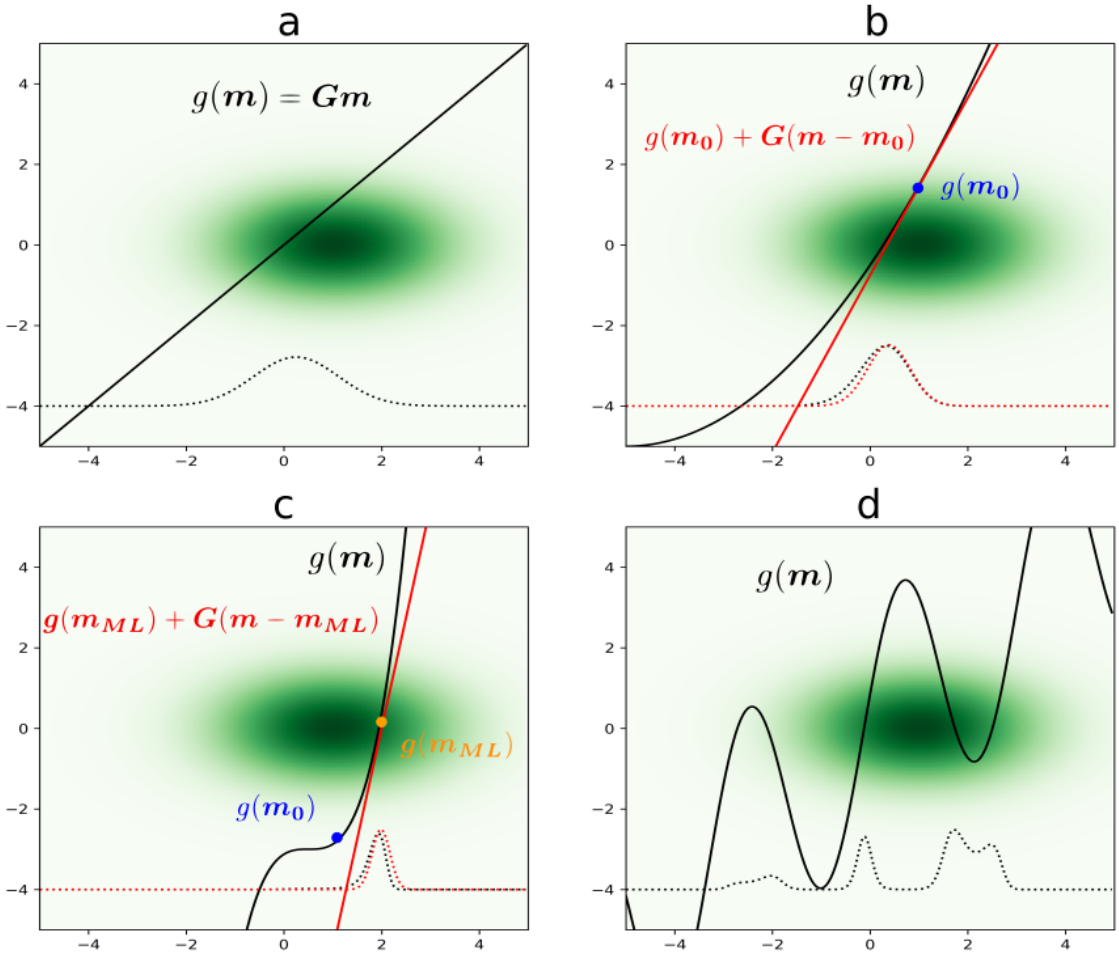

FIGURE 3.6: Analysis of linearity effects on posterior probability distribution and relevance of linearization (after Tarantola (2005)). As in figure 3.2 the vertical axes represent the data space $\mathcal{D}$, the horizontal axes the model space $\mathcal{M}$ and the surface in between the $\mathcal{D} \times \mathcal{M}$ space. The green two dimensional Gaussian is the joint probability distribution of the prior model and data. Contrary to figure 3.2 the theory (solid black lines) is represented by a simple line (not a thick shady area) since within the Gaussian hypothesis one may consider that the modeling errors are data errors. The tangent dotted red lines are the linearizations of the theory if applicable. The dotted black curves are the *a posteriori* model distributions from the theory and the dotted red curves are the *a posteriori* model distributions from the linearized theory if applicable. a) The theory is purely linear, the *a posteriori* model probability distribution is Gaussian, analytical solutions exist. b) The theory is weakly non-linear, a linearization around the *a priori* model (blue dot) is relevant, linear theory can be used within the linearization. c) The theory is more non-linear, a linearization around the prior model (blue dot) is not relevant but it is relevant around the maximum likelihood location (orange dot), linear theory can be used with the linearization. d) The theory is highly non-linear, any linearization would give unrealistic results.

a *sensitivity kernel*. In chapter 2, where we derived the finite frequency sensitivity kernels, we make implicit such a linearization. The model parameters are actually perturbations with respect to a reference model and the linear forward problem actually contains the derivatives of the data (the phase *delays*) with respect to small perturbations in the model (the elastic parameters). In chapter 5 where we apply in one step the Backus–Gilbert theory to recover the S-wave velocity from phase delay measurements, we are therefore in the approximation of weakly non-linear forward theory linearized around a reference model. Note that Snieder (1991) proposed a formalism to extend the Backus–Gilbert theory to non-linear problems. Actually this extension is based on that same idea of the linearization of a weakly non-linear problem around some reference model.

If the problem is more severely non-linear (figure 3.6 c), a linearization around the prior model location (blue dot) would not lead to realistic results. However a linearization where the theory is at the maximum joint probability for the model and data is still possible (orange dot). This location is called the *maximum likelyhood*. To find that location some iterative, non-linear optimization methods (Newton-like methods for example) can be used. Once the maximum likelihood location has been found, one may linearize the theory:

$$\boldsymbol{g}(\boldsymbol{m}) = \boldsymbol{g}(\boldsymbol{m}_{ML}) + \boldsymbol{G}(\boldsymbol{m} - \boldsymbol{m}_{ML}), \tag{3.39}$$

where $\boldsymbol{G}$ is a linear operator, a matrix, that contains the derivatives of the forward theory with respect to the model at the maximum likelihood location:

$$G_{ij} = \left(\frac{\partial g_i(m)}{\partial m_j} \right)_{\boldsymbol{m}_{ML}} = \left(\frac{\partial d_i}{\partial m_j} \right)_{\boldsymbol{m}_{ML}} . \tag{3.40}$$

The relation between the path-averaged S-wave velocities and the secondary observables encountered in chapter 2 belongs to such a situation. Maggi et al. (2006b) use the automated algorithm of Debayle (1999) based on the approach of Cara & Lévêque (1987) who use the non-linear optimization algorithm of Tarantola & Valette (1982).

Finally there is the case of strongly non-linear problems. As illustrated on figure 3.6 d the posterior probability distribution is highly non-Gaussian. Any linear approximation would lead to unrealistic results. No analytical solution exists. The whole model space may be explored, some Monte-Carlo methods may be used or the problem may be simplified by trial and error methods. Note that it would be very difficult to give a meaning to some concepts like 'error bars' in that case. The treatment of highly non-linear problems is outside the scope of

my study.

3.6 Conclusion

Once an equation predicting some data from a model of the Earth is set up (the forward problem), retrieving the model from measured data (the inverse problem) is not an easy task. Solving the inverse problem can be done following one of two main approaches: the traditional data–fitting inversions or the Backus–Gilbert point of view. To conclude this chapter I propose a sketch that compares the two approaches (figure 3.7). The sketch must be nuanced since variations of the main approaches have been introduced over time to overcome their shortcomings. In this chapter I first presented the classical data-fitting inversions based on the tradeoff between data misfit and model coherency (left side of figure 3.7). The main shortcomings of this approach are that it requires an *a priori* on the model itself that may bias the solution, there is no control on the model uncertainties and resolution, the estimation of model uncertainties and resolution can be computationally expensive though both are required for robust interpretations. These observations led me to present the Backus–Gilbert point of view and especially its reformulation as Subtractive Optimally Localized Averages (SOLA) inversion that is central in my thesis (right side of figure 3.7). Contrary to data fitting inversions, this approach is based on a tradeoff between the fit to a target resolution and the minimization of the model uncertainties. It requires no *a priori* on the model itself. It provides a direct control on the model resolution and uncertainties and, by construction, produces them together with the model estimate. In the next two chapters, we aim to apply the SOLA inversion in the context of surface waves. The chapter 4 is the application of the SOLA inversion in the simple ray-theory framework, with the two-step approach described in the first part of chapter 2. The chapter 5 is the application of the SOLA inversion in the more elaborated and more meaningful finite frequency framework, with the three-dimensional and one-step approach, described in the second part of chapter 2.

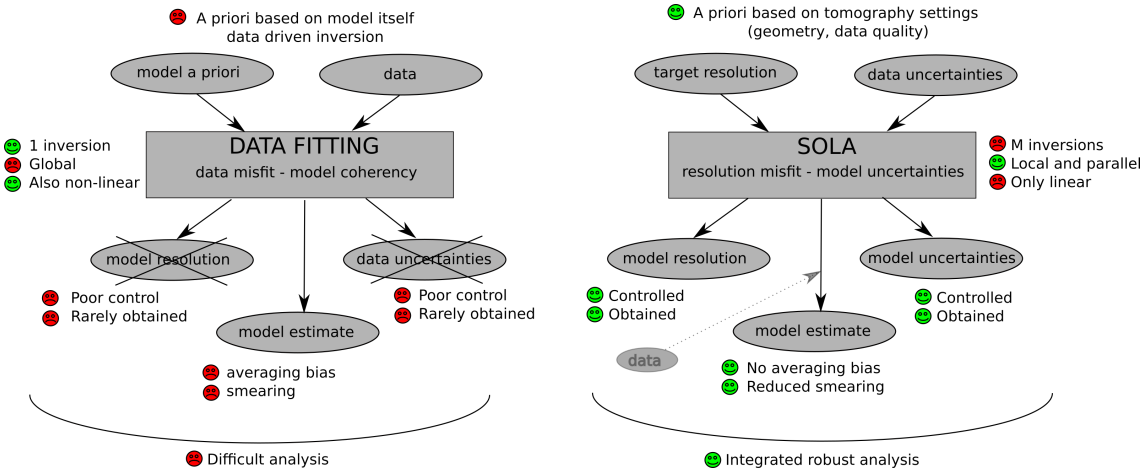

FIGURE 3.7: Comparison between data fitting-like inversions and SOLA inversion. The data fitting inversion aims to fit predicted data to the actual data while guaranteeing high model coherency. It requires an *a priori* directly on the model that may introduce a bias in the solution. There is no or a poor control on the resolution and uncertainties and estimating them is difficult, making the interpretations of the model solution complicated. The SOLA inversion aims to fit the actual resolution to a pre-defined target resolution while keeping the model uncertainties at a reasonable level. Thus it allows a direct control on the model resolution and uncertainties and produces them together with the model estimate. This sketch must be nuanced since variations of the main approaches have been introduced to overcome some limitations.

Chapter 4

Ray theory SOLA tomography

A common complaint we hear is that people do not want to hear about ranges of models, error bars, or all this messy statistics. Perhaps the answer is to avoid speaking of "inverting data." Perhaps we should tell people that we are measuring the risks associated with various interpretations of the data.

Scales and Snieder, *To Bayes or not to Bayes?*, 1997.

Foreword

This chapter has been published in *Geophysical Journal International*. In this study we apply the SOLA inversion method to surface wave tomography within the framework of ray theory. We also design a workflow to account for the resolution and uncertainties in the analysis of the tomographic model.

Summary

Since most tomographic problems deal with imperfect data coverage and noisy data, an estimate of the seismic velocity in the Earth can only be a local average of the 'true' velocity with some attached uncertainty. We use the SOLA (Subtractive Optimally Localized Averages) method, a Backus–Gilbert-type method based on the resolution-uncertainty trade-off, to build a range of models of Rayleigh wave velocities in the Pacific upper mantle. We choose one solution and show how to analyse the model using its resolution and uncertainties. We exploit the model statistics to evaluate the significance of deviations from a theoretical prediction: a half space cooling model of the Pacific lithosphere. We investigate a slow velocity anomaly located north-east of Hawaii, at about 200 km depth, and a pattern of alternatively slow and fast velocity bands, aligned approximately north-west to south-east, between 200 and 300 km depth. According to our resolution and uncertainty analyses, both features seem to be resolved.

4.1 Introduction

To understand how Earth's upper mantle behaves, we require robust estimates of its physical properties and how they vary laterally and with depth (e.g. Mégnin et al., 1997; Foulger, 2011; Simmons et al., 2019; Freissler et al., 2020). We can estimate one such property, S-wave velocity, using surface-wave tomography.

Most tomographic studies are performed by minimizing the squared differences between data predicted using the model and actual measured data, using one of many variations of the damped-least-squares inversion scheme (e.g. Maggi et al., 2006b; Zhou et al., 2006; Nettles & Dziewoński, 2008; Panning, Lekić & Romanowicz, 2010; Ekström, 2011; French, Lekic & Romanowicz, 2013a; Auer et al., 2014; Liu & Zhou, 2016a; Isse et al., 2019). The studies cited show consistent images of large scale structures (lithosphere cooling signatures, super-swells, cratons) and of structures that produce strong, localized S-wave velocity anomalies (subduction zones, ridges). These images differ, however, at shorter scales and for structures that produce weaker anomalies. For instance, the model savani of Auer et al. (2014) is 'slow' in the region of Hawaii at 200 km depth; on the contrary, this region is 'fast' in the model SEMum2 of French, Lekic & Romanowicz (2013a) (see for example fig. S7 from Isse et al. (2019) showing comparisons of various models).

Although some of these discrepancies may be imputed to differences in theoretical approaches (forward or inverse methods) used by the aforementioned

studies, many discrepancies simply reflect how large uncertainties in the initial seismic measurements propagate into the final tomographic models. To compare tomographic models with each other – or to compare them to some prior, tectonic-based, conceptual model of the Earth – we need reliable estimates of their uncertainties (e.g. Rawlinson et al., 2014; Simmons et al., 2019; Freissler et al., 2020). Unfortunately, because many damped-least-squares inversion schemes are optimized to invert large volumes of data to constrain large numbers of model parameters (e.g. Debayle & Sambridge, 2004), they often do not keep track of how data uncertainties propagate into the tomographic models; for large scale tomographic problems, most studies using these methods do not compute explicit model uncertainties, yet robust interpretation of features requires comparing the magnitude of the anomalies with the model uncertainties. For smaller scale tomographic problems, these methods only provide at best an *a posteriori* estimate of the uncertainties and cannot control them directly.

This difficulty derives from the manner in which earthquakes and seismic stations are distributed geographically: some regions may be sampled by many independent surface-wave ray paths; other regions may be poorly constrained. This irregular data coverage causes the inverse problem to be under-determined: within poorly covered parts of a region, the model can change widely without changing how it fits the data. Which model we choose is, in some sense, arbitrary (Scales & Snieder, 1997; Nolet, 2008). Some tomographic studies make use of irregular or adapted meshes to account for the heterogeneous distribution of the data (e.g. Sambridge & Rawlinson, 2005). Many tomographic studies use *ad-hoc* regularization constraints to reduce the non-uniqueness of the model solution; they often minimize the model's complexity by damping the inversion (e.g. Nolet, 2008, Chapter 14) – hence the name *damped*-least-squares inversion. Such inversions may underestimate seismic velocity anomalies where data coverage is poor; less intuitively, they can also overestimate velocity anomalies where data coverage is highly uneven. In either case, we call such models *locally biased* (in the sense of 'averaging bias' effects, as reported by Zaroli, Koelemeijer & Lambotte, 2017).

Half-a-century ago, Backus and Gilbert proposed an original approach to invert linear geophysical data designed to produce complete uncertainty information, optimize local resolution, and eliminate bias (Backus & Gilbert, 1967; Backus & Gilbert, 1968; Backus & Gilbert, 1970). Instead of searching for a model that fits the data with some smoothness criterion, the Backus-Gilbert method searches for a model that has optimal resolution given the geometry and uncertainties of the data. Pijpers & Thompson (1992) and Pijpers & Thompson (1993) reformulated

the method, applied it to helio-seismology, and named it *Subtractive Optimally Localized Averages* (SOLA). More recently, Zaroli (2016) introduced and adapted the SOLA method to seismic tomography problems with large numbers of parameters; he then applied this new inversion scheme to obtain a body wave tomographic model of the lower mantle. The SOLA Backus-Gilbert method still suffers from a form of non-uniqueness, as model resolution and model uncertainties trade-off against each other. Despite not being designed for that purpose, the method also leads to models that fit the data. Note that SOLA tomography can deal with heterogeneous spatial distribution of the data and usually produces models with no averaging bias. Computationally, the SOLA formulation of the Backus-Gilbert approach remains tractable even when dealing with large-scale tomographic problems (Zaroli, 2016; Zaroli, Koelemeijer & Lambotte, 2017). Lastly, it provides the full resolution and model uncertainties, which are the model statistics necessary to draw well-informed conclusions from the tomographic model.

In this study, we use the SOLA inversion to produce tomographic images of the Pacific upper mantle from path-averaged shear-wave velocity profiles obtained from surface-waves. After discussing how resolution and uncertainty trade-off in our models, we illustrate how to use them to perform meaningful comparisons of tomographic images with a geodynamic prediction. Taking as a reference a simple half-space cooling model (Parker & Oldenburg, 1973), we point out anomalous regions in our tomographic model and we argue about their statistical significance and whether they are resolved or not.

4.2 Data and method

Most surface-wave tomography studies that produce 3D shear-wave velocity models proceed in a sequence of two steps: either they first make 2D phase- or group-velocity maps at various frequencies (linear tomographic inversion), then combine them to obtain depth-dependent shear-wave velocity profiles at each point in the map (non-linear inversion) – examples are Ekström (2011) or Liu & Zhou (2016a); or they first invert for 1D shear-wave profiles as a function of depth along each source-station path (non-linear inversion), then combine these path-averaged velocity profiles into maps at each depth (linear tomographic inversion) – examples are Maggi et al. (2006b) or Isse et al. (2019). Each sequence contains both a linear and a non-linear inversion. Only the linear inversion can be performed using the SOLA method.

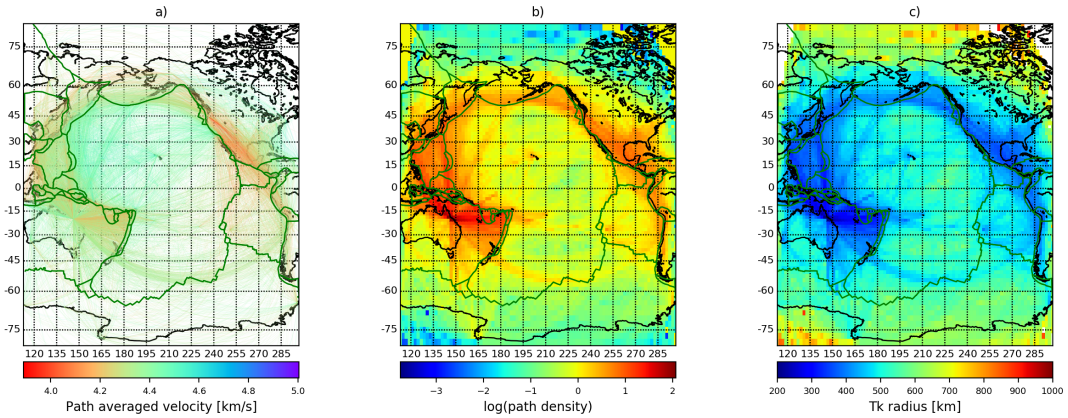

FIGURE 4.1: Data geometry and target resolution at 75 km depth. Thick green lines indicate plate boundaries. (a) Each thin line represents one of the ∼15 000 paths from Maggi et al. (2006b) used as input to the SOLA tomography; the color of each path is the path-average shear wave-speed at 75 km depth in the 1D model corresponding to the path; (b) Path density (total path length that falls in each cell normalized by the total path length over the entire model); (c) Target-kernel radii.

4.2.1 Path-averaged velocity and uncertainty

As we aim to discuss how SOLA can improve the way we interpret seismic tomography images, we have chosen to apply the method on a pre-existing dataset of path-averaged shear-wave velocity profiles obtained from Rayleigh waves (Maggi et al., 2006b). These profiles range from 50 km to 450 km depth, and were obtained by inverting over 56 000 multi-mode surface-waves whose paths crossed the Pacific Ocean, using the Debayle (1999) automation of the Cara & Lévêque (1987) secondary observables method. After obtaining a shear-wave velocity profile for each path, Maggi et al. (2006b) gathered similar paths (those whose end-points were within 200 km of each other) into ∼15 000 clusters, obtained the average velocity profile of each cluster (Fig. 4.1a), and estimated the uncertainty of the velocities using the standard-deviation in each cluster. These clustered path-averaged shear-wave velocities are the input data for our SOLA inversion.

The robustness of the analysis later in this paper relies on the reliability of the data uncertainty estimates. The approach of Maggi et al. (2006b) to estimate the data uncertainty captures the stochastic uncertainty: it measures the variability between adjacent paths within one cluster due, for example, to random measurement errors or to random errors in the location of the earthquakes in the cluster. However, it does not account for errors that would affect identically all paths in a cluster; for example, neglecting off-great circle paths due to some

TABLE 4.1: χ^2_{red} values at various depths for the damped-least-squares model of Maggi et al. (2006b).

depth [km]	50	75	100	150	200	250	300	350	400
χ^2_{red}	3.378	3.199	2.630	2.216	1.648	1.561	1.542	1.579	1.497

lateral heterogeneity or mislocating all earthquakes in the same direction due to lateral heterogeneities or network configuration. Data uncertainties from Maggi et al. (2006b) decrease at larger depths because paths along which long-period and higher-mode data were unavailable were damped toward the background model, a smoothed version of PREM (Dziewonski & Anderson, 1981). As all the path-averaged models tend toward the same values when the sensitivity decreases, the stochastic uncertainties also decrease.

Since the Maggi et al. (2006b) approach considers only stochastic uncertainties, it underestimates the full data uncertainties. Because the data uncertainties influence the SOLA inversion and propagate directly into model uncertainties (see section 4.2.2), we needed more reliable estimates of them. We calculated the χ^2_{red} for the final model of Maggi et al. (2006b) (e.g. Nolet, 2008):

$$\chi^2_{\text{red}}(\widetilde{m}) = \frac{1}{N}\sum_{i=1}^{N}\frac{[(\sum_{j=1}^{M} G_{ij}\widetilde{m}_j) - d_i]^2}{\sigma^2_{d_i}}, \tag{4.1}$$

where $\widetilde{m}_j$ is the j-th model parameter, M the number of model parameters, d_i the i-th datum, N the number of data, G_{ij} the elements of the sensitivity matrix of size $N \times M$ such that $\sum_{j=1}^{M} G_{ij}\widetilde{m}_j$ is the i-th predicted data, and σ_{d_i} the i-th data uncertainty. The values of χ^2_{red} at all depths are much greater than one (see Table 4.1). Two reasons may explain these values. First Maggi et al. (2006b) may have chosen an overdamped solution to ensure that all features in their model were interpretable. Second, the data uncertainties may be underestimated because they do not account for systematic bias. To obtain more reliable data uncertainty estimates, we assume that the final model of Maggi et al. (2006b) is a model that explains the data so that the χ^2_{red} values should be one, then we rescaled the data uncertainties by the factor required to bring $\chi^2_{\text{red}} = 1$, i.e. we multiplied each data uncertainty by $(\chi^2_{\text{red}})^{1/2}$ at the corresponding depth (see Table 4.1).

4.2.2 Regionalization with SOLA

We divide the Pacific region into independent depth layers, each of them divided into cells of 2° in latitude and longitude. Each model parameter m_j ($j = 1, ..., M$)

represents the shear-wave velocity in cell j. Each datum d_i ($i = 1, ..., N$) represents the average shear-wave velocity along the i-th source-receiver path. The sensitivity matrix $\boldsymbol{G}$ linearly relates the data to the velocities as follows:

$$d_i = \sum_{j=1}^{M} G_{ij} m_j + n_i, \tag{4.2}$$

where n_i denotes a noise term (we assume uncorrelated zero mean Gaussian noise). The tomographic problem is ill-posed because some regions are undersampled and contradictions may arise from the noise in the data. Therefore the linear sensitivity matrix $\boldsymbol{G}$ is not invertible and we have to seek a 'generalized' inverse matrix $\boldsymbol{G^\dagger}$, such that the k-th parameter estimate $\widetilde{m}_k$ can be written as a linear combination of the data:

$$\widetilde{m}_k = \sum_{i=1}^{N} G_i^{\dagger(k)} d_i = \sum_{i=1}^{N} \sum_{j=1}^{M} G_i^{\dagger(k)} G_{ij} m_j + \sum_{i=1}^{N} G_i^{\dagger(k)} n_i. \tag{4.3}$$

Here k refers to the k-th grid cell, $\boldsymbol{G^{\dagger(k)}} = (G_i^{\dagger(k)})_{i=1,..,N}$ represents the k-th row of the $\boldsymbol{G^\dagger}$ matrix (k may vary from 1 to M) and $\boldsymbol{R} = \boldsymbol{G^\dagger G}$ is called the resolution matrix. We define the k-th averaging (or resolving) kernel as:

$$\boldsymbol{A^{(k)}} = (A_j^{(k)} = R_j^{(k)} / \mathcal{S}_j)_{j=1,...,M}, \tag{4.4}$$

where $R_j^{(k)} = \sum_{i=1}^{N} G_i^{\dagger(k)} G_{ij}$ are the elements of the k-th row of the resolution matrix. The factor $\mathcal{S}_j$ is, in our case, the cell surface area; it appears because the model parameterization has cells with different sizes.

If the problem were well-posed, the sensitivity matrix would be invertible, the resolution matrix would be the identity matrix, and the model estimate $\widetilde{\boldsymbol{m}}$ would equal the true model $\boldsymbol{m}$. In practice, the model estimates are local averages of the true Earth. The k-th row of the resolution matrix $\boldsymbol{R^{(k)}}$ (closely related to the k-th averaging kernel through the term $\mathcal{S}_j$) relates $\widetilde{m}_k$ to the true parameters ($\widetilde{m}_k \approx \sum_{j=1}^{M} R_j^{(k)} m_j = \sum_{j=1}^{M} \mathcal{S}_j A_j^{(k)} m_j$). In the Backus–Gilbert approach, we want each averaging kernel to be centered and peak-shaped around the location of its corresponding model parameter.

The model estimate $\widetilde{m}_k$ also contains the term $\boldsymbol{G^{\dagger(k)} n}$ that reflects propagation of data noise into model space. Note that smaller averaging kernel sizes lead to higher model uncertainties (Menke, 1989). This can be understood intuitively: fewer data can be averaged within smaller averaging kernels, leading to fewer chances for data errors to cancel out. There is, therefore, a trade-off between

good resolution and low model uncertainties.

The model uncertainty is defined statistically as:

$$\sigma_{\tilde{m}_k} = \sqrt{\sum_{i=1}^{N} {G_i^{\dagger(k)}}^2 \sigma_{d_i}^2}. \tag{4.5}$$

In this study we assume uncorrelated zero-mean Gaussian data uncertainty. Thus the data covariance matrix is diagonal: $\boldsymbol{C_d} = diag(\sigma_{d_i}^2), i = 1, ..., N$. Note that it would be possible to consider non-diagonal data covariance matrix in the SOLA approach (Pijpers & Thompson, 1992) but we ignore off-diagonal terms for simplicity.

The key idea of the SOLA method is to specify an *a priori* target form, $\boldsymbol{T^{(k)}} = (T_j^{(k)})_{j=1,...,M}$, for each averaging kernel, $\boldsymbol{A^{(k)}}$. We specify some *a priori* information on the model resolution, which is fundamentally different from specifying *a priori* information on the model itself (as in data-fitting methods such as Bayesian methods and damped-least-squares). Rather than minimizing the spread (spatial extent) of each averaging kernel, $\boldsymbol{A^{(k)}}$, as in the original Backus-Gilbert approach, the SOLA variant aims to minimize the integrated squared difference between each averaging kernel, $\boldsymbol{A^{(k)}}$, and its corresponding target kernel, $\boldsymbol{T^{(k)}}$. A minimization problem directly computes each generalized inverse vector for each k-th parameter:

$$\begin{cases} \underset{\boldsymbol{G^{\dagger(k)}} \in R^N}{\arg\min} \sum_{j=1}^{M} \mathcal{S}_j (A_j^{(k)} - T_j^{(k)})^2 + \eta^2 \sigma_{\tilde{m}_k}^2 \\ \text{such that } \sum_{j=1}^{M} \mathcal{S}_j A_j^{(k)} = 1, \end{cases} \tag{4.6}$$

where η is a trade-off parameter to give more weight to the resolution or to the model uncertainties in the optimization. Equation 4.6 is independent for each model parameter therefore efficient parallel computations are possible. We could adapt the trade-off parameter η for each model parameter but this would reduce the optimization of calculation; here we adapt only the target resolution. The constraint that the averaging kernels should be unimodular means that SOLA tomographic models should be free of averaging bias; a condition that cannot usually be guaranteed with inversion methods incorporating regularization (Zaroli, Koelemeijer & Lambotte, 2017).

The target resolution for a parameter is non-zero only in a circular region around that parameter's location; the circle's radius is computed from the path density:

$$r(\rho) = r_{\max} - (r_{\max} - r_{\min}) \left(\frac{\log_{10}(\rho) - \log_{10}(\rho_{\min})}{\log_{10}(\rho_{\max}) - \log_{10}(\rho_{\min})} \right), \tag{4.7}$$

where r is the target kernel radius, ρ is the path density, $\rho_{\min}$ and $\rho_{\max}$ are the minimal and maximal path densities, and $r_{\min}$ and $r_{\max}$ are the minimal and maximal target kernel radii. The values of $r_{\min}$ and $r_{\max}$ are chosen based on an estimate of the *a priori* resolving-length bounds, which depends on the dominant wavelengths and path lengths within the dataset. The logarithms lower the spatial variations of the target kernel radii compared to those of the path density. This smoothing is important to avoid tomographic images that would be difficult to interpret if nearby averaging kernels had widely different sizes. Other formulae could be chosen to reduce even further the spatial variability of the target kernel radii. Figs 4.1(b) and (c) show the path densities and target resolution length calculated for the path distribution in Fig. 4.1(a). We show several target kernels in Fig. 4.2(a).

The optimization problem (equation 4.6) involves the rows of the generalized inverse through the averaging kernels $\boldsymbol{A}^{(k)}$ (equation 4.4) and model uncertainties $\sigma_{\widetilde{m}_k}$ (equation 4.5). It leads to a set of independent equations whose unknowns are the rows of the generalized inverse. Derivation of these equations from equation 4.6 can be found in Zaroli (2016). These equations are solved using the LSQR algorithm of Paige & Saunders (1982) as proposed by Nolet (1985) and Zaroli (2016). Once the k-th row of the generalized inverse $\boldsymbol{G}^{\dagger(k)}$ has been computed, one obtains the associated model solution $\widetilde{m}_k$ from equation 4.3, the model uncertainty $\sigma_{\widetilde{m}_k}$ from equation 4.5, and the averaging kernel $\boldsymbol{A}^{(k)}$ from equation 4.4. For further details, the reader is referred to Zaroli (2016), Zaroli, Koelemeijer & Lambotte (2017), and Zaroli (2019).

4.3 Tomographic results

In this section, we present the effects of varying the trade-off parameter η in equation 4.6, choose a value for η, describe in more detail the features of the resulting tomographic model, and illustrate how to take resolution and uncertainty into account when comparing a tomographic model to the theoretical predictions of a simple geodynamic model (half-space cooling).

4.3.1 Resolution, uncertainty, and model estimate for various trade-off parameters

All tomographic inversions have trade-offs. In damped-least-squares inversions, model smoothness trades-off against data fit (smooth models fit the data poorly,

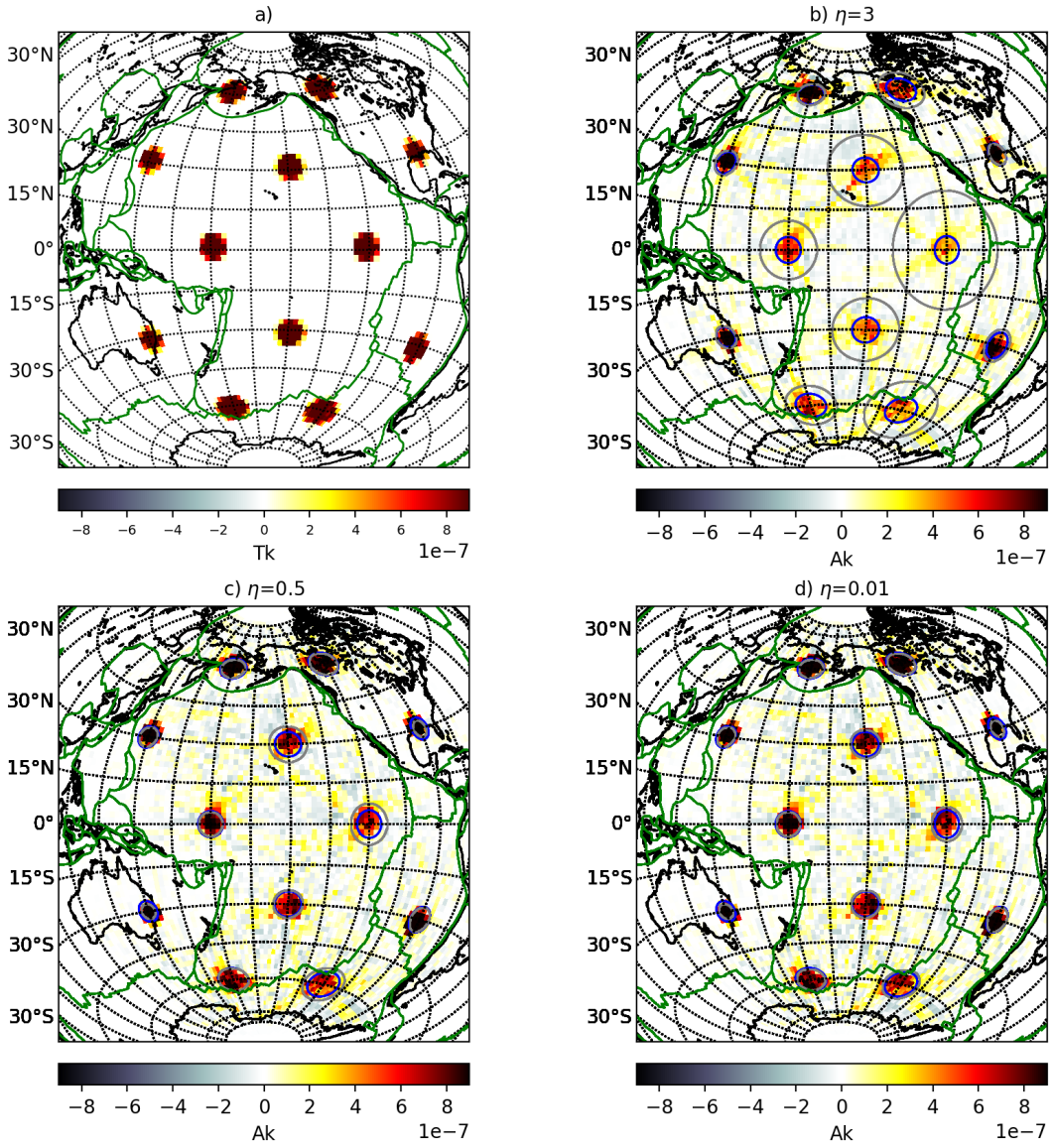

FIGURE 4.2: Examples of SOLA target kernels $\boldsymbol{T}^{(k)}$ (a) and corresponding averaging kernels $\boldsymbol{A}^{(k)}$ (b-d) at 75 km depth for η=3, 0.5 and 0.01. Blue circles indicate the edge of the target kernel disks; grey circles contain 68% of the averaging kernel amplitude. For convenience, several target (or averaging) kernels are plotted on the same map.

but rough models risk fitting the noise part in the data). In SOLA, model resolution trades-off against model uncertainty. Fig. 4.2 shows a selection of target kernels $\boldsymbol{T}^{(k)}$ and averaging kernels $\boldsymbol{A}^{(k)}$ for three values of the trade-off parameter η. The averaging kernels have dome-like centers and ramified extremities and are better focused for lower trade-off parameter values. They look like the results of the synthetic spike or point-spread tests used in some tomographic studies to approximate the resolution of their models (e.g. Rawlinson & Spakman, 2016). For a trade-off that favors low model uncertainties but poor resolution, Fig. 4.2(b), the ramifications of the averaging kernels extend far from the model parameter location, their magnitudes are non negligible, and they follow the non-uniform azimuthal path coverage. This is the well-known smearing effect, visible in the averaging kernel in the north-east of Hawaii, where paths have a predominant north-east to south-west orientation. In regions where the azimuthal path coverage is better, we do not see such artifacts. This is the case, for example, in the north-east of Japan where the averaging kernels are compact and nearly circular. Improving the resolution by lowering η makes the averaging kernels more circular and decreases the length and magnitude of the ramifications. The averaging kernels may have a small negative component, which is physically meaningless. A strong negative component would indicate that the target resolution was badly chosen and invalidate the results; in our case, it is small enough to be ignored.

A complete set of averaging kernels – one map for each model parameter – would fully represent the resolution of a SOLA inversion, but would be cumbersome and difficult to use when interpreting tomographic models. To simplify this information, we compute for each model parameter k a *resolution length* L_k corresponding to the radius of a circle that contains 68% of the averaging kernel – a proxy to the standard deviation for a 2D Gaussian (gray circles in Fig. 4.2). This proxy to the resolution is not ideal if the averaging kernel has a very complex shape, especially in case of smearing. For example, the gray circles on Fig. 4.2(b) do not represent well the averaging kernels when the ramifications are long and strong (especially for those in the middle of the Pacific plate). Note that other simplifications of the resolution could be used; for instance we could fit an ellipse to the averaging kernels to obtain a main direction in case of anisotropic resolution (smearing). However, since our averaging kernels are mostly circular, we use the circular approximation for simplicity. The top row of Fig. 4.3 shows resolution maps for three values of the trade-off parameter. In all maps the resolution is bad at the model borders and in the central Pacific Ocean, where path coverage is poor. As the trade-off parameter decreases, resolution improves in the central Pacific, though the improvement seems to level off between $\eta = 0.5$ and $\eta = 0.01$.

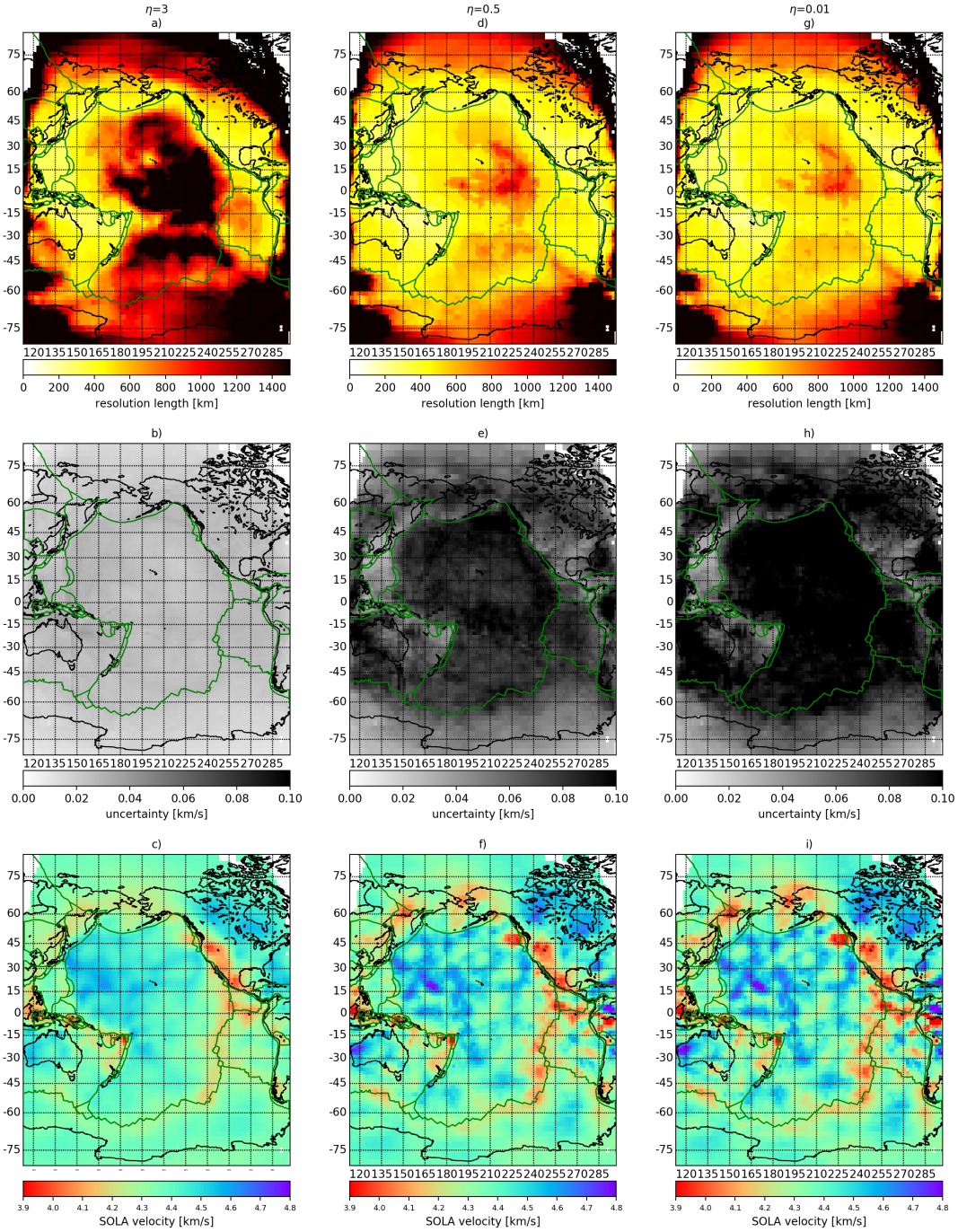

FIGURE 4.3: SOLA inversion results at 75 km depth for three values of trade-off parameters: η=3, 0.5, 0.01. Each column corresponds to a value of η and from top to bottom, maps show resolution lengths (L_k) (a, d, g), model uncertainties (b, e, h) and shear-wave velocities (c, f, i).

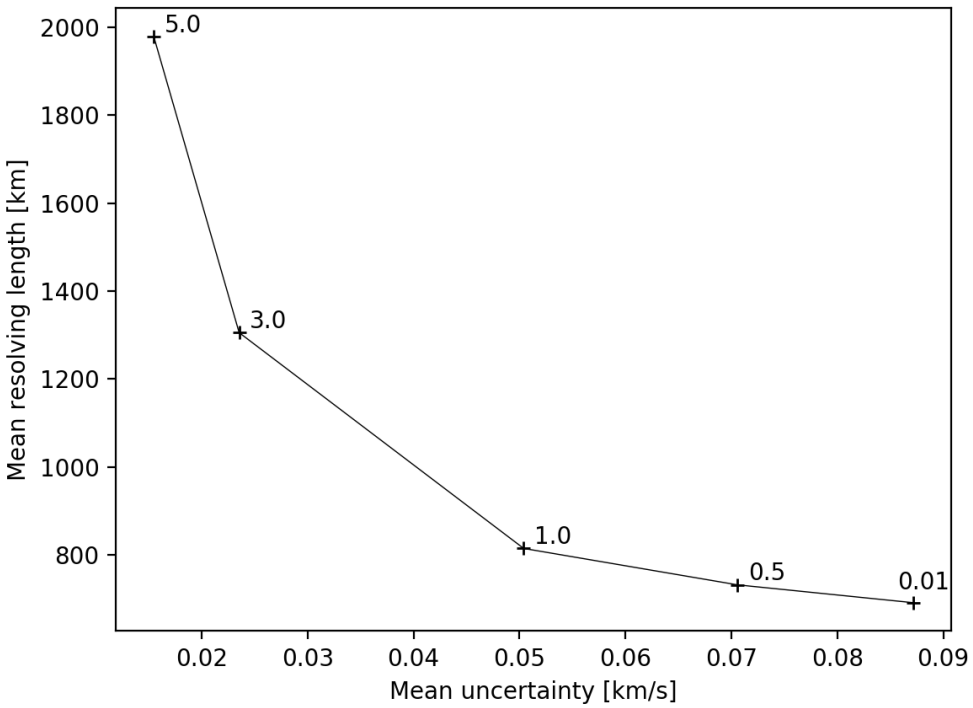

FIGURE 4.4: Mean resolution versus mean uncertainty of SOLA results for five values of the trade-off parameter η (5, 3, 1, 0.5, 0.01) indicated on the curve. The slope from $\eta = 3$ to $\eta = 0.5$ is more negative than from $\eta = 0.5$ to $\eta = 0.01$. This is consistent with the apparent variations of the model statistics on Fig. 4.3. As η changes, model resolution and uncertainties follow an L-curve.

Before choosing a value for η, we must also examine the influence on the model uncertainties. Note that in this paper we express the uncertainties in the 1σ sense: there is a 68% probability that the true locally averaged shear-wave velocity lies within the uncertainty interval around the estimated value. The middle row of Fig. 4.3 shows model uncertainties for the same three values of η. As predicted by the nature of the trade-off, model uncertainties worsen as the trade-off parameter decreases, whereas model resolution improves. Decreasing η from 3 to 0.5 improves resolution greatly while increasing model uncertainties only slightly; however, decreasing η again from 0.5 to 0.01 improves resolution only slightly while increasing model uncertainties greatly. As η changes, model resolution and uncertainties follow a well-known L-curve (see Backus & Gilbert, 1970). Fig. 4.4 shows mean resolution ($\frac{1}{M}\sum_{k=1}^{M} L_k$) versus mean uncertainty ($\frac{1}{M}\sum_{k=1}^{M} \sigma_{\widetilde{m}_k}$) for five values of the trade-off parameter, including 3, 0.5 and 0.01.

The bottom row of Fig. 4.3 shows tomographic models at 75 km depth for the same three η values discussed above. As expected, the tomographic models are smoother where resolution lengths are large and uncertainties low, and rougher where resolution lengths are low and uncertainties high. No single model is intrinsically better than another: the poor resolution, low uncertainty model in Fig. 4.3(c) would be appropriate if we were interested in high precision estimates of the average shear-wave velocity over large patches; the better resolution, higher uncertainty models in Fig 4.3(f) or (i) would be appropriate if we were interested in smaller anomalies we expect to be strong enough to be detectable despite the increased uncertainties.

In the next subsection, we describe in more detail the $\eta = 0.5$ tomographic solution, whose resolution lengths are on average short enough that the model is not too smooth, and whose uncertainties are on average low enough not to swamp all its features.

4.3.2 Detailed analysis of one tomographic solution

For any tomographic inversion, resolution, model uncertainty, and model smoothness are intrinsically linked to path coverage and data quality. The best-sampled regions for our inversion are the eastern, northern and western borders of the Pacific ocean (Fig. 4.1): these regions are strongly seismogenic and host many seismic stations. The interior of the Pacific ocean and its southern boundary are sparsely sampled, except near Hawaii and French Polynesia where Maggi et

al. (2006b) exploited both permanent stations and temporary deployments (Barruol, 2002) to increase local path coverage.

The resolution map in Fig. 4.3(d) shows that the well-sampled regions have the best lateral resolution: the radii of the circles that approximate the averaging kernels in these regions are between 300 km and 500 km. The Pacific ocean itself has a poor resolution, around 800 km on average. The regions west of Hawaii and west of the French Polynesia have better resolution (550 km) because the seismic networks installed within those archipelagos record earthquakes that occur on the western boundary of the Pacific plate. The best resolved region is northeast Australia, where the resolution length is below 300 km; the worst resolved region away from the model's edges is located southeast of Hawaii, where the resolution length is greater than 1000 km. But the resolution is not only related to the path coverage: the data uncertainties also influence the achievable resolution and model uncertainties.

The uncertainty map in Fig. 4.3(e) shows that model uncertainties and model resolution do not always correlate. In some well-resolved regions, such as the Philippine Sea, Tonga-Kermadek, and central America, the locally-averaged shear-wave velocities are known to within 0.02 km/s. In these regions, we can resolve and interpret small features, even those that generate only moderate shear-wave velocity signatures. In some poorly-resolved regions, such as the central Pacific Ocean, shear-wave velocities are known to within greater bounds (0.07 km/s on average); here it becomes harder to interpret features unless they are large and generate strong shear-wave velocity signatures. Well-resolved regions may also display high model uncertainties: in the northern Pacific and off the coast of north-east Australia, the resolution length is close to 300 km, yet the uncertainties are similar to those in the central Pacific. In such regions, we can interpret features, regardless of their size, only if they generate strong shear-wave velocity signatures. This is a reminder that we need both resolution and uncertainty information for interpreting tomographic models.

The shear-wave velocity maps at 75 km depth (Fig. 4.3f), 125 km depth (Fig. 4.5c), and 400 km depth (Fig. 4.5f) show all the large-scale geological features we may expect in tomographic images in oceanic regions: low shear-wave velocities down to $\sim$100 km depth beneath the East Pacific Rise and the Pacific-Antarctic Ridge; fast velocities in the subduction zones (at least down to 200 km depth) and lower velocities in their back-arc regions; high velocities from 75 to $\sim$200 km depth in the North American and Australian cratons; velocities that increase with distance from the mid-ocean ridges down to depths of $\sim$150 km. Unsurprisingly, given we have used their shear-wave velocity profiles, Maggi et al. (2006b) also saw similar

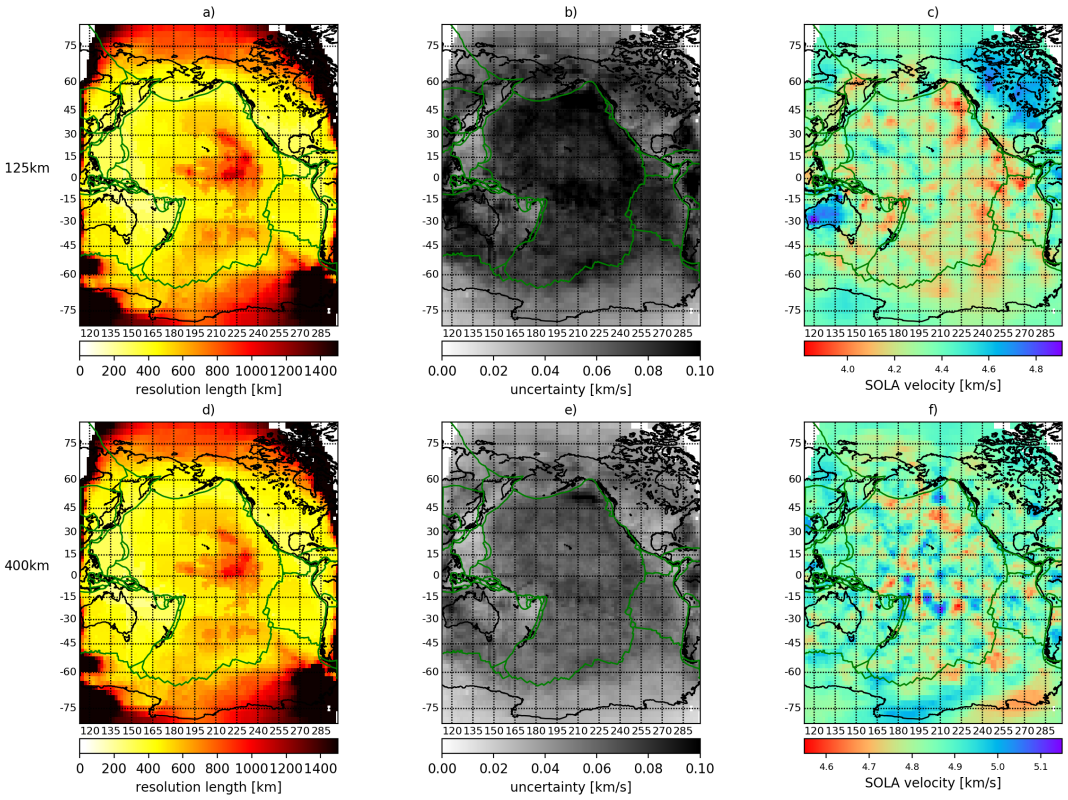

FIGURE 4.5: SOLA inversion results at 125 km (first row) and 400 km depth (second-row) for $\eta = 0.5$: (a, d) resolution lengths; (b, e) model uncertainties; (c, f) shear-wave velocities.

features, though with slightly poorer resolution, as their damped-least-squares tomographic inversion used a single smoothing parameter for all locations in the model.

The resolution and uncertainty maps at 125 km and 400 km depth (Fig. 4.5) look like those at 75 km depth (Figs 4.3d and e). This is not what we would expect given the behaviour of surface waves. Deeper regions of the upper mantle can only be resolved by longer-period or higher-mode surface-waves, both of which have long wavelengths (so poor lateral resolution) and cannot be observed clearly on all paths; therefore, we would expect the resolution lengths to increase with depth. The reason those in Fig. 4.5 stay constant stems from the data we used in the SOLA inversions: path-averaged shear-wave velocity profiles from Maggi et al. (2006b), each one the result of a non-linear inversion of surface-wave measurements. Where long-period and higher-mode data were available, shear-wave velocity profiles were constrained by data down to 400 km depth; where these data were unavailable, the profiles were damped, at depth, towards the background model: a smoothed version of PREM (Dziewonski & Anderson, 1981). It is likely, therefore, that many of the velocity profiles used for the SOLA inversion are uninformative below ∼300 km depth; we could not remove them from our inversion without redoing Maggi et al. (2006b)'s entire analysis, which was outside the scope of this study. In the following, therefore, bear in mind that the resolution maps (and for a similar reason the uncertainty maps) in Fig. 4.5 are overly optimistic at depths beyond ∼300 km.

4.4 Model assessment based on a plate cooling model

The tomographic maps of Fig 4.3 show an increase in seismic velocity with distance from the mid-oceanic ridges. This is connected with the well-known phenomenon of plate cooling (e.g. Ritzwoller, Shapiro & Zhong, 2004; Faul & Jackson, 2005; Priestley & Mckenzie, 2006; Isse et al., 2019). Armed with complete resolution and uncertainty information, we investigated if any features of these tomographic images deviated significantly from the predictions of a theoretical cooling model and if such deviations were well-resolved.

4.4.1 The reference model

We chose to use the simple half-space cooling model of Parker & Oldenburg (1973) to illustrate our process of comparing tomographic images to theoretical predictions, not because we believed it to be the best thermodynamic fit to

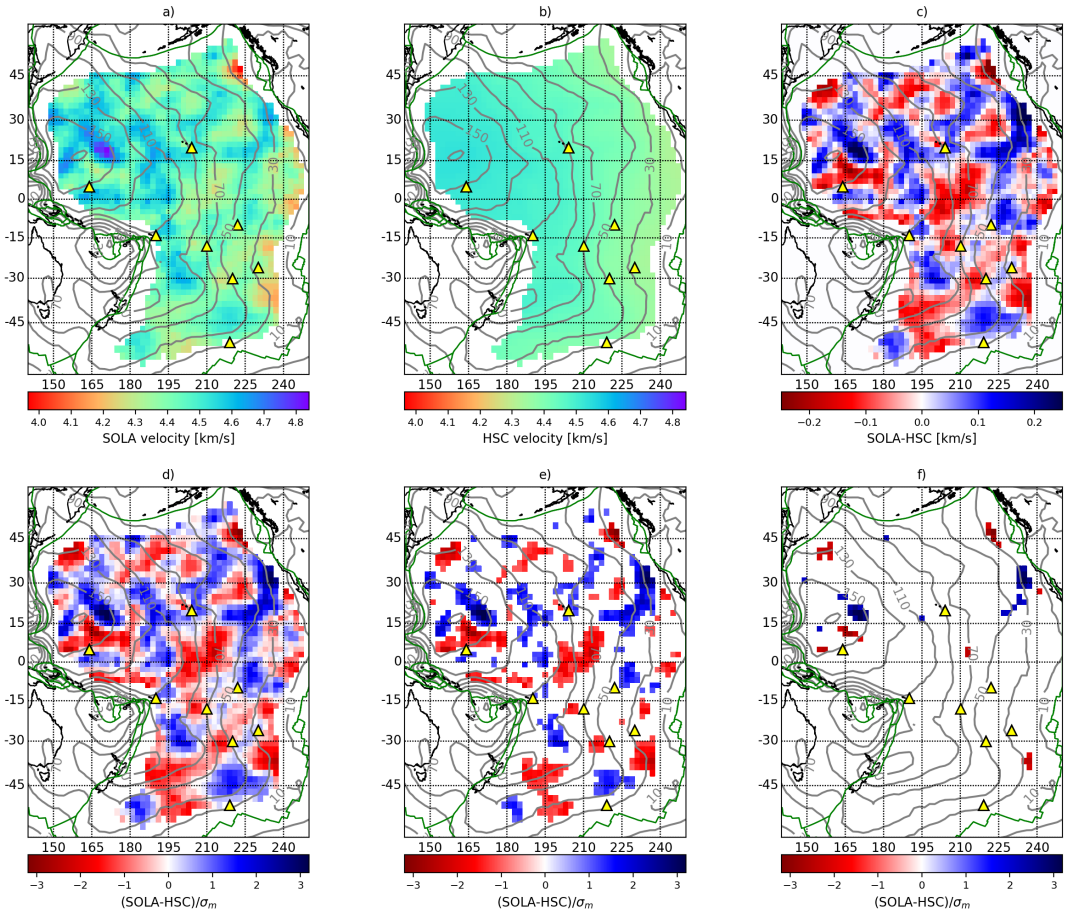

FIGURE 4.6: Comparison at 75 km depth between the SOLA tomographic model and the predictions of the half-space cooling (HSC) model from Parker & Oldenburg (1973) on the Pacific plate, excluding ridges and subduction zones. a) shear-wave velocities from SOLA; b) shear-wave velocities predicted for the HSC model; c) difference between SOLA and HSC; d) difference between SOLA and HSC scaled by the tomographic uncertainties σ_m; e) and f) same as d) but with masks to remove deviations smaller than $\pm 1\sigma_m$ or $\pm 2\sigma_m$ respectively. Grey contour lines indicate lithosphere age from Müller et al. (2008) and yellow triangles locate hot-spots from Courtillot et al. (2003).

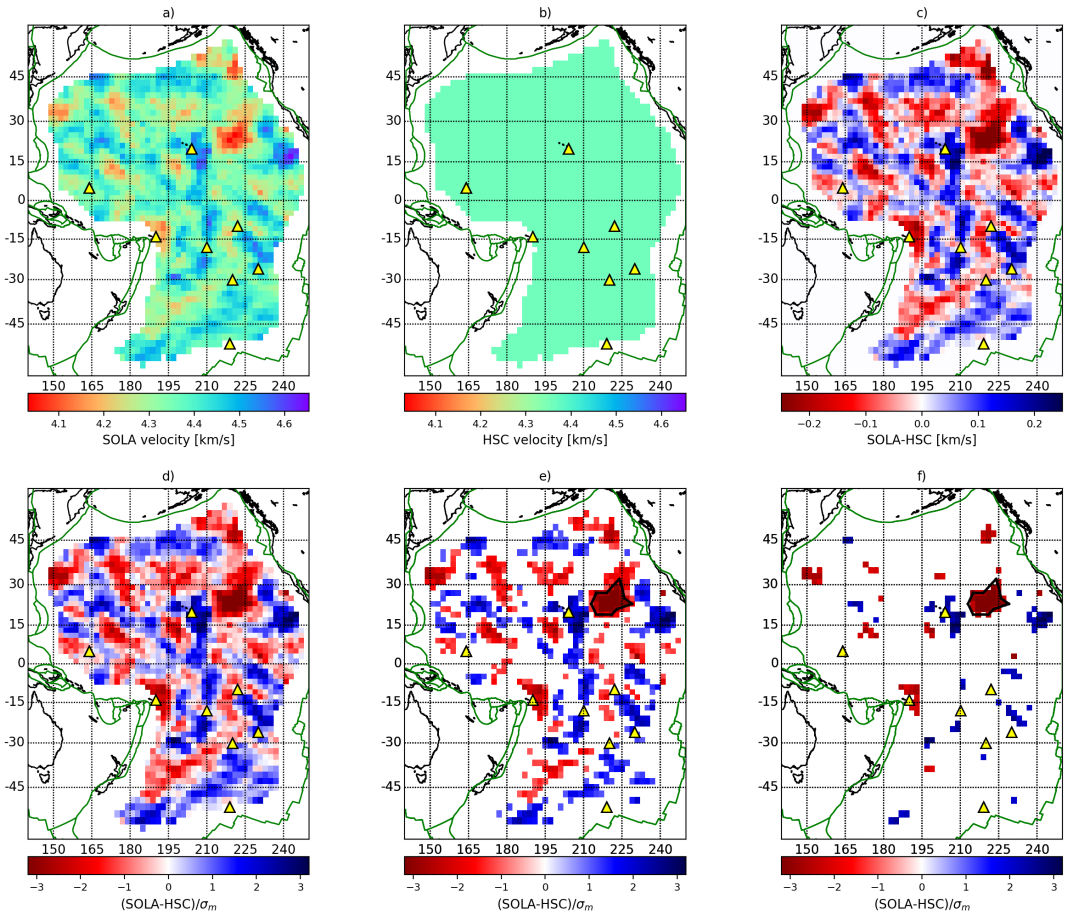

FIGURE 4.7: Same as Fig. 4.6 but at 200 km depth (note that at this depth the HSC model shows no age-dependence). The black line indicates the contour of the anomaly located to the north-east of Hawaii.

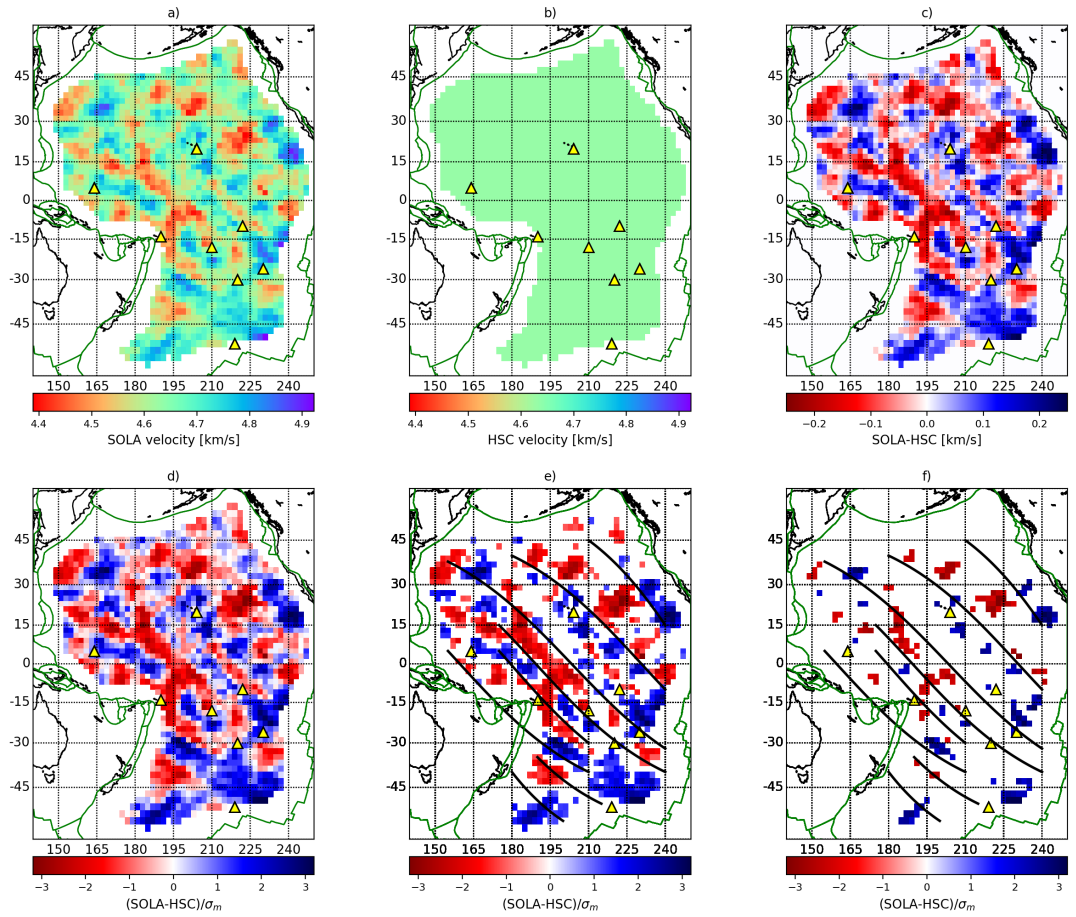

FIGURE 4.8: Same as Fig. 4.6 but at 275 km depth. The black lines indicate low velocity anomalous bands (the lines follow approximately the zeroes between anomalous bands).

the ocean-cooling problem, but because it has the fewest adjustable parameters. Even with an unsuitable reference model, the analysis would still be relevant as it would simply lead us to state that the tomographic velocities differ significantly from the reference model.

The half-space cooling model describes the lithosphere as an infinite half-space of thermal diffusivity k that cools from a starting temperature Θ_m. It predicts the temperature of the lithosphere as a function of age t and depth z from the following expression:

$$\Theta(t,z) = \Theta_m \text{erf}\left(z\sqrt{\frac{1}{4kt}}\right), \tag{4.8}$$

where erf stands for the error function. We take $\Theta_m = 1300°C$ and $k = 1.10^{-6}\text{m}^2\text{s}^{-1}$, as suggested by Ritzwoller, Shapiro & Zhong (2004). We turned this expression into temperature maps at each depth by relating age to geographic position using the age model of Müller et al. (2008), then projected them onto our tomographic grid: the predicted temperature in cell j at depth z is given by $\Theta_j(z) = \Theta(t_j, z)$, where t_j is the average age of cell j.

We then had to relate temperatures predicted as a function of position with tomographic images that contained velocity estimates representing finite-resolution local averages. In order to make meaningful comparisons, we needed to account for this resolution and consider equivalent local averages of the predicted temperatures rather than the temperatures themselves. We obtained these local temperature averages using the resolution matrix : $\widetilde{\Theta_k}(z) = \sum_{j=1}^{M} R_j^{(k)}(z)\Theta_j(z)$, a procedure known as *tomographic filtering* (e.g. Ritsema, McNamara & Bull, 2007a; Simmons et al., 2019).

In order to convert the locally-averaged predicted temperatures to shear-wave velocities, we needed to make some assumptions about the relationship between these two physical quantities that were at least partially supported by rock physics. We assumed that, in regions distant from both ridges and subduction zones, mantle temperature and shear-wave velocities were linearly related (e.g. Chen et al., 1996; Foulger, 2011, section 5.1.2 pp. 147). We therefore performed a linear regression between the locally-averaged temperature maps and our tomographic images to obtain locally-averaged predicted shear-wave velocities. In the following, we will refer to this predicted shear-wave model as the HSC (Half Space Cooling) reference model.

Figs 4.6(a) and (b), 4.7(a) and (b), and 4.8(a) and (b) show comparisons between the SOLA tomography results and the HSC model predictions at 75 km,

TABLE 4.2: Proportion of points remaining after masking values within the $1\sigma_m$ or $2\sigma_m$ error bar(s) at various depths. For a normal distribution, we would expect proportions of 0.32 for $1\sigma_m$ and 0.05 for $2\sigma_m$.

Depth (km)	50	75	100	150	200	250	300	350	400
For $1\sigma_m$	0.32	0.33	0.33	0.33	0.38	0.41	0.46	0.49	0.43
For $2\sigma_m$	0.06	0.03	0.03	0.07	0.09	0.10	0.14	0.13	0.12

200 km, and 275 km depth on the Pacific plate. Unsurprisingly, the HSC predictions look like the long-wavelength component of the tomographic images. The lithospheric cooling signature is visible at 75 km depth, but absent below the deepest extent of the oceanic lithosphere (∼150 km).

4.4.2 Deviations from the reference model

Figs 4.6(c), 4.7(c), and 4.8(c) show the differences between the tomographic model and the HSC reference model at 75 km, 200 km, and 275 km depth. Red anomalies correspond to areas where the tomographic model is slower than HSC; blue anomalies correspond to areas where the tomographic model is faster than HSC. We used the model uncertainties to assess the significance of these anomalies. Panels (d) of the same figures show the deviations from the reference model scaled by the uncertainties. A region could be considered anomalous with a confidence threshold of 68% if the velocity difference with respect to the reference model exceeds the tomographic uncertainties by more than $\pm 1\sigma_m$ (panels (e) of the same figures). A region could be considered anomalous with a confidence threshold of 95% if the velocity difference with respect to the reference model exceeds the tomographic uncertainties by more than $\pm 2\sigma_m$ (panels (f) of the same figures). Since the estimation of the data uncertainties could be improved, so could the model uncertainties, we present $\pm 1\sigma_m$ and $\pm 2\sigma_m$ maps to appreciate a range of uncertainties.

However, just identifying anomalies as exceeding $\pm 1\sigma_m$ or $\pm 2\sigma_m$ is not enough to declare them *significant*, because even if the Earth were in reality identical to the prediction of the half-space cooling model, we would still expect 32% of points in a tomographic model with uncertainties σ_m to exceed $\pm 1\sigma_m$ and 5% of them to exceed $\pm 2\sigma_m$. We could be justified in declaring anomalies to be *significant* only if more points than expected exceed the $\pm 1\sigma_m$ and $\pm 2\sigma_m$ thresholds, or if these points organized geographically in coherent regions and these anomalous regions could indeed be resolved by the tomography (anomalies larger than the resolving lengths). This definition of significance is stricter than the one used in

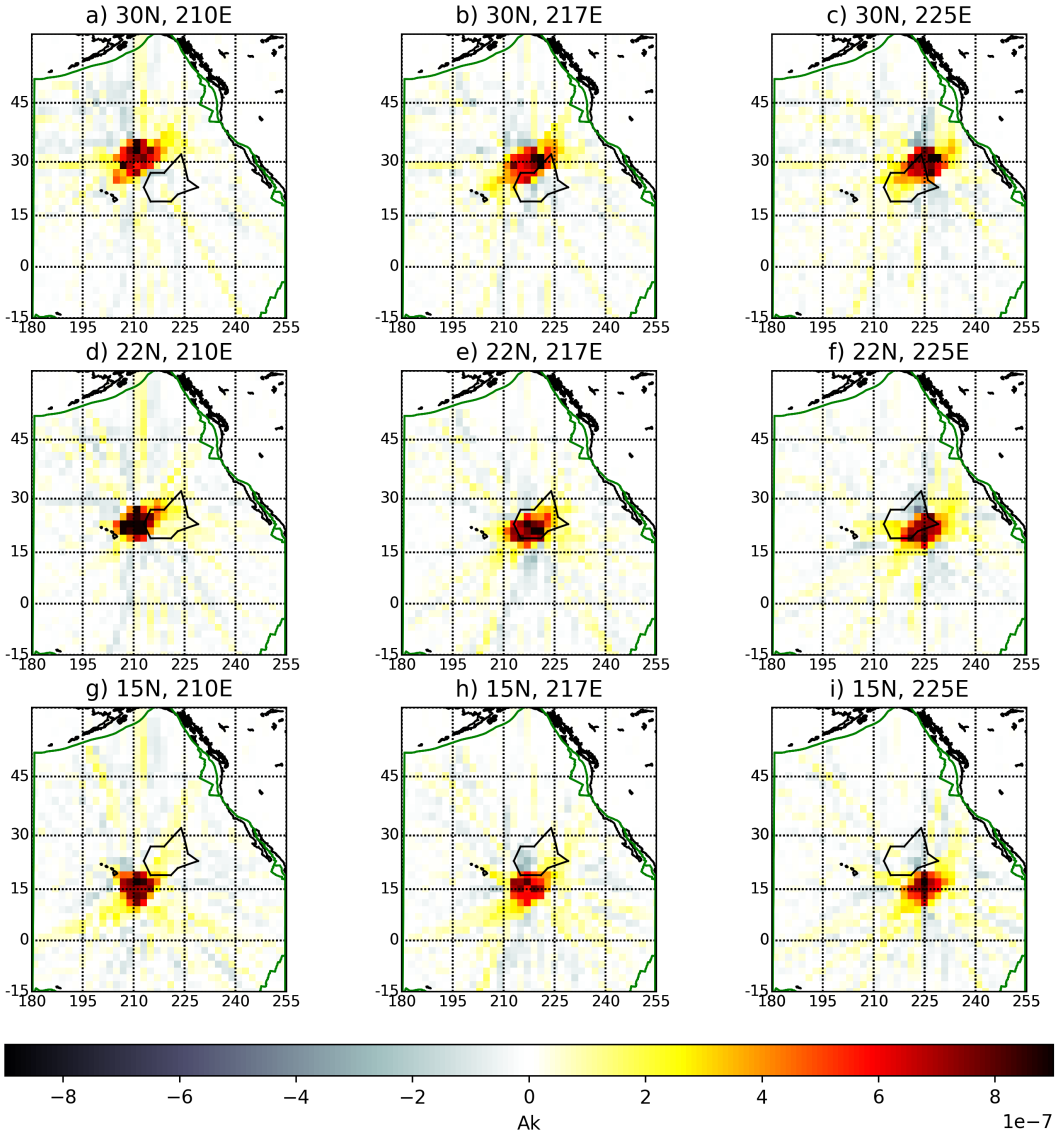

FIGURE 4.9: Selection of averaging kernels around the slow velocity anomaly located to the north-east of Hawaii (see Fig. 4.7) at 200 km depth. The black line represents the anomaly contour.

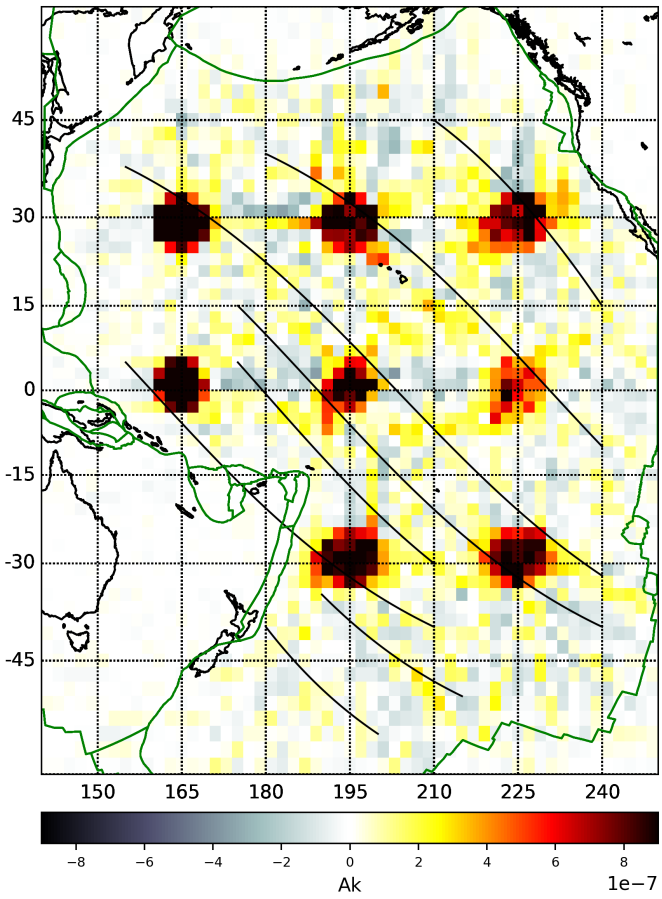

FIGURE 4.10: Selection of averaging kernels in the Pacific at 275 km depth. The black lines represent the pattern of anomalous velocity bands observed on Fig. 4.8. The averaging kernels are located at: (30N, 165E), (30N, 195E), (30N, 225E), (0N, 165E), (0N, 195E), (0N, 225E), (-30N, 165E), (-30N, 195E), (-30N, 225E). For convenience, we plot the averaging kernels on the same map.

most tomographic studies, including Maggi et al. (2006b), and underlines the importance of correctly estimating the data uncertainties that feed into the estimates of σ_m.

Table 4.2 shows the proportion of points that remain in the tomographic models after applying the $\pm 1\sigma_m$ and $\pm 2\sigma_m$ masks: at lithospheric depths, the proportions of such points do not exceed greatly the expected ones (0.32 and 0.05); however, as depth increases, so do the proportions of points exceeding the $\pm 1\sigma_m$ and $\pm 2\sigma_m$ levels. In section 4.2.1 we discussed that the data-uncertainties from Maggi et al. (2006b), and hence our estimates of σ_m, may have been underestimated especially below $\sim$ 300 km. For this reason, we have limited our analysis of significant anomalies to depths shallower than $\sim$ 300 km.

4.4.3 Significant anomalies

At lithospheric depths (75 km), the proportion of points still visible in the tomographic image after applying the $\pm 1\sigma_m$ and $\pm 2\sigma_m$ masks is not significant (see Table 4.2). What about the geographic distribution of these points? Figs 4.6(e) and (f) shows that the positions of unmasked low-velocity anomalous regions at 75 km depth do not correlate with hot-spot locations published by Courtillot et al. (2003), and that anomalies that exceed the $\pm 2\sigma_m$ thresholds are much smaller than the correlation lengths from Fig. 4.3(d). We therefore concluded that the lithosphere corresponding to the Pacific plate contains no significant shear-wave anomalies with respect to predictions made by the half-space cooling model, at least given the data set of Maggi et al. (2006b).

At shallow asthenospheric depths (200 km), a greater proportion of points remains in the masked tomographic images (see Table 4.2 and Figs 4.7e and f). A strong low velocity anomaly appears to the north-east of Hawaii at 20°N 220°E. This anomaly of 12° ($\sim$ 1400 km) radius is visible between 125 km and 250 km depth, and is about 0.25 km/s slower than the half-space cooling model (stronger than -3σ_m). Not only is the anomaly strong, it is also larger than the local resolution length of 750 km (Fig. 4.5a). Fig. 4.9 shows individual averaging kernels within and around the anomaly: the kernels are all of similar size or smaller than the anomaly and are all well focused, indicating absence of smearing. Given the amplitude and size of the anomaly with respect to the tomographic model's uncertainty σ_m and its resolution length, we considered it to be *significant*. We need to carefully analyse averaging kernels when interpreting the size and shape of

anomalies. Since the averaging kernels are spread in space, the velocity anomalies tend to appear larger than they really are. The shape of the anomaly in the tomographic image can also be misleading. For example the anomaly to the north-east of Hawaii shows two bumps, one to the north and one to the east, which may be due to the complex shape of the averaging kernels, or to data noise propagated into the model. Only features outside the uncertainty range with size greater than the resolution should be interpreted.

Deeper in the asthenosphere, a pattern of alternatively slow and fast velocity bands appears, oriented approximately south-east to north-west (Fig. 4.8). The bands are approximately 15° wide (∼1700 km), 70° (∼8000 km) long, and are visible between 275 km and 400 km depth. The bands seem to follow the absolute plate motion of the Pacific plate (e.g. Gripp & Gordon, 1990). They also resemble the bands observed by French, Lekic & Romanowicz (2013a) at depths between 200 km and 350 km and the low anisotropy channels observed at 100 km depth by Montagner (2002). The width and length of these bands are greater than the resolution length. To exclude possible smearing, always an issue when tomographic images show elongated features, we have shown several averaging kernels in Fig. 4.10. Given the amplitude and size of the highly-correlated bands and the focused nature of the averaging kernels, we again considered these bands to be *significant* features of the tomographic model.

4.5 Discussion

We have produced a tomographic model of shear-wave velocities in the Pacific upper mantle using the SOLA Backus-Gilbert method (Zaroli, 2016; Zaroli, Koelemeijer & Lambotte, 2017), and have shown how to exploit the full model resolution and uncertainty information to evaluate the true significance of deviations from a theoretical prediction.

4.5.1 Model statistics – a rare commodity

Several authors have inverted surface-wave data to obtain velocity models of the upper mantle, either globally or in the Pacific, using different forward theories and inversion methods (e.g. Zhou et al., 2006; Ekström, 2011; French, Lekic & Romanowicz, 2013a; Liu & Zhou, 2016a; Isse et al., 2019). Although they agree with each other at large scales, they often display different local features. These discrepancies may be partly explained by the differing data-sets (fundamental-mode Rayleigh waves, multi-mode Rayleigh waves, or full-waveforms) and inversion

schemes, but may also be due to the complex relationship between the heterogeneous path coverage of the Pacific region, irregular resolution, and data-errors.

Without full resolution and uncertainty information – model statistics – we cannot give strong quantitative arguments for or against the significance of any small-scale feature of a tomographic model (e.g. Foulger et al., 2013). Unfortunately, most damped-least-squares or iterative conjugate-gradient inversion do not provide model statistics or control them during the inversion, as they focus instead on minimising the misfit between observed measurements and those predicted by the tomographic model. It is possible to approximate the model statistics for these inversion schemes (see for example Rawlinson et al., 2014; Rawlinson & Spakman, 2016, for reviews of various techniques), but such methods are rarely used in practice as they are computationally costly and often provide only crude estimates of the model statistics. For the tomography problem considered here, it would indeed be possible to explicitly compute the $G^{\dagger}$ matrix from a 'traditional' damped-least-squares inversion and then propagate the data uncertainties into model uncertainties; but the advantage of the SOLA method is that it allows a direct control on the model resolution and uncertainties.

4.5.2 Advantages of Backus-Gilbert type inversions

Beyond delivering model resolution and uncertainties at no extra cost, there are other important advantages of using inversion schemes based directly on the model statistics, such as those proposed by Backus & Gilbert (1967), Backus & Gilbert (1968), and Backus & Gilbert (1970), Pijpers & Thompson (1992) and Pijpers & Thompson (1993), Zaroli (2016), and Zaroli, Koelemeijer & Lambotte (2017). Firstly, these inversion schemes constrain model uncertainties to vary smoothly over the parameter space. Secondly these schemes drive the inversion to produce well-focused local averages (averaging kernels) that limit smearing along predominant paths (with SOLA this requires imposing well-focused target kernels, in our case circular ones). Thirdly, these schemes guarantee that the weights of the local averaging kernels (i.e. the rows of the resolution matrix) sum exactly to one, thereby eliminating the averaging bias that occurs with heterogeneous spatial distributions of data.

4.5.3 Model statistics – required for tomographic filtering and evaluating significance

Before comparing two different tomographic models, or a tomographic model to other data with different spatial resolution, we need to homogenize their resolutions, a process called *tomographic filtering* (Ritsema, McNamara & Bull, 2007a; Simmons et al., 2019). This requires the knowledge of the full resolution matrix. In our study, we considered a simple temperature model of lithosphere cooling based on the half space cooling model of Parker & Oldenburg (1973) that we filtered to the resolution of the tomographic model. Because the temperature model was very smooth, the tomographic filtering had only a minor effect. However, such filtering would be critical when comparing tomographic images with sharper models (Mégnin et al., 1997; Simmons et al., 2019; Freissler et al., 2020).

To assess if some parts of a tomographic model significantly deviate from some reference we need to know the model uncertainties at each location. Because we had this information, we were able to mask deviations from the half-space cooling predictions that were smaller than $\pm 1\sigma_m$ and $\pm 2\sigma_m$ and argue for the significance of certain anomalies. The process we illustrated in section 4.2.2 could replace statistical appraisal techniques and other tomographic resolution tests that are not always well understood (Lévêque, Rivera & Wittlinger, 1993; Rawlinson et al., 2014; Rawlinson & Spakman, 2016).

4.5.4 Two significant anomalies in the Pacific region

We have focused on the significance of two anomalies: a low-velocity anomaly located to the north-east of Hawaii at 200 km depth and coherent bands of fast and slow velocities at 275 km depth.

Anomaly NE of Hawaii

This emerges strongly from the background with an amplitude about 0.25 km/s slower than the average shear-wave velocity of the Pacific plate, where the uncertainty is around 0.07 km/s, thus corresponding to about -3σ_m (Figs 4.7e and f). Despite using the same data-set, the model produced by Maggi et al. (2006b) shows a much weaker anomaly at the same location, probably because it was smoothed out by their damped-least-squares inversion and regularization. This anomaly has also been seen, though at weaker amplitudes than in this study, in tomographies constructed using fundamental mode Rayleigh waves with a finite-frequency scheme (Liu & Zhou, 2016a) or multi-mode Love and Rayleigh waves

(Isse et al., 2019), while it was entirely missed by the GDM52 model of Ekström (2011) based on fundamental mode Love and Rayleigh wave dispersion data. Given the different data-sets, forward theories, inversion and damping schemes of these studies, it is hard to pinpoint the reason for their weaker anomaly, but we speculate that the anomaly was probably over-smoothed by the regularization of their inversions.

Coherent SE-NW bands

We see these alternating fast and slow bands emerging from the background at 275 km depth with deviations from HSC up to ± 0.25 km/s ($\pm 1\sigma_m$ and $\pm 2\sigma_m$, see Fig. 4.8). Maggi et al. (2006b) do not show these bands in their 275 km depth image, suggesting that the SOLA inversion scheme was able to extract more information from the same dataset. Other studies have observed similar patterns: Ekström (2011) show a very weak pattern in their isotropic results, probably because fundamental-mode surface waves are only weakly sensitive at these depths; French, Lekic & Romanowicz (2013a) see a stronger pattern with their full-waveform inversion; and, intriguingly, Liu & Zhou (2016a) show similar bands in their dispersion maps at 30s and 50s, which are sensitive to much shallower depths.

4.5.5 Limits and perspectives

The SOLA inversion seems promising because it gives a way to control the model statistics (uncertainties and resolution) and to obtain them explicitly. The main problem is that it assumes the forward problem is linear while surface-wave physics is not (the dispersion characteristics of surface-waves are non-linearly related to the shear-wave velocity as a function of depth). In this study, as in Maggi et al. (2006b), each depth in the tomographic model was inverted independently, so vertical coherence could not be imposed or evaluated using resolution kernels. Furthermore, as the inputs to the SOLA inversion were 1D path-averaged shear-wave velocity models defined on the same depth range, the geographical coverage was identical for each depth, and did not take into account the greater sensitivity to depth of some paths (illuminated by longer-period or higher-mode surface waves) with respect to others.

To obtain a fully 3D shear-wave velocity model directly from frequency dependent measurements of surface-waves in a single linear step with SOLA, and to take the full depth-sensitivity of individual measurements into account, we

would need to adopt a finite-frequency description of surface waves to help linearize the tomographic problem (e.g. Zhou, Dahlen & Nolet, 2004; Yoshizawa & Kennett, 2005). This would also allow us to obtain a fully 3D model with 3D resolution kernels, and therefore be able to apply the same statistical rigor to interpreting any vertical structures within the model (e.g. plumes, the lithosphere depth).

Like any other process, the pertinence of the SOLA outputs rest upon the quality of the inputs. In particular, the model errors we have relied upon to decide the significance of anomalies are nothing more than a propagation into the model space of the data errors. While traditional damped-least-squares schemes use data uncertainties to weigh data relatively to each other and to evaluate model quality (using χ^2_{red} measures, for example), SOLA uses them more directly to evaluate uncertainties in the model which then drive the inversion through their trade-off with resolution. In order to be able to trust the magnitude of the model errors in SOLA, it is necessary for the magnitude of the data errors to be correct. This is the reason why we upscaled the data uncertainties using the χ^2_{red} values of the damped-least-squares model of Maggi et al. (2006b); however a more rigorous assessment of the data uncertainties is still required.

Our study calls for other surface wave tomography studies based on the SOLA inversion in other regions of the world, with new data sets, and particular care in estimating data uncertainties. Our tomographic model, together with its resolution and uncertainty maps, calls for new data in the Pacific to observe other seismic velocity anomalies significant enough to be interpreted robustly.

4.6 Conclusion

Rayleigh wave tomography of the Pacific upper mantle shows large scale geological features (e.g. lithosphere cooling) but both the model uncertainties and resolution are required for interpretations at smaller scales. We exploited the SOLA tomographic inversion scheme (Zaroli, 2016) to propose a workflow to analyse the tomographic model using its resolution and uncertainties, that is:

1. Define some reference, Earth-like, physical model;
2. Filter the reference model to the tomographic resolution;
3. Compute the deviations from the reference model;
4. Normalize the deviations by the model uncertainties;

5. Mask model estimates that are within one or two error bars to focus only on significant seismic anomalies;

6. Compare those non-masked anomalies to the local resolution to discuss their resolvability and spot artifacts, if any.

In this study, we used a half space cooling description of the Pacific lithosphere as a reference model. We observed a low velocity anomaly to the north-east of Hawaii at 200 km depth and a pattern of alternatively slow and fast anomalous bands oriented approximately south-east to north-west at 275 km depth. Both features are reliable given the model statistics. Our study shows that the model statistics can be properly analysed in surface wave tomography using the SOLA inversion; the same scheme could be applied in other regions of the globe.

In this study, the data uncertainties were estimated using multiple sampling with ray paths close to each other, then upscaled because apparently underestimated. We should aim collectively to characterize more accurately uncertainties in seismological data sets - clearly a challenging but crucial task.

Data and code availability

The computer codes for the SOLA inversions and the data used in this study are available from C.Z. (c.zaroli@unistra.fr) and A.M. (alessia.maggi@unistra.fr), respectively.

Acknowledgements

The authors are grateful to Huajian Yao (editor), Frederik Tilmann, and an anonymous reviewer whose constructive comments helped to improve this paper.

Afterword

In this study we showed that the SOLA inversion provides reliable model uncertainties, resolution and model solution. We designed an interpretation workflow that accounts for the model uncertainties and resolution. Using this workflow we could discuss with statistical arguments the robustness of anomalous patterns in the Pacific upper mantle.

However the study suffers from limits that we may overcome using finite frequency theory. Applying the SOLA inversion to finite frequency surface wave tomography is the subject of the next chapter.

Chapter 5

Finite frequency SOLA tomography

To estimate resolution and uncertainty is a major task that will usually consume far more time than the actual inversion.

Nolet, *A Breviary of Seismic Tomography*, 2008.

5.1 Introduction

In the previous chapter we built a tomographic model of the Pacific upper mantle from surface wave data using the classical two-step approach. The first path-specific step was performed by Maggi et al. (2006b) with a non-linear inversion method. It produced path-averaged S-wave velocity profiles. The second step was fully linear and we applied the SOLA inversion to produce a set of two-dimensional S-wave velocity maps at various depths. The SOLA inversion proved to be powerful to extract unbiased information from the data and to produce useful model statistics (uncertainties, resolution) to robustly interpret the model solution. However the study suffered from strong limits: (1) data uncertainty estimates were poor and (2) the SOLA inversion could only be two-dimensional (no vertical constraint).

In the second part of chapter 2 I described an extension of ray-theory to laterally heterogeneous media. Using the Born approximation, this finite frequency theory relates phase delays to the three-dimensional S-wave velocity: it embeds the two steps of the two-step approach into a single linear step. In this chapter I combine this three-dimensional forward theory and the SOLA inversion scheme. Red boxes (as box 1) at the end of the chapter contain details about the computer programs developed for this study. If the computational background is of no interest for the reader they can be ignored without missing the main messages of the chapter.

Figure 5.1 illustrates the workflow for this chapter (see also Box 2). First I describe the measurement process developed to build a phase delay database: I show how I produced synthetic waveforms for a radial Earth model (section 2.1), how I measured phase delays (section 2.2), and how I estimated data uncertainty (section 2.3). Then I describe the tomographic setup I used to invert the phase delays; it includes the construction of the three-dimensional sensitivity kernels (section 3.1) and target resolution (section 3.2). Section 4 is dedicated to a synthetic tomography: I invert phase delays measured on synthetic waveforms that I obtained for a known three-dimensional model of the Earth.

5.2 Data and data uncertainties

In this section I show how to construct synthetic waveforms for a radial reference model using the routines from Masters, Misha & Susan (2014). I also describe how I measured phase delays and estimated data uncertainties.

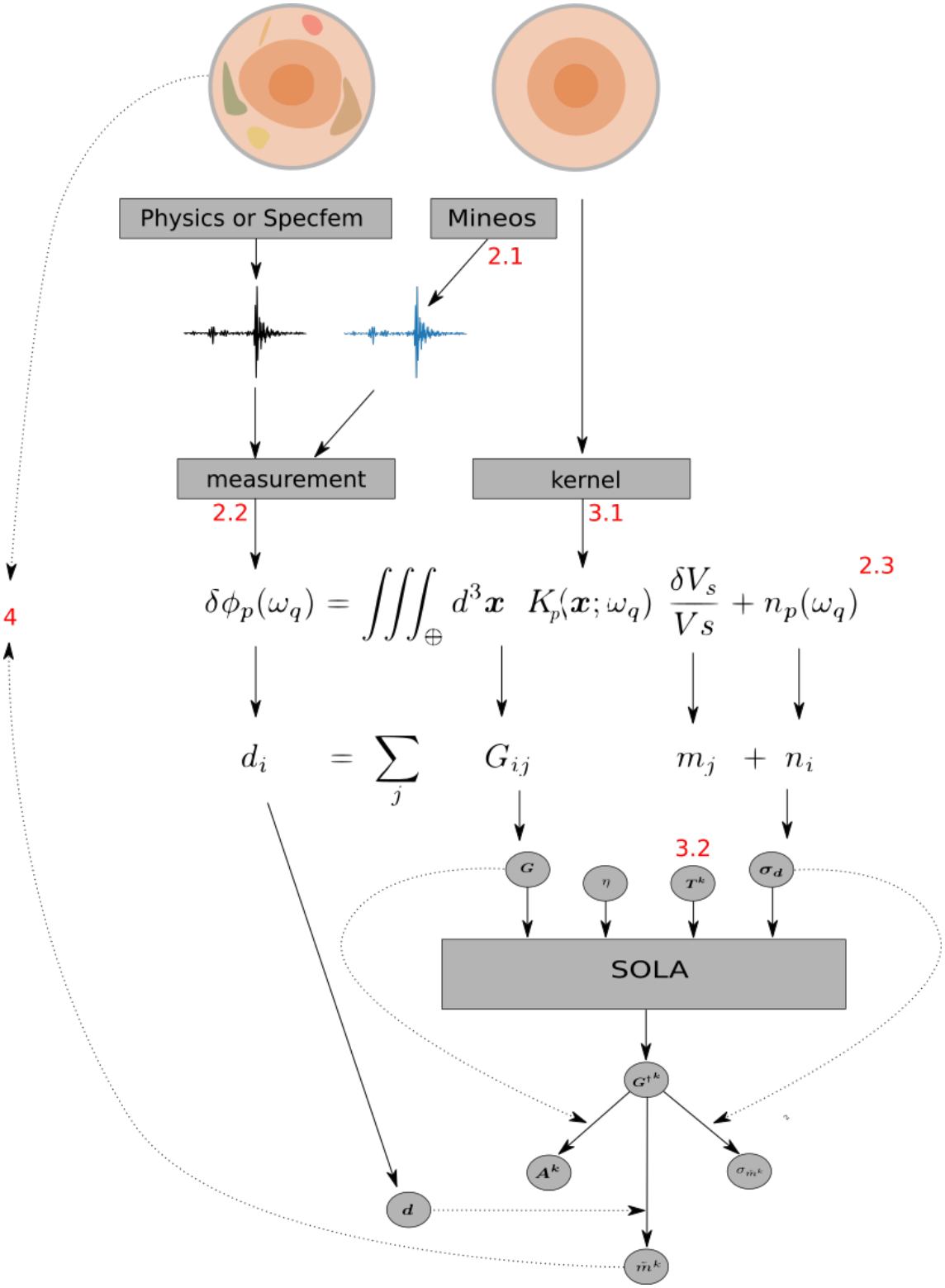

FIGURE 5.1: Workflow for the chapter. Numbers in red indicate the sections where the topic is discussed. From the Earth structure (or an arbitrary input three-dimensional model of the Earth) waveforms are generated. From a radial reference model synthetic waveforms are produced. A phase delay $\delta\phi$ is measured for each source-receiver pair p and frequency ω_q; and data uncertainties σ_d are estimated. Three-dimensional sensitivity kernels K_p are also built for the reference model and a three-dimensional target resolution $\boldsymbol{T}^{(k)}$ is set up. Finally the workflow is applied for a known three-dimensional model of the Earth to investigate to what extent our tomographic process developed allows to make inferences about the input model.

5.2.1 Synthetic waveforms

The very first step to build the synthetic waveform (Box 4) is to determine the normal mode solutions for a given radial reference Earth model. In this study the reference model used is *CPacific*. It can be found in the *MINEOS* normal mode package (Masters, Misha & Susan, 2014). It corresponds to some location in the Central Pacific (the last layer of the model is therefore an ocean layer). The distribution with depth of the vertically and horizontally polarized P and S waves, as well as the density and bulk and shear attenuations of this model are drawn on figures D.1 and D.2 in appendix D.2.

As I have restricted the analysis to the vertical component of Rayleigh waves, only eigenfunctions of displacement corresponding to the spheroidal modes need to be computed. The dispersion diagram (the phase velocity as a function of frequency) and some functions of displacement ${}_nU_l$ for various angular orders n and harmonic degrees l are given in chapter 2. As discussed in chapter 2, normal modes can be interpreted in terms of surface waves in the limit $l/4 \gg n$. Therefore the computation of the normal mode solutions should be restricted to the first overtones (e.g. $n \leq 3$). We also discussed the difficulty of observing overtones. Compared to the fundamental modes their amplitude is usually lower and they tend to interfere. Therefore I further restricted my work to the fundamental modes only and I plan to integrate higher modes in the future. I have also limited the computation to angular orders l corresponding to the frequency band from 0 to 80mHz. In this band surface waves have little attenuation so that they can be observed at distances relevant for this study (in the order of thousands of kilometers).

Using the eigensolutions the green function observed at a seismic station location can be computed for a point source at some seismic source location. Then, the green function is convolved with the seismic source moment tensor and source time function to get the full response to the seismic source. An approximate description of seismic events can be obtained from the Global Centroid Moment Tensor (GCMT) catalog (Dziewonski, Chou & Woodhouse, 1981; Ekström, Nettles & Dziewoński, 2012). The catalog provides the source location, time and moment tensor for earthquakes that occured from 1977 up to present with magnitude greater than 5. It also provides uncertainty estimates. Detailed information for seismic stations can be obtained from the Incorporated Research Institutions for Seismology (IRIS). Their data service provides the station metadata, i.e. the channels orientations, operational time, locations and instrumental responses (see also Box 3). The vertical component synthetic and observed waveforms for a source-receiver pair is given on figure 5.2 in various frequency bands. Though

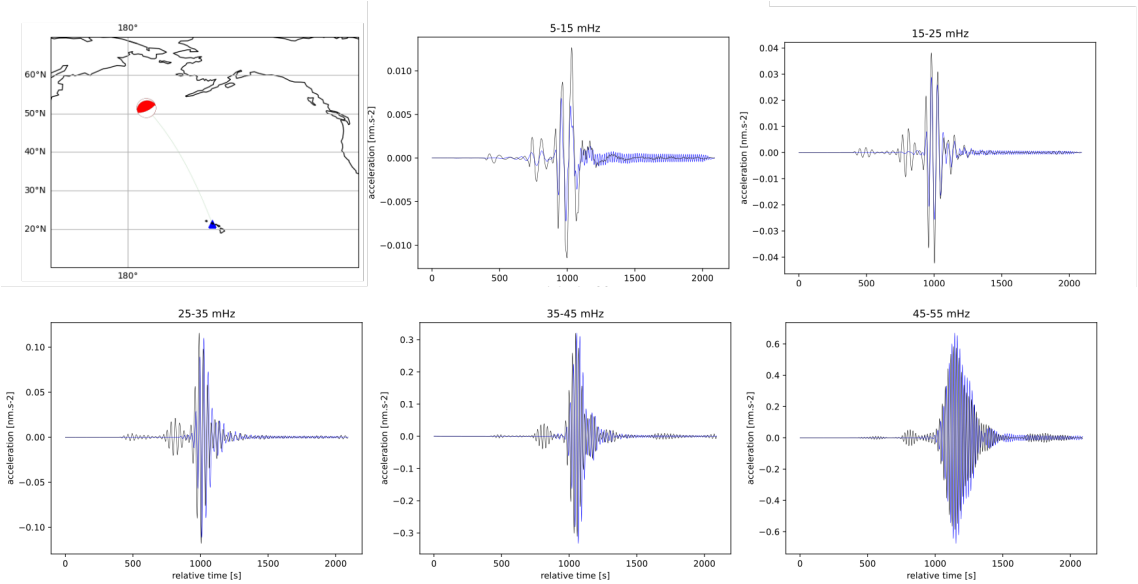

FIGURE 5.2: The first subpanel is a map showing the seismic source with GCMT name C201308301625B (red beachball), the seismic station KIP (blue triangle) and the great-circle connecting them (green line). The other captions are the synthetic (blue) and observed (black) waveforms. The waveforms have been sliced from the event origin time to around 2000s after the event, tapered with a Hann taper and filtered in the frequency bands indicated in the title of each subpanel.

the observed waveform contains more details that the synthetic one, the normal modes prediction is a good representation of the observation. Parameters for the sources and stations used to illustrate this chapter are given in appendix D. Note that since the last layer of the reference model is an ocean but the seismic stations are on land, I set them at the bottom of the ocean.

The crust is known to be highly heterogeneous and to strongly affect the measurements, and potentially in a non-linear way (e.g. Marone & Romanowicz, 2007; Bozdağ & Trampert, 2008; Panning, Lekić & Romanowicz, 2010; Liu & Zhou, 2013). However, in the framework of this study, it is not possible to model the crust in the inversion (e.g. coarse gridding, poor constraints) and neither the forward problem nor the SOLA inversion that we use in this study can handle non-linear processes. Therefore it is necessary to apply some crustal correction to remove the effect of the crust from the data and do not get its contribution in the tomographic model. The crustal correction I use is estimated in the framework of ray theory using the crustal model *CRUST1.0* (Laske et al., 2013). For each source-receiver pair, I use a path-specific radial reference model that is just the common reference model *CPacific* with the crustal model averaged along the path on top. I assume that the synthetic waveform computed for such a model

contains the information about the crust so that the phase delay between the synthetic and observed waveforms does not depend on the crust. This holds to the extent that *CRUST1.0* is a good crustal model and is strictly applicable only in the ray approximation. In the future, more elaborated crustal corrections could be applied to tackle these limits.

5.2.2 Phase delay measurement

We may write the synthetic waveform $s(\omega) = A(\omega)\exp^{\phi(\omega)}$ and the observed waveform $o(\omega) = A^o(\omega)\exp^{\phi^o(\omega)}$; where $A(\omega)$ is the amplitude, $\phi(\omega)$ is the phase and the superscript ^{o} stands for 'observed'. The phase is the sum of various components: $\phi = \phi_s + \phi_r + \phi_c + \phi_p$ (e.g. Ekström, 2011; Ma et al., 2014; Moulik et al., 2021); where ϕ_s is the source phase, ϕ_r is the phase of the receiver, ϕ_c is the static phase that comes from caustics and ϕ_p is the phase accumulated during the propagation from the source to the receiver. The synthetic waveforms account for all these components (ϕ_s from the moment tensor, ϕ_r from the channel orientation, ϕ_c from the Maslov index and ϕ_p from the normal modes solution). If we assume that the source and station characteristics are perfectly known (or that errors fall into some uncertainty estimates), subtracting the phase of the observed and synthetic waveforms leaves only a perturbation in the propagation component: $\delta\phi = \phi^o - \phi = \phi_p^o - \phi_p$. $\delta\phi$ is the observable for which the sensitivity kernels were derived in chapter 2 and measuring it is the subject of this section (see also Box 5).

Preprocessing

Before performing the measurements, a waveform pre-processing and a time window selection step is required. Since the synthetic waveforms do not contain the instrumental response it is necessary to remove it from the observed waveforms. Then the observed waveforms need to be resample to the same sampling rate as the synthetics (1 Hz).

Next it is necessary to restrict the analysis to a narrow time window that contains only the information relevant given the forward theory. For example, when measuring for a particular surface wave mode, one needs to define a time window that excludes other modes (that are more or less separated as discussed in chapter 2). In this chapter the measurement is restricted to the fundamental modes only. The time window is chosen centered on the group arrival time (which depends on the frequency considered) with a 801s length. The group velocity is computed for the fundamental modes in the reference model and the

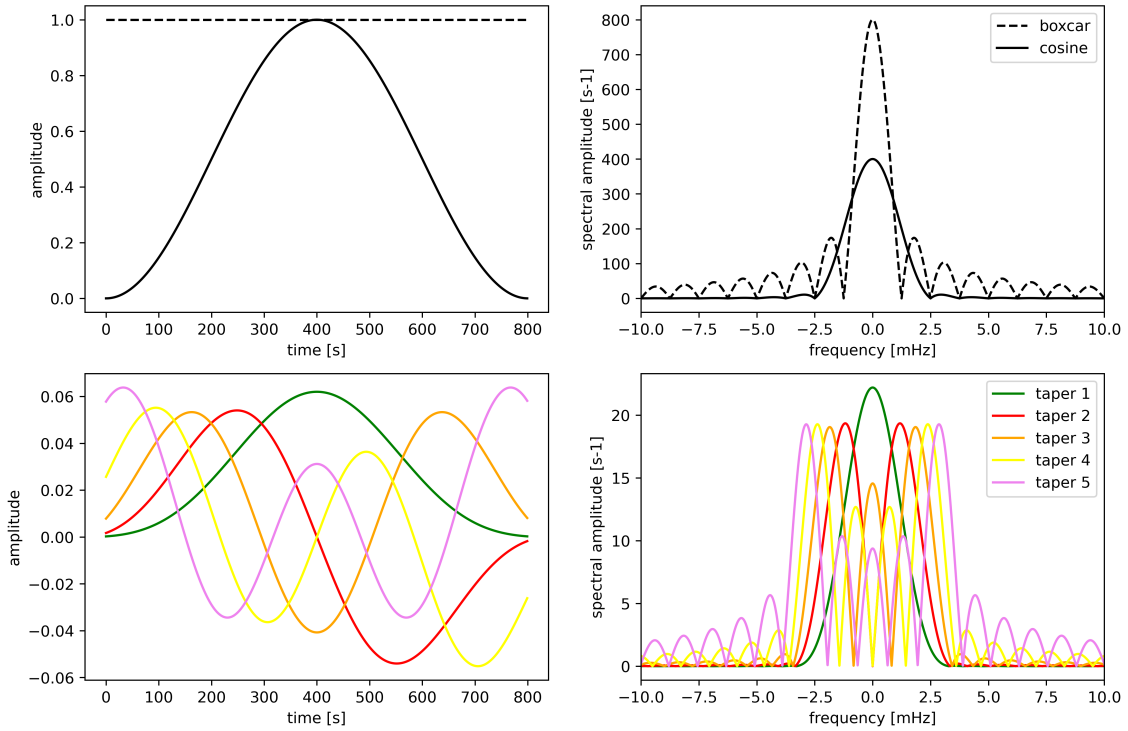

FIGURE 5.3: Examples of tapers in the time domain (left) and their amplitude spectrum in the frequency domain (right). Top: boxcar and cosine tapers, bottom: the first five Slepians used in this chapter.

group arrival time is predicted from the source-receiver distance. Any linear trend or mean is removed from the sliced observed and synthetic waveforms.

Observing the data in a time window is equivalent to applying a taper, i.e. multiplying the waveform $s(t)$ with some function of time $h(t)$. When slicing the data, the taper is a boxcar function that is zero everywhere except in the defined time window, as represented by the dashed black line on figure 5.3 (upper-left). Multiplying the signal with the taper in the time domain is equivalent to convolution in the frequency domain, i.e. the spectrum of the tapered data is $s_h(\omega) = s(\omega) \otimes h(\omega)$. If the taper has a wide spectrum, it averages distant frequencies from the spectrum of the original waveform. Since distant frequencies *leak* into other frequencies, this effect is refered to as *frequency leakage*. For example the boxcar function has a spectrum with significant *sidelobes* (figure 5.3 dashed line upper right) so that frequency leakage involves very distant frequencies. Simply slicing the waveforms, i.e. applying a boxcar taper, would be a very bad choice. Therefore the sliced waveforms are tapered with another time function, like the cosine taper (solid lines on top of figure 5.3), that has a narrower frequency spectrum so that it leads to spectrum estimates with less frequency leakage. Unfortunately the cosine taper is not constant in time, it reduces the

weight of the time series far from the center of the time window which biases the measurement. While choosing a taper, there is a tradeoff between frequency leakage in the frequency domain and bias in the time domain.

To overcome this issue, Thomson (1982) proposed to use the first few of an infinite series of tapers, that have optimal frequency spectrum and that weight different parts of the waveform. These tapers, called *discrete prolate spheroidal sequences*, or *Slepians* from its discoverer Slepian (1978), are orthogonal to each other. The Fourier transform is computed using each of these tapers and optimal estimates (in term of frequency leakage) with reduced bias (because the use of several tapers illuminates well the whole waveform) are obtained by averaging. This approach has been applied with short period data (e.g. Park, Lindberg & Vernon, 1987; Park, Vernon & Lindberg, 1987) and surface waves data (e.g. Laske, Masters & Zu¨rn, 1994; Laske & Masters, 1996; Hjorleifsdottir, 2007). Finite-frequency surface wave tomography also includes the possibility to use the multitaper technique (e.g. Zhou, Dahlen & Nolet, 2004; Zhou, 2009a) and we take advantage of it in the measurement process designed for this study. With a 1 Hz sampling rate and 801 seconds-long time series we should use the first five Slepians (see Percival & Walden, 1993, section 7, pp. 331 for statistical arguments). Figure 5.3 (bottom) shows these tapers in the time and frequency domains. The measurement process described in the following is applied to each tapered waveform.

Measurement

As the phase delay depends on frequency, the measurement workflow described here is applied for a series of frequencies, ranging from 10 to 50 mHz by steps of 1 mHz. First the tapered waveforms are bandpass filtered in a 10mHz-large frequency band centered on the measurement frequency. The waveforms are also normalized to remove any effect of amplitude differences on the measurement. Filtered waveforms at various frequencies for the first two tapers are drawn on figure 5.4. The observed signal is best represented by the synthetic for the first taper at low frequencies. As frequency increases the synthetic waveform gets more delayed. It also seems to be delayed by more than a complete phase cycle (2π radians) after 40mHz. Moreover, early in the time window, we observe some wingles in the observed waveforms but not in the synthetic ones. This is the first overtone but its effect is attenuated by the shape of the first taper. In this case the time window has been well chosen to favor the fundamental mode. The fit between the synthetic and observed waveforms is much poorer for the second taper

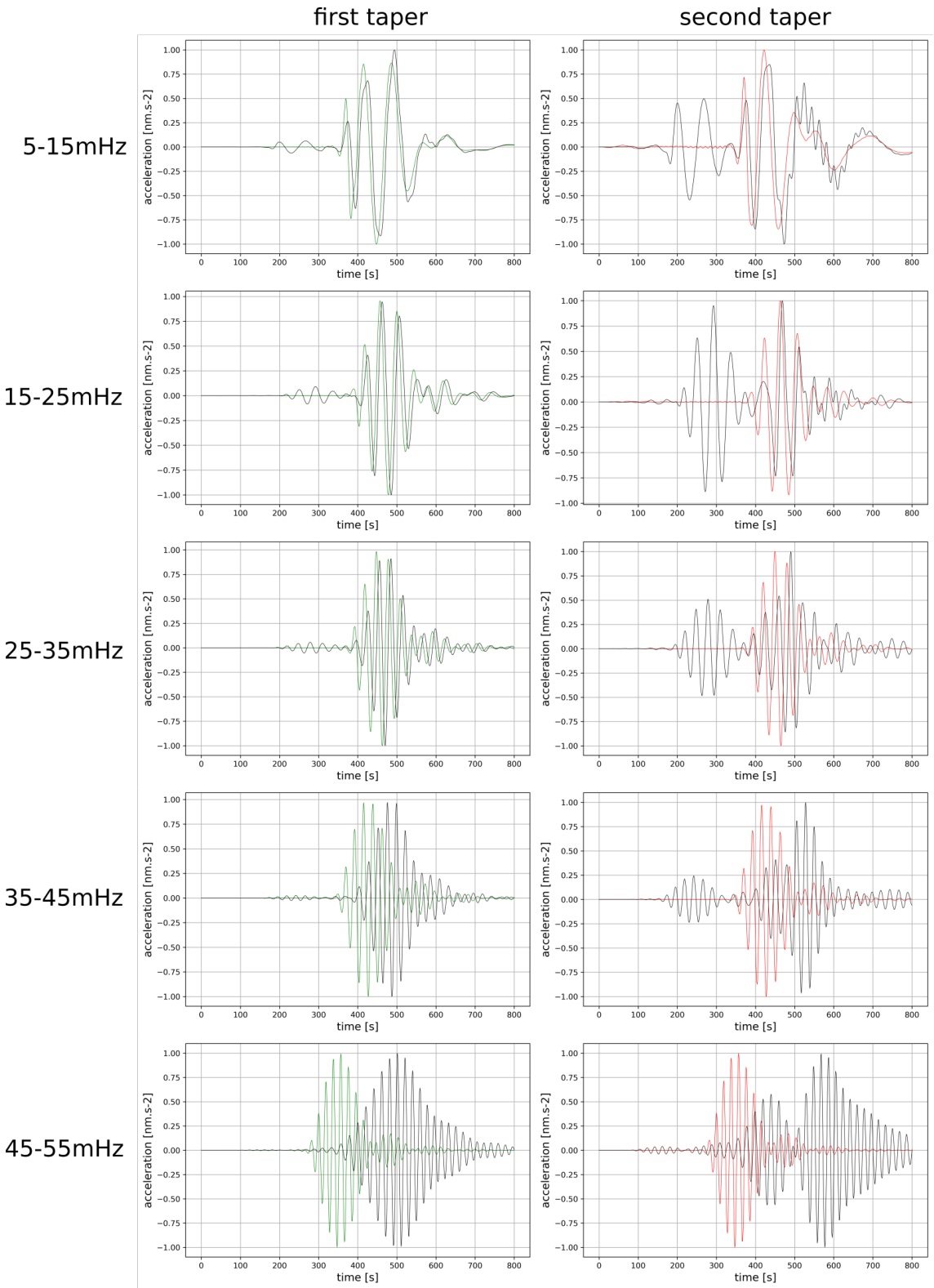

FIGURE 5.4: Tapered synthetic (green or red) and observed waveforms (black) with the first (left column) and second (right column) Slepians, filtered at the center frequencies 10mHz, 20mHz, 30mhz, 40mHz and 50mHz (from top to bottom). The source-station pair is the same as shown on the map of figure 5.2

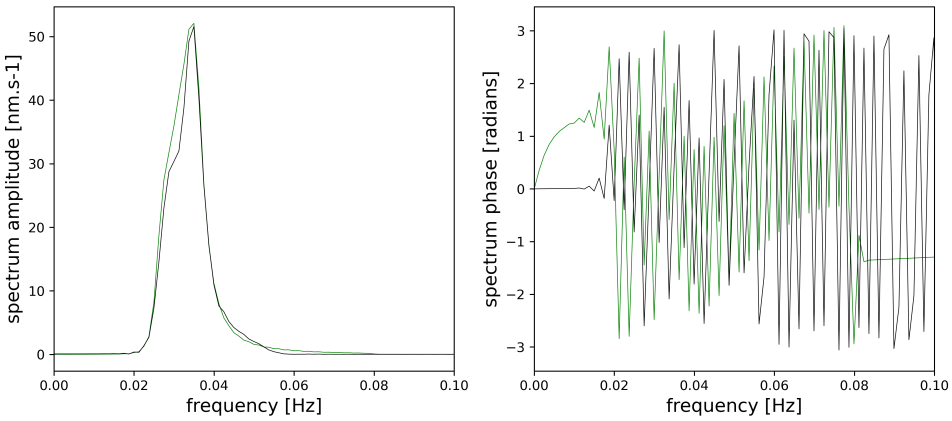

FIGURE 5.5: Amplitude (left) and phase (right) spectra for the synthetic (green) and observed (black) waveforms tapered with the first eigentaper and bandpass filtered around 30mHz.

(second column). In this case the first overtone seems to have gained importance. This is due to the shape of the second taper (figure 5.3 lower left).

The spectra of the tapered synthetic and observed waveforms are obtained using the Fast Fourier Transform algorithm. The estimated spectra for the first taper around 30 mHz is given on figure 5.5. As expected the energies of the signals are confined in the frequency band 25-35mHz and are similar for both of them since they have been normalized. The phase component of the spectra looks chaotic. In fact there are $\pm 2\pi$ shifts that can be corrected afterward. Finally the phase delay, for each taper and each frequency, is obtained as the difference between the phase of the observed and synthetic spectrums.

The phase delay as a function of frequency takes the name *dispersion curve*. The dispersion curves obtained for the first two tapers are drawn as solid lines on figure 5.6 (top). The curves make jumps of $\pm 2\pi$ outside the $\pm\pi$ range represented by the gray horizontal lines. These jumps are not physical and the curves can be corrected by adding or removing 2π. This leads to the dashed lines. After this correction the curves can still make jumps of $\pm 2\pi$, but in this case the jumps are physical. It is the well known *cycle-skip*: the mathematical procedure can only measure a phase delay within the range $\pm\pi$ but what if one waveform is delayed by more than a complete phase cycle? I assume that at low frequency it is very unlikely that there is more than one phase cycle of difference between the observed and synthetic waveforms. Then, for increasing frequencies, when a jump greater than a certain value (4 radians seems to be a good value) is detected, the curve is corrected by adding or removing 2π. On figure 5.6 (bottom) are drawn again as dashed lines the curves corrected for the non-physical jumps and

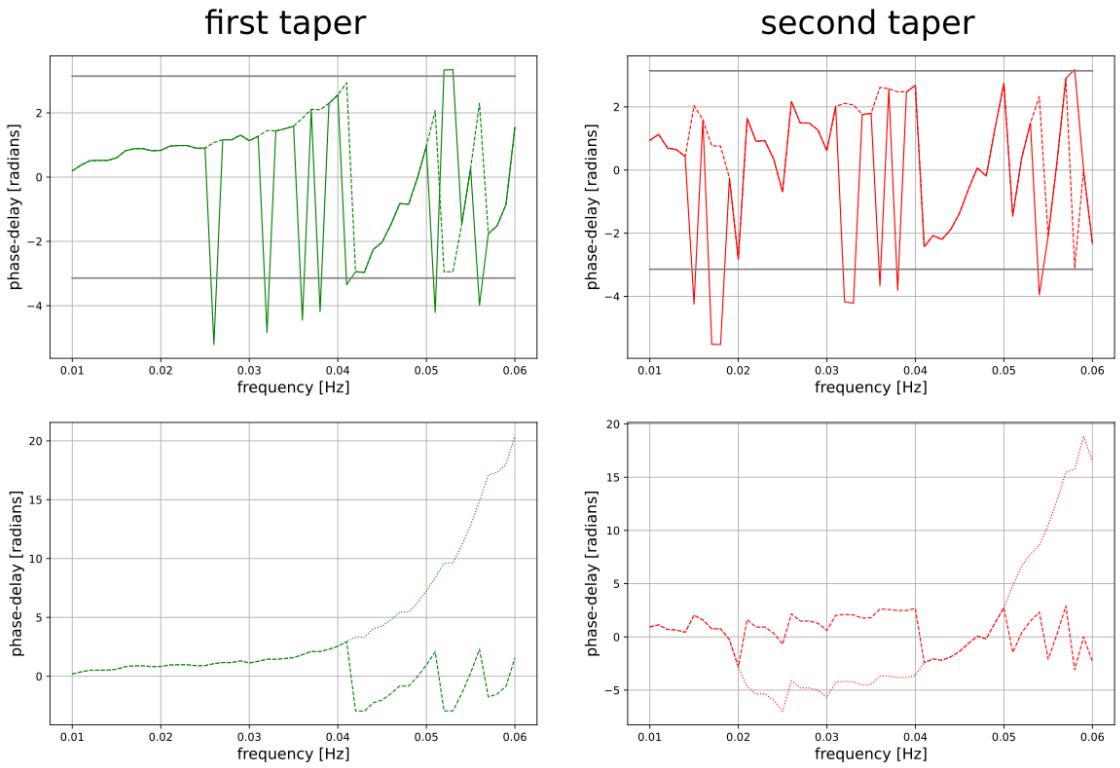

FIGURE 5.6: Corrections for non-physical (top) and physical cycle-skip (bottom) jumps of the dispersion curves for the first (left) and second (right) tapers. Top: the solid curve is prior to correction, it jumps of $\pm 2\pi$ outside of the $\pm\pi$ range (indicated by the horizontal gray lines); the dashed curve is after correction. Bottom: the dashed curve is prior to cycle-skip correction and the dotted curve is corrected for cycle-skip.

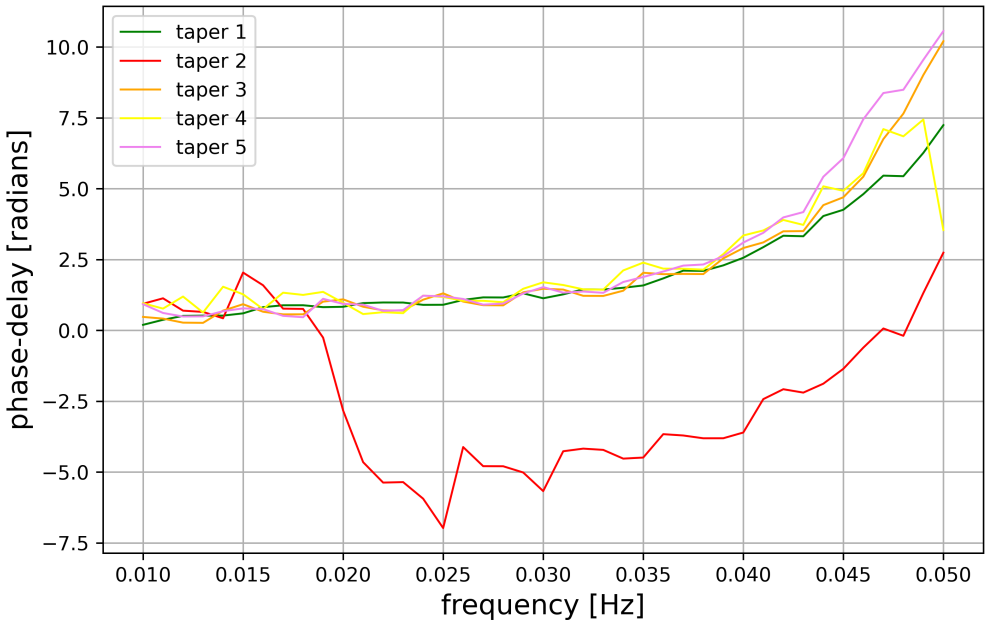

FIGURE 5.7: Final dispersion curves for the five tapers.

as dotted lines the curves also corrected for cycle-skip. In the case of the first taper a cycle-skip was detected around 40 mHz (figure 5.6 lower-left). This full phase cycle difference between the signals was already noticed on figure 5.4. The second taper also detects this cycle-skip (figure 5.6) but it detects another one around 20 mHz that is not observed with the first taper. It turns out that all the three other tapers do not detect any cycle-skip at this frequency. As we observed on figure 5.4, it is very likely that the second taper leads to bad results because of the significance of the first overtone and that the cycle-skip at 20 mHz is a false detection.

Figure 5.7 represents the final dispersion curves for the five tapers. All tapers lead to similar dispersion curves except the second one. It is shifted by -2π at frequencies higher than 20 mHz because of the false cycle-skip detection. Finally figure 5.8 shows the mean of the five dispersion curves (black line) with the standard deviation (grey lines). The standard deviation increases significantly at 20 mHz. This is due to the false cycle-skip detection with the second taper. Detecting correctly the cycle-skips is difficult. In their study, Moulik et al. (2021) compare various phase delay datasets and observe $\pm 2\pi$ discrepancies that come from this difficulty to detect cycle-skip (see their figure 6). Beyond minimizing frequency leakage and bias in the time domain, the multitaper technique has three major advantages in this study. First it reduces the risk of poor choices

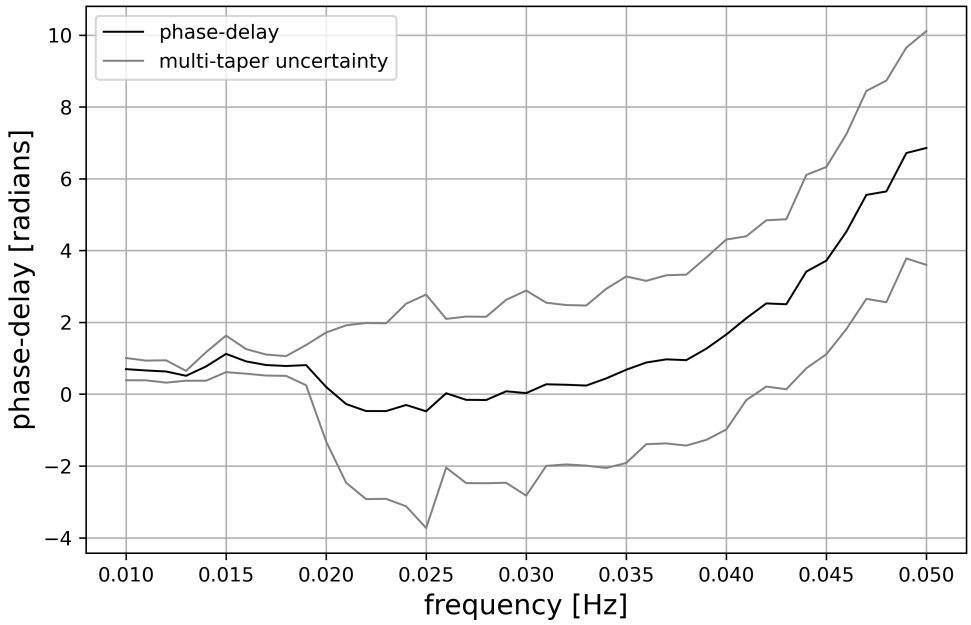

FIGURE 5.8: Mean of all five dispersion curves and standard deviation.

for the time window by illuminating various parts of the time domain waveform. Second, potential errors with one taper (such as cycle-skip mis-detection) are attenuated by averaging the results from several tapers. Last, it provides an uncertainty estimate for the measurement. Data uncertainties are the suject of the next section.

5.2.3 Phase delay uncertainties

The SOLA inversion accounts for the propagation of data uncertainties into model uncertainties. However the reliability of the model uncertainties depends on the quality of the data uncertainty estimates.

As described in the previous section, the phase delay estimate is an average of phase delays obtained with several tapers that weight differently the time domain waveform. An uncertainty estimate can be derived as the standard deviation of the set of measurements (for example the gray lines on figure 5.8). This uncertainty component accounts for the time window positioning and inaccurate spectrum estimation (bias and frequency leakage). As noted previously it can also account for cycle-skip mis-detection. On figure 5.9 are given the distribution of the multitaper uncertainty estimates for each measurement frequency for a selection of source-receiver-frequency triplets that we use later in this chapter (see

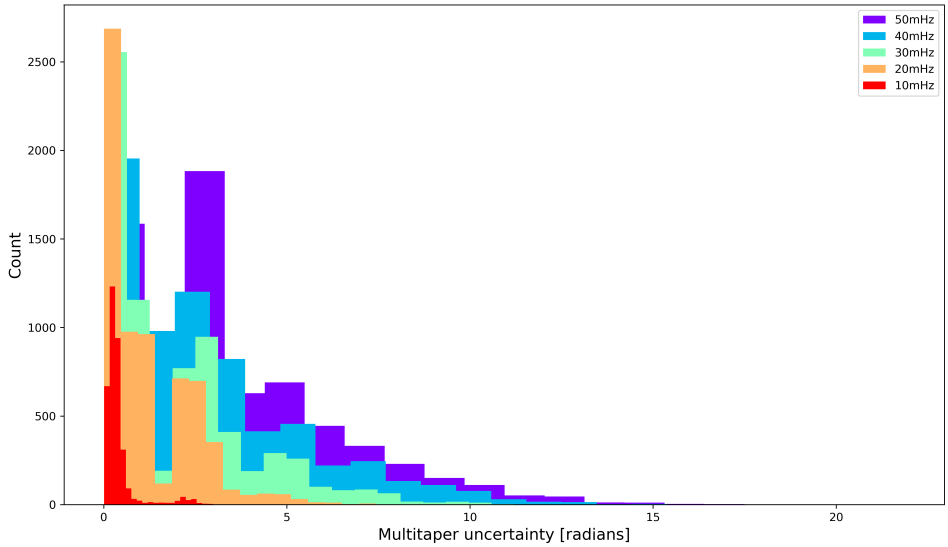

FIGURE 5.9: Distribution of uncertainties obtained from the multitaper technique for various frequencies.

section 5.4.2). Table B.1 in appendix B gives some statistics for the distribution of the uncertainties from the multitaper technique. In general the uncertainty increases with frequency with mean ranging from a tenth of a phase cycle at 10 mHz to half a phase cycle at 50 mHz.

Another important source of uncertainty is the imperfect knowledge of the seismic source parameters (centroid longitude, latitude, depth, time, and the six independent components of the moment tensor). In the best cases the GCMT catalog provides uncertainty estimates for these parameters. The distributions of the uncertainties for the source parameters for a set of sources that we use later in this chapter (see section 5.4.2) are given in figure 5.10 and some statistics are given in table B.2 (appendix B). Zero values are ignored: if the uncertainty of some parameter is zero, it will be set to the mean uncertainty of the whole dataset for that parameter. It seems that these uncertainty values are underestimated.

To investigate how much an error in a source parameter induces an error in the estimated phase delay, I use an approach close to *Monte Carlo* methods. I consider one source-receiver pair and I simulate 70 sources by perturbing the source parameter following a normal distribution using the source parameter uncertainty as standard deviation. The perturbed phase delays as a function of the perturbations in the source parameters are shown on figure 5.11. The errors for the event origin time generate very small (or even zero) errors in the measured phase delay. This is because the errors are too small given the 1 Hz sampling rate. It seems

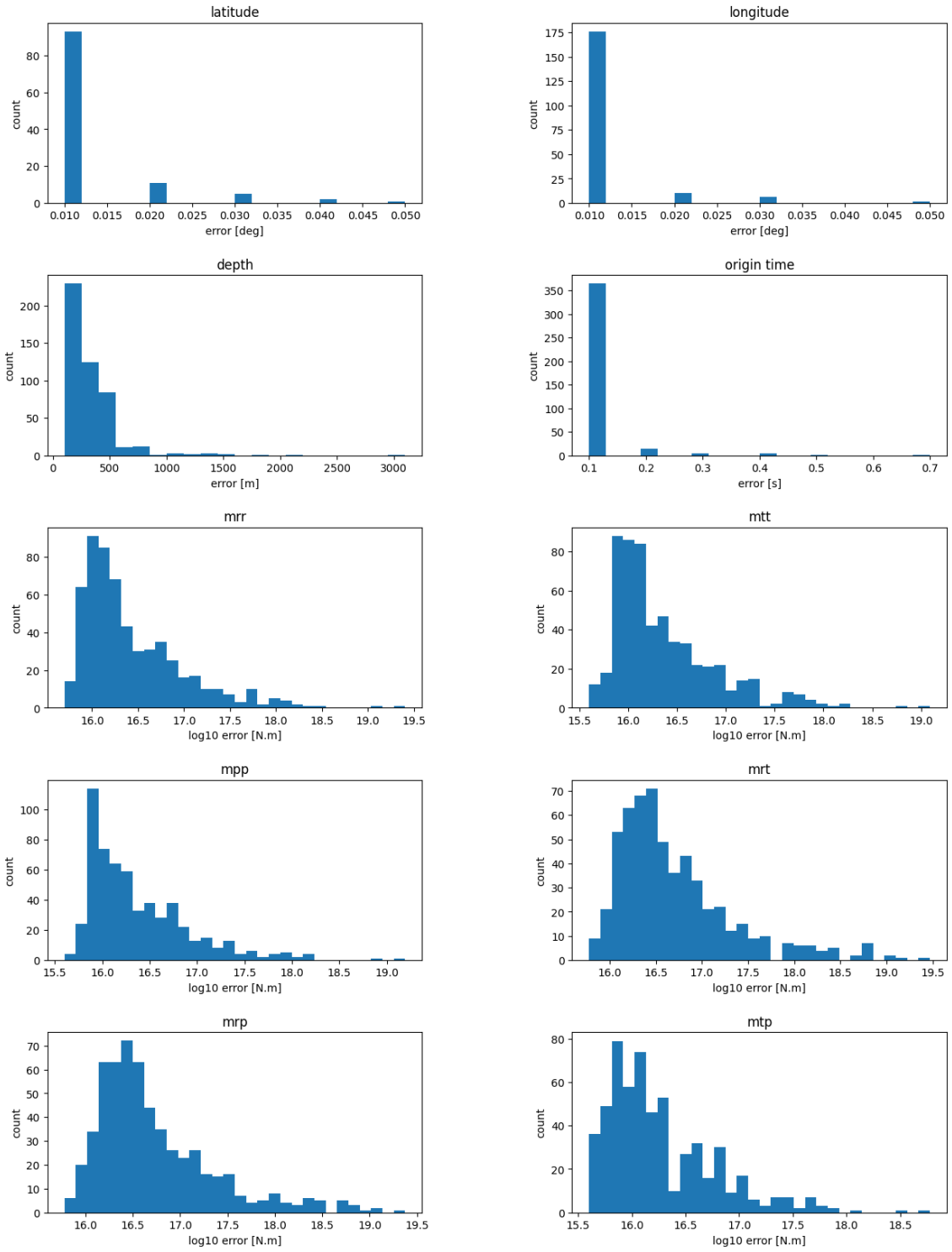

FIGURE 5.10: Distribution of uncertainties for various source parameters (576 events from the GCMT catalog).

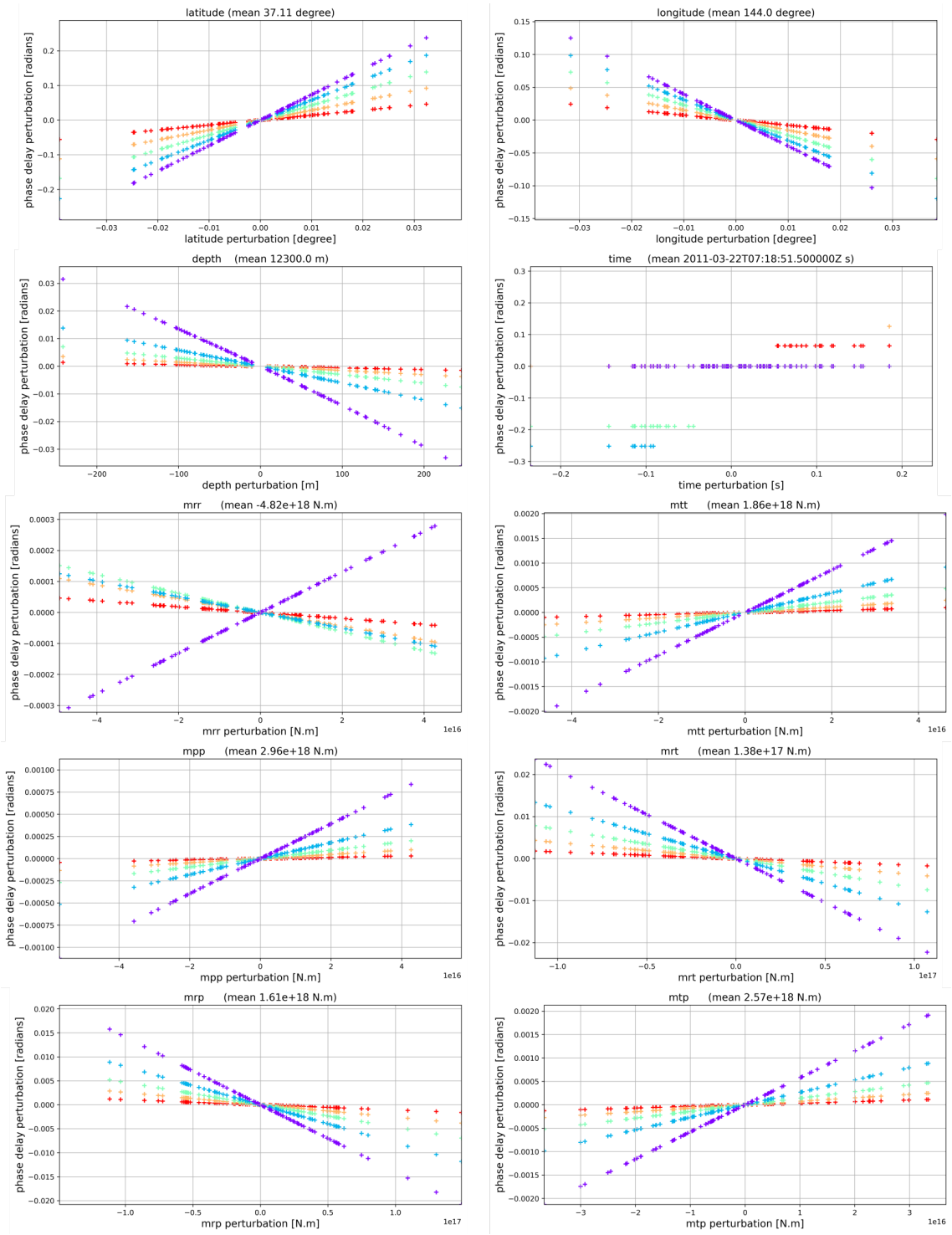

FIGURE 5.11: Phase delay produced by perturbations in the source parameters. This example is for the source with GCMT name C201103220718A and station RAO. For each parameter 70 sources are simulated with perturbation in the parameter following a normal distribution with standard error given by the parameter uncertainty. The coloring convention is the same as in figure 5.9: it goes from red to blue as frequency increases from 10 to 50 mHz by steps of 10 mHz.

that within the region of the source parameter uncertainties, the relation between the source parameter perturbation and the perturbed phase delay is linear. The phase delay perturbations for this example are also represented as distributions on figure 5.12. The linearity makes that the distributions are mainly Gaussian and we could use the standard deviations of these Gaussians as phase delay uncertainties propagated from the source uncertainty. In general, the uncertainty in a parameter induces an uncertainty in the measured phase delay that increases with frequency. The uncertainty in the latitude, longitude and depth of the events seem to have the largest effect on the phase delay compared with the uncertainty in the moment tensor components. Of course these results depend on the source-receiver pair (depth of the source, moment tensor, orientation of the station with respect to the focal mechanism). The best would be to apply the same procedure to each source-receiver pair to propagate the source uncertainties into phase delay uncertainties. Unfortunately this task is computationally expensive.

To get a more general idea of the propagation of source uncertainties into phase delay uncertainties I apply the same procedure to a set of 29 randomly chosen source-receiver pairs. Some statistics on this set of propagated uncertainties are given in tables B.3, B.4, and B.5 in appendix B. Again we observe that the propagated uncertainties are very small for the source origin time and for all parameters it increases with frequency. The propagated uncertainties are much larger for the latitude, longitude and depth components than for the moment tensor ones. Note that the data selection involves a criterion that accounts for the orientation of the station with respect to the source moment tensor. This selection reduces the uncertainties from the moment tensor components since it avoids strong phase changes that are expected close to the nodal planes of the focal mechanism. In the following I consider only the maximum of propagated uncertainty for each parameter and I combine them to obtain an uncertainty estimate for the source errors that depends on frequency only. I believe that the source errors have been highly underestimated. The uncertainties obtained from the source are of the order of 10 times lower that the uncertainties obtained from the multitaper technique. It turns out to be very difficult to have an estimate of the uncertainties from the source errors that is reasonable. However the relative amplitude of the estimates at various frequencies may be informative. I decide to multiply the propagated uncertainties from the source by 10 for them to weight at the same level as the multitaper uncertainties in the inversion and in the tomographic model. The final estimates are given in table 5.1. For each measurement, the uncertainty from the source errors at the data frequency is added to the uncertainty estimate from the multitaper technique.

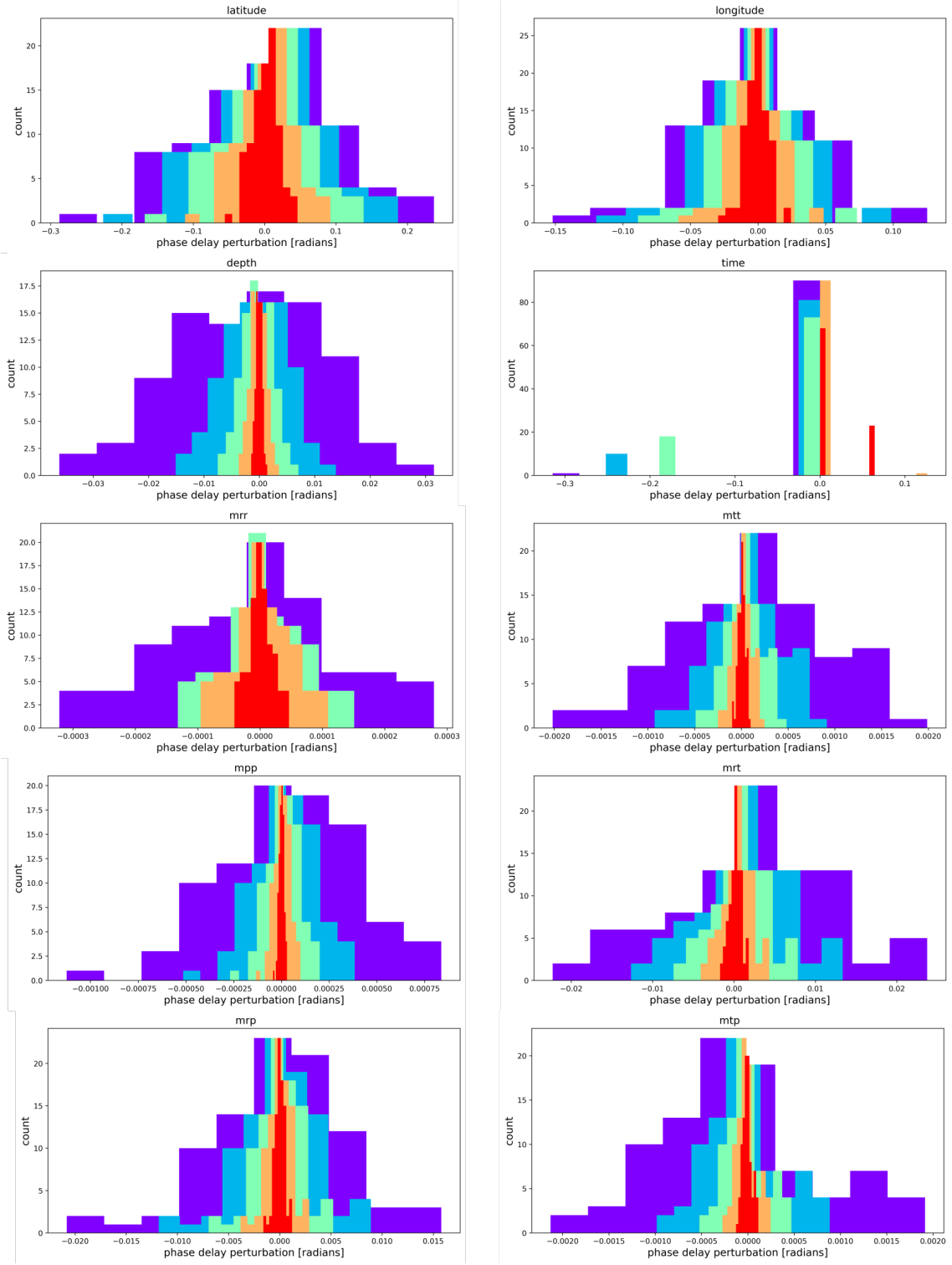

FIGURE 5.12: Same data as in figure 5.11 but plotted as the distribution of the perturbed phase delay produced by perturbations in source parameters. The coloring convention is the same as in figure 5.9.

TABLE 5.1: Phase delay uncertainties from errors in the seismic source parameters as a function of frequency.

frequency	10mHz	20mHz	30mHz	40mHz	50mHz
phase delay uncertainty (radians)	1.16	1.80	2.32	3.07	3.86

Clearly this estimation of data uncertainties is very rough. First the propagated uncertainties are similar for all source-receiver pairs while they might depend strongly on the source location and on the source-receiver orientation. To get the data uncertainty estimate I combine all sources of error as if they were independent while there might be correlations between the uncertainties that I do not account for in this study. Furthermore, some sources of errors are neglected. For example one may wonder what is the uncertainty generated by the imperfect crustal correction or by the parameterization (next section). Last, this study assumes that all error distributions are perfectly Gaussian though the errors for the source parameters may not be normally distributed and the relation between source error and phase delay error may not even be linear. Here I only attempted to get crude estimates of data uncertainties for the remaining of the study. Estimating the data uncertainties turns out to be a difficult task but it is also a crucial task, especially when using the SOLA inversion since it propagates data uncertainties into model uncertainties. This difficult but crucial task of estimating data uncertainties in tomography should be adressed more seriously in the future.

5.3 Tomographic setup

5.3.1 Three-dimensional sensitivity kernels

In chapter 2 I presented the derivation of the finite frequency sensitivity kernels that relate a phase delay for a source-receiver pair to the three-dimensional perturbations in some physical parameters. Here I assume that the phase delays are mostly sensitive to perturbations in the isotropic vertically polarized S-wave velocity $\delta \ln V_s(\boldsymbol{x})$. This is justified because measurements are made on the vertical component of seismograms, far from the source. The forward problem for the source-receiver pair p at frequency ω_q can be written:

$$\delta\phi_p(\omega_q) = \iiint_{\oplus} K_p(\omega_q, \boldsymbol{x}) \delta \ln V_s(\boldsymbol{x}) d^3\boldsymbol{x}, \tag{5.1}$$

with

$$K_p(\omega, \boldsymbol{x}) = -\operatorname{Im}\left(\frac{\mathcal{K}(\omega, \boldsymbol{x})}{s(\omega)}\right). \tag{5.2}$$

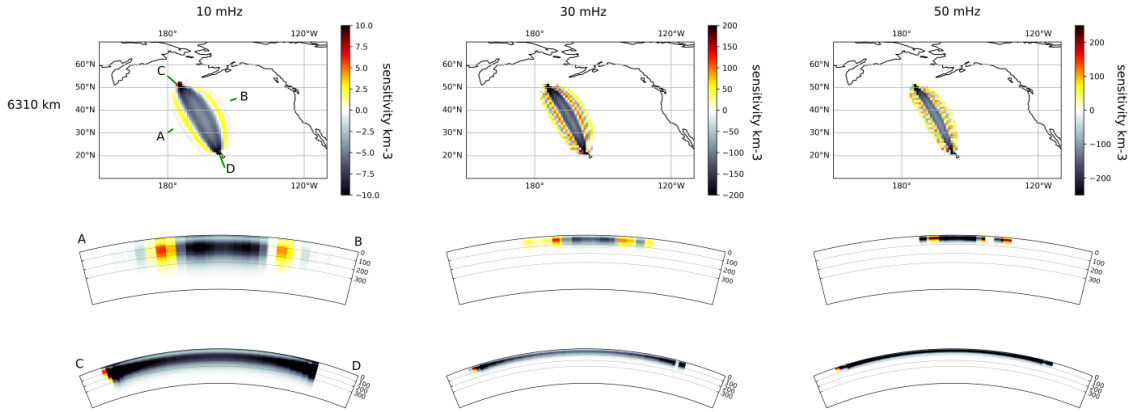

FIGURE 5.13: Sensitivity kernel for the source C201308301625B and station KIP at 10 mHz (left), 30 mHz (middle) and 50 mHz (right). Top: depth slice at 70 km depth, middle: transversal cross-section, bottom: longitudinal cross-section. The grid cell size is $1^\circ \times 1^\circ \times$ 10km.

where $\mathcal{K}(\omega, \boldsymbol{x})$ is the scattered waveform kernel: $\delta s(\omega, \boldsymbol{x}) = \mathcal{K}(\omega, \boldsymbol{x}) \times \delta \ln V_s(\boldsymbol{x})$. To be consistent with the measurements, the sensitivity kernels are based on the normal mode solutions for the radial reference model *CPacific*.

The expression 5.2 stands for untapered waveforms, however the measurements are made from tapered waveforms. For full consistency between the data and the forward problem it is therefore necessary to taper the sensitivity kernels as well. In the case of multi-taper measurement the tapered sensitivity kernel is given by:

$$K(\omega, \boldsymbol{x}) = -\operatorname{Im}\left(\frac{\sum_j \mathcal{K}_j(\omega, \boldsymbol{x}) s_j^*(\omega)}{\sum_j s_j(\omega) s_j^*(\omega)}\right), \tag{5.3}$$

where $s_j(\omega) = s(\omega) \otimes h_j(\omega)$ and $\mathcal{K}_j(\omega, \boldsymbol{x}) = \mathcal{K}(\omega, \boldsymbol{x}) \otimes h_j(\omega)$ are the tapered waveforms and tapered scattered waveform kernel with the j-th taper h_j. The $\otimes$ symbol denotes convolution. Tapering the sensitivity kernel would require to compute it for a broad range of frequencies, not only at the frequencies where the measurements are made. Assuming tapers with narrowly concentrated spectra, Zhou, Dahlen & Nolet (2004) show that:

$$\mathcal{K}_j(\omega, \boldsymbol{x}) \approx \mathcal{K}(\omega, \boldsymbol{x}) \times h_j[t = \Delta'/C'(\omega) + \Delta''/C''(\omega)], \tag{5.4}$$

and,

$$s_j(\omega, \boldsymbol{x}) \approx s(\omega) \times h_j[t = \Delta/C(\omega)]. \tag{5.5}$$

where $\Delta/C(\omega)$ is the group arrival time of the initial wave and $\Delta'/C'(\omega) +$

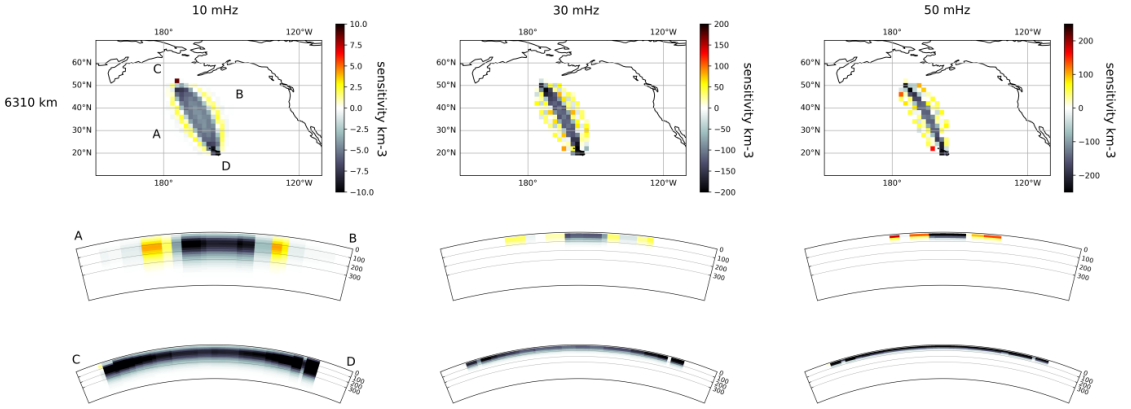

FIGURE 5.14: Same as figure 5.13 but with a coarser grid ($2^\circ \times 2^\circ \times$ 25km).

$\Delta''/C''(\omega)$ is the group arrival time of the scattered wave at frequency ω. Tapering the waveform and the scattered waveform kernel at some frequency ω simply requires multiplying it with the value of the taper at the predicted group arrival time for the initial and scattered waves.

I compute the three-dimensional sensitivity kernels using the computer programs from Zhou, Dahlen & Nolet (2004) and Zhou (2009a). The kernel is computed at the depths of the reference model. At each depth, every one degree along the source-receiver great-circle, the kernel is sampled at 32 equidistant points within two Fresnel zones in the orthogonal direction to the great-circle (Box 6). To set up the forward problem the kernel must be projected onto the tomographic grid (Box 7). For one lateral location the kernel is interpolated at the grid depths using splines. Then the value for one cell is the mean of all samples that fall in that cell. The sensitivity kernel for the source C201308301625B and station KIP, for the fundamental mode ($n = 0$) at three frequencies, projected onto a grid with cells of size $1^\circ \times 1^\circ \times 10$km, is drawn on figure 5.13. In general the sensitivity is shallow compared with higher modes kernels (see chapter 2). Restriction to the fundamental mode will make it difficult to image the mantle deeper than the first hundred kilometers. We observe that the higher the frequency the shallower the sensitivity. This is in connection with the observations made with the eigenfunctions of displacement in chapter 2. Moreover we observe that the higher the frequency the narrower the kernel laterally. This is also expected that for increasing frequency the kernel tends to the ray approximation. The low frequency kernel is also low amplitude (note the colorscale ranges on figure 5.13). Therefore we may expect a poorer resolution at great depths.

Unfortunately it is necessary to increase the gridding size to avoid high computational costs. In the following the grid has cells with size $2^\circ \times 2^\circ \times 25$km. The

kernel projected on such a grid is drawn on figure 5.14. Though the projection degrades the kernel, it seems to retain its main properties.

5.3.2 Three-dimensional target kernels

Since the forward problem is fully three-dimensional the target resolution needs to be designed in three-dimensions. The target kernels are designed as ellipsoids. Taking into account the physical behaviour of surface waves the target kernels need to be flattened laterally and to reduce smearing effect they can be chosen to be circular laterally. Therefore the target kernel for the cell k is an ellipsoid defined by two values: r_v^k is the ellipsoid minimal axis along the vertical direction and r_l^k is the two other ellipsoid axes along the lateral directions (east, north). To set the vertical and lateral target resolution length r_v^k and r_l^k for all cells I use the same approach to that in chapter 4. For one direction, the minimum and maximum target resolution lengths $r_{\min}$ and $r_{\max}$ corresponding to the maximal and minimal data densities $\rho_{\min}$ and $\rho_{\max}$ are set and the resolution length r for any cell as a function of the data density ρ in that cell is obtained using the linear relation:

$$r(\rho) = r_{\max} - (r_{\max} - r_{\min}) \left(\frac{\log_{10}(\rho) - \log_{10}(\rho_{min})}{\log_{10}(\rho_{max}) - \log_{10}(\rho_{min})} \right) \tag{5.6}$$

The use of the $\log_{10}$ is to avoid strong spatial variations in the target resolution that would induce strong spatial variations in the actual resolution. Note that in this chapter equation 5.6 defines the target resolution radii everywhere in the three-dimensional space, as much as the sensitivity is defined everywhere in the three-dimensional space.

The target kernels need to be projected onto the tomographic grid. This is achieved by a process close to Riemann integrations. A subgrid that contains the target kernel with very small cell sizes is designed. The value of the projected target kernel in cell k is the sum of the volumes of the cells of the subgrid that belong both to the target kernel and cell k. Moreover the target kernels are normalized such that $\sum_{j=1}^{M} T_j^{(k)} V_j = 1$.

The projection of the target kernels for cells at 60 km and 160 km depths are shown on figure 5.15. The size of the target kernels has been computed based on the sensitivity obtained with the data selection used in the next section. On the maps we observe that the target kernels are circular. This circular shape should help to reduce artifacts such as smearing effects. Contrary to the target kernels designed in chapter 4, the target kernels in this chapter also have a vertical extent that will help to constrain the resolution with depth. Since the sensitivity

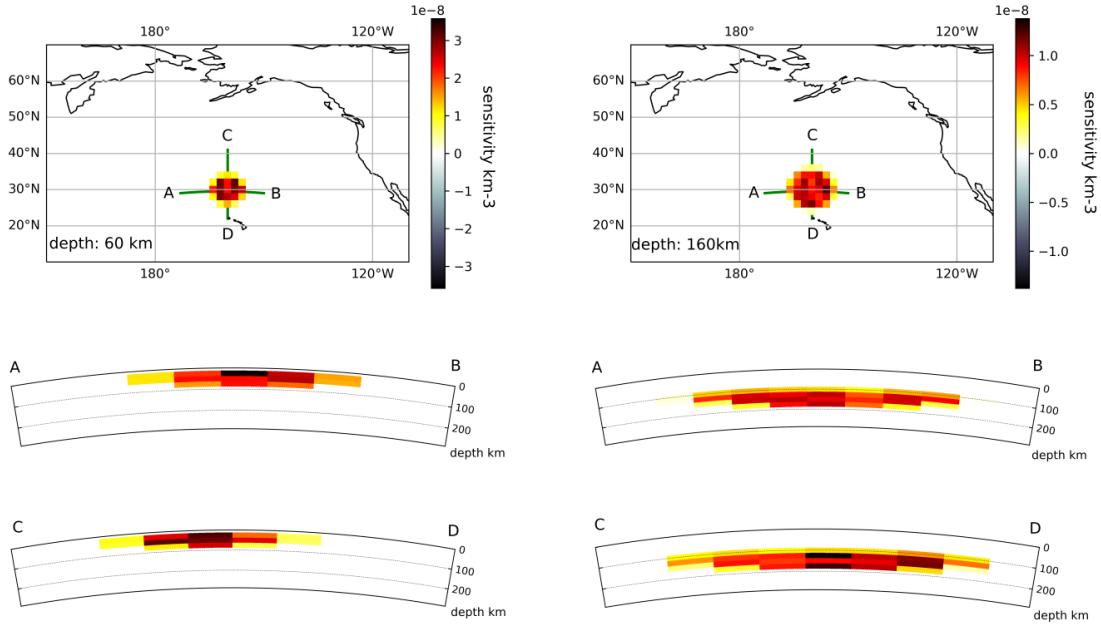

FIGURE 5.15: Target kernels located at 199°E, 31°N, at 60km (left) and 160km depth (right).

at 60 km depth is higher that at 160 km, the shallower averaging kernel has a smaller spatial extent.

All the tools necessary for the three-dimensional SOLA tomography have been presented and the next section is dedicated to the application of the tomographic process in a synthetic case.

5.4 Synthetic tomography

5.4.1 Motivations

The forward theory used for the problem to be fully three-dimensional has been applied only in few studies by the research group that developed the sensitivity kernels (e.g. Zhou, Dahlen & Nolet, 2004; Zhou et al., 2005; Zhou et al., 2006; Zhou, 2009a; Ruan & Zhou, 2010; Tian et al., 2011; Liu & Zhou, 2013; Liu & Zhou, 2016a; Liu & Zhou, 2016b). The SOLA inversion has been adapted to seismic tomography only recently (Zaroli, 2016). Its use in the framework of surface waves is even more recent (Ouattara, Zigone & Maggi, 2019; Latallerie et al., 2022). The use of the SOLA inversion for surface wave tomography in a complete three-dimensional framework is, to the best of my knowledge, completely new.

For this reason it is safer to start with a synthetic tomography where the role of the 'true' Earth is played by a known input model. This synthetic tomography

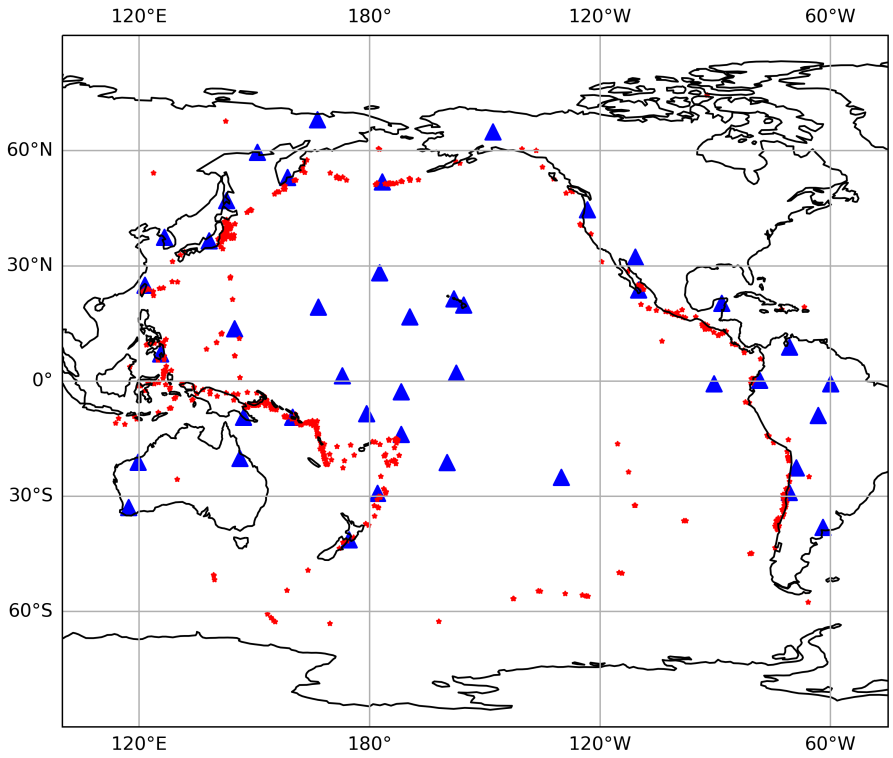

FIGURE 5.16: Seismic events (red stars) and seismic stations (blue triangles) used in this synthetic tomography.

will help to check the reliability of the measurement process (production of synthetic seismograms and phase delay measurement), the uncertainty estimates, the three-dimensional sensitivity kernels and the overall consistency of the process. Moreover, by comparing the input Earth with the results (recovered Earth, model uncertainties and resolution), this synthetic tomography will help to understand the power of the three-dimensional SOLA surface wave tomography and spot any biases and artifacts.

5.4.2 Settings

The synthetic waveforms that play the role of observations for this synthetic tomography are produced by the *specfem3D* software. The *specfem3D* software produces synthetic seismograms in any three-dimensional Earth model using the spectral-element method (e.g. Komatitsch & Vilotte, 1998; Komatitsch & Tromp, 2002a; Komatitsch & Tromp, 2002b). Synthetics are pre-computed for events in the GCMT catalog by the Princeton's *Global ShakeMovie* project (Tromp et al., 2010) for the three-dimensional model *S362ANI* from Kustowski, Ekström & Dziewoński (2008). Vertical component synthetics can be obtained from the IRIS repository (Hutko et al., 2017). The aim is now to retrieve the three-dimensional model

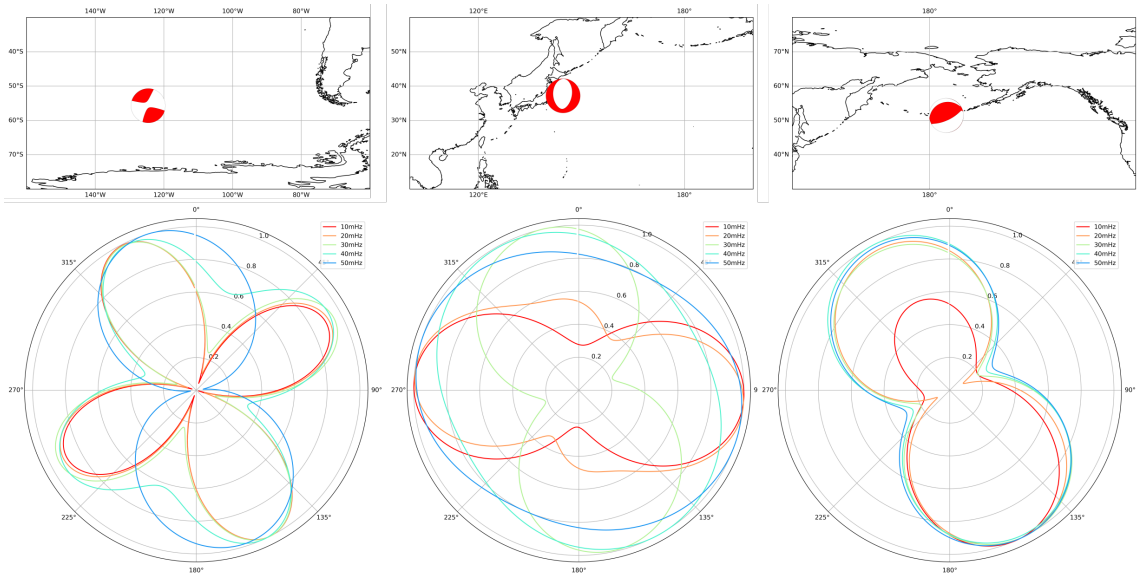

FIGURE 5.17: Focal mechanisms (top) and radiation patterns (bottom) for the sources with GCMT names C201111111041A (left), C201310251710A (middle) and C201308301625B (right). The coloring convention is the same as in figure 5.9: it goes from red to blue as frequency increases from 10 to 50 mHz by steps of 10 mHz. The radiation at all azimuths is normalized by the maximum radiation.

S362ANI that plays the role of the 'true' Earth using the tomographic process developed in this chapter.

A total of 576 seismic events that occured between January 2010 and December 2017 are selected from the GCMT catalog. Events have been selected such that the source depth ranges from 10 to 80 km to avoid strong influence from the crust with shallow events and significant overtones with deep sources. Events are also selected with moment magnitude Mwc ranging from 6 to 7.8 for event to be small enough to avoid source finiteness effects (the forward theory assumes point source in space) but strong enough for good signal-to-noise ratio. Events are also selected to have occured within the Pacific ocean or at the continent-ocean border, to avoid effects of continental lithosphere since the reference model is chosen to reflect the oceanic domain. 45 seismic stations are selected from the IU virtual network and channel information is obtained from IRIS (Hutko et al., 2017). Stations are selected such that the source-receiver path is confined to the Pacific ocean, again to avoid the effect of the continental lithosphere that is not represented in the reference model and that would complicate the waveforms. All selected events and stations are located on figure 5.16.

A source-receiver-frequency specific selection is also applied (see also Box 8). To guarantee the far-field approximation used in the forward theory only data that are predicted to have accomplished at least five phase cycles are selected (i.e.

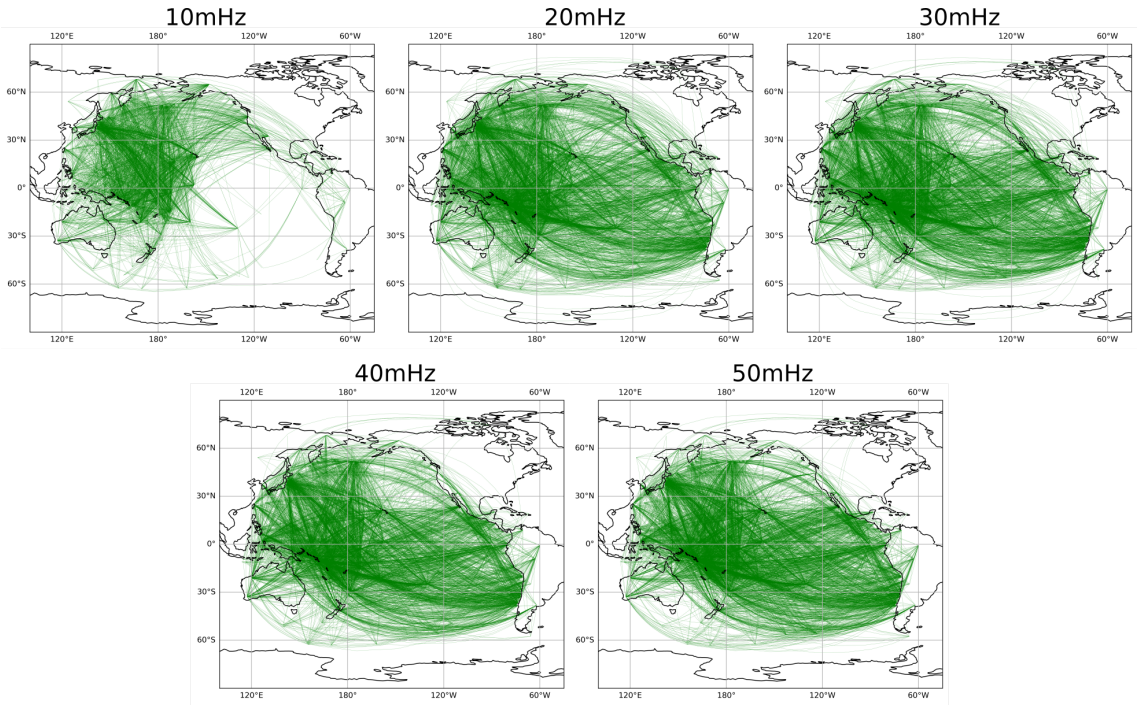

FIGURE 5.18: Ray coverage for each frequency considered for the inversion.

$k\Delta \geq 10\pi$ radians, with k the wavenumber in radians per angular degree and Δ the source-receiver distance in angular degrees). In addition only source-receiver distances less than 120° (i.e. $\Delta \leq 120°$) are selected to stay within the paraxial approximation. A selection criterion could be based on the source-receiver pair orientation with respect to the focal mechanism to ensure enough energy is radiated for the signal-to-noise ratio to be high and to avoid strong phase changes near a nodal plane. However, as noted in chapter 2 the radiation pattern for surface waves actually depends on frequency and source depth. On figure 5.17 radiation patterns for the measurement frequencies are drawn for three sources. We observe indeed a strong variability with frequency. Source-receiver-frequency data are selected if the radiation in the direction of the receiver is at least 50% of the maximum radiation. Last, the maximum correlation between the tapered and filtered synthetic and observed waveforms is computed. The waveform is selected if the maximum correlation (the mean for all five tapers) exceeds 0.85. Finally we end up with 31062 phase delays. The number of measurements per frequency is given in table 5.2. The ray coverage for each frequency is given on figure 5.18. The sensitivity, i.e. the sum of the absolute value of the sensitivity kernels that fall in each cell ($\sum_i |G_{ij}|$) is plotted on figure 5.19. As expected from the source and station lateral selection the sensitivity is confined to the Pacific region. Moreover it is highly heterogeneous, with a sensitivity greater in the west of the Pacific

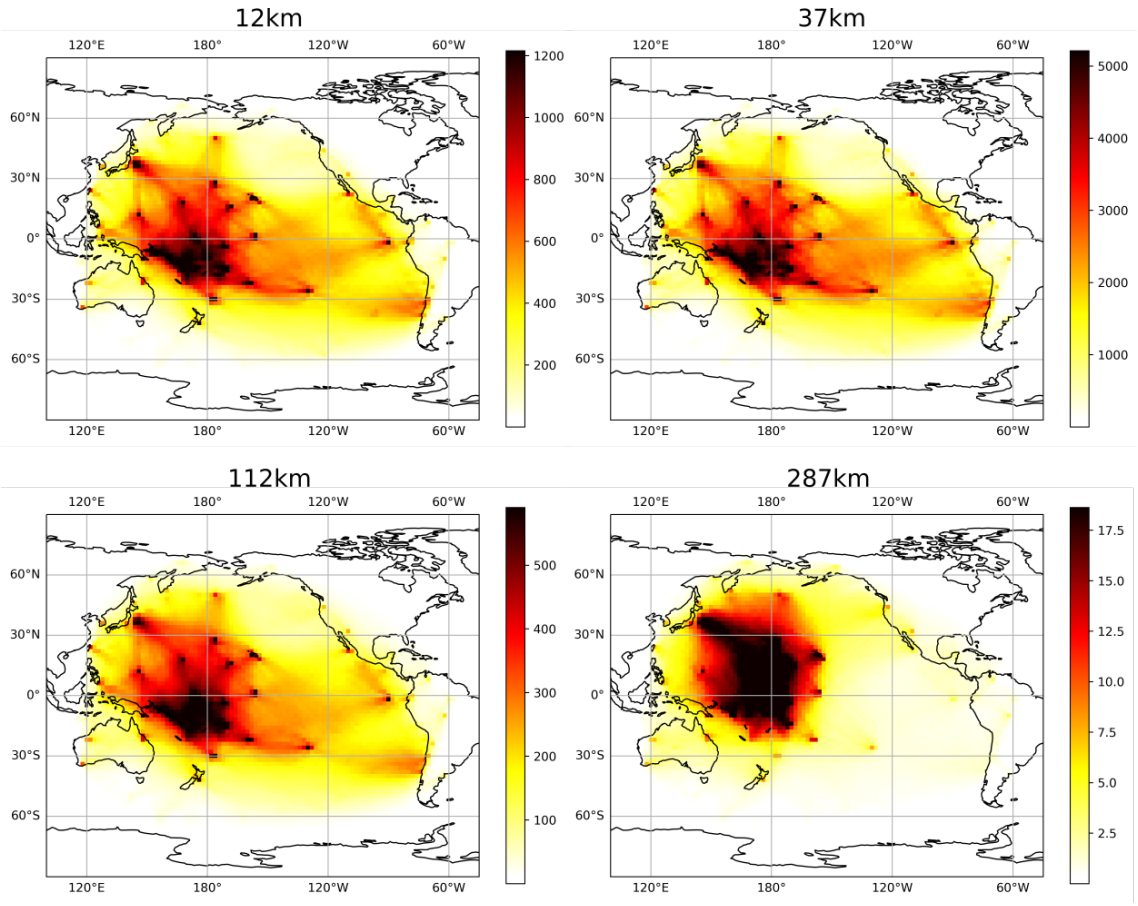

FIGURE 5.19: Sensitivity, or sum of the absolute value of kernels that fall in each cell, or $\sum_i |G_{ij}|$.

ocean. Vertically, the sensitivity is very shallow. This is because only the fundamental modes are considered here. To highlight deeper part in the mantle it will be necessary to also consider higher modes.

From the sensitivity, the vertical and lateral radii of the ellipsoidal target kernels are computed using equation 5.6 (see also Box 9). Figure 5.20 gives the lateral and vertical radii of all target kernels at 37km depth where $r^l_{\text{min}} = 750\text{km}$, $r^l_{\text{max}} = 5000\text{km}$, $r^v_{\text{min}} = 25\text{km}$ and $r^v_{\text{max}} = 125\text{km}$. All inputs are set up and phase delays can be inverted using the SOLA scheme (see also Box 10). Note that a numerical account for the whole process is given in appendix C.

5.4.3 Results

On figure 5.21 are represented the input model, the output model and the model uncertainties at 37 km and 112 km depth (see also Box 11). This synthetic tomography is a crude preliminary test: the dataset is relatively small and some input parameters may be better tuned. However it is interesting to draw the first

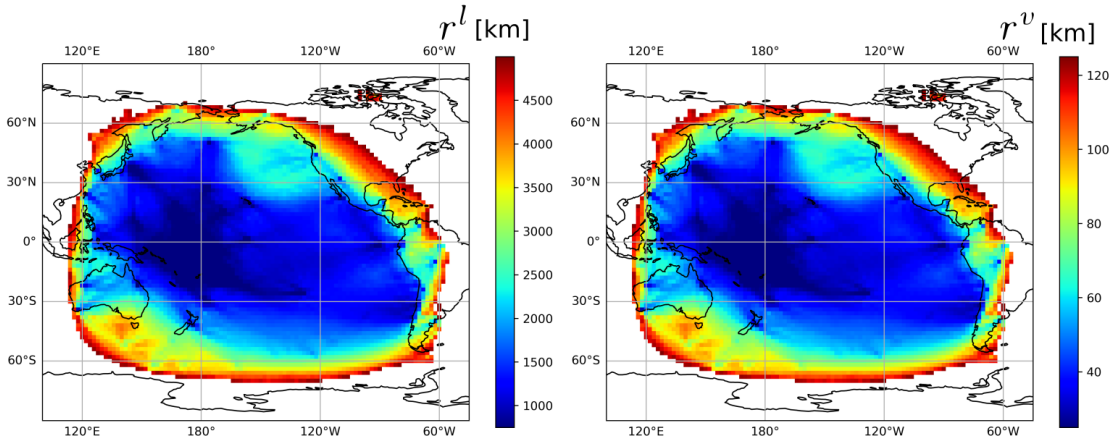

FIGURE 5.20: Lateral (left) and vertical (right) radii of target kernels at 37km depth. In this case $r^l_{\text{min}} = 750$km, $r^l_{\text{max}} = 5000$km, $r^v_{\text{min}} = 25$km and $r^v_{\text{max}} = 125$km.

TABLE 5.2: Number of data per frequency.

frequency [mHz]	data count
10	3503
20	6835
30	7162
40	6685
50	6877

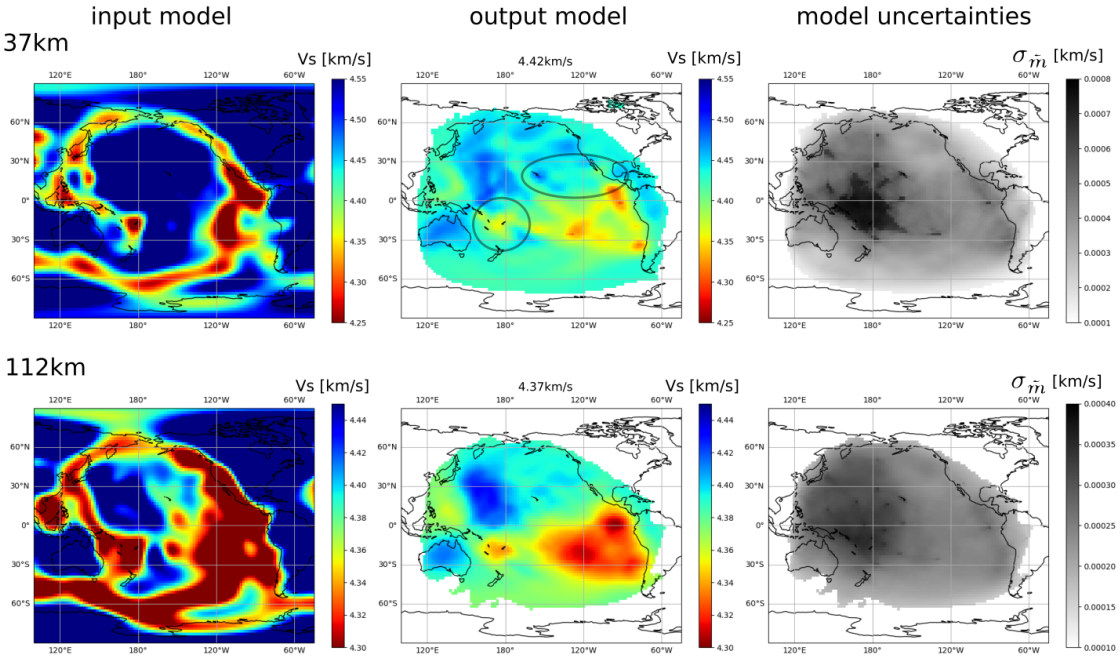

FIGURE 5.21: Input model (left), output model (middle) and output model uncertainties (right) at 37 km depth (top) and 112 km depth (bottom). The mean velocity of the output model is indicated above each caption. The gray ellipses on the output model at 37 km locate the features discussed in the text.

conclusions about the tomography presented in this chapter, to show potential artifacts and biases, and to point the areas for improvement in the future.

The model uncertainties seem extremely low. This may be due to underestimated data uncertainties. It may also be due to the target resolution since there is a tradeoff between the resolution and the uncertainties. The resolution may be too pessimistic (target kernels too large or tradeoff parameter η too high). We may achieve a better resolution given the dataset. The model uncertainties have a pattern close to that of the sensitivity (figure 5.19). It is not surprising since the sensitivity was used as a proxy to design the target resolution. This pattern may indicate that the target resolution is too optimistic where the sensitivity is high, or too pessimistic were the sensitivity is low. The uncertainties are lower at 112 km depth than at 37 km depth but the model is also smoother. Again this can be explained by the relation between the sensitivity and the target resolution: since the sensitivity decreases with depth, the target kernels are larger. As a consequence the resolution of the model is larger leading to a smoother model with lower uncertainties.

Since the output model is a 'filtered' version of the input model, it contains lower amplitude anomalies. There are discrepancies but we retrieve the main features of the input model, especially for large scale and strong anomalies. The slow velocity anomaly between the Pacific and Philipine sea plates at 37 km depth appears in the output model. The slow velocity anomaly that surrounds the Nazca plate is also retrieved. The increase of velocity in the northwest direction from the East-Pacific-Rise (a lithosphere cooling signature) appears clearly in the output model. The high velocity Australian craton, the slow velocity anomaly in the Samoa region as well as the transition from slow to fast velocity at the Tonga-Kermadec trench are strong features in the output model.

The slow velocity anomalies associated with the 'ring of fire' (the borders of the Pacific to the north) and the Pacific-Antarctic ridge are missing in the output model. In these regions the sensitivity is low. As a consequence the resolution is large so that the model is close to global average (i.e. it contains no information). The output model shows high velocity in the Solomon sea region while it is not the case in the input model. This is also a region where the model uncertainties are high. Accounting for the uncertainties would help to avoid wrong conclusions.

At 37 km depth the model shows spurious strong velocity anomalies at the locations of the seismic stations (figure 5.16). This is related to the very high sensitivity near the stations. The heterogeneous spatial resolution in these regions may complicate the interpretations. However these regions are also associated

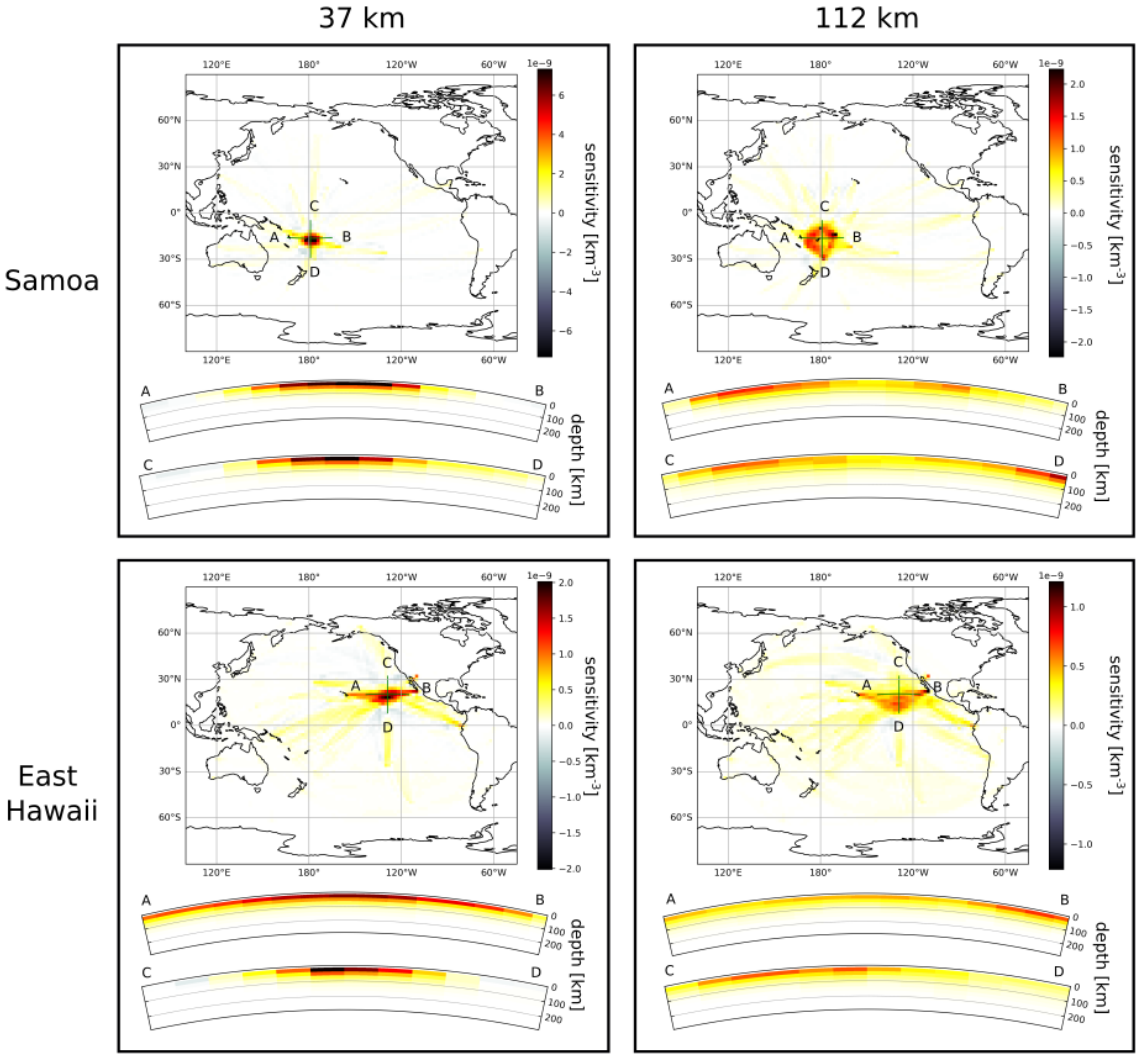

FIGURE 5.22: Three-dimensional averaging kernels for cells in the Samoa region (top) and to the east of Hawaii (bottom) at 37 km depth (left) and 112 km depth (right). The maps show depth-slices at the depth of the cells. Below the maps are vertical cross-sections as indicated on the maps.

with high model uncertainties that may prevent from interpreting them. To remove this effect, i.e. to homogeneise the resolution, it could be desirable to design a larger target resolution around the stations.

As examples I consider the two features indicated by the gray ellipses on figure 5.21: Samoa and the east of Hawaii. I discuss them regarding the resolution and uncertainties as if I did not know the input model. Unfortunately, since the uncertainties seem to be highly underestimated, the comparison with them is of little significance. However their relative amplitudes may be of interest.

What could be said about the Samoa low velocity using the resolution and model uncertainties? The uncertainties in this region are high (relatively to other location) but the anomaly is strong ($\sim$0.06km/s slower than mean). Figure 5.22

(top) shows the three-dimensional averaging kernels in this regions at 37 km and 112 km depth. At 37 km depth the averaging kernel is mainly circular. This guarantees that there is no artifact such as a smearing effect. Moreover the averaging kernel has a small spatial extent (its radius is $\sim$ 400km) which indicates that this anomaly is well resolved. At 112 km depth the averaging kernel is still circular but it has a much larger spatial extent. The vertical cross-sections show that the averaging kernel samples the information at depths shallower than 112 km. The shallow 'true Earth' leaks into the solution at 112 km depth. This is because the sensitivity is very shallow since we used only the fundamental modes. Note that without finite frequency theory we could not show this effect since the averaging kernels would not depend on depth. We conclude, using the model uncertainties and resolution, that this anomaly is robust at 37 km depth, that it may exist at 112 km depth but there is a depth bias and the model may show it smoother than it is in reality. We can confirm these interpretations since we know the input model.

What could be said about the elongated feature to the east of Hawaii? This feature has a velocity close to the global mean but it is slower than the surrounding region by $\sim$ 0.04 km/s. In this region the uncertainties are low. However, the averaging kernels represented in figure 5.22 (bottom) show that the resolution itself is elongated in the same direction as the feature. We conclude that this elongated feature in the model is probably an artefact from the resolution. Indeed the input model shows no such elongated feature. Actually such a smearing effect is not surprising given the ray coverage in this region (figure 5.18). To reduce such a smearing effect a larger target resolution could be designed in regions where the ray coverage is highly anisotropic.

5.5 Conclusion

The application of the SOLA inversion with the two-step approach in chapter 4 proved to be powerful to extract reliable information from the data and well informative resolution and model uncertainties. However strong limits remained with the estimation of the data uncertainties and the inherent two-dimensionality of the problem. In this chapter I go beyond ray theory to make the problem fully three-dimensional and I try another approach to estimate the data uncertainties.

Within the finite frequency framework based on the Born approximation, phase-delay data are related to the three-dimensional S-wave velocity. Phase delay data are measured using the multitaper technique. Data uncertainties, that account for

measurement and source errors are estimated. A three-dimensional target resolution based on the data sensitivity is designed. Finally the SOLA inversion is applied to produce a three-dimensional model with a direct control on its three-dimensional resolution and uncertainties.

Since this approach combines recent developments I start with a synthetic tomography: I apply the tomographic scheme to synthetic waveforms generated by a known input three-dimensional model of the Earth. The comparison of the input and output models shows that the three-dimensional SOLA surface wave tomography is reliable. This is a crude test, the dataset is small and input parameters could be better tuned, but it has the advantage to show potential artifacts and to point areas for improvement.

The model uncertainties are very small. It may be due to the data uncertainties since they result from them. It may also be due to the target resolution and to the chosen resolution-uncertainty tradeoff. The model uncertainties depend strongly on the sensitivity (laterally and with depth). They could be homogeneised by designing a larger target resolution where the sensitivity is high. Strong anomalies appear near the seismic stations due to very small target kernels (since the sensitivity at these locations is very high). This may be partly due to the far-field approximation used for the sensitivity kernels, the coarse parameterization at the stations and simply to the data distribution. However the model uncertainties are also high, preventing from interpreting them. The target resolution could be designed smoother to homogeneise the resolution in such regions. I show that the resolution helps to spot artifacts such as smearing effects. The anisotropy of the ray coverage could be quantified (as in Simons et al., 2002) and used as a proxy to design a larger target resolution in regions subject to smearing effects. I point a 'depth bias'. Since only the fundamental modes are used, the sensitivity is very shallow. As a consequence the model at great depths (for example at 112 km) actually represents averages that are shallower: the shallow 'true Earth' leaks into the solution at great depths. It is the combination of the finite frequency and SOLA approaches, making possible to constrain the resolution in three-dimensions, that allows to show the depth leaking. This effect was already noticed (e.g. Nolet, 2008, section 15.3, page 285-288). In this chapter we found a mean to quantify it.

The tomographic process developed in this chapter, that combines the advantages of finite frequency theory and SOLA inversion, is highly promising to tackle some of the main issues encountered in seismic tomography. Nevertheless some work is still required. Here is a list of potential improvements from most highest to lowest priority:

- The estimation of the data uncertainties is still rough and should be investigated more seriously. A better estimation of data uncertainties may account for example for the parameterization, the crustal correction or the approximations in the forward theory. It would also require more realistic source uncertainties and their propagation into data uncertainties should be source-receiver pair dependent, not only frequency dependent.

- The measurement should be extended to account for overtones. Without that only a very shallow picture of the mantle can be drawn and the advantages of the three-dimensionality of the forward theory may be lost.

- The far-field approximation for the sensitivity kernels can be broken using the near-field Green tensor estimation (Liu & Zhou, 2016b).

- Other crustal corrections can be tried, using finite frequency for example (e.g. Liu & Zhou, 2013).

- Other observables can be investigated (e.g. amplitude, polarization, other seismic channel orientations) and other model parameters can be mapped (e.g. P-wave velocity, attenuation, density, anisotropy) (e.g. Zhou, 2009a; Zhou, 2009b).

Of course, the tomographic process developed in this chapter should be applied soon with real data. Then the workflow designed in chapter 4 will be applied to discuss the three-dimensional structure of the Pacific upper mantle.

Box 1: About boxes

I think that it might be useful to give some details about the codes developed for this study. Not to blur the main messages with technical details, I use these boxes for that purpose. All the codes can be downloaded from the gitlab repository at: https://gitlab.com/FranckLatallerie/sola_ffsw.git. Note that only a tiny piece of these codes have been written by myself. A part of the codes come from my advisors Pr. Maggi, Dr. Lambotte and Dr. Zaroli. The production of the synthetics uses routines from Masters, Misha & Susan (2014), and the production of the sensitivity kernels uses routines from Zhou, Dahlen & Nolet (2004).

Box 2: General organization

The organigram below illustrates the main file system organization for the project. Names in rectangles are directories and names alone are the most important files. The main *input* directory contains external data. The main *output* directory contains computed data necessary for the tomography (measurements, sensitivity kernels). The *solaIO* directory contains input/output data for the SOLA inversion. The *sola_ffswk* directory contains programs. Programs use parameters defined in the configuration file *ffswk_sola_params.cfg*.

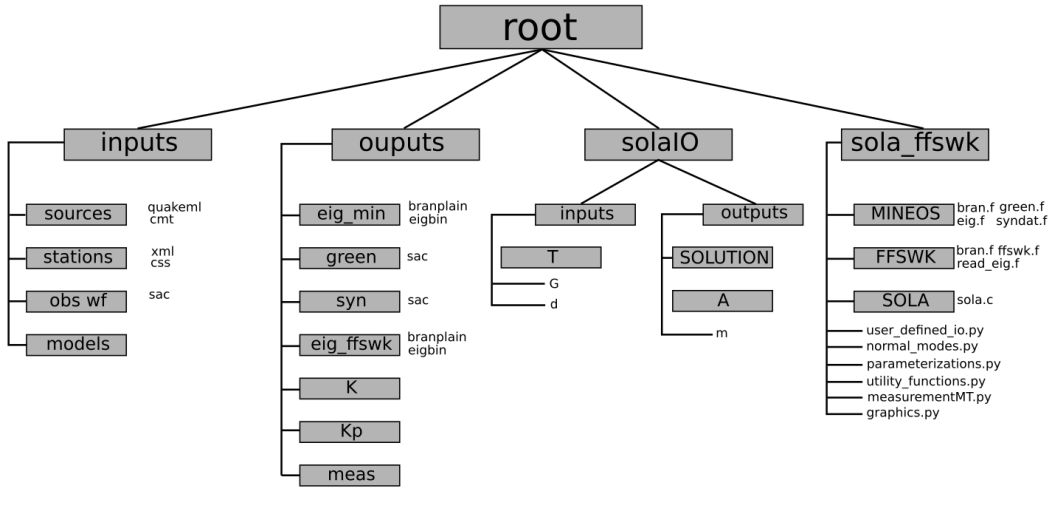

Box 3: External inputs

The tomographic study requires observed waveforms and seismic source and seismic stations/channels metadata to be saved locally. The observed waveforms must be saved in the *sac* format in the *inputs/obswf* directory. The sources metadata need to be saved in the *cmt* format (one file per source) in the *inputs/sources/* directory. Some functions in the script `user_defined_io.py` may help for conversions between the various formats.

Box 4: Computing synthetic waveforms

Computing synthetic waveforms requires three distinct steps: (1) compute the normal mode solutions for a radial Earth model, (2) use the solutions to compute the green functions for a source-receiver pair and (3) convolve the green functions with the source moment tensor to obtain the synthetic waveforms. Below is an example for the reference model *CPacific*, considering only the fundamental spheroidal modes, for the source with GCMT name C201001100027A and the station KIP of the network IU.

```
1  from normal_modes import compute_eigen_solution_MINEOS, compute_green, compute_synthetic_data
2  compute_eigen_solution_MINEOS( model_file="CPacific", basename_eig="cpacific", parser=parser, mode='S', nmin=0, nmax=0)
3  compute_green( basename_eig="cpacific", parser=parser, sourcefile="C201001100027A", basename_stachan="IU_KIP", modes='S')
4  compute_synthetic_data( basename_green="cpacific_C201001100027A_IU_KIP", parser=parser, sourcefile="C201001100027A", modes='S')
```

Many synthetic waveforms are computed in parallel using the script `syn_paral.py`. It takes as inputs a file that contains many source names, a network and station code and the number of CPUs to use. For example, in bash:

```
1  python syn_paral.py sourcesfile IU KIP 24
```

Note that for crustal corrections *CRUST1.0* crustal model needs to be added on top of the reference model. For a set of source-receiver pairs this is achived by running:

```
1  python crust_paral.py sourcesfile KIP 24
```

Box 5: Measuring

The phase delay between two waveforms as a function of frequency is computed using the script `measurement_MT.py`. One needs to provide the source and station names, the paths to the waveforms and the basename for the normal mode solutions. For example, in bash:

```
python measurement_MT.py C201001100027A IU_KIP ./../outputs/syn/cpacific_C201001100027A_IU_KIP_C201001100027A_syn_S.sac/BHZ ./../inputs/obswf/C201001100027A_IU_KIP.sac cpacific
```

Many measurements can be made in parallel:

```
python measurement_MT_paral.py sourcesfile IU KIP 24
```

Box 6: Computing finite frequency sensitivity kernels

The computation of the sensitivity kernels requires two disctinct steps: (1) compute the normal mode solutions for a radial Earth model and (2) use the solutions to compute the finite frequency sensitivity kernel for a given source-receiver pair and source moment tensor. For example to compute the sensitivity kernel at 30mHz for the source C201001100027A and station KIP:

```
1  from normal_modes import compute_eigen_solution_FFSWK, compute_sensitivity_kernel
2  compute_eigen_solution_FFSWK( model_file="CPacific", basename="cpacific", parser=parser, mode='S', nmin=0, nmax=0)
3  compute_sensitivity_kernel( basename_eig="cpacific", parser=parser, sourcefile="C201001100027A", basename_stachan="IU_KIP", freq=30, mode='S', n=0)
```

One can compute many sensitivity kernels in parallel using the script `ker_paral.py`:

```
1  python ker_paral.py sourcesfile IU KIP 24
```

This script also projects the sensitivity kernels onto the tomographic grid (see box 7).

Box 7: Grid

The tomographic grid is managed using the object oriented paradigm. Below are examples how to use the grid:

```
from parameterizations import SBG_param_3D_sphere_latlonradgrid
from graphics import mapp
from user_defined_io import read_sensitivity_kernel, write_projected_sensitivity_kernel
grid = SBG_param_3D_sphere_latlonradgrid( parser) # Generate grid
k = grid.whereami( latlonrad_to_xyz( 40, 170, 6271) # Find cell
latlonrad = grid.centerpoints[ k] # Check
K = read_sensitivity_kernel( "cpacific_C201001100027A_IU_KIP_030.00_S_bv")
Kp, err = grid.project_sens_kernel( K) # return proj K and proj error
mapp = plot_map() # Generate map
mapp.plot_grid_depth_section( grid=grid, rad=6271, data=Kp) # Plot Kp
write_projected_sensitivity_kernel( "cpacific_C201001100027A_IU_KIP_030.00_bv")
```

Box 8: Setting the forward problem

Once sensitivity kernels and phase delays and data uncertainties have been computed, a clean forward problem, considering selection criterions, needs to be set up. This is achieved by running:

```
python sola_format_data.py
```

Note that for data selection the radiation patterns are required. They can be computed in parallel with:

```
python radiat_paral.py sourcesfile 24
```

Box 9: Target resolution

The radii of the target kernels are computed with:

```
1    python target_preproc.py
```

The target kernels for cells specified in the file *ks* are projected in parallel with:

```
1    python target.py ks 24
```

10: Inversion and tomographic results

For some technical reasons it is necessary, to start with:

```
1    python sola_preproc.py
```

To the inversion (in parallel) run:

```
1    python sola_lsqr.py ks 24
```

The model solution and uncertainties are obtained by running:

```
1    python sola_postproc.py 24
```

Averaging kernels for cells specified in the *ks* file are obtained by running:

```
1    python sola_ak.py ks 24
```

11: Plotting the solutions

Here is just a small example how to plot the results in python:

```
1  from user_defined_io import read_A
2
3  A = read_A( "A_36452") # Read averaging ker
4  m = np.loadtxt( "./../solaIO/outputs/m") # read ↩
       model, sigma m
5  v, s = m[:,1], m[:,2] # extract velocities, sigma m
6  mapp = plot_map()
7  mapp.plot_grid_depth_section( grid=grid, rad=6271, ↩
       data=A) # Plot A
8  mapp.plot_grid_depth_section( grid=grid, rad=6271, ↩
       data=v) # Plot Vsv
9  mapp.plot_grid_depth_section( grid=grid, rad=6271, ↩
       data=s) # Plot std
```

Chapter 6

Conclusions

6.1 General conclusion

Seismic tomography is the only tool powerful to infer informations about the three-dimensional structure of the Earth. Tomographic models can play the role of observations to discuss geodynamical predictions. However the seismic data is noisy and the spatial coverage is highly uneven. As a result the tomographic models have a complex resolution that may induce biases and artifacts and data uncertainties propagate into model uncertainties. The model uncertainties and resolution are required to guarantee reliable interpretations. Yet they are a rare comodity in seismic tomography. Data fitting methods used to obtain a model solution have great difficulties to estimate the model uncertainties and resolution. Often they rely on crude approximations. In all cases they depend on an a priori on the model solution and no direct control is possible.

The Backus–Gilbert-type SOLA inversion, recently introduced in seismic tomography by Zaroli (2016) takes the point of view of the model resolution and uncertainties to solve the inverse problem. Though it is applicable only to linear problems, it does not need any a priori on the model itself and it provides a direct control on the model uncertainties and resolution. By construction it produces the model together with its uncertainties and resolution. All these advantages are very appealing in a region where the data coverage is highly uneven, like the Pacific region. In my thesis the challenge was to apply the SOLA inversion in the context of surface wave tomography to interpret the structure of the Pacific upper mantle.

The first application was made in the framework of ray theory with a two-step approach. In the first step path-averaged S-wave velocity versus depth profiles were produced by Maggi et al. (2006b). The second step was a regionalization to produce S-wave velocity maps at discrete depths. Since the regionalization is linear we could use the SOLA inversion. The SOLA inversion proved to provide a strong control on the model resolution and uncertainties and we obtained very consistent model solution, model uncertainties and resolution. We proposed a workflow to analyse the tomographic model using its uncertainties and resolution: (1) filter a reference model to the tomographic resolution, (2) spot statistically significant anomalies regarding the model uncertainties and (3) check the resolution to guarantee that the anomaly is resolved and that there is no bias or artifact. Using this workflow we could argue with strong statistical arguments that there seems to be a reliable pattern of anomalous slow and fast velocity bands aligned approximately southeast to northwest below the Pacific

lithosphere (∼275 km depth). Such a pattern may be related to small scale sub-lithospheric convection cells. This study was a first step toward reliable interpretations in seismic tomography. However this approach suffered from strong limits: (1) data uncertainty estimates were poor and (2) the SOLA inversion could only be two-dimensional (no vertical constraint).

The second application was made in the more elaborate framework of finite frequency theory based on the Born approximation. In this context we could invert phase delay data into a three-dimensional S-wave velocity model in one single linear step using the SOLA inversion. We designed a measurement workflow to obtain the phase delay data and we proposed an approach to estimate data uncertainties that accounts for the source and measurement errors. Since the use of the SOLA inversion for surface wave tomography in a fully three-dimensional framework is completely new, we applied this tomographic process in a synthetic case where the 'true' Earth is a known input three-dimensional model. The results showed that SOLA is powerful to produce a three-dimensional picture of the Earth interior in surface wave tomography. We showed that the knowledge of the model uncertainties and resolution provided by the SOLA inversion can be powerful to make robust interpretations of the model solution (quantifying for example horizontal smearing or depth leaking). The results of this study are very promising but it requires some more work to be fully reliable. It should be soon applied with real data to produce a three-dimensional SOLA model of the Pacific upper mantle that could be analyzed using the interpretation workflow that we proposed in Latallerie et al. (2022).

6.2 Perspectives

I believe that my thesis tackles some of the main challenges in seismic tomography. In the context of surface wave tomography we removed the need for an a priori constraint on the model solution, made possible to control and produce the model uncertainties and resolution. We found a way for more robust analysis of tomographic models with an interpretation workflow that accounts for the model uncertainties and resolution. We made these advances tractable in a fully three-dimensional framework using finite frequency theory. However these progresses can be improved further and new opportunities are opened.

6.2.1 Improving the finite frequency surface wave SOLA approach

The application of the SOLA inversion in a fully three-dimensional framework in this study can be further improved. The measurement process accounts only for the fundamental modes. Yet we showed that to highlight deeper in the mantle it is necessary to account for overtones. The measurement should be extended to higher modes soon to really take advantage of the three-dimensional framework.

In the application of SOLA with ray theory the data uncertainties were estimated by multiple sampling. The estimation of the data uncertainties was a little further improved in the application of SOLA with finite frequency theory. It was not based on the dataset itself but on an estimation of the measurement errors with the multitaper technique and source error propagation by a technique close to Monte Carlo methods. However this estimation was still very rough. The estimation of the data uncertainties should be taken more seriously. The influence of each parameter should be investigated more closely. Other source of uncertainty such as the parameterization or the crustal correction should be accounted for. The correlations between the various error components should be evaluated. At present, the estimation of the data uncertainties remains a challenging but crucial task.

In this study we have restricted the measurement on the vertically polarized Rayleigh wave to obtain phase delays. It would be interesting to extend the measurement to horizontal components, to consider also Love waves or to measure other kind of observables (e.g. polarization angle, amplitude). This would provide additional data. These new data could also be used to constrain other type of model parameters such as the P-wave velocity, the density, the attenuation or the anisotropy. The sensitivity kernels have been derived for all such kind of observables or data (e.g. Zhou, Dahlen & Nolet, 2004; Zhou, 2009b; Zhou, 2009a). Comparing models of various parameters can provide more information about the Earth interior than considering the models separately. However comparing models with complex resolution and uncertainties can be a tricky task, especially when these quantities are unkown. Here the SOLA inversion could be highly beneficial.

Recently Zaroli (2019) introduced a continuous version of the SOLA inversion in seismic tomography. Adapting the continuous formulation of the SOLA inversion in surface wave tomography could contribute to reduce the bad effects of the parameterization.

6.2.2 Toward joint inversion with body waves

Surface wave physics is inherently two dimensional. This characteristic has led to the two-step approaches in surface wave tomography that do not produce a real three-dimensional model but a set of two-dimensional maps at discrete depths. On the contrary body wave physics is three-dimensional by nature. This discrepancy made difficult the combination of these two very different kind of data. However this barrier has been removed with finite frequency theory that makes surface wave tomography a fully three-dimensional problem. For example, using finite frequency theory, Tian et al. (2011) combined SH, SS and Love waves to produce S-wave velocity models of the North American mantle with a data fitting inversion.

The combination of surface wave and body wave data has a major advantage: surface waves are mostly sensitive in the upper mantle and body waves are mostly sensitive in the lower mantle but both have a sensitivity that rapidly decreases at the transition zone (440 km - 660 km); combining surface and body wave data may shed light on the transition zone. It is quite clear that the Clapeyron slope at 410 km depth would favor the passage of rising plumes and sinking slabs but it is not clear for the 660 km discontinuity. Combining surface wave and body wave data could help to discuss such a question. Using the SOLA inversion, we could assess how much the combination of surface and body wave data improves the resolution in the transition zone.

6.2.3 Near future

I will pursue my investigations as a postdoctoral research associate at the Oxford university within the *Mantle Circulation Constrained* (MC2) project. The project aims to understand the nature and evolution of upwellings in the Earth's mantle. My role will be to produce tomographic models that can be used to test geodynamical predictions. This position is a great opportunity to address the perspectives with the SOLA surface wave tomography, to produce real models and make robust assesments of geodynamical predictions using the knowledge of the model uncertainties and resolution. Since this project is mainly centered on oceanic regions, I may have the opportunity to image, and argue, for example about plume-like upwelling structures using the SOLA surface wave tomography that I developed during my thesis.

Appendix A

Response to a seismic source

In this appendix I present some general objects and their properties that are useful to describe the seismic wavefield. Most of this appendix is a synthetis of developments found in Nolet (2008). First I introduce the Green tensor as the response to an instantaneous point source and I show that the wavefield produced by a more complex source function naturally derives from the Green tensor. Second I show that the response to an earthquake source, that is a moment tensor, also derives naturally from the Green tensor.

A.1 From instantaneous point source to finite source function

An instantaneous point source is a force that acts on an infinitesimal surface during an infinitesimal time. Mathematically it is a Dirac distribution (see Figure A.1 top). It is usually easier to find the response of a system to such a simple force rather than to a complex source function. Here I show that the full response to a finite source function (Figure A.1 bottom) is obtained easily from the response to a point source using the linearity of the wave equation and the sampling property of the Dirac distribution.

By definition, the Green tensor is the response of a system to a point source. The (i,j) component of the Green tensor is the response of the system in the i-th direction to the point force in the j-th direction. Using the $\mathcal{L}$ operator for the wave equation, the Green tensor observed at $\boldsymbol{x}$ for a point source at $\boldsymbol{x}'$ satisfies,

$$\mathcal{L}\boldsymbol{G}(\boldsymbol{x},\boldsymbol{x}') = \boldsymbol{I}\delta(\boldsymbol{x}-\boldsymbol{x}'). \tag{A.1}$$

Let $\boldsymbol{f}(\boldsymbol{x})$ be a finite source function, and let $\boldsymbol{u}(\boldsymbol{x})$ be the wavefield produced by such a source. Then,

$$\mathcal{L}\boldsymbol{u}(\boldsymbol{x}) = \boldsymbol{f}(\boldsymbol{x}). \tag{A.2}$$

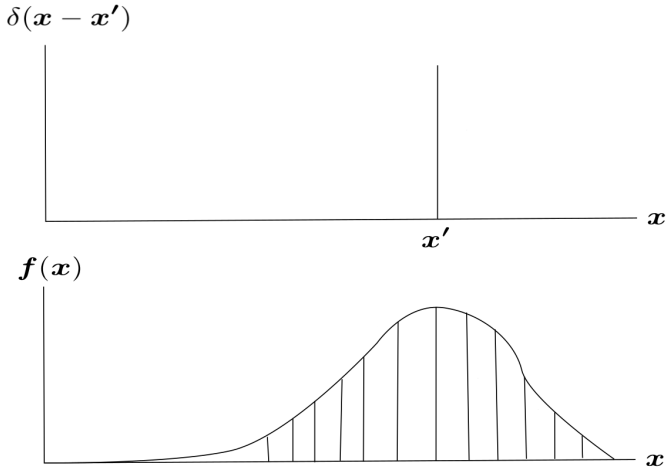

FIGURE A.1: Top: Illustration of a point source at $\boldsymbol{x}'$ as a Dirac distribution. An instantaneous point source is a force that acts on an infinitesimal surface with an infinitesimal duration. Bottom: A finite source function. A finite source function can be expressed as a sum of Dirac distributions.

Usgin the sampling property of the Dirac function we can write the source function as a superposition of Dirac functions:

$$\boldsymbol{f}(\boldsymbol{x}) = \iiint_{\oplus} \delta(\boldsymbol{x}-\boldsymbol{x}')\boldsymbol{I}\cdot\boldsymbol{f}(\boldsymbol{x}')d^3\boldsymbol{x}' \tag{A.3}$$

Replacing in A.2,

$$\mathcal{L}\boldsymbol{u}(\boldsymbol{x}) = \iiint_{\oplus} \delta(\boldsymbol{x}-\boldsymbol{x}')\boldsymbol{I}\cdot\boldsymbol{f}(\boldsymbol{x}')d^3\boldsymbol{x}' \tag{A.4}$$

Using the definition for the Green tensor (equation A.1) we have,

$$\mathcal{L}\boldsymbol{u}(\boldsymbol{x}) = \iiint_{\oplus} \mathcal{L}\boldsymbol{G}(\boldsymbol{x},\boldsymbol{x}')\cdot\boldsymbol{f}(\boldsymbol{x}')d^3\boldsymbol{x}' \tag{A.5}$$

Since the equation of motion is linear, it does not depend on the integration so that it cancels out on both sides of the equation and we finally have,

$$\boldsymbol{u}(\boldsymbol{x}) = \iiint_{\oplus} \boldsymbol{G}(\boldsymbol{x},\boldsymbol{x}')\cdot\boldsymbol{f}(\boldsymbol{x}')d^3\boldsymbol{x}' \tag{A.6}$$

This equation shows that having the response to a point source, the full response to a more complicated source function is obtained by multipliyng the response by the source function and integrating everywhere (note that the same principle applies for the time component). In other words, the response to a finite source function is the superposition of the responses of each of its fundamental components. This result is useful to derive the response to a seismic source in a radial

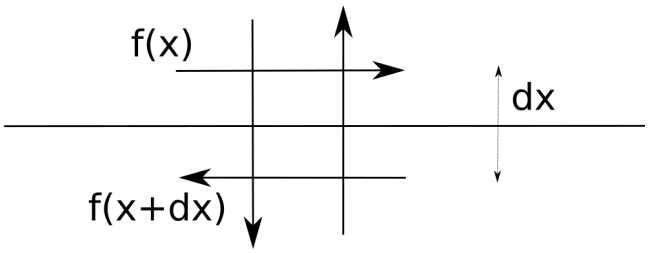

FIGURE A.2: Illustration of the earthquake source. A couple of forces (assumed equal in norm and opposed in directions) act on both side of the fault plane. A perpendicular couple of forces appears in reaction.

model of the Earth but also to derive the response in a laterally heterogeneous system where we integrate the seismic wavefields continuously produced by lateral heterogeneities.

A.2 From single force to double couple

For an earthquake source the system of forces is conveniently expressed in terms of the moment tensor. An illustration of the earthquake source is given on figure A.2. Everywhere along the fault, on each side of the fault, moving blocks apply forces in opposite directions. In response, pushed or pulled blocks apply forces in the other perpendicular directions. Let $\boldsymbol{f}(\boldsymbol{x}')$ be the force on one side of the fault. We may assume some symmetry so that on the other side of the fault, at $\boldsymbol{x}' + \boldsymbol{dx}'$ the force is $\boldsymbol{f}(\boldsymbol{x}' + \boldsymbol{dx}') = -\boldsymbol{f}(\boldsymbol{x}')$.

Therefore, using the property of the Green function, the response to both forces is,

$$\begin{aligned} &\boldsymbol{u}(\boldsymbol{x}) \\ &= \boldsymbol{G}(\boldsymbol{x},\boldsymbol{x}')\cdot\boldsymbol{f}(\boldsymbol{x}') + \boldsymbol{G}(\boldsymbol{x},\boldsymbol{x}'+\boldsymbol{dx}')\cdot\boldsymbol{f}(\boldsymbol{x}'+\boldsymbol{dx}') \\ &= \boldsymbol{G}(\boldsymbol{x},\boldsymbol{x}')\cdot\boldsymbol{f}(\boldsymbol{x}') - \boldsymbol{G}(\boldsymbol{x},\boldsymbol{x}'+\boldsymbol{dx}')\cdot\boldsymbol{f}(\boldsymbol{x}') \\ &= (\boldsymbol{G}(\boldsymbol{x},\boldsymbol{x}') - \boldsymbol{G}(\boldsymbol{x},\boldsymbol{x}'+\boldsymbol{dx}'))\cdot\boldsymbol{f}(\boldsymbol{x}') \\ &= \nabla_{\boldsymbol{x}'}\boldsymbol{G}(\boldsymbol{x},\boldsymbol{x}')\cdot\boldsymbol{dx}'\cdot\boldsymbol{f}(\boldsymbol{x}') \end{aligned} \tag{A.7}$$

where the gradient of the Green tensor with respect to the source location is a three-order tensor defined as $(\nabla_{\boldsymbol{x}'}\boldsymbol{G}(\boldsymbol{x},\boldsymbol{x}'))_{ijk} = \partial_{x'_k}\boldsymbol{G}(\boldsymbol{x},x'_k)_{ij}$. We define the moment tensor as $M_{jk} = dx'_k f_j$. Finally the wavefield can be expressed as a function of the gradient of the Green tensor and the moment tensor:

$$\boldsymbol{u} = \boldsymbol{M} : \nabla_{\boldsymbol{x}'}\boldsymbol{G}(\boldsymbol{x},\boldsymbol{x}') \tag{A.8}$$

where we use the Gibbs notation such that: $u_i = \sum_j \sum_k M_{jk}[\nabla_{\boldsymbol{x'}} \boldsymbol{G}(\boldsymbol{x}, \boldsymbol{x'})]_{ijk}$. Considering the time coordinate for the source, we have the following general formula in the frequency domain:

$$\boldsymbol{u} = -i\omega \boldsymbol{M} : \nabla_{\boldsymbol{x'}} \boldsymbol{G}(\boldsymbol{x}, \boldsymbol{x'}) \tag{A.9}$$

The response to a full moment tensor is the convolution of the moment tensor with the derivative of the response to a single point source.

Appendix B

Data uncertainties

TABLE B.1: Statistics of the uncertainties from the multitaper technique. Minimum, maximum, mean and standard deviation are in radians.

frequency [mHz]	number	minimum	maximum	mean	standard deviation
10	3503	0.013	2.981	0.401	0.452
20	6835	0.008	9.29	1.225	1.194
30	7162	0.013	12.46	1.976	1.947
40	6685	0.019	19.22	2.811	2.558
50	6877	0.029	21.862	3.485	2.807

TABLE B.2: Minimum, maximum and mean value of the errors for each source parameter investigated for the set of 576 sources considered in this study. Zeroes are ignored.

parameter	minimum	maximum	mean
latitude (deg)	0.01	0.05	0.0128
longitude (deg)	0.01	0.05	0.0115
depth (m)	100	3100	316
centroid time (s)	0.1	0.70	0.113
Mrr (N.m)	5e15	2.54e19	1.47e17
Mtt (N.m)	4e15	1.23e19	0.90e17
Mpp (N.m)	4e15	1.56e19	1.05e17
Mrt (N.m)	6e15	2.96e19	3.40e17
Mrp (N.m)	6e15	2.37e19	3.30e17
Mtp (N.m)	4e15	6.00e19	0.61e17

TABLE B.3: Mean phase delay uncertainties for 29 randomly selected source-receiver pairs.

	10mHz	20mHz	30mHz	40mHz	50mHz
latitude	1.25e-02	2.51e-02	3.78e-02	5.09e-02	6.47a-02
longitude	1.24e-02	2.47e-02	3.72e-02	5.00e-02	6.35e-02
depth	9.57e-19	2.87e-18	9.57e-19	9.57e-18	1.34e-17
time	6.27e-04	9.92e-04	1.26e-03	1.50e-03	1.77e-03
mrr	7.52e-04	5.97e-04	4.64e-04	4.18e-04	4.68e-04
mtt	9.32e-04	6.94e-04	7.57e-04	7.81e-04	8.71e-04
mpp	9.32e-04	6.94e-04	7.57e-04	7.81e-04	8.71e-04
mrt	3.39e-03	3.94e-03	3.96e-03	4.35e-03	5.21e-03
mrp	3.69e-03	4.63e-03	4.97e-03	5.53e-03	6.26e-03
mtp	8.26e-04	7.40e-04	6.66e-04	6.63e-04	7.98e-04

TABLE B.4: Maximum phase delay uncertainties for 29 randomly selected source-receiver pairs.

	10mHz	20mHz	30mHz	40mHz	50mHz
latitude	2.50e-02	5.01e-02	7.55e-02	1.02e-01	1.29e-01
longitude	2.05e-02	4.09e-02	6.16e-02	8.28e-02	1.05e-01
depth	2.23e-02	2.79e-02	3.71e-02	5.90e-02	8.25e-02
time	1.39e-17	2.78e-17	2.78e-17	1.11e-16	1.11e-16
mrr	2.54e-03	3.26e-03	3.49e-03	3.58e-03	3.94e-03
mtt	4.90e-03	3.66e-03	3.40e-03	1.77e-03	1.51e-03
mpp	3.51e-03	3.51e-03	2.76e-03	2.57e-03	4.62e-03
mrt	1.82e-02	2.32e-02	2.57e-02	2.94e-02	2.71e-02
mrp	1.58e-02	2.43e-02	2.01e-02	2.42e-02	2.87e-02
mtp	2.96e-03	3.36e-03	2.25e-03	2.51e-03	4.44e-03
sum	1.16e-01	1.80e-01	2.32e-01	3.07e-01	3.86e-01

TABLE B.5: Standard deviation of phase delay uncertainties for 29 randomly selected source-receiver pairs.

	10mHz	20mHz	30mHz	40mHz	50mHz
latitude	6.36e-03	1.28e-02	1.93e-02	2.59e-02	3.30e-02
longitude	4.89e-03	9.77e-03	1.47e-02	1.98e-02	2.51e-02
depth	5.08e-03	7.88e-03	1.00e-02	1.39e-02	2.24e-02
time	3.52e-18	8.45e-18	5.06e-18	2.55e-17	2.79e-17
mrr	6.53e-04	9.33e-04	9.35e-04	9.46e-04	1.08e-03
mtt	1.02e-03	8.90e-04	6.33e-04	4.21e-04	4.37e-04
mpp	9.49e-04	8.12e-04	7.23e-04	7.58e-04	9.80e-04
mrt	4.52e-03	5.35e-03	4.92e-03	5.53e-03	5.59e-03
mrp	3.92e-03	5.12e-03	4.99e-03	5.40e-03	6.17e-03
mtp	8.34e-04	9.36e-04	5.87e-04	5.87e-04	8.80e-04
sum	2.82e-02	4.45e-02	5.68e-02	7.33e-02	9.55e-02

Appendix C

Numerical considerations

The tomographic study of chapter 5 requires successive tasks that may be computationally expensive. In table C.1 I summarize the main computational costs in term of memory usage (RAM) and computing time. These are given for the specific example of chapter 5 but they may change for example because of the gridding size, the number of data, the size of the target kernels.

This example is given for 20 stations and 571 sources leading to 20x571=11420 source-receiver pairs. The computation of the synthetic waveforms thus takes 11420 pairs x 2.2 sCPU/pair = 25124 sCPU (7hCPU) and the measurement takes 11420 pairs x 50 sCPU/pair = 571000 sCPU (159 hCPU). For one pair 5 frequencies are considered leading to 5 data/pair x 11420 pairs = 57100 data. Thus the computation of the sensitivity kernels takes 57100 data x 76 sCPU/data = 4339600 sCPU (1205 hCPU). Finally computing the data and sensitivity kernels takes approximately 1371 hours CPU time. In fact I run the code in parallel on nodes with 24 CPUs and I use 20 nodes, one for each station. Therefore setting up the forward problem takes approximately 3 hours in user time (instead of 57 days).

Say we decide to solve the inverse problem for 67104 cells. It takes 67104 cells x 7 sCPU/cell = 469728 s (130 hCPU) to project the target kernels, 67104 cell x 25 sCPU/cell = 1677600 s (466 hCPU) to compute the generalized inverse, 67104 cells x 0.6 sCPU/cell = 40262 sCPU (11 hCPU) to compute the model solution and model uncertainties and 67104 cells x 1.6 sCPU = 107366 sCPU (29 hCPU) to compute the averaging kernels. Finally solving the inverse problem takes approximately 636 hCPU. In fact I run the code in parallel on nodes with 24 CPUs and I use 8 nodes, one for each depth of the grid. Therfore it takes 3h20min to solve the inverse problem (instead of 26 days).

That the longest tasks are embarassingly parallel is a great advantage and allows to scale the problem up with more source-receiver pairs and more accurate gridding. However care must be taken on the RAM usage, especially in the inversion part. In this example 25997 data are considered (that passed selection criterion) and the grid has 194400 cells. Therefore the sensitivity matrix

TABLE C.1: Summary of the main computational costs. The first column is the python script to be run. The second colum is the RAM usage. Some scripts require to load once the G and/or Q matrices while others, that use several CPUs in parallel require to load the matrices for each CPU leading to high RAM usage. The third column is the computation time. Values in sCPU/pair indicate the time to do the task for one source-receiver pair on one CPU. Values in sCPU/cell indicate the time to do the task for one cell of the grid on one CPU. Values in seconds indicate the global time to run the script. The last colum is the time to load matrices in RAM.

task	RAM	computing time	loading time
radiat.py		0.4 sCPU/source	
syn_paral.py		50 sCPU/pair	
measurement_MT_paral.py		50 sCPU/pair	
ker_paral.py		76 sCPU/data	
sola_format_data.py	G (3.9Go)	2300 s	
target_preproc.py	G (3.9Go)	88 s	
target.py		7 sCPU/cell	
sola_preproc.py	G+Q (4+9)Go	880 s	
sola_lsqr.py	Q/CPU (9Go/CPU)	25 sCPU/cell	75s
sola_postproc.py		0.6 sCPU/cell	
sola_ak.py	G/CPU (4Go/CPU)	1.6 sCPU/cell	93s

has dimensions 25997x194400. It is highly sparse so that we end up with only 108532480 elements to store. On disk it takes 2.6Go. More importantly, on RAM it takes 3.9Go. Therefore, to use 24 CPUs at the same time to compute the averaging kernels one needs a node with at least 93.6Go of RAM. Solving the inverse problem requires another matrix Q that is less sparse than G. Folowing Zaroli (2016) the sparsity of Q can optimized by setting the first row of G as the sparsest one. Doing so, in this case study, the Q matrix takes 3Go on disk but on RAM it takes 9Go. Therefore, if one wants to solve the inverse problem with 24 CPU, one needs a node with 216Go of RAM.

Appendix D

Source/receiver parameters and models

D.1 Source/receiver parameters

TABLE D.1: Table of parameters for the sources used in the text.

GCMT id	time (UTC)	latitude	longitude	depth (km)	Mwc (N.m)
C201308301625B	2013/08/28 16:25:09.5	-175.12	51.44	26.7	6.97
C201403152351A	2014/03/15 23:51:34.5	-81.1	-5.65	32.5	6.28
C201308301625B	2013/08/30 16:25:09.5	51.44	184.88	26.7	6.97
C201103220718A	2011/03/22 07:18:51.5	37.11	144.00	12.3	6.41
C201111111041A	2011/11/11 10:41:42.9	-55.72	235.43	20.9	6.02
C201310251710A	2013/10/25 17:10:25.3	37.17	144.66	14.9	7.14

TABLE D.2: Table of parameters for the stations used in the text.

network	station id	latitude (N)	longitude (E)	elevation (m)
IU	LVC	-22.61	-68.91	2930
IU	PTCN	-25.07	-130.1	220
IU	RAO	-29.25	-177.93	60
IU	KIP	21.42	201.99	77

D.2 Models

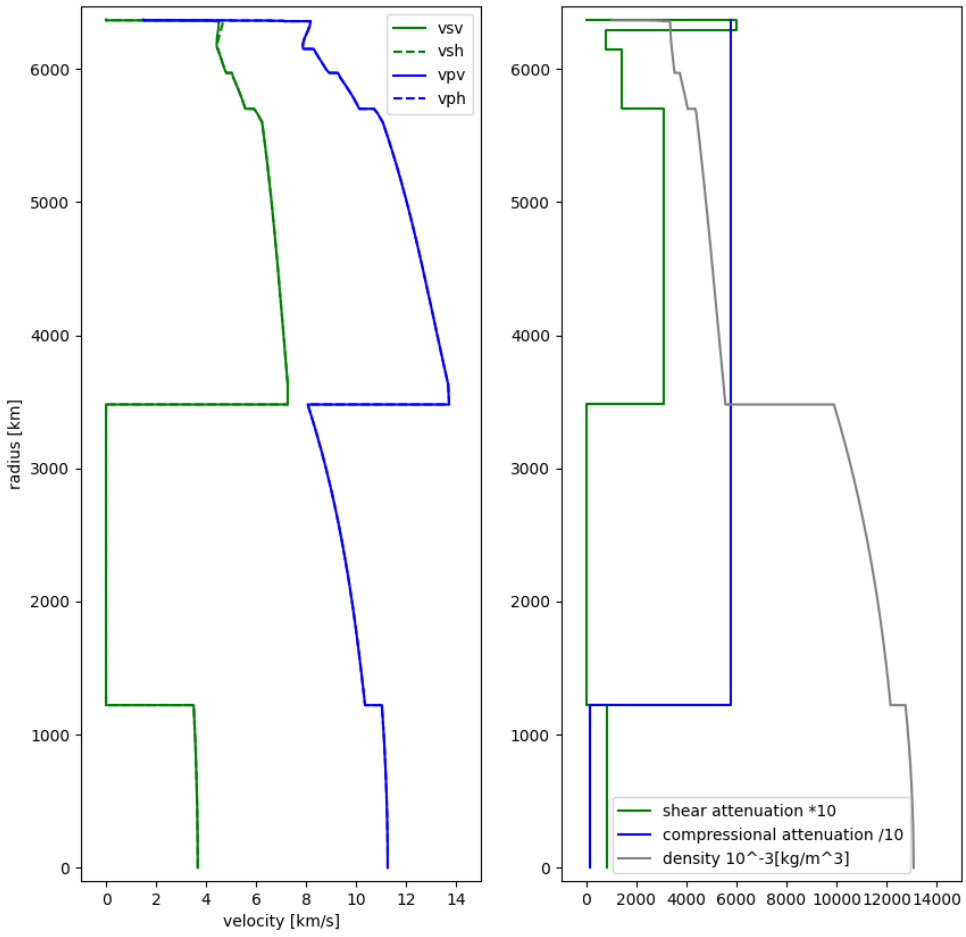

FIGURE D.1: Reference model used to compute the normal-mode solutions. Left: S (green) and P(blue) wave velocity for vertical (continuous) and horizontal (dashed) polarizations. Right: Density (gray), shear (green) and compressional (blue) attenuations. For display purposes the shear attenuation has been multiplied by 10 and compressional attenuation has been divided by 10. This model was part of the MINEOS package and represents a point in central Pacific. It is therefore well adapted for the study of the Pacific in this thesis.

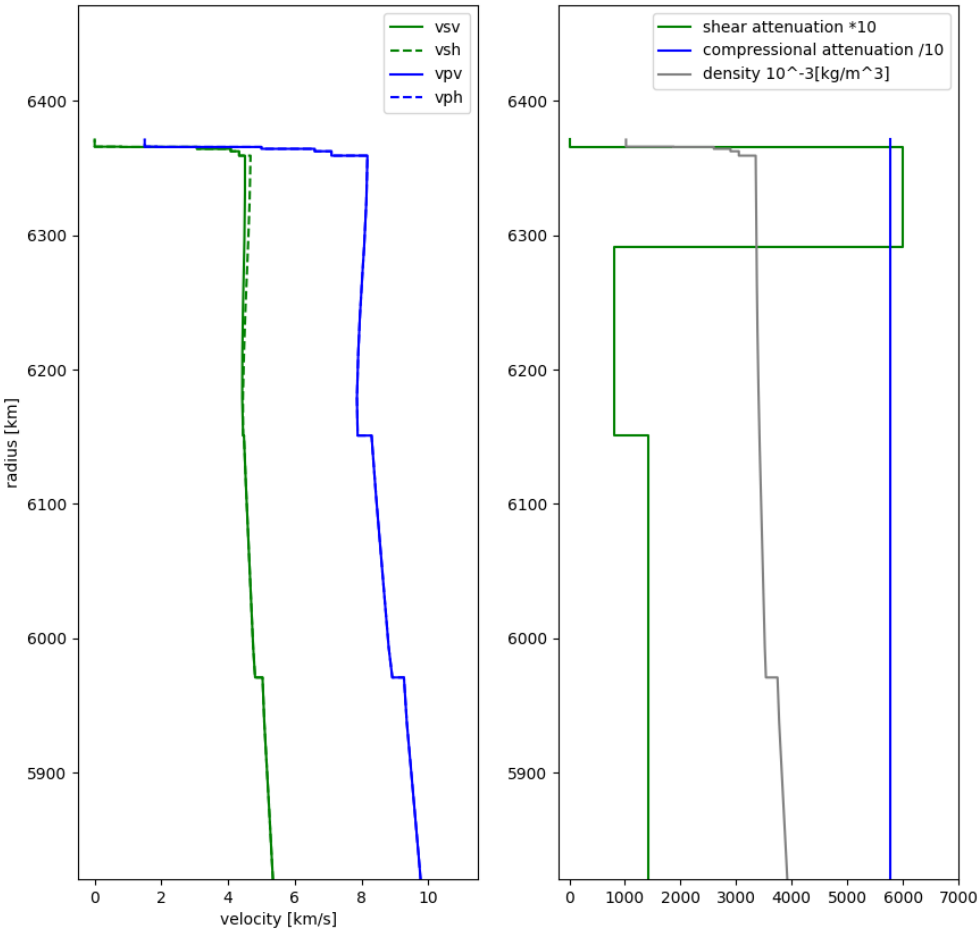

FIGURE D.2: Same as figure D.1 but close-up in the upper-mantle.

Bibliography

An, M. (Nov. 2012). "A simple method for determining the spatial resolution of a general inverse problem". en. In: *Geophysical Journal International* 191.2, pp. 849–864. DOI: 10.1111/j.1365-246X.2012.05661.x.

Arndt, N. (Sept. 2000). "Hot heads and cold tails". en. In: *Nature* 407.6803, pp. 459–461. DOI: 10.1038/35035176.

Auer, L. et al. (Apr. 2014). "*Savani* : A variable resolution whole-mantle model of anisotropic shear velocity variations based on multiple data sets". en. In: *J. Geophys. Res. Solid Earth* 119.4, pp. 3006–3034. DOI: 10.1002/2013JB010773.

Baba, K. et al. (Feb. 2006). "Mantle dynamics beneath the East Pacific Rise at 17°S: Insights from the Mantle Electromagnetic and Tomography (MELT) experiment: MANTLE DYNAMICS BENEATH THE EPR AT 17°S". en. In: *J. Geophys. Res.* 111.B2, n/a–n/a. DOI: 10.1029/2004JB003598.

Backus, G. E. & F. Gilbert (1970). "Uniqueness in the inversion of inaccurate gross Earth data". en. In: *Phil. Trans. R. Soc. A.* Series A, Mathematical and Physical Sciences 266.1173, p. 74. DOI: https://doi.org/10.1098/rsta.1970.0005.

Backus, G. E. & J. F. Gilbert (July 1967). "Numerical Applications of a Formalism for Geophysical Inverse Problems". en. In: *Geophys J Int* 13.1-3, pp. 247–276. DOI: 10.1111/j.1365-246X.1967.tb02159.x.

Backus, G. & F. Gilbert (Oct. 1968). "The Resolving Power of Gross Earth Data". en. In: *Geophys J Int* 16.2, pp. 169–205. DOI: 10.1111/j.1365-246X.1968.tb00216.x.

Ballmer, M. D. et al. (June 2009). "Intraplate volcanism with complex age-distance patterns: A case for small-scale sublithospheric convection: INTRAPLATE VOLCANISM FROM SMALL-SCALE CONVECTION". en. In: *Geochem. Geophys. Geosyst.* 10.6, n/a–n/a. DOI: 10.1029/2009GC002386.

Barmin, M. P., M. H. Ritzwoller & A. L. Levshin (2001). "A Fast and Reliable Method for Surface Wave Tomography". en. In: *Pure appl. geophys.* 158, p. 25.

Barruol, G. (2002). "PLUME investigates South Pacific Superswell". en. In: *Eos Trans. AGU* 83.45, pp. 511–514. DOI: 10.1029/2002EO000354.

Bijwaard, H. & W. Spakman (Mar. 1999). "Tomographic evidence for a narrow whole mantle plume below Iceland". en. In: *Earth and Planet. Sc. Lett.* 166.3-4, pp. 121–126. DOI: 10.1016/S0012-821X(99)00004-7.

Bird, P. (Mar. 2003). "An updated digital model of plate boundaries: UPDATED MODEL OF PLATE BOUNDARIES". en. In: *Geochem. Geophys. Geosyst.* 4.3. DOI: 10.1029/2001GC000252.

Bonadio, R. et al. (June 2021). "Optimal resolution tomography with error tracking and the structure of the crust and upper mantle beneath Ireland and Britain". en. In: *Geophysical Journal International* 226.3, pp. 2158–2188. DOI: 10.1093/gji/ggab169.

Bozdağ, E. & J. Trampert (Mar. 2008). "On crustal corrections in surface wave tomography". en. In: *Geophys. J. Int.* 172.3, pp. 1066–1082. DOI: 10.1111/j.1365-246X.2007.03690.x.

Cara, M. & J. J. Lévêque (Oct. 1987). "Waveform inversion using secondary observables". en. In: *Geophys. Res. Lett.* 14.10, pp. 1046–1049. DOI: 10.1029/GL014i010p01046.

Chang, S.-J., A. M. G. Ferreira & M. Faccenda (Apr. 2016). "Upper- and mid-mantle interaction between the Samoan plume and the Tonga–Kermadec slabs". en. In: *Nat Commun* 7.1, p. 10799. DOI: 10.1038/ncomms10799.

Chen, G. et al. (Jan. 1996). "Selected elastic moduli and their temperature derivatives for olivine and garnet with different Mg/(Mg+Fe) contents: Results from GHz ultrasonic interferometry". en. In: *Geophys. Res. Lett.* 23.1, pp. 5–8. DOI: 10.1029/95GL03604.

Chen, L. et al. (Mar. 2020). "Subduction tectonics vs. Plume tectonics—Discussion on driving forces for plate motion". en. In: *Sci. China Earth Sci.* 63.3, pp. 315–328. DOI: 10.1007/s11430-019-9538-2.

Courtillot, V. et al. (Jan. 2003). "Three distinct types of hotspots in the Earth's mantle". en. In: *Earth and Planet. Sc. Lett.* 205.3-4, pp. 295–308. DOI: 10.1016/S0012-821X(02)01048-8.

Dahlen, F. A. (2000). "Fre¨ chet kernels for ¢nite-frequency traveltimesöI. Theory". en. In: p. 18.

Dahlen, F. & J. Tromp (1998). *Theoretical Global Seismology*.

Debayle, E. (June 1999). "SV-wave azimuthal anisotropy in the Australian upper mantle: preliminary results from automated Rayleigh waveform inversion". en. In: *Geophys. J. Int.* 137.3, pp. 747–754. DOI: 10.1046/j.1365-246x.1999.00832.x.

Debayle, E. & B. L. N. Kennett (Nov. 2000). "The Australian continental upper mantle: Structure and deformation inferred from surface waves". en. In: *J. Geophys. Res.* 105.B11, pp. 25423–25450. DOI: 10.1029/2000JB900212.

Debayle, E. & J. J. Lévêque (Feb. 1997). "Upper mantle heterogeneities in the Indian Ocean from waveform inversion". en. In: *Geophys. Res. Lett.* 24.3, pp. 245–248. DOI: 10.1029/96GL03954.

Debayle, E. & M. Sambridge (Feb. 2004). "Inversion of massive surface wave data sets: Model construction and resolution assessment". en. In: *J. Geophys. Res.* 109.B2. DOI: 10.1029/2003JB002652.

DeMets, C. et al. (May 1990). "Current plate motions". en. In: *Geophysical Journal International* 101.2, pp. 425–478. DOI: 10.1111/j.1365-246X.1990.tb06579.x.

Duputel, Z. et al. (Aug. 2012). "Uncertainty estimations for seismic source inversions: Uncertainty estimations for source inversions". en. In: *Geophys. J. Int.* 190.2, pp. 1243–1256. DOI: 10.1111/j.1365-246X.2012.05554.x.

Dziewonski, A., J. Mills & S. Bloch (Feb. 1972). "Residual dispersion measurement—a new method of surface-wave analysis". en. In: *Bulletin of the Seismological Society of America* 62.1, pp. 129–139. DOI: 10.1785/BSSA0620010129.

Dziewonski, A. M. & D. Anderson (1981). "Preliminary reference Earth model". In: *Phys. Earth planet. Inter.* 25.4, pp. 297–356.

Dziewonski, A. M., T.-A. Chou & J. H. Woodhouse (Apr. 1981). "Determination of earthquake source parameters from waveform data for studies of global and regional seismicity". en. In: *J. Geophys. Res.* 86.B4, pp. 2825–2852. DOI: 10.1029/JB086iB04p02825.

Ekström, G., M. Nettles & A. Dziewoński (June 2012). "The global CMT project 2004–2010: Centroid-moment tensors for 13,017 earthquakes". en. In: *Physics of the Earth and Planetary Interiors* 200-201, pp. 1–9. DOI: 10.1016/j.pepi.2012.04.002.

Ekström, G. (Dec. 2011). "A global model of Love and Rayleigh surface wave dispersion and anisotropy, 25-250 s: Global dispersion model GDM52". en. In: *Geophys. J. Int.* 187.3, pp. 1668–1686. DOI: 10.1111/j.1365-246X.2011.05225.x.

Ekström, G., J. Tromp & E. W. F. Larson (Apr. 1997). "Measurements and global models of surface wave propagation". en. In: *J. Geophys. Res.* 102.B4, pp. 8137–8157. DOI: 10.1029/96JB03729.

Faul, U & I Jackson (May 2005). "The seismological signature of temperature and grain size variations in the upper mantle". en. In: *Earth and Planet. Sc. Lett.* 234.1-2, pp. 119–134. DOI: 10.1016/j.epsl.2005.02.008.

Foulger, G. R. et al. (Aug. 2001). "Seismic tomography shows that upwelling beneath Iceland is confined to the upper mantle". en. In: *Geophysical Journal International* 146.2, pp. 504–530. DOI: 10.1046/j.0956-540x.2001.01470.x.

Foulger, G. R. (2011). *Plates vs plumes: a geological controversy*. John Wiley and Sons.

Foulger, G. R. et al. (Aug. 2013). "Caveats on tomographic images". en. In: *Terra Nova* 25.4, pp. 259–281. DOI: 10.1111/ter.12041.

Freissler, R. et al. (Oct. 2020). "Tomographic filtering via the generalized inverse: a way to account for seismic data uncertainty". en. In: *Geophys. J. Int.* 223.1, pp. 254–269. DOI: 10.1093/gji/ggaa231.

French, S., V. Lekic & B. Romanowicz (Oct. 2013a). "Waveform Tomography Reveals Channeled Flow at the Base of the Oceanic Asthenosphere". en. In: *Science* 342.6155, pp. 227–230. DOI: 10.1126/science.1241514.

French, S. W. & B. A. Romanowicz (Dec. 2014). "Whole-mantle radially anisotropic shear velocity structure from spectral-element waveform tomography". en. In: *Geophysical Journal International* 199.3, pp. 1303–1327. DOI: 10.1093/gji/ggu334.

French, S., V. Lekic & B. Romanowicz (Oct. 2013b). "Waveform Tomography Reveals Channeled Flow at the Base of the Oceanic Asthenosphere". en. In: *Science* 342.6155, pp. 227–230. DOI: 10.1126/science.1241514.

Ghosh, D. et al. (Aug. 2020). "Cold Plumes Initiated by Rayleigh-Taylor Instabilities in Subduction Zones, and Their Characteristic Volcanic Distributions: The Role of Slab Dip". en. In: *JGR Solid Earth* 125.8. DOI: 10.1029/2020JB019814.

Gilbert, F. (Jan. 1976). "The Representation of Seismic Displacements in Terms of Travelling Waves". en. In: *Geophysical Journal International* 44.1, pp. 275–280. DOI: 10.1111/j.1365-246X.1976.tb00287.x.

Granet, M., M. Wilson & U. Achauer (Dec. 1995). "Imaging a mantle plume beneath the French Massif Central". en. In: *Earth and Planetary Science Letters* 136.3-4, pp. 281–296. DOI: 10.1016/0012-821X(95)00174-B.

Greenfield, T. et al. (Feb. 2022). "Post-Subduction Tectonics of Sabah, Northern Borneo, Inferred From Surface Wave Tomography". en. In: *Geophysical Research Letters* 49.3. DOI: 10.1029/2021GL096117.

Gripp, A. E. & R. G. Gordon (July 1990). "Current plate velocities relative to the hotspots incorporating the NUVEL-1 global plate motion model". en. In: *Geophys. Res. Lett.* 17.8, pp. 1109–1112. DOI: 10.1029/GL017i008p01109.

Haxby, W. F. & J. K. Weissel (Mar. 1986). "Evidence for small-scale mantle convection from Seasat altimeter data". en. In: *J. Geophys. Res.* 91.B3, pp. 3507–3520. DOI: 10.1029/JB091iB03p03507.

Hjorleifsdottir, V. (2007). "Earthquake source characterization using 3D Numerical Modeling". en. In: p. 144.

Hoggard, M. J. et al. (2017). "Oceanic residual depth measurements, the plate cooling model, and global dynamic topography: GLOBAL OCEANIC RESIDUAL DEPTH ANALYSIS". en. In: *J. Geophys. Res. Solid Earth*. DOI: 10.1002/2016JB013457.

Hosseini, K. et al. (May 2018). "SubMachine: Web-Based Tools for Exploring Seismic Tomography and Other Models of Earth's Deep Interior". en. In: *Geochem. Geophys. Geosyst.* 19.5, pp. 1464–1483. DOI: 10.1029/2018GC007431.

Hutko, A. R. et al. (May 2017). "Data Products at the IRIS-DMC: Growth and Usage". en. In: *Seismological Research Letters* 88.3, pp. 892–903. DOI: 10.1785/0220160190.

Isse, T. et al. (Mar. 2019). "Surface wave tomography for the Pacific Ocean incorporating seafloor seismic observations and plate thermal evolution". en. In: *Earth and Planet. Sc. Lett.* 510, pp. 116–130. DOI: 10.1016/j.epsl.2018.12.033.

Komatitsch, D. & J. Tromp (May 2002a). "Spectral-element simulations of global seismic wave propagation-I. Validation". en. In: *Geophysical Journal International* 149.2, pp. 390–412. DOI: 10.1046/j.1365-246X.2002.01653.x.

— (July 2002b). "Spectral-element simulations of global seismic wave propagation-II. Three-dimensional models, oceans, rotation and self-gravitation". en. In: *Geophysical Journal International* 150.1, pp. 303–318. DOI: 10.1046/j.1365-246X.2002.01716.x.

Komatitsch, D. & J.-P. Vilotte (1998). "The Spectral Element Method: An Efficient Tool to Simulate the Seismic Response of 2D and 3D Geological Structures". en. In: p. 25.

Kooi, H. (Mar. 2016). "Groundwater flow as a cooling agent of the continental lithosphere". en. In: *Nature Geosci* 9.3, pp. 227–230. DOI: 10.1038/ngeo2642.

Kustowski, B., G. Ekström & A. M. Dziewoński (June 2008). "Anisotropic shear-wave velocity structure of the Earth's mantle: A global model". en. In: *J. Geophys. Res.* 113.B6, B06306. DOI: 10.1029/2007JB005169.

Laske, G. & G. Masters (July 1996). "Constraints on global phase velocity maps from long-period polarization data". en. In: *J. Geophys. Res.* 101.B7, pp. 16059–16075. DOI: 10.1029/96JB00526.

Laske, G., G. Masters & W. Zu¨rn (July 1994). "Frequency-dependent polarization measurements of long-period surface waves and their implications for global phase-velocity maps". en. In: *Physics of the Earth and Planetary Interiors* 84.1-4, pp. 111–137. DOI: 10.1016/0031-9201(94)90037-X.

Laske, G. et al. (2013). *EGU2013-2658 Update on CRUST1.0: A 1-degree Global Model of Earth's Crust*.

Latallerie, F. et al. (Apr. 2022). "Analysis of tomographic models using resolution and uncertainties: a surface wave example from the Pacific". en. In: *Geophysical Journal International* 230.2, pp. 893–907. DOI: 10.1093/gji/ggac095.

Lebedev, S. & G. Nolet (Jan. 2003). "Upper mantle beneath Southeast Asia from *S* velocity tomography: UPPER MANTLE BENEATH SE ASIA". en. In: *J. Geophys. Res.* 108.B1. DOI: 10.1029/2000JB000073.

Lekić, V. & B. Romanowicz (May 2011). "Inferring upper-mantle structure by full waveform tomography with the spectral element method: SEM based global tomography". en. In: *Geophysical Journal International* 185.2, pp. 799–831. DOI: 10.1111/j.1365-246X.2011.04969.x.

Lerner-Lam, A. L. & T. H. Jordan (Dec. 1983). "Earth structure from fundamental and higher-mode waveform analysis". en. In: *Geophysical Journal International* 75.3, pp. 759–797. DOI: 10.1111/j.1365-246X.1983.tb05009.x.

Liu, K. & Y. Zhou (Feb. 2013). "Effects of crustal thickness variations on surface wave phase delays". en. In: *Geophys. J. Int.* 192.2, pp. 773–792. DOI: 10.1093/gji/ggs048.

— (Apr. 2016a). "Global Rayleigh wave phase-velocity maps from finite-frequency tomography". en. In: *Geophys. J. Int.* 205.1, pp. 51–66. DOI: 10.1093/gji/ggv555.

— (Apr. 2016b). "Travelling-wave Green tensor and near-field Rayleigh-wave sensitivity". en. In: *Geophys. J. Int.* 205.1, pp. 134–145. DOI: 10.1093/gji/ggv564.

Liu, Q. & Y. Gu (Sept. 2012). "Seismic imaging: From classical to adjoint tomography". en. In: *Tectonophysics* 566-567, pp. 31–66. DOI: 10.1016/j.tecto.2012.07.006.

Lévêque, J. J., L Rivera & G. Wittlinger (Oct. 1993). "On the use of the checker-board test to assess the resolution of tomographic inversions". en. In: *Geophys. J. Int.* 115.1, pp. 313–318. DOI: 10.1111/j.1365-246X.1993.tb05605.x.

Lévêque, J., E. Debayle & V. Maupin (June 1998). "Anisotropy in the Indian Ocean upper mantle from Rayleigh- and Love-waveform inversion". en. In: *Geophys. J. Int.* 133.3, pp. 529–540. DOI: 10.1046/j.1365-246X.1998.00504.x.

Ma, Z. et al. (Oct. 2014). "A comprehensive dispersion model of surface wave phase and group velocity for the globe". en. In: *Geophysical Journal International* 199.1, pp. 113–135. DOI: 10.1093/gji/ggu246.

Maggi, A et al. (Oct. 2006a). "Azimuthal anisotropy of the Pacific region". en. In: *Earth and Planet. Sc. Lett.* 250.1-2, pp. 53–71. DOI: 10.1016/j.epsl.2006.07.010.

Maggi, A. et al. (Sept. 2006b). "Multimode surface waveform tomography of the Pacific Ocean: a closer look at the lithospheric cooling signature". en. In: *Geophys. J. Int.* 166.3, pp. 1384–1397. DOI: 10.1111/j.1365-246X.2006.03037.x.

Magrini, F. et al. (Mar. 2022). "Surface-Wave Tomography of the Central-Western Mediterranean: New Insights Into the Liguro-Provençal and Tyrrhenian Basins". en. In: *JGR Solid Earth* 127.3. DOI: 10.1029/2021JB023267.

Maguire, R. et al. (Jan. 2018). "Evaluating the Resolution of Deep Mantle Plumes in Teleseismic Traveltime Tomography: RESOLUTION OF DEEP MANTLE PLUMES". en. In: *J. Geophys. Res. Solid Earth* 123.1, pp. 384–400. DOI: 10.1002/2017JB014730.

Marignier, A., A. M. G. Ferreira & T. Kitching (Sept. 2020). "The Probability of Mantle Plumes in Global Tomographic Models". en. In: *Geochem. Geophys. Geosyst.* 21.9. DOI: 10.1029/2020GC009276.

Marone, F. & B. Romanowicz (Feb. 2007). "Non-linear crustal corrections in high-resolution regional waveform seismic tomography". English. In: *Geophys. J. Int.* 170, pp. 460–467. DOI: 10.1111/j.1365-246X.2007.03399.x.

Marquering, H., G. Nolet & F. Dahlen (Mar. 1998). "Three-dimensional waveform sensitivity kernels". en. In: *Geophys. J. Int.* 132.3, pp. 521–534. DOI: 10.1046/j.1365-246X.1998.00426.x.

Masters, G., B. Misha & K. Susan (Apr. 2014). *Mineos User Manual v 1.0.2*. English.

McKenzie, D. & R. Parker (1967). *The North Pacific: An Example of Tectonics on a Sphere*.

Menke, W (1989). *Geophysical Data Analysis: Discrete Inverse Theory*. Academic Press.

Montagner, J. P. (2002). "Upper mantle low anisotropy channels below the Pacific Plate". In: *Earth and Planet. Sc. Lett.* 202.2, pp. 263–274.

Montagner, J. (1986). *Regional three-dimensional structures using long-period surface waves*.

Monteiller, V. et al. (Aug. 2015). "Three-dimensional full waveform inversion of short-period teleseismic wavefields based upon the SEM–DSM hybrid method". en. In: *Geophysical Journal International* 202.2, pp. 811–827. DOI: 10.1093/gji/ggv189.

Montelli, R. et al. (Jan. 2004). "Finite-Frequency Tomography Reveals a Variety of Plumes in the Mantle". en. In: *Science* 303.5656, pp. 338–343. DOI: 10.1126/science.1092485.

Moulik, P et al. (Dec. 2021). "Global reference seismological data sets: multi-mode surface wave dispersion". en. In: *Geophysical Journal International* 228.3, pp. 1808–1849. DOI: 10.1093/gji/ggab418.

Movaghari, R & G. J. Doloei (Mar. 2020). "3-D crustal structure of the Iran plateau using phase velocity ambient noise tomography". en. In: *Geophysical Journal International* 220.3, pp. 1555–1568. DOI: 10.1093/gji/ggz537.

Mégnin, C. et al. (June 1997). "Imaging 3-D spherical convection models: What can seismic tomography tell us about mantle dynamics?" en. In: *Geophys. Res. Lett.* 24.11, pp. 1299–1302. DOI: 10.1029/97GL01256.

Müller, R. D. et al. (Feb. 1997). "Digital isochrons of the world's ocean floor". en. In: *J. Geophys. Res.* 102.B2, pp. 3211–3214. DOI: 10.1029/96JB01781.

Müller, R. D. et al. (Apr. 2008). "Age, spreading rates, and spreading asymmetry of the world's ocean crust". en. In: *Geochem. Geophys. Geosyst.* 9.4. DOI: 10.1029/2007GC001743.

Neall, V. E. & S. A. Trewick (Oct. 2008). "The age and origin of the Pacific islands: a geological overview". en. In: *Phil. Trans. R. Soc. B* 363.1508, pp. 3293–3308. DOI: 10.1098/rstb.2008.0119.

Nettles, M. & A. M. Dziewoński (Feb. 2008). "Radially anisotropic shear velocity structure of the upper mantle globally and beneath North America". en. In: *J. Geophys. Res.* 113.B2, B02303. DOI: 10.1029/2006JB004819.

Nolet, G. (Dec. 1985). "Solving or resolving inadequate and noisy tomographic systems". en. In: *J. Comput. Phys.* 61.3, pp. 463–482. DOI: 10.1016/0021-9991(85)90075-0.

— (2008). *A Breviary of Seismic Tomography: Imaging the Interior of the Earth and Sun*. en. Cambridge: Cambridge University Press. DOI: 10.1017/CBO9780511984709.

Nolet, G., R. Montelli & J. Virieux (July 1999). "Explicit, approximate expressions for the resolution and *a posteriori* covariance of massive tomographic systems". en. In: *Geophys. J. Int.* 138.1, pp. 36–44. DOI: 10.1046/j.1365-246x.1999.00858.x.

Nolet, G., J. van Trier & R. Huisman (Jan. 1986). "A formalism for nonlinear inversion of seismic surface waves". en. In: *Geophys. Res. Lett.* 13.1, pp. 26–29. DOI: 10.1029/GL013i001p00026.

Nolet, G. et al. (Dec. 2019). "Imaging the Galápagos mantle plume with an unconventional application of floating seismometers". en. In: *Sci Rep* 9.1, p. 1326. DOI: 10.1038/s41598-018-36835-w.

Ouattara, Y., D. Zigone & A. Maggi (Nov. 2019). "Rayleigh wave group velocity dispersion tomography of West Africa using regional earthquakes and ambient seismic noise". en. In: *J Seismol* 23.6, pp. 1201–1221. DOI: 10.1007/s10950-019-09860-z.

Paige, C. C. & M. A. Saunders (Mar. 1982). "LSQR: An Algorithm for Sparse Linear Equations and Sparse Least Squares". en. In: *ACM Trans. Math. Softw.* 8.1, pp. 43–71. DOI: 10.1145/355984.355989.

Panning, M. P., V. Lekić & B. A. Romanowicz (Dec. 2010). "Importance of crustal corrections in the development of a new global model of radial anisotropy". en. In: *J. Geophys. Res.* 115.B12, B12325. DOI: 10.1029/2010JB007520.

Park, J., C. R. Lindberg & F. L. Vernon (1987). "Multitaper spectral analysis of high-frequency seismograms". en. In: *J. Geophys. Res.* 92.B12, p. 12675. DOI: 10.1029/JB092iB12p12675.

Park, J., F. L. Vernon & C. R. Lindberg (1987). "Frequency dependent polarization analysis of high-frequency seismograms". en. In: *J. Geophys. Res.* 92.B12, p. 12664. DOI: 10.1029/JB092iB12p12664.

Parker, R. L. (May 1977). "Understanding Inverse Theory". en. In: *Annu. Rev. Earth Planet. Sci.* 5.1, pp. 35–64. DOI: 10.1146/annurev.ea.05.050177.000343.

Parker, R. & D. Oldenburg (1973). "Thermal Model of Ocean Ridges". In: *Nature Physical Science* 242.122, pp. 137–139.

Parsons, B. & D. McKenzie (1978). "Mantle convection and the thermal structure of the plates". en. In: *J. Geophys. Res.* 83.B9, p. 4485. DOI: 10.1029/JB083iB09p04485.

Parsons, B. & J. G. Sclater (Feb. 1977). "An analysis of the variation of ocean floor bathymetry and heat flow with age". en. In: *J. Geophys. Res.* 82.5, pp. 803–827. DOI: 10.1029/JB082i005p00803.

Percival, D. B. & A. T. Walden (1993). *Spectral analysis for physical applications: multitaper and conventional univariate techniques*. Cambridge University Press.

Pijpers, F. & M. Thompson (1992). "Faster formulations of the optimally localized averages method for helioseismic inversions". In: *Astron. Astrophys.* 262, pp. 33–36.

— (1993). "The SOLA method for helioseismic inversion". In: *Astron. Astrophys.* 281, pp. 231–240.

Pipatprathanporn, S. & F. J. Simons (Sept. 2021). "One year of sound recorded by a mermaid float in the Pacific: hydroacoustic earthquake signals and infrasonic ambient noise". en. In: *Geophysical Journal International* 228.1, pp. 193–212. DOI: 10.1093/gji/ggab296.

Priestley, K & D Mckenzie (Apr. 2006). "The thermal structure of the lithosphere from shear wave velocities". en. In: *Earth and Planet. Sc. Lett.* 244.1-2, pp. 285–301. DOI: 10.1016/j.epsl.2006.01.008.

Priestley, K. (2003). "Seismic evidence for a moderately thick lithosphere beneath the Siberian Platform". en. In: *Geophys. Res. Lett.* 30.3, p. 1118. DOI: 10.1029/2002GL015931.

Priestley, K. & D. McKenzie (Nov. 2013). "The relationship between shear wave velocity, temperature, attenuation and viscosity in the shallow part of the mantle". en. In: *Earth and Planet. Sc. Lett.* 381, pp. 78–91. DOI: 10.1016/j.epsl.2013.08.022.

Rawlinson, N. & W. Spakman (May 2016). "On the use of sensitivity tests in seismic tomography". en. In: *Geophys. J. Int.* 205.2, pp. 1221–1243. DOI: 10.1093/gji/ggw084.

Rawlinson, N. et al. (2014). "Seismic Tomography and the Assessment of Uncertainty". In: *Adv. Geophys.* 55, pp. 1–76. DOI: https://doi.org/10.1016/bs.agph.2014.08.001..

Ritsema, J. (2005). "Global seismic structure maps". en. In: *Plates, plumes and paradigms*. Geological Society of America. DOI: 10.1130/0-8137-2388-4.11.

Ritsema, J., H. J. van Heijst & J. H. Woodhouse (Feb. 2004). "Global transition zone tomography: GLOBAL TRANSITION ZONE TOMOGRAPHY". en. In: *J. Geophys. Res.* 109.B2. DOI: 10.1029/2003JB002610.

Ritsema, J., H. J. v. Heijst & J. H. Woodhouse (Dec. 1999). "Complex Shear Wave Velocity Structure Imaged Beneath Africa and Iceland". en. In: *Science* 286.5446, pp. 1925–1928. DOI: 10.1126/science.286.5446.1925.

Ritsema, J., A. K. McNamara & A. L. Bull (Jan. 2007a). "Tomographic filtering of geodynamic models: Implications for model interpretation and large-scale mantle structure". en. In: *J. Geophys. Res.* 112.B01303. DOI: 10.1029/2006JB004566.

Ritsema, J., A. K. McNamara & A. L. Bull (2007b). "Tomographic filtering of geodynamic models: Implications for model interpretation and large-scale mantle structure". en. In: p. 8.

Ritzwoller, M. H., N. M. Shapiro & S.-J. Zhong (Sept. 2004). "Cooling history of the Pacific lithosphere". en. In: *Earth and Planet. Sc. Lett.* 226.1-2, pp. 69–84. DOI: 10.1016/j.epsl.2004.07.032.

Ruan, Y. & Y. Zhou (Apr. 2010). "The effects of 3-D anelasticity (Q) structure on surface wave phase delays". en. In: *Geophysical Journal International* 181.1, pp. 479–492. DOI: 10.1111/j.1365-246X.2010.04514.x.

Rösler, B. & S. van der Lee (Mar. 2020). "Using Seismic Source Parameters to Model Frequency-Dependent Surface-Wave Radiation Patterns". en. In: *Seismological Research Letters* 91.2A, pp. 992–1002. DOI: 10.1785/0220190128.

Sambridge, M. & N. Rawlinson (2005). "Seismic tomography with irregular meshes". en. In: *Geophysical Monograph Series*. Ed. by A. Levander & G. Nolet. Vol. 157. Washington, D. C.: American Geophysical Union, pp. 49–65. DOI: 10.1029/157GM04.

Scales, J. A. & R. Snieder (1997). "To Bayes or not to Bayes?" en. In: *Geophysics* 62.4, pp. 1045–1046.

Schmeling, H., G. Marquart & V. Nawa (May 2017). "The role of hydrothermal cooling of the oceanic lithosphere for ocean floor bathymetry and heat flow: HYDROTHERMAL COOLING OF LITHOSPHERE". en. In: *J. Geophys. Res. Solid Earth* 122.5, pp. 3934–3952. DOI: 10.1002/2016JB013881.

Seredkina, A. I. (May 2019). "Surface Wave Tomography of the Arctic from Rayleigh and Love Wave Group Velocity Dispersion Data". en. In: *Izv., Phys. Solid Earth* 55.3, pp. 439–450. DOI: 10.1134/S106935131903008X.

Shapiro, N. M. et al. (Mar. 2005). "High-Resolution Surface-Wave Tomography from Ambient Seismic Noise". en. In: *Science* 307.5715, pp. 1615–1618. DOI: 10.1126/science.1108339.

Simmons, N. A. et al. (June 2019). "Resolution and Covariance of the LLNL-G3D-JPS Global Seismic Tomography Model: Applications to Travel time Uncertainty and Tomographic Filtering of Geodynamic Models". en. In: *Geophys. J. Int.* 217.3, pp. 1543–1557. DOI: 10.1093/gji/ggz102.

Simon, J. D., F. J. Simons & J. C. E. Irving (Sept. 2021). "Recording earthquakes for tomographic imaging of the mantle beneath the South Pacific by autonomous MERMAID floats". en. In: *Geophysical Journal International* 228.1, pp. 147–170. DOI: 10.1093/gji/ggab271.

Simons, F. J. et al. (Dec. 2002). "Multimode Rayleigh wave inversion for heterogeneity and azimuthal anisotropy of the Australian upper mantle". en. In: *Geophys. J. Int.* 151.3, pp. 738–754. DOI: 10.1046/j.1365-246X.2002.01787.x.

Simons, F. J. (2021). "Twenty-Thousand Leagues Under the Sea- Recording Earthquakes with Autonomous Floats". en. In: *Acoust. Today* 17.2, p. 42. DOI: 10.1121/AT.2021.17.2.42.

Slepian, D. (May 1978). "Prolate Spheroidal Wave Functions, Fourier Analysis, and Uncertainty-V: The Discrete Case". en. In: *Bell System Technical Journal* 57.5, pp. 1371–1430. DOI: 10.1002/j.1538-7305.1978.tb02104.x.

Snieder, R (June 1991). "An extension of Backus-Gilbert theory to nonlinear inverse problems". en. In: *Inverse Problems* 7.3, pp. 409–433. DOI: 10.1088/0266-5611/7/3/008.

Snieder, R. (1986). "3-D linearized scattering of surface waves and a formalism for surface wave holography". en. In: p. 25.

Snieder, R. & G. Nolet (1987). "Linearized scattering of surface waves on a spherical Earth". en. In: p. 9.

Sobolev, S. V. et al. (Sept. 2011). "Linking mantle plumes, large igneous provinces and environmental catastrophes". en. In: *Nature* 477.7364, pp. 312–316. DOI: 10.1038/nature10385.

Spakman, W. et al. (Oct. 1989). "Resolution experiments for NW Pacific subduction zone tomography". en. In: *Geophys. Res. Lett.* 16.10, pp. 1097–1100. DOI: 10.1029/GL016i010p01097.

Steinberger, B. & T. W. Becker (Oct. 2018). "A comparison of lithospheric thickness models". en. In: *Tectonophysics* 746, pp. 325–338. DOI: 10.1016/j.tecto.2016.08.001.

Tarantola, A. (Jan. 2005). *Inverse Problem Theory and Methods for Model Parameter Estimation*. en. Society for Industrial and Applied Mathematics. DOI: 10.1137/1.9780898717921.

— (Aug. 2006). "Popper, Bayes and the inverse problem". en. In: *Nature Phys* 2.8, pp. 492–494. DOI: 10.1038/nphys375.

Tarantola, A. & B. Valette (1982). "Generalized nonlinear inverse problems solved using the least squares criterion". en. In: *Rev. Geophys.* 20.2, p. 219. DOI: 10.1029/RG020i002p00219.

Thomson, D. (1982). "Spectrum estimation and harmonic analysis". en. In: *Proc. IEEE* 70.9, pp. 1055–1096. DOI: 10.1109/PROC.1982.12433.

Tian, Y. et al. (Feb. 2011). "Structure of North American mantle constrained by simultaneous inversion of multiple-frequency *SH* , *SS* , and Love waves". en. In: *J. Geophys. Res.* 116.B2, B02307. DOI: 10.1029/2010JB007704.

Tikhonov, A. N. (1963). "Solution of incorrectly formulated problems and the regularization method". In: 4, pp. 1035–1038.

Toomey, D. R. et al. (1998). "Mantle Seismic Structure Beneath the MELT Region of the East Pacific Rise from P and S Wave Tomography". en. In: p. 4.

Trampert, J (June 1998). "Global seismic tomography: the inverse problem and beyond". en. In: *Inverse Problems* 14.3, pp. 371–385. DOI: 10.1088/0266-5611/14/3/002.

Trampert, J. & R. Snieder (Mar. 1996). "Model Estimations Biased by Truncated Expansions: Possible Artifacts in Seismic Tomography". en. In: *Science* 271.5253, pp. 1257–1260. DOI: 10.1126/science.271.5253.1257.

Tromp, J. et al. (Oct. 2010). "Near real-time simulations of global CMT earthquakes: Near real-time simulations of CMT earthquakes". en. In: *Geophysical Journal International* 183.1, pp. 381–389. DOI: 10.1111/j.1365-246X.2010.04734.x.

Tsekhmistrenko, M. et al. (Aug. 2021). "A tree of Indo-African mantle plumes imaged by seismic tomography". en. In: *Nat. Geosci.* 14.8, pp. 612–619. DOI: 10.1038/s41561-021-00762-9.

W. Jason Morgan (1972). "Deep Mantle Convection Plumes and Plate Motions". en. In: *Bulletin* 56. DOI: 10.1306/819A3E50-16C5-11D7-8645000102C1865D.

Wegener, A. (1922). "Die entstehung der kontinente und ozeane". In:

Wessel, P. & L. W. Kroenke (Dec. 2000). "Ontong Java Plateau and late Neogene changes in Pacific plate motion". en. In: *J. Geophys. Res.* 105.B12, pp. 28255–28277. DOI: 10.1029/2000JB900290.

Wiggins, R. A. (1972). "The general linear inverse problem: Implication of surface waves and free oscillations for Earth structure". en. In: *Rev. Geophys.* 10.1, p. 251. DOI: 10.1029/RG010i001p00251.

Yoshizawa, K. & B. L. N. Kennett (Feb. 2004). "Multimode surface wave tomography for the Australian region using a three-stage approach incorporating finite frequency effects: THREE-STAGE SURFACE WAVE TOMOGRAPHY". en. In: *J. Geophys. Res.* 109.B2. DOI: 10.1029/2002JB002254.

— (Sept. 2005). "Sensitivity kernels for finite-frequency surface waves". en. In: *Geophys. J. Int.* 162.3, pp. 910–926. DOI: 10.1111/j.1365-246X.2005.02707.x.

Zaroli, C. (Nov. 2016). "Global seismic tomography using Backus-Gilbert inversion". en. In: *Geophys. J. Int.* 207.2, pp. 876–888. DOI: 10.1093/gji/ggw315.

— (July 2019). "Seismic tomography using parameter-free Backus-Gilbert inversion". en. In: *Geophys. J. Int.* 218.1, pp. 619–630. DOI: 10.1093/gji/ggz175.

Zaroli, C., P. Koelemeijer & S. Lambotte (Nov. 2017). "Toward Seeing the Earth's Interior Through Unbiased Tomographic Lenses". en. In: *Geophys. Res. Lett.* 44.22, pp. 11,399–11,408. DOI: 10.1002/2017GL074996.

Zhao, D., S. Maruyama & S. Omori (Jan. 2007). "Mantle dynamics of Western Pacific and East Asia: Insight from seismic tomography and mineral physics". en. In: *Gondwana Research* 11.1-2, pp. 120–131. DOI: 10.1016/j.gr.2006.06.006.

Zhou, Y. (Mar. 2009a). "Multimode surface wave sensitivity kernels in radially anisotropic earth media". en. In: *Geophysical Journal International* 176.3, pp. 865–888. DOI: 10.1111/j.1365-246X.2008.04010.x.

— (Sept. 2009b). "Surface-wave sensitivity to 3-D anelasticity". en. In: *Geophysical Journal International* 178.3, pp. 1403–1410. DOI: 10.1111/j.1365-246X.2009.04230.x.

Zhou, Y., F. A. Dahlen & G. Nolet (July 2004). "Three-dimensional sensitivity kernels for surface wave observables". en. In: *Geophys. J. Int.* 158.1, pp. 142–168. DOI: 10.1111/j.1365-246X.2004.02324.x.

Zhou, Y. et al. (Dec. 2005). "Finite-frequency effects in global surface-wave tomography". en. In: *Geophys. J. Int.* 163.3, pp. 1087–1111. DOI: 10.1111/j.1365-246X.2005.02780.x.

Zhou, Y. et al. (2006). "Global upper-mantle structure from finite-frequency surface-wave tomography". en. In: *J. Geophys. Res.* 111.B04304. DOI: 10.1029/2005JB003677.